Leibniz-Institut für
Astrophysik Potsdam

The Milky Way disks, bulge, and bar sub-populations: a chemo-dynamical view of our Galaxy in the APOGEE + Gaia era

Anna Barbara de Andrade Queiroz

dissertation
zur Erlangung des akademischen Grades

doctor rerum naturalium
(Dr. rer. nat.)

in der Wissenschaftsdisziplin
Astrophysik

Eingereicht an der
Mathematisch-Naturwissenschaftlichen Fakultät
der Universität Potsdam

Datum der Disputation: 4. April 2023

Betreuer

Dr. Cristina Chiappini/Prof. Dr. Matthias Steinmetz
Leibniz Institute für Astrophysik Potsdam (AIP)

Gutachter

Dr. Cristina Chiappini
Leibniz Institute für Astrophysik Potsdam (AIP)

Prof. Dr. Matthias Steinmetz
Leibniz Institute für Astrophysik Potsdam (AIP)

Prof. Dr. Francesca Figueras
Universitat de Barcelona (UB)

Published online on the
Publication Server of the University of Potsdam:
https://doi.org/10.25932/publishup-59061
https://nbn-resolving.org/urn:nbn:de:kobv:517-opus4-590615

Abstract

In recent decades, astronomy has seen a boom in large-scale stellar surveys of the Galaxy. The detailed information obtained about millions of individual stars in the Milky Way is bringing us a step closer to answering one of the most outstanding questions in astrophysics: how do galaxies form and evolve? The Milky Way is the only galaxy where we can dissect many stars into their high-dimensional chemical composition and complete phase space, which analogously as fossil records can unveil the past history of the genesis of the Galaxy. The processes that lead to large structure formation, such as the Milky Way, are critical for constraining cosmological models; we call this line of study Galactic archaeology or near-field cosmology.

At the core of this work, we present a collection of efforts to chemically and dynamically characterise the disks and bulge of our Galaxy. The results we present in this thesis have only been possible thanks to the advent of the *Gaia* astrometric satellite, which has revolutionised the field of Galactic archaeology by precisely measuring the positions, parallax distances and motions of more than a billion stars. Another, though not less important, breakthrough is the APOGEE survey, which has observed spectra in the near-infrared peering into the dusty regions of the Galaxy, allowing us to determine detailed chemical abundance patterns in hundreds of thousands of stars. To accurately depict the Milky Way structure, we use and develop the Bayesian isochrone fitting tool/code called `StarHorse`; this software can predict stellar distances, extinctions and ages by combining astrometry, photometry and spectroscopy based on stellar evolutionary models. The `StarHorse` code is pivotal to calculating distances where *Gaia* parallaxes alone cannot allow accurate estimates.

We show that by combining *Gaia*, APOGEE, photometric surveys and using `StarHorse`, we can produce a chemical cartography of the Milky way disks from their outermost to innermost parts. Such a map is unprecedented in the inner Galaxy. It reveals a continuity of the bimodal chemical pattern previously detected in the solar neighbourhood, indicating two populations with distinct formation histories. Furthermore, the data reveals a chemical gradient within the thin disk where the content of α-process elements and metals is higher towards the centre.

Focusing on a sample in the inner MW we confirm the extension of the chemical duality to the innermost regions of the Galaxy. We find stars with bar shape orbits to show both high- and low-α abundances, suggesting the bar formed by secular evolution trapping stars that already existed. By analysing the chemical orbital space of the inner Galactic regions, we disentangle the multiple populations that inhabit this complex region. We reveal the presence of the thin disk, thick disk, bar, and a counter-rotating population, which resembles the outcome of a perturbed proto-Galactic disk. Our study also finds that the inner Galaxy holds a high quantity of super metal-rich stars up to three times solar suggesting it is a possible repository of old super-metal-rich stars found in the solar neighbourhood.

We also enter into the complicated task of deriving individual stellar ages. With `StarHorse`, we calculate the ages of main-sequence turn-off and sub-giant stars for several public spectroscopic surveys. We validate our results by investigating linear relations between chemical abundances and time since the α and neutron capture elements are sensitive to age as a reflection of the different enrichment timescales of these elements. For further study of the disks in the solar neighbourhood, we use an unsupervised machine learning algorithm to delineate a multidimensional separation of chrono-chemical stellar groups revealing the chemical thick disk, the thin disk, and young α-rich

stars. The thick disk is shown to have a small age dispersion indicating its fast formation contrary to the thin disk that spans a wide range of ages.

With groundbreaking data, this thesis encloses a detailed chemo-dynamical view of the disk and bulge of our Galaxy. Our findings on the Milky Way can be linked to the evolution of high redshift disk galaxies, helping to solve the conundrum of galaxy formation.

Zusammenfassung

In den letzten Jahrzehnten hat die Astronomie mit großen galaktischen Durchmusterungen einen Boom erlebt. Die dadurch gewonnenen detaillierten Informationen über Millionen von Einzelsternen in der Milchstraße bringen uns der Beantwortung einer der wichtigsten Fragen der Astrophysik einen Schritt näher: Wie entstehen und entwickeln sich Galaxien? Die Milchstraße ist die einzige Galaxie, in der wir viele Sterne in ihre hochdimensionale chemische Zusammensetzung und ihren vollständigen Phasenraum zerlegen können, was analog zu fossilen Aufzeichnungen die Entstehungsgeschichte der Galaxie enthüllen kann. Für kosmologische Modelle ist es von entscheidender Bedeutung, die Prozesse zu verstehen, die zur Bildung großer Strukturen wie der Milchstraße führen; wir nennen diese Studienrichtung Galaktische Archäologie oder Nahfeldkosmologie.

Im Mittelpunkt dieser Arbeit stehen die Bemühungen, die Scheiben und den Bulge unserer Galaxie chemisch und dynamisch zu charakterisieren. Die Ergebnisse, die wir in dieser Arbeit vorstellen, waren nur dank des starts des astrometrischen Satelliten *Gaia* möglich, der das Gebiet der galaktischen Archäologie durch die präzise Messung der Positionen, Parallaxenwinkel und Eigenbewegungen von mehr als einer Milliarde Sterne revolutioniert hat. Ein weiterer, aber nicht minder wichtiger Durchbruch ist die APOGEE-Durchmusterung, die Spektren im nahen Infrarot beobachtet hat, was es uns erlaubt, durch die staubigen Regionen der Milchstraße hindurchzublicken und die chemischen Fingerabdrücke von Hunderttausenden von Sternen zu bestimmen. Um die Struktur der Milchstraße genau darzustellen, verwenden und entwickeln wir das Isochrone-fitting-Tool `StarHorse`; diese Software kann Sternentfernungen, Aussterbezeiten und Alter vorhersagen, indem sie Astrometrie, Photometrie und Spektroskopie auf der Grundlage von Modellen der Sternentwicklung kombiniert. Der Code `StarHorse` ist von zentraler Bedeutung für die Berechnung von Entfernungen, bei denen *Gaia*-Parallaxen allein keine Bestimmung ermöglichen.

Wir zeigen, dass wir durch die Kombination von *Gaia*, APOGEE und `StarHorse` eine chemische Kartographie der Milchstraßenscheiben von ihrem äußersten bis zum innersten Teil erstellen können. Eine solche Karte ist in der inneren Galaxis beispiellos und zeigt ein bimodales chemisches Muster, das auf zwei Populationen mit unterschiedlichen Entstehungsgeschichten hinweist. Darüber hinaus bestätigen die Daten einen chemischen Gradienten innerhalb der dünnen Scheibe, bei dem der Gehalt an Elementen und Metallen aus α-Prozessen zum Zentrum hin zunimmt ist. Eine Überdichte in der Anzahl der Sterne bestätigt zudem die Signatur eines Balkens in der inneren Galaxie.

Modelle der Galaxienentstehung sagen gewöhnlich deren Beginn im galaktischen Zentrum voraus. Wir konzentrieren uns auf eine Stichprobe in der inneren Galaxie und erwarten, dass wir primordiale stellare Populationen finden. Wir bestätigen die chemische Bimodalität der inneren Galaxie und dass der galaktische Balken sowohl aus Sternen mit hohem als auch mit niedrigem α besteht, was darauf hindeutet, dass sich der Balken durch säkulare Evolution gebildet hat, bei der bereits existierende Sterne eingefangen wurden. Durch die Analyse des chemischen Orbitalraums der inneren galaktischen Regionen können wir die verschiedenen Populationen, die diese komplexe Region bewohnen, unterscheiden. Wir zeigen das Vorhandensein einer dünnen Scheibe, einer dicken Scheibe, eines Balkens und einer gegenläufig rotierenden Population, die dem Ergebnis einer gestörten proto-galaktischen Scheibe ähnelt. Unsere Studie zeigt auch, dass die innere Galaxie eine große Menge an supermetallreichen Sternen enthält, die bis zum Dreifachen der solaren Metallizität reichen. Möglicherweise handelt es sich bei der Gruppe alter supermetallreicher Sterne, die in der Sonnenumgebung gefunden wurden um Kandidaten für Migranten aus den innersten Regionen.

Wir befassen uns auch mit der komplizierten Aufgabe der Bestimmung individueller Sternalter. Mit `StarHorse` berechnen wir das Alter von Hauptreihenabzweig- und Unterriesensternen für mehrere öffentliche spektroskopische Durchmusterungen. Wir validieren unsere Ergebnisse, indem wir lineare Abhängigkeiten zwischen den chemischen Häufigkeiten und der Zeit untersuchen, da die α- und Neutroneneinfang-Elemente empfindlich auf das Alter reagieren, was auf die unterschiedlichen Zeitskalen der Anreicherung dieser Elemente zurückzuführen ist. Zur weiteren Untersuchung der Scheiben in der Sonnenumgebung verwenden wir einen nicht überwachten Algorithmus für maschinelles Lernen, um eine mehrdimensionale Trennung der chrono-chemischen Sterngruppen vorzunehmen. Dies macht die chemisch dicke Scheibe, die dünne Scheibe und junge α Sterne erkennbar. Es zeigt sich, dass die dicke Scheibe eine geringe Altersstreuung aufweist, was auf ihre schnelle Entstehung hindeutet, während die dünne Scheibe eine große Altersspanne abdeckt.

Mit bahnbrechenden Daten liefert diese Arbeit ein detailliertes chemodynamisches Bild der Scheibe und des Bulge der Galaxis. Unsere Erkenntnisse über die Milchstraße können mit der Entwicklung von Scheibengalaxien mit hoher Rotverschiebung in Verbindung gebracht werden und so zur Lösung des Rätsels der Galaxienbildung beitragen.

“quando as pessoas atravessam a rua
e percebem no meio do caminho
que o sinal vai abrir e correr vai ser
necessário, acontecem feições que
deveriam se perpetuar mais. quando
estão sozinhas, evitam. mas quando
em dupla ou grupo, todos, todos
correm o pedaço que falta par terra
firme rindo, gargalhando. na urgência
em chegar, uma lombra infantil surge
e ninguém permanece adulto nos
metros que faltam. e eu até me
confundo pensando “olha,
pessoas apaixonadas”,
só porque correm sorrindo.”
Leticia Novaes
(hahahaha, Zaralha.)

“Als das Kind Kind war,
war es die Zeit der folgenden Fragen:
Warum bin ich ich und warum nicht du?
Warum bin ich hier und warum nicht dort?
Wann begann die Zeit und wo endet der Raum?
Ist das Leben unter der Sonne nicht bloß ein Traum?
Ist was ich sehe und höre und rieche
nicht bloß der Schein einer Welt vor der Welt?
Gibt es tatsächlich das Böse und Leute,
die wirklich die Bösen sind?
Wie kann es sein, daß ich, der ich bin,
bevor ich wurde, nicht war,
und daß einmal ich, der ich bin,
nicht mehr der ich bin, sein werde?”
Peter Handke
(Lied Vom Kindsein)
(Der Himmel über Berlin - Wim Wenders)

Contents

1 Introduction

The Milky Way, our cosmic home, can be observed as the silvery band that stretches across the night sky. Also Known as the "Silver River" in China, the "Backbone of Night" in Southern Africa, and the "Path of the Tapir" by indigenous tribes in Brazil, this celestial phenomenon has puzzled humans for millennia. The Milky Way (MW, thereafter) holds valuable and essential insights into the evolution and formation of the universe.

Despite predictions from scientists and philosophers that the MW is composed of countless stars, empirical evidence did not become available until the telescope was invented in the 17th century. However, it wasn't until the 20th century that scientists fully understood the vastness of the universe, with the discovery that the MW is just one of countless galaxies. In 1926, Edwin Hubble's observations of the Andromeda nebula proved that it was a separate galaxy (Hubble 1926), far beyond the outskirts of the MW, resolving the great debate that had begun in the 1920s (Shapley & Curtis 1921). Since then, advancements in technology have revolutionized the field of astronomy, leading to the construction of powerful telescopes, spectrographs, and space missions that continue to expand our understanding of the universe and the MW.

The early observations of Edwin Hubble led to the discovery and classification of several types of galaxies, including ellipticals, lenticulars, spirals, and irregulars. The traditional Hubble tuning fork diagram (Figure 1.1) illustrates this classification scheme. Although we cannot observe our Galaxy from the outside, observations of HII gas regions, stellar counts, and comparisons with other spiral galaxies suggest that the MW is likely a spiral barred galaxy (SB-SBc type) as seen in (Gerhard 2002; Bland-Hawthorn & Gerhard 2016). A selection of MW analogues is illustrated in Figure 1.1, based on work by Efremov (2011). Disk galaxies like the MW are typical among luminous galaxies, as reported in (Mo et al. 2010; van Dokkum et al. 2013)

On a larger scale, the Earth and the MW are located within the Local Group (LG), which also includes the Andromeda nebulae (a large spiral galaxy) and numerous dwarf galaxies spanning a diameter of approximately three megaparsecs. (McConnachie 2012). The LG and other groups of galaxies aggregate into filaments forming large structures such as super-clusters. The Laniakea supercluster, which is home to the Local Group and hundreds of thousands of galaxies, spans distances of up to 160 megaparsecs (Tully et al. 2014).

Since light travels at a finite speed, observing galaxies at different distances allows us to witness various stages of galaxy evolution. With the power of space missions such as Hubble, we have been able to contemplate the Universe from cosmic dawn to present ($z \approx 11-0$) (Madau et al. 1996; Oesch et al. 2016). Recently, the advent of the James Webb Space Telescope (Gardner et al. 2006) is pushing these limits further, identifying new candidates for the most distant galaxies ever observed, with redshifts of $z \approx 13$, dating back only to 320 million years after the big bang (Donnan et al. 2023; Robertson et al. 2022).

Still, even after observing thousands of galaxies, there are many open questions about galaxy formation and evolution. The baryon dissipation processes are key to understanding how the Universe evolved after the start of the re-ionization phase. The most acceptable cosmological model today, is the Λ cold dark matter (ΛCDM; e.g., White & Frenk 1991; Bullock & Johnston 2005; Springel et al. 2008), where Λ is the cosmological constant associated with the energy that accelerates the Universe's expansion. This model, which explains many of the observable features of the Universe (e.g., cosmic microwave background (CMB), large-scale structures, the abundances of He, H, and

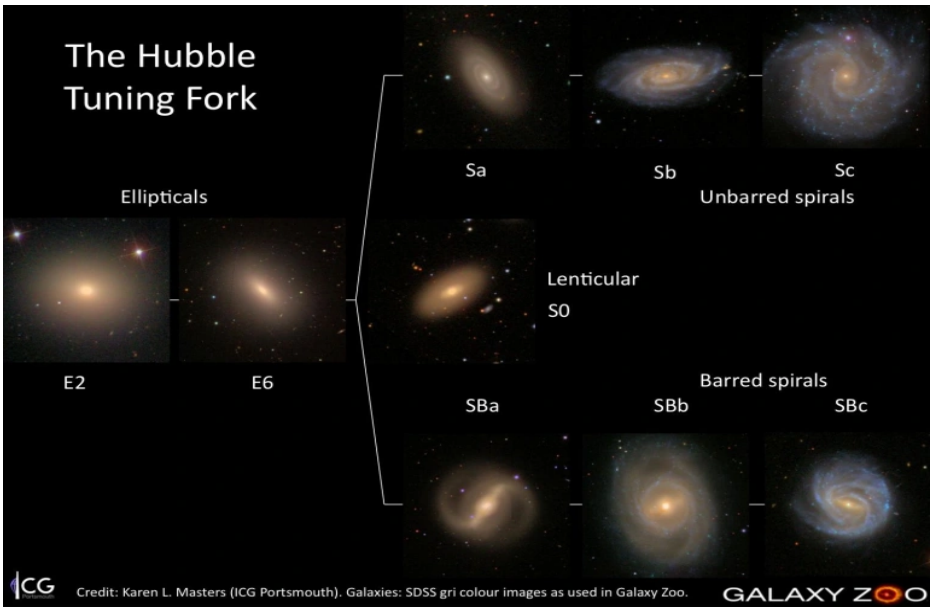

(a) The Hubble sequence is a morphological classification scheme for galaxies created by Edwin Hubble in 1926, the galaxies exemplified in the diagram are taken from the SDSS survey in griz colour, credit: Karen Masters; Galaxy Zoo.

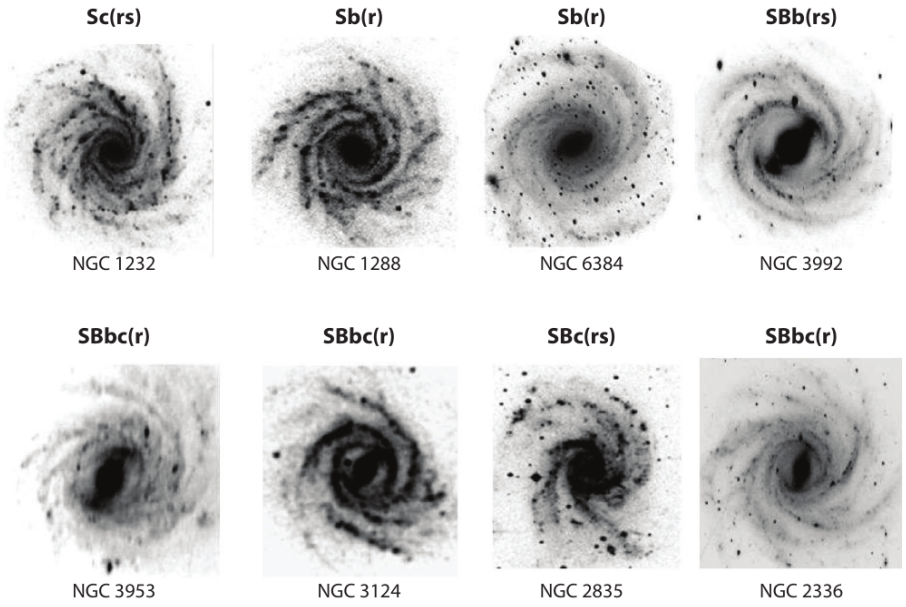

(b) Selection of Milky Way analogues, image was taken from Efremov (2011). The classification is within the Hubble-Vaucouleurs morphological scheme, an extended version of the Hubble tuning fork.

Figure 1.1: galaxy morphology and MW analogues

Li), proposes that around 200 million years after the Big Bang, H and He atomic clouds started to cool down enough to allow molecular hydrogen to form and collapse under gravity, leading to the birth of the first stars. The ΛCDM paradigm further proposes that baryonic matter forms gas and stars within dark matter bubbles or haloes. These dark matter haloes do not interact with light or electromagnetic forces but only through the force of gravity. Gravity then attracts other dark matter haloes with stars, forming larger structures, such as the MW, the LG, and the Laniakea super-cluster.

The MW provides a unique view of galaxy evolution, and can assist in the development of more complete cosmological models and theories. There is no other galaxy we can study in such intricate detail by examining its individual stars. Nowadays, we can observe millions of stars in our Galaxy and precisely derive their atmospherical parameters, chemical composition, kinematics, and sometimes even their age. Such a level of instruction is still unimaginable for extragalactic sources. The chemical compositions of Galactic stars hold vital fossil information that remains unaltered throughout the lifetime of each star. By connecting this information with kinematics and ages, we can trace the assembly of the Galaxy and unveil its evolution, rewinding the clock of the cosmos. Therefore, our Galaxy is the ultimate piece to solve the distant Universe evolution puzzle (Freeman & Bland-Hawthorn 2002).

In the following sections, we review the main research topics in Galactic Archaeology, a rapidly growing field of astrophysics. We start discussing the main findings that led to the characterization of the Galaxy structure with photometric surveys and the *Gaia* revolution. Subsequently, we explore the impact and history of using stellar chemical abundances and kinematics to predict MW formation scenarios. Finally, we focus on the recent advances of the *Gaia* (Brown 2021) era and spectroscopic surveys for the chemo-dynamical view of the MW components in the inner Galaxy.

1.1 The Milky Way structure and the *Gaia* revolution

Given that we are situated within the enormous structure of the MW, how do we determine its shape and structure? While we have the advantage of observing individual stars in our Galaxy, this comes at the cost of not having a comprehensive view of the MW as a whole. The solution to this problem lies in the precise measurements of stellar distances; this is a fundamental parameter we can use to reconstruct the MW three-dimensional morphology. Yet, measuring precise distances for a large number of stars is a challenging task.

1.1.1 The first steps towards mapping the MW

Our understanding of the shape and structure of the MW as a galaxy has evolved over time, with new discoveries and advancements in technology allowing for more precise measurements. One of the first reliable methods to measure stellar distances was created in the early 1900s when Henrietta Leavitt discovered the period-luminosity relation of Cepheid variables (Leavitt & Pickering 1912), allowing one of the first estimations of the MW dimensions by Harlow Shapley. He observed the over-density of globular clusters in the Sagittarius constellation and defined it as the Galactic Center (Thereafter GC), and suggested their spherical distribution inferred the presence of a stellar halo. However, these initial estimates had much room for improvement, as the effects of interstellar extinction were not yet well understood.

As more data and techniques became available, the study of open clusters by Trumpler (1930) revealed inconsistencies with their colour indices[1]. Open clusters would appear redder due to

1 To measure the colour index, one observes the magnitude of an object successively through two different filters or pass bands. According to Wien's law, the colour is also directly related to the temperature.

the absorption and scattering of electromagnetic radiation caused by dust, an effect particularly pronounced along the Galactic plane.[2]. Interstellar extinction obscures the disks and the GC. Therefore, the spiral arms and the Galactic bar were first detected by the motion of hydrogen gas, (Oort et al. 1958; Rougoor & Oort 1960; de Vaucouleurs & Pence 1978; Binney et al. 1991). (Oort et al. 1958) determined kinematic distances by analyzing the Doppler shift of 21-cm neutral hydrogen under the assumption that this gas was in a circular motion around the GC. This first map clearly showed signatures of spiral arms, similar to what we see in external Galaxies. The study of the gas kinematics in the inner Galaxy showed substantial differences from the circular motion in the disk, suggesting the existence of a Galactic bar. Binney et al. (1991) demonstrated that the orbital families of a barred galaxy could well explain the non-circular movement of the gas in the GC.

Still, it was necessary to prove and further understand if the stars would follow the same structure as the hydrogen clouds in the spiral and barred components.

1.1.2 Large photometric surveys

The use of extensive photometric surveys has dramatically advanced our understanding of the shape and structure of the MW. These surveys measure the apparent brightness of objects in the sky in many passbands, which allows scientists to trace different types of stars and regions. The observations at various ranges in the electromagnetic spectra and areas of the sky also helped us overcome the challenging effects of stellar extinction, which had previously obscured our view of the Galaxy's structure.

The use of the colour-magnitude diagram (CMD), or Hertzsprung–Russell diagram (HRD) (Devorkin 1977), in photometric surveys has been an efficient method for calculating distances for many stars. The "photometric distance" or "photometric parallax" is a common technique to indirectly estimate distances using the relation between apparent and absolute magnitude[3]. The absolute magnitude is estimated by fitting stellar evolutionary models to CMDs. However, this method is not without limitations. Significant uncertainties arise from degeneracies at specific stages of a star's life.

Using the photometric parallax technique for F and G type stars, Gilmore & Reid (1983); Yoshii (1982) fitted density profiles in the solar neighbourhood and found for the first time evidence for two distinct components coexisting in the Galactic disk. This was later confirmed on a much larger scale by Jurić et al. (2008) using data from the **S**loan **D**igital **S**ky **S**urvey (SDSS York et al. 2000). They analyzed a stellar number density map of the MW disk and found that two exponential functions well represented the observed vertical density, with scale heights of ≈ 300 pc and ≈900 pc at the solar radius. These are the so-called geometrically defined thin and thick disks. The same study also derived a precise offset of the Sun from the Galactic midplane of Z_0=25 kpc. The technique of photometric parallax works well with SDSS data since most of the stars are faint and are likely to sit in the main sequence. The vertical distribution is also less affected by extinction.

Photometric surveys operating in the near-infrared, especially space missions, were a significant leap in mapping the stars in the disk of our Galaxy. Since lower frequencies of the electromagnetic spectrum are less affected by extinction, photometric surveys operating in the near-infrared provided a significant advancement in mapping the stars in the MW disk. Such examples of surveys are the **D**iffuse **I**nfrared Background **E**xperiment instrument (DIRBE) on board the **C**osmic **B**ackground **E**xplorer (COBE) satellite (Hauser 1993), the Two **M**icron **A**ll-**S**ky **S**urvey ((2MASS) Skrutskie et al. 2006), the **W**ide-**f**ield **I**nfrared **S**urvey **E**xplorer (WISE Wright et al. 2010), the Space Infrared

2 plane on which the majority of a disk-shaped Galaxy mass lies
3 intrinsic brightness that a star would have if at a fixed distance of 10 pc

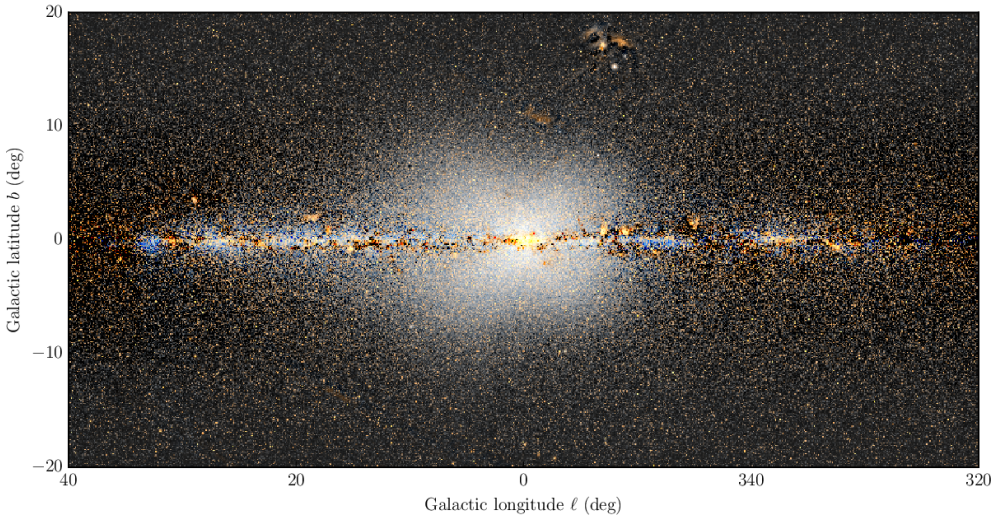

(a) WISE image for W1 and W2 in Galactic coordinates zoom in the GC. The median of each row of the image if subtracted to provide a better contrast which reveals the X-shape, the image was taken from (Ness et al. 2016).

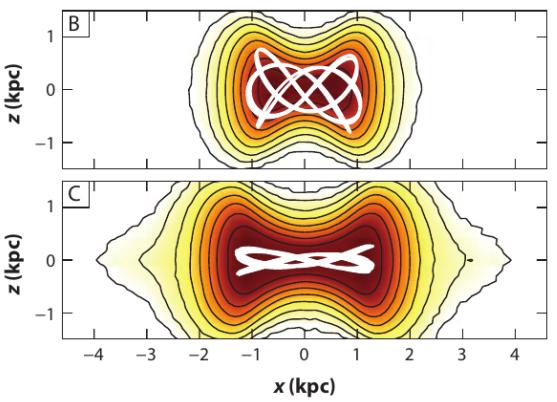

(b) Family of orbits B and C supporting the B/P shape from the model of Portail et al. (2015). The image was taken from the review of Bland-Hawthorn & Gerhard (2016) which is a modified version of the Figures in Portail et al. (2015).

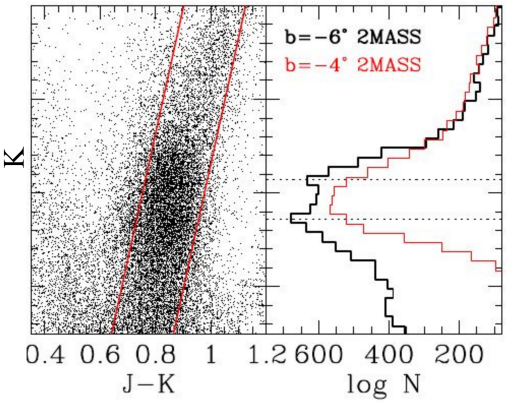

(c) Colour magnitude diagram and luminosity functions of bulge fields at l,b=(0,-6) and l,b=(0,-5) with 2MASS photometry. The image was taken from McWilliam & Zoccali (2010).

Figure 1.2: View of the inner Galaxy through near-infrared surveys

Telescope Facility (Spitzer Werner et al. 2004) and the **V**ISTA **V**ariables in the **V**ia Lactea (VVV Minniti et al. 2010).

The images from DIRBE first revealed the boxy/peanut (B/P, thereafter) nature of the Galactic bulge (Weiland et al. 1994; Binney et al. 1997). The same was confirmed by 2MASS, WISE, and Spitzer. Shortly after, the B/P shape was established to represent the inner three-dimensional part of the Galactic bar (McWilliam & Zoccali 2010; Nataf et al. 2010; Wegg & Gerhard 2013). In Figure 1.2, we show the clear image of the X-shape in the GC made by the stellar counts of the WISE survey and a dynamical model by (Portail et al. 2015), which can reproduce orbital characteristics of the X-shape structure of the Galactic bulge. To characterize the 3D structure of the inner Galaxy, most authors used the red-clump (RC) stars as tracers. The luminosity of the RC depends very weekly on its metallicity and age, making it a good indicator for stellar distances. Using this indicator McWilliam & Zoccali (2010) showed that one side of the bar is closer to the Sun, a characteristic translated into distances by the double RC in Figure 1.2 and also seen in the X shape images, where one side of the X seems to form a higher structure. Using the VVV — which exceeds the depth of the 2MASS survey by four mag — with nearly 8 million red clump giants, (Wegg & Gerhard 2013) showed that the B/P bulge has an angle of 27°, with respect to the Sun-GC line.

The same infrared missions also helped to delineate the stellar spiral anatomy of the MW disk. Benjamin et al. (2005); Drimmel (2000) detected with mid and near-infrared surveys two stellar arms, the Perseus arm, and the Scutum-Centaurus arm. This disagreed with previous observations of young OB stars and HII regions, indicating the existence of four spiral arms (Georgelin & Georgelin 1976). The disagreements arose because of the different tracers used to delineate the spiral arms: some of the arms are older and better traced by the infrared surveys, while surveys with ultraviolet or blue passbands better trace young stars.

1.1.3 Bayesian isochrone matching distances: `StarHorse`

As we have shown in the previous sections, there is enormous power in determining distances using CMD fitting. For example, Gilmore & Reid (1983) and Jurić et al. (2008) used large photometric surveys to probe extensive structures and a wide range of populations across the Galaxy. Since the discovery of the CMD, not only distances, but several astrophysical parameters can be extracted by fitting theoretical isochrones to it. It can also help filter background stars in order to detect clusters and streams (Balbinot et al. 2011; Luque et al. 2016). Elaborate methods must approach this fitting procedure with statistics to assign uncertainties to the derived parameters efficiently. Standard procedures have been applied in the literature when fitting isochrones to CMDs, e.g., minimum square root (Catelan et al. 1998; Brown et al. 2003) or maximum likelihood (Naylor & Jeffries 2006). More recently, in the last decade, Bayesian methods became the most sophisticated procedure for fitting stellar evolutionary models to data (Jørgensen & Lindegren 2005; Burnett & Binney 2010; Souza et al. 2020). Bayesian methods can minimize uncertainties by considering prior knowledge about our Galaxy, such as stellar density and chemical distributions. This statistical inference is based on the Bayes theorem:

$$P(A|B) = \frac{P(B|A)P(A)}{P(B)}; \qquad P(x_0|x,\sigma_x) = \frac{P(x,\sigma_x|x_0)P(x_0)}{P(x,\sigma_x)}, \tag{1.1}$$

where P(A|B) is the conditional or posterior probability of A given B, we transform this probability formalism in a model (x_0) to observation (x, σ_x) relation in the right side of equation 1.1, where x can be any observable that is also a parameter in the stellar evolutionary models (x_0 e.g., magnitudes at different photometric systems, surface temperatures and gravity). The function $P(x,\sigma_x|x_0)$, called likelihood, is where we quantitatively compare models to observation. One of the most standard

functions to do so is the use of Gaussians, assuming that most uncertainty measurements follow Gaussian distributions, namely:

$$P(x, \sigma_x | x_0) = \prod_i \frac{1}{\sqrt{2\pi\sigma_{x_i}^2}} \exp\left[-\frac{(x_i - x_{0_i})^2}{2\sigma_{x_i}^2}\right], \tag{1.2}$$

where $P(x_0)$ are the priors considered in an application and $P(x, \sigma_x)$ is the normalization across observations. We apply this formalism in a code called `StarHorse` (Santiago et al. 2016; Queiroz et al. 2018; Anders et al. 2019), which is thoroughly used and developed in the course of this thesis. The set of observables input is very flexible and can be used for different input datasets and data quality.

1.1.4 The *Gaia* Revolution

Since its launch in 2013, the *Gaia* satellite operated by the European Space Agency (ESA) (Gaia Collaboration et al. 2016) has made remarkable scientific discoveries. The ESA mission is designed for astrometry, which is the precise measurement of the positions, parallaxes[4], and proper motions[5] of celestial objects. Trigonometric parallax provides the most reliable distance determination since it is a direct measurement and does not depend on a specific tracer. The Hipparcos satellite (Høg et al. 2000) measured astrometry for about 1 million stars, limited to the solar neighbourhood (100 pc), *Gaia* then took astrometry to an unprecedented scale measuring nearly 1.46 billion (1.46×10^9) sources up to *Gaia* magnitudes of $G < 21$ mag. The resolution power of *Gaia* is equivalent to measuring the width of a human hair from a distance of over 1 000 kilometres. This has undoubtedly caused a revolution in the field of Galactic astrophysics and also impacted neighbouring disciplines. Up until the date of this thesis *Gaia* has made four impacting releases (DR1, DR2, EDR3, DR3; Gaia Collaboration et al. 2016, 2018b, 2021, 2022) additionally to measuring full astrometric solutions for 1.5 billion stars it also provides the community 1.8 billion magnitudes in G passband, 8 million radial velocity[6] spectra from the **R**adial **V**elocity **S**pectrometer (RVS Cropper et al. 2018), and 219 million sources with BP/RP low-resolution spectra (De Angeli et al. 2022). For an informative review of the impact that *Gaia* has brought to Galactic astrophysics, we recommend the reader to Brown (2021). Here we focous on the main advances *Gaia* has brought to Galactic archaeology.

An impressive result obtained with *Gaia* is the large range of distances, which allows us to reconstruct the three-dimensional structure of the Galaxy. In Anders et al. (2019) we used the Bayesian isochrone-fitting tool `StarHorse` to derive distances using *Gaia* parallaxes and large photometric surveys (2MASS, WISE) as observables. The use of `StarHorse` significantly improves the accuracy of the distances, especially when the parallaxes have high uncertainties (Bailer-Jones 2015). The distances derived with `StarHorse` can be seen in Figure 1.3, superimposed on an artist's impression of the top-down view of the Galaxy. It is almost as if we were able to travel to Andromeda and take a face-on photograph of the MW, and in some way it is much more accurate than a photograph, as we reconstruct the position of each star. The results from `StarHorse` clearly show the overdensity of the bar and, at some lines of sight, the overdensities corresponding to the spiral arms.

Another significant result for characterising the structure of the MW is the resolution and extent of the various extinction maps, which have been considerably improved with the advent of *Gaia*; the three-dimensional dust maps of Green et al. (2019) are enhanced by a factor of four in the

4 the apparent annual motion of a source on the sky as an observer orbit around the solar system barycentre
5 displacement of a source on the sky due to its motion with respect to the solar system barycentre
6 velocity along the line of sight of the observer

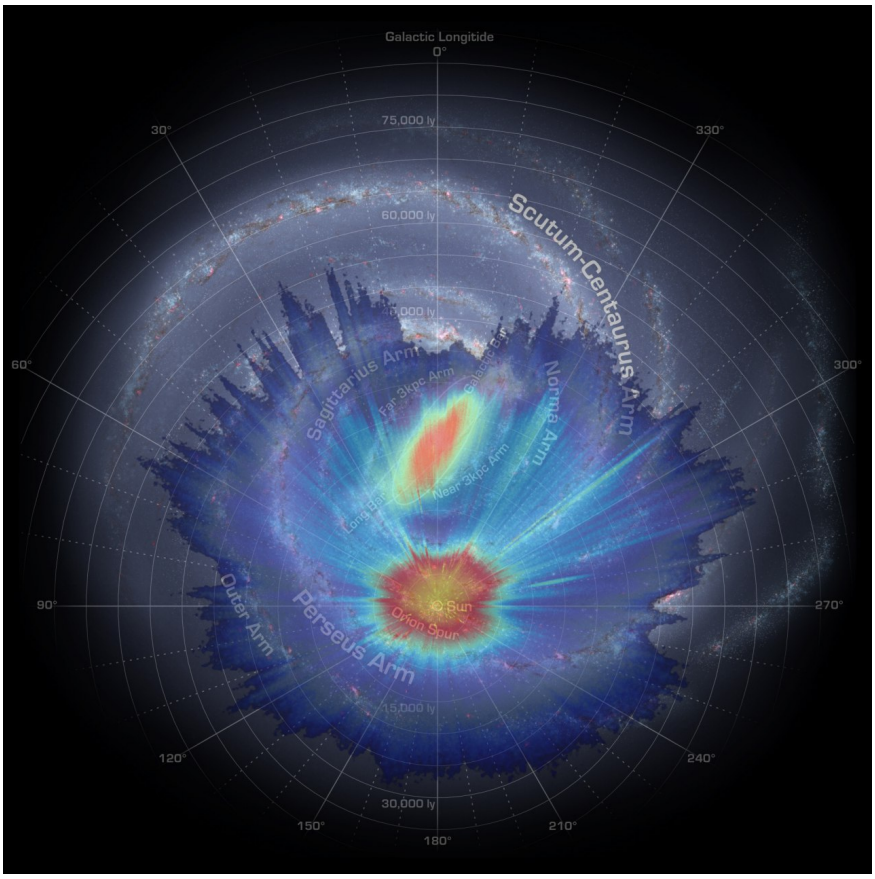

Figure 1.3: Illustration road map of the Galaxy by NASA/JPL-Caltech/R. Hurt (SSC/Caltech) superimposed to the reconstructed three-dimensional density map of the MW obtained with `StarHorse` and *Gaia* (Anders et al. 2019). Credit: Arman Khalatyan `StarHorse` team.

resolution of the extinction density with distance, see also (Capitanio et al. 2017; Lallement et al. 2022). The dust content of Green et al. (2019) outlines the four spiral arms, consistent with the studies of high-mass star-forming regions in Xu et al. (2016); the Perseus, Sagittarius, Norma and Scutum arms are shown in the artist's impression of Figure 1.3.

The ability of the *Gaia* is not only confined to precise static measurements of distance, but this mission is a revolution because it also measures the motions of the stars and, for a large fraction (≈ 8 million) radial velocities are also available, allowing a complete 6D phase space characterization. As first demonstrated in Gaia Collaboration et al. (2018c), the *Gaia* data can unravel the velocity gradients of the Galaxy characteristic of the non-axisymmetric features of the disk such as the Galactic bar, spiral arms and warp. These and other kinematical imprints left in the full phase space data enable the characterization of the Galactic potential and the size and location of the Galactic bar, spiral arms and warp (Poggio et al. 2018; Khoperskov et al. 2020; Trick et al. 2021; Robin et al. 2022). The mass of the MW has also been measured to a great extent using the phase space from *Gaia* (Monari et al. 2018; Cautun et al. 2020; Watkins et al. 2019).

In the ΛCDM scenario, accretion events have a crucial role in building up the mass of the Galaxy. Multiple works using *Gaia* data have uncovered some of the building blocks of the MW, thanks to the incredible extension of the measured 6D phase space. One of the most striking examples is the discovery of the *Gaia*-Enceladus-Sausage merger event (Helmi et al. 2018; Belokurov et al. 2018; Haywood et al. 2018b) a massive galaxy ($\approx 10^{10} M_{\odot}$) that possibly collided with the MW about 10

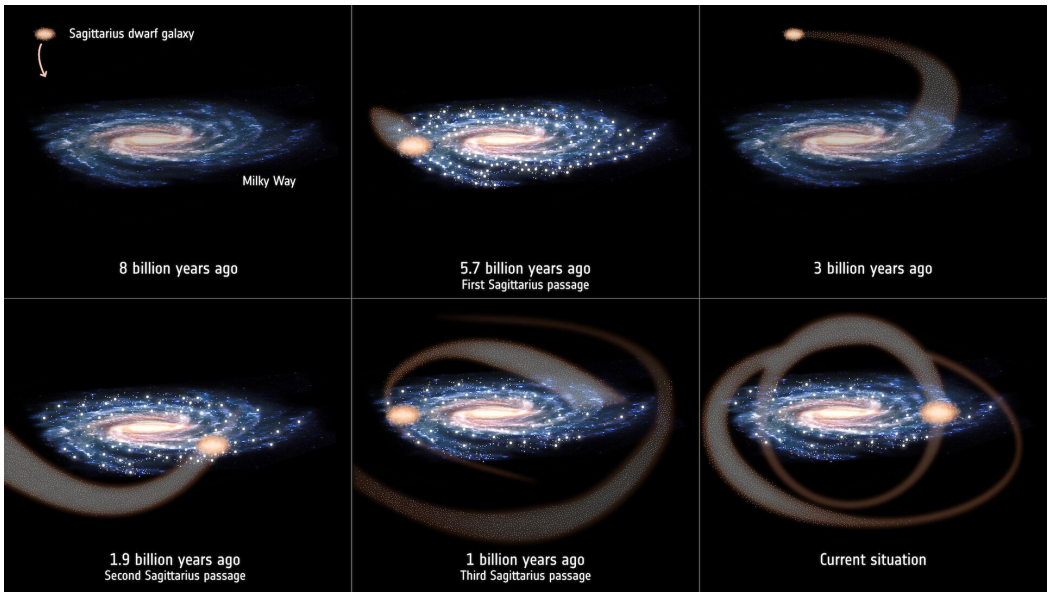

Figure 1.4: Artistic impression of the subsequent passages of the Sagittarius dwarf galaxy as it orbits our galaxy, and its impact on the MW's star formation activity, as inferred based on data from ESA's star-mapping mission, *Gaia*. Credit: ESA.

million years ago (Gallart et al. 2019). The influence of the *Gaia*-Enceladus was also detected in the portrayal of the Galactic halo shown by large-scale analysis of the CMD using *Gaia* magnitudes and parallaxes (Gaia Collaboration et al. 2018a). Furthermore, other significant massive mergers have been detected with *Gaia* (e.g., Sequoia, Helmi stream, Kraken; Myeong et al. 2019; Massari et al. 2019; Naidu et al. 2020; Helmi 2020; Kruijssen et al. 2019). Additionally, *Gaia* also plays a crucial role in the search for stellar stream (Ibata et al. 2021; Balbinot & Helmi 2021), in (Ibata et al. 2021) the authors find about eight streams entangled in a region close to the inner Galaxy.

The mapping of the stellar velocity space also reveals the perturbations that the in-situ stars from our Galaxy experience during this merger events. In Antoja et al. (2018) the authors presented evidence that the MW disk is not in equilibrium and is heavily perturbed by the passages of the Sagittarius dwarf (Ibata et al. 1994; Majewski et al. 2003). As illustrated in Figure 1.4, in this accretion process, the downfall of the Sagittarius dwarf into the MW triggered star formation activity around 5.7, 1.9, and 1 Gyr ago (Ruiz-Lara et al. 2020). The Sun itself might have been an outcome due to the first passage of the Sagittarius dwarf. Many other works have shown the footprints and impact of the Saggitarius dwarf in our Galaxy using *Gaia* data (e.g., Laporte et al. 2019; Carrillo et al. 2019).

The ESA *Gaia* mission has ushered in a new era of Galactic archaeology by providing the most comprehensive measurement of parallaxes to date. The full phase-space reconstruction offers insights into the past events that have shaped the stellar populations of the MW. By combining *Gaia* data with spectroscopic surveys, which hold unaltered information about the origins of the stars through their chemistry, we can gain a comprehensive understanding of the formation and evolution of our Galaxy.

1.2 The Fossil records of the Milky Way

One essential aspect of Galactic archaeology is the use of chemical abundances to trace back the history of star formation in a galaxy. By analyzing the chemical composition of stars, we can better

understand the conditions under which they formed, and analyse the evolution of the MW. As archaeologists study the material remains of past cultures and societies, astronomers inquire the chemical signature of the stars to understand the past-present evolution of our Galaxy.

1.2.1 Chemical imprints

Except for light elements (e.g., H, D, ^{3}He, ^{4}He, ^{7}Li Schramm & Turner 1998) which were formed right after the Big Bang, all elements that make up the Earth and humans were once formed in the interior of stars, where high temperatures and pressures cause atomic nuclei to fuse. There are different ways a star can create elements; Galactic chemical evolution models can predict their origin through nucleosynthesis theories. We show in the upper panel of Figure 1.5 the main five nucleosynthetic sites known today and how much they contribute to the production of elements according to the models of Kobayashi et al. (2020).

Hydrogen and helium are the most abundant elements in the Universe. They comprise about 99% of all baryonic matter and were the first elements to form. The metallicity[7] of the stars account for everything heavier than helium. Therefore, metallicity is intrinsically related to cosmic evolution, since elements heavier than helium accumulate within the gas where the stars form and die. Nonetheless, the relationship between age and metallicity is not straightforward because different parts of the Galaxy will experience different star formation rates and initial compositions. Similarly, elements tracking different nucleosynthetic paths will link the time evolution and the processes that involved star formation in the distinct structures of the MW. For a recent review on the matter, see Matteucci (2021).

Beatrice Tinsley was one of the pioneers in the study of chemo-dynamical models (Tinsley 1980). The Wallerstein-Tinsley diagram (Wallerstein 1962) is a helpful tool to analyse the chemical imprints in galaxies, since it correlates the metallicity against the α-abundances. The α-capture elements (built from ^{42}He nuclei, e.g. ^{12}C, ^{16}O, ^{20}Ne, ^{24}Mg) can be seen in Figure a) 1.5 as the elements produced in core-collapse supernovae (CCSNe). CCSNe are some of the most energetic events in the universe. When massive stars[8] burn all their fuel, their cores collapse into a tremendous explosion leaving behind traces of oxygen, silicon, and magnesium (Woosley et al. 2002). These stars are thought to be more common in the early universe, when the interstellar medium (ISM) was denser, and the star formation rate was high. Because of the high temperatures and pressures in a massive star, they live very short lives of only a few million years, quickly burning through their fuel and being the first to contribute to the chemical enrichment of the ISM (Langer 2012). Therefore, the high α abundances usually track older populations, and the [α/Fe] vs [Fe/H] diagram has been extensively used as a general classifier of the MW components, starting with Edvardsson et al. (1993) and Fuhrmann (1998). In the lower panel of Figure 1.5, we show some relations of nucleosynthetic processes such as α-abundances with age, where a clear correlation can be observed for open clusters in our Galaxy.

In Figure 1.6, we see the traditional chemical classification done in (Fuhrmann 1998): metal-poor stars fall into the halo; intermediate metal-poor and high-α stars in the thick disk; and high metallicity stars with low-α in the Solar neighbourhood, also known as the "thin disk". However, the stars defined as chemical "thin" and "thick" disks in this diagram do not match precisely the geometric thin and thick disks discussed in detail in Kawata & Chiappini (2016). One of the first attempts to explain the stellar chemical composition in a Galaxy formation model was made by

7 metallicity is often represented by the fraction of iron to hydrogen content relative to the Sun [Fe/H]. Across this thesis, we use $[X/Y] = \log_{10}(N_X/N_Y)_{\rm star} - \log_{10}(N_X/N_Y)_{\odot}$, where N_X and N_Y are the number of atoms from the respective element X or Y per unit of volume.

8 defined as those with a mass >8$M_{\odot}$ at solar metallicity (Poelarends et al. 2008)

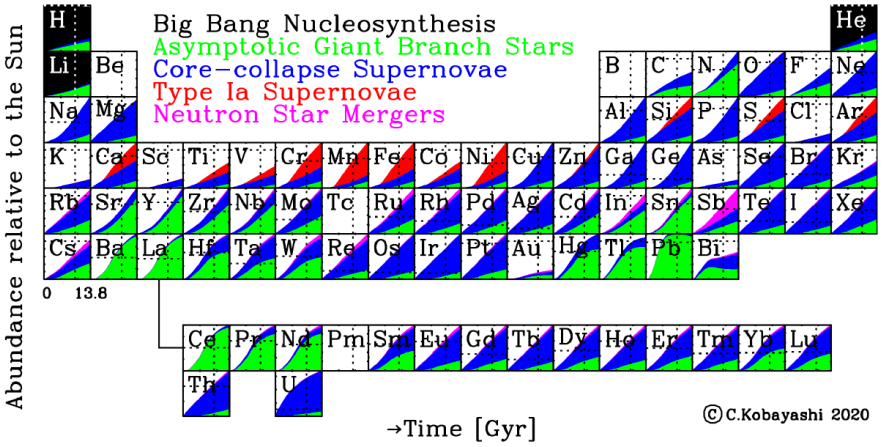

(a) The origin of elements in the periodic table according to the models of Kobayashi et al. (2020), the solar values are represented by the solid lines and the contribution of each element by the five nucleosynthetic sites is indicated by the colours in the Figure legend. Image was taken from Kobayashi et al. (2020).

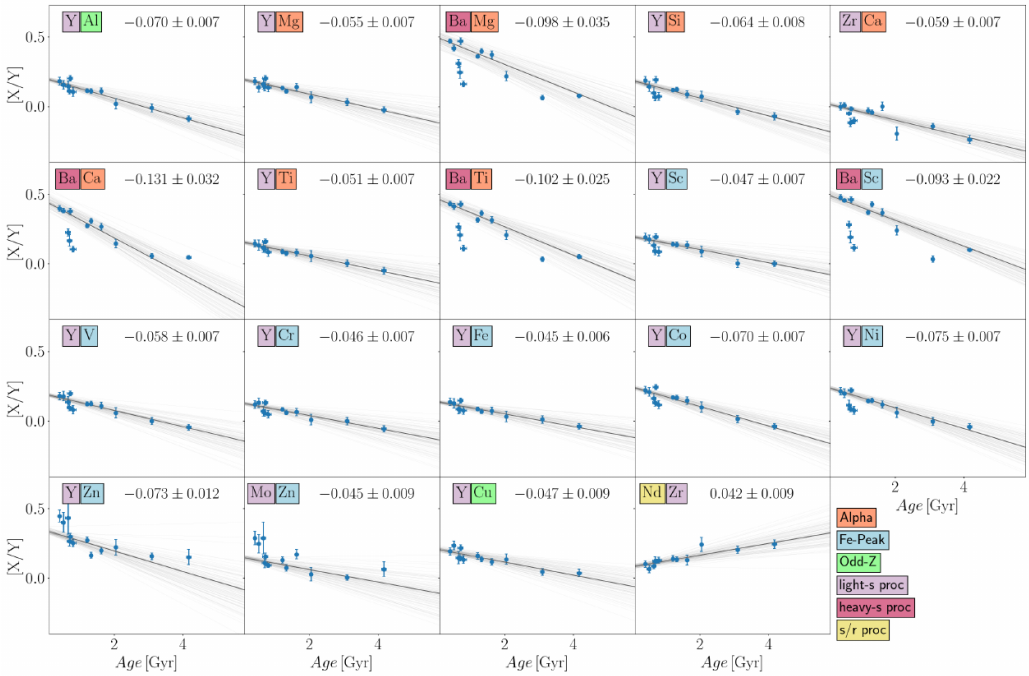

(b) Various abundance ratios that follow a close relation with age for a sample of open clusters in our Galaxy, elements are colour coded by their main nucleosynthetic process indicated in the bottom corner. Figure was taken from Casamiquela et al. (2021b)

Figure 1.5: A view of the nucleosynthesis sites and processes that lead to elements in the Universe

Eggen, Lynden-Bell, and Sandage (ELS) in Eggen et al. (1962). The authors propose the method of Galaxy formation as a monolithic collapse from a large spherical cloud of gas and dust, based on the assumption that the metal-deficient stars formed first in this spherical distribution. As the cloud collapses almost instantaneously, it becomes denser and hotter and begins to spin faster. The material at the centre of the cloud collapses more quickly than the material at the edges, creating a dense, rotating disk of gas and dust. The material that does not fall into the disk remains in the outskirts of the cloud, forming a more diffuse spherical structure known as the halo. The ELS model remains an essential foundation for modern galaxy formation and evolution theories. However, the ELS model does not explain well the chemical thick and thin disks as seen in Figure 1.6, nor the observations of globular clusters and dwarf galaxies with an extensive range of abundances independent of the direction in the halo (Canterna 1975; Pagel 1997; Matteucci 2001). The formation of the halo is primarily explained, as we have seen in previous sections, by the accretion of smaller galaxies. The disk formation and in-situ halo could be part of the scenario first described by ELS. The two-infall model outlined in (Chiappini et al. 1997) explains well the chemical dichotomy between the thin and thick disks by proposing two main gas infall episodes, where the thick disk was formed in a shorter time scale. After a hiatus, a second infall episode begins forming the thin disk component in a much longer timescale. In Figure 1.6, we show an updated two infall model by Spitoni et al. (2019) with the ages interval in the [α/Fe] vs [Fe/H] sequence.

Beyond α elements and metallicity, many other chemical abundances can be tied to evolution models to explain the origin of stellar populations. It is helpful to classify the chemical elements into families that reflect their main production sites and nucleosynthetic channels. In the lower panel of Figure 1.5, we see four different nucleosynthetic processes (where *s*-process is divided into light and heavy) and their combined correlation with time for open clusters in our Galaxy.

The slow neutron capture elements (*s*-process) are formed when a seed nucleus[9] (e.g., Fe, Ni) suffers the addition of neutrons to form a new isotope, which is typically unstable and undergoes β-decay. This changes the atomic number of the isotope and creates a new element. The rate of neutron capture is slow, which leads to the formation of isotopes with lower numbers of neutrons than those produced by the *r*-process (rapid neutron capture process) (Sneden et al. 2008; Travaglio et al. 2004). The *s*-process elements, such as Sr, Y, Zr (first peak), Ba, La, Ce, Nd, Sm (second peak) and Pb (third peak), are produced in the asymptotic giant branch (AGB) stars as indicated in the upper panel of Figure 1.5, only intermediate- to low-mass stars undergo the AGB phase. By computing the neutron capture with the α abundance fraction of elements in stars, we have a relation between the composition created by intermediate-mass and high-mass stars with different timescales of formation. This fraction increases as we approach the present time, since the present ISM forms intermediate-mass stars more efficiently, allowing us to measure stellar ages by looking at their chemistry.

Odd-Z elements have an odd number of protons in their atomic nuclei. they are formed together with α elements in massive stars during hydrostatic phases of carbon and neon-burning shells (e.g., ^{27}Al, ^{23}Na, ^{63}Cu, ^{31}P) (Sukhbold et al. 2016; Heger & Woosley 2002). A fraction of these elements is also produced and destroyed in the AGB phase during hot-bottom processes, as indicated in Figure 1.5 (Renzini et al. 2015). The odd-Z elements are shown to depend on metallicity, where deficient metallicity stars have low [Al/Fe], which is a different behaviour than general α-elements. Although for most stars, Al behaves similarly to α, and [Y/Al] shows a strong correlation with age as well as [Y/Mg], as shown in Figure 1.5 (Casamiquela et al. 2021b).

Iron-peak elements have an atomic number and local maximum in the vicinity of Fe (e.g, Mn, Cr, Ni, Ca); they are abundantly formed in sites such as type Ia supernovae (SNe-Ia; Nomoto et al. 1984).

9 isotope that is the starting point of a nuclear chain reaction

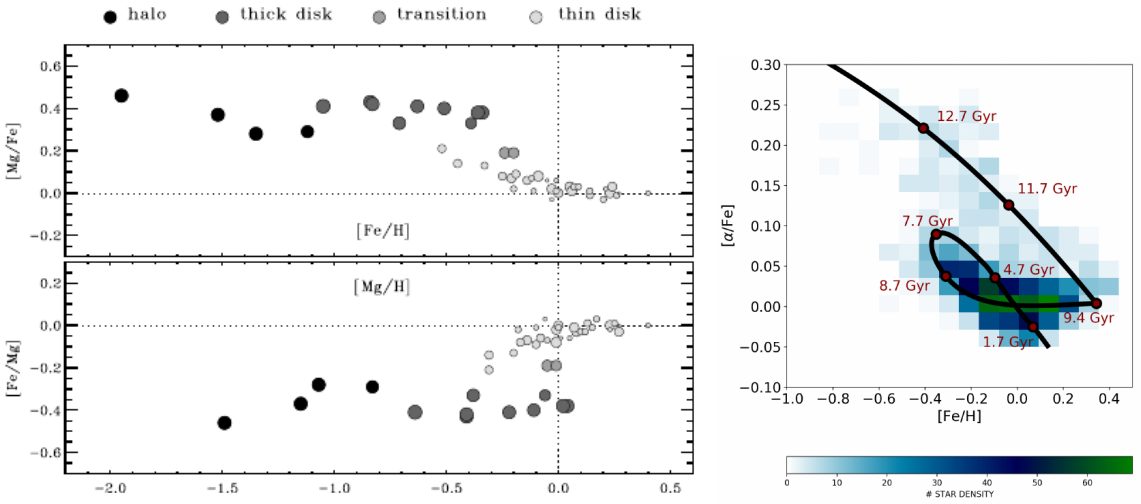

Figure 1.6: The Wallerstein-Tinsley diagram. Left panel: F and G type stars in the solar neighbourhood classified according to kinematics, age and chemical abundance; Figure was taken from Fuhrmann (1998). Right panel: Stellar density of stars in the Kepler field of APOGEE superimposed with an updated two infall model. Image was taken from Spitoni et al. (2019).

When mass accretion or merging happens between binary stars and one of the pairs is a white dwarf, if the white dwarf exceeds its Chandrasekhar limit (mass>1.4$M\odot$; Chandrasekhar 1931), the star will collapse in a SNe-Ia. Iron peak elements can also be formed in CCSNe, so they trace the life of intermediate-mass and high-mass stars since white dwarfs are the remnant core of the AGB phase. As seen in Figure 1.5, family abundances of *s*-process/iron-peak elements are also sensitive to age.

For a broad chemical view of the Galaxy, we need large surveys covering different parts of the electromagnetic spectra to measure many chemical elements and nucleosynthetic paths.

1.2.2 Large spectroscopic surveys

Spectroscopic surveys are crucial for understanding Galactic archaeology. The decomposition of light shows the patterns created by the absorption and emission of photons by the elements in the star's atmosphere. It also reveals the star's radial velocity through its Doppler effect, atmospheric temperature, and gravity. Combining radial velocities and chemistry with astrometry from surveys such as *Gaia* has the immense scientific capability to disentangle the Galaxy's star formation history.

In the last years, we experienced the results of many successful large spectroscopic surveys in different wavelengths, mapping the distinct components of our Galaxy. From low- to medium-resolution, very good examples that have impacted the Galactic archaeology field are the **RA**dial **V**elocity **E**xperiment (RAVE Steinmetz et al. 2006; Zwitter et al. 2008; Kunder et al. 2017; Steinmetz et al. 2020a), the **S**loan **E**xtension for **G**alactic **U**nderstanding and **E**xploration (SEGUE Yanny et al. 2009; Alam et al. 2015), the **L**arge sky **A**rea **M**ulti-**O**bject fiber **S**pectroscopic **T**elescope (LAMOST Cui et al. 2012; Zhao et al. 2012) and quite recently the *Gaia*-**R**adial **V**elocity **S**pectrometer (*Gaia*-RVS Recio-Blanco et al. 2022). Since 2003, RAVE has assembled medium-resolution CaII-triplet spectra (R $\approx$ 7500, λ = 8410 - 8795 Å) for about 500 000 stars with typical distances within 3 kpc from the Sun. The radial velocities and metallicities from RAVE gave us the first hints that the MW disk was not in equilibrium (Siebert et al. 2011; Williams et al. 2013) and, by calculating the escape velocity at several Galactocentric radii, Piffl et al. (2014) determined with reasonable precision, the total mass of the MW (baryons + dark matter $1.3^{+0.4}_{-0.3} \times 10^{1}2M_{\odot}$). SEGUE-1 and 2 are part of the SDSS III

project (Alam et al. 2015); they were designed to observe mostly metal-poor distant stars in the halo, with a spectrograph of low resolution (R≈2000) in a broad optical range (385 - 920 nm). SEGUE data made important contributions to the characterization of the halo and thick disk (Carollo et al. 2010; Lee et al. 2011; Bovy & Rix 2013; Bovy et al. 2012b; Minchev et al. 2013). In Carollo et al. (2010), they show with orbital analysis that the halo has an inner component with slightly higher metallicities ([Fe/H]<2) and less eccentric orbits. By dissecting mono-age populations across the disk, Bovy et al. (2012b) show that the older populations of the disk are centrally concentrated, implying an inside-out formation. In combination with *Gaia*, SEGUE achieves better distances and has recently helped characterize stream structures in the Galactic halo (Perottoni et al. 2022; Limberg et al. 2022b). From the low-resolution surveys, LAMOST and *Gaia*-RVS have the most extensive scale so far, observing more than 4 million sources each. LAMOST has great coverage of the outer disk, which helped constrain the MW rotation curve up to 100 kpc (Huang et al. 2016). In the *Gaia* era and with LAMOST data, the authors of Xiang & Rix (2022) produced age metallicity relations for sub-giant stars, which revealed two distinct phases in the formation of the MW, where the outcome of the thick disk (high α sequence) dates back to only 0.8 Gyr after the Big Bang. The radial velocities of *Gaia*-RVS have been available since the first data release of *Gaia*, but the chemical composition and atmospherical parameters are only part of the third data release available since July 2022. Since then, some interesting works have been done to improve the RVS output as the low metallicity end (Matsuno et al. 2022) and neutron capture elements (Contursi et al. 2022).

High-resolution spectroscopic surveys such as the **A**pache **P**oint **O**bservatory **G**alactic **E**volution **E**xperiment (APOGEE; Majewski et al. 2017), the **GAL**actic **A**rchaeology with **H**ERMES (GALAH; De Silva et al. 2015; Martell et al. 2017) and the ***G**aia*-**ES**O survey (GES; Gilmore 2012) derived exquisite chemical abundances and transformed our view of the Galaxy. These surveys were and are crucial in the chemical, dynamical, and spatial characterization of the MW. The GES survey observes all the significant components of our Galaxy for a total of 100 000 targets in its latest release, with two different high-resolution spectrographs in the optical spectral range (GIRAFFE spectrograph R≈20 000 and UVES spectrograph R≈47 000) and delivers abundances for 24 elements (Smiljanic et al. 2014). GES has extended studies about the bimodality of chemical thin and thick disks in volumes outside the solar vicinity and has abundances of eight different elements covering nucleosynthetic paths from α to neutron capture processes (Mikolaitis et al. 2014). GES also helped to characterize of age-metallicity relation and showed evidence that the inner disk is more metal-rich and older than the outer disk (Bergemann et al. 2014); recent works using machine learning algorithms also conclude that metal-rich stars from the inner Galaxy have migrated to the solar vicinity (Dantas et al. 2022). GES has also made significant advances in the inner Galaxy, by measuring its multi-peaked metallicity distribution function (Rojas-Arriagada et al. 2014). GALAH is a survey targeting about 500 000 in the Galactic disk; it operates with a multi-band spectrograph covering spectral ranges in the blue, red, green and infrared. The high resolution of GALAH (R≈28 000) enables high signal-to-noise abundances for 30 elemental abundances covering five nucleosynthetic paths. Multiple works using GALAH, combined with Gaia, analysed the structure of the disks: in Bland-Hawthorn et al. (2019), they recover the phase-spirals in the solar neighbourhood and further investigate the passages and mass reconstruction of the Sagittarius dwarf, in Spina et al. (2021) the authors inspect the distribution of open clusters with multiple abundances to find that the gradients which trace the clusters chemical distribution do not precisely match the stellar distributions. GALAH has also been very important in the characterization of accreted dwarfs and chemical tagging in (Buder et al. 2022; Limberg et al. 2022a). The APOGEE survey stands out from the spectroscopic surveys, since it observes with high resolution (R ≈ 20 000) in the near-infrared. Therefore APOGEE can peer into the far, dusty regions of the Galaxy. Joining *Gaia* with APOGEE has resulted in multiple breakthroughs of Galactic science: the discovery of the *Gaia*-Enceladus (Haywood et al. 2018b; Helmi et al. 2018)

and its robust analysis (Mackereth et al. 2019; Di Matteo et al. 2019); the metallicity gradients in the chemical thin disk (Anders et al. 2014; Hayden et al. 2015); the three-dimensional maps of the Local spiral arm (Lallement et al. 2018); and the chemo-dynamical view of the inner Galaxy (Bovy et al. 2019; Rojas-Arriagada et al. 2019; Hasselquist et al. 2020; Horta et al. 2021; Lucey et al. 2022). Although we also provided results for other surveys, we mainly use APOGEE throughout this thesis. In subsequent sections, we explain in more detail the use of spectroscopic surveys in defining the chemo-dynamics of the disks and bulge.

1.2.3 The Chemical thick and thin disks

One of the most striking chemical features of the Galactic disks is the dichotomy between high-α and low-α sequences first observed in Fuhrmann (1998) and shown here in Figure 1.6. This is also known as the chemically defined thin and thick disks. It is expected that most of the old high-α sequence has hotter kinematics and follows the vertical bimodality distributions detected in Gilmore & Reid (1983); Jurić et al. (2008), like the geometrically defined thin and thick disks. Because the phase space of disks significantly overlaps with each other, as shown in Adibekyan et al. (2012); Bensby et al. (2014), pre-selected thin and thick disk by geometry does not always follows the [α/Fe]-high ([α/Fe]-low) sequence. Especially in the outer disks, we see that thin disks stars flare and have larger contributions for higher distances from the plane (Minchev et al. 2019).

The existence of any separation, either chemically or geometrically, was heavily debated after Bovy et al. (2012a) had shown with G dwarfs from SEGUE that analysing mono-age-abundances and considering the selection function of the survey would result in a very smooth transition between thin-thick disks. Nonetheless, the advent of spectroscopic surveys such as APOGEE, LAMOST, and GALAH has proven incontestably the chemical bi-modality of the thin and thick disks with different selection functions and extending to large Galactocentric radii (Adibekyan et al. 2012; Bensby et al. 2014; Anders et al. 2014; Hayden et al. 2015). The first year of APOGEE is very well explored in (Anders et al. 2014), showing the [α/Fe] vs [Fe/H] abundances across a range of Galactocentric radii and quantifying their differences. In Figure 1.7, we show the Figure produced by Hayden et al. (2015) using the APOGEE data release 12 (Zasowski et al. 2013), which exemplifies well the extent of the [α/Fe] vs [Fe/H] through the Galactic disk, similarly to Anders et al. (2014), but also for different Galactic heights. The authors find that the high-α sequence has very similar characteristics throughout different Galactocentric radii. Still, its appearance vanishes for large distances of the GC and closer to the Galactic plane. They also interpreted that in the inner radii ($3 < R < 5$kpc), the [α/Fe] vs [Fe/H] converges to one single track. The low α-sequence seen across the Galaxy in Figure 1.7 has a considerable change in shape and its mean metallicity shifts from high to low from the inner to the outer Galaxy, respectively. The negative gradient of the thin chemical disk has been shown by other works as well, in Mikolaitis et al. (2014) using GES, Cheng et al. (2012) using SEGUE, in Boeche et al. (2013) with RAVE and again in the first year of APOGEE in Anders et al. (2014). The radial gradient of the chemically thin disk indicates it is not well mixed as the high-α-disk, which likely formed in a shorter time scale.

When analysing the metallicity distribution of stars at different Galactic radii, one particular effect can complicate the comparison with chemical evolution theories and models. That is radial migration, a dynamic process by which stars change their orbits within a galaxy, moving outward or inward from their birth radii. This can occur due to various physical processes, such as interactions with the Galaxy's spiral arms or with other stars that can change their angular momentum. In Minchev et al. (2013), the authors compute a high-resolution cosmological simulation with a pure chemical model of the MW and quantify the effect of radial migration using RAVE. They found that typically old stars present a stronger fraction of radial migration and that most of the metal-rich

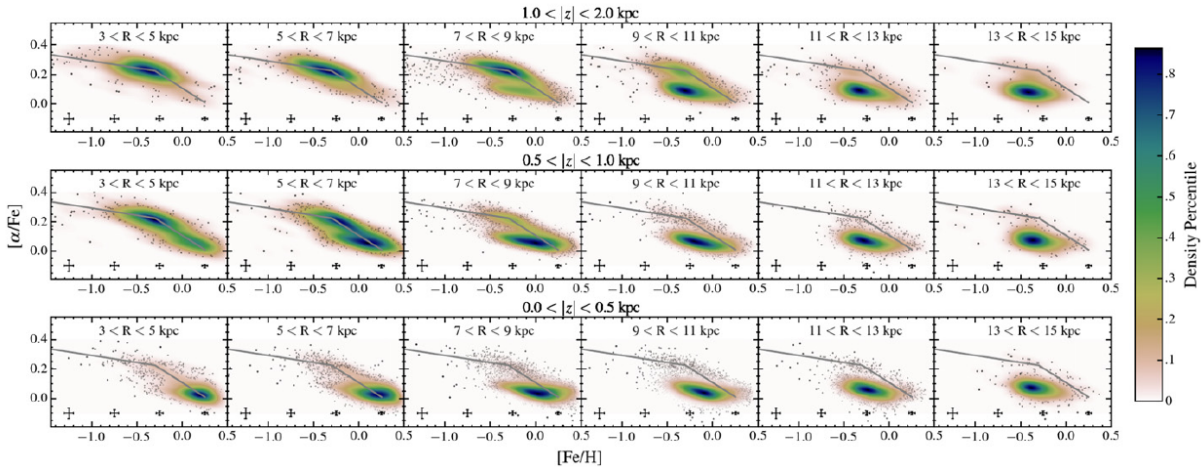

Figure 1.7: Image taken from Hayden et al. (2015). The Figure shows the distribution of stars in the [α/Fe] vs [Fe/H] plane for different ranges of Galactrocentric Radii: increasing radii from left to right; and Galactic Height: increasing from bottom to top.

stars, with $[Fe/H] > 0.15$, observed in the solar neighbourhood are migrants from the inner Galaxy. Some dynamical simulations also argue that radial migration is the main process behind forming the thick chemical disk (Schönrich & Binney 2009).

Precise ages are needed to fully understand the disk formation scenario, the dichotomy between high- and low-α sequence (Miglio et al. 2017) and, on a large scale, to fundamentally constrain the chemical dynamical models. Studies using asteroseismology can tackle this task by determining precise ages. Asteroseismology studies stellar oscillations, which can be used to probe their internal structure and properties. The frequencies of the oscillations are sensitive to the density and sound speed inside the star, which in turn depends on the star mass. From the mass of a star, one can determine its age with quite good precision (≈10%) using stellar evolutionary models (Rodrigues et al. 2014). A recent work using asteroseismology of red giants from the Kepler satellite and APOGEE Miglio et al. (2021) finds that the chemically defined thick disk is compatible with a coeval old (≈ 11 Gyr; z ≈ 2) population with an age dispersion of only 1.5 Gyr. The chemical discontinuity from high-α to low-α in the data analysed in Miglio et al. (2021) corresponds to an abrupt change in velocity dispersion and completely different age distributions, suggesting their distinct chemo-dynamical histories.

After the discovery of the massive satellite *Gaia*-Enceladus ($M_{\rm virial} > 10^{10} M_\odot$) accreted by the MW, multiple works have associated this merger event with the formation of the high-α sequence (Belokurov et al. 2018; Helmi et al. 2018; Myeong et al. 2019; Orkney et al. 2022), although using asteroseismology Montalbán et al. (2021) has demonstrated with exquisite ages and chemical abundances that a considerable part of the chemical thick disk had already been formed prior to the *Gaia*-Enceladus assembly.

The study and analysis of the chemical thin and thick disks is still a hot topic in Galatic archaeology, and new studies are arising with the powerful information that combining *Gaia* + spectroscopic releases enables. New surveys with asteroseismology will also help trace the chemo-dynamical history of the disks, and machine learning approaches can use the multiple chemistry information, such as in (Anders et al. 2018).

1.3 The inner Galaxy decoded into chemo-kinematics

The inner Galaxy, or the Galactic "bulge," plays a major role in helping us disentangle the evolutionary history and formation of the MW. It contains a significant amount of the baryon mass (approximately half of the disk mass 1.5-2.4 $\times 10^{10} M_{\odot}$, Cao et al. 2013; Simion et al. 2017; Portail et al. 2017; Valenti et al. 2016), and as in the halo and thick disk, the bulge is expected to host the oldest stars of our Galaxy (Chiappini et al. 2011; Friaça & Barbuy 2017). It is also crucial to compare the contribution of the disks in the inner Galaxy to unveil their properties and evolution processes such as dynamical instabilities, hierarchical merging, dissipational collapse, and the quantification of the radial migration history.

The hurdle of studying the bulge is that it presents several observational obstacles because of the high extinction and stellar crowding. Since the Sun is in the MW disk, we must look past many stars and dust until we reach the bulge area (distance Sun-GC = 8.2 kpc GRAVITY Collaboration et al. 2019; Bland-Hawthorn & Gerhard 2016). This issue has mostly been resolved in the large near-infrared missions commented on in Sec. 1.1.2, which first revealed the B/P shape of the bulge. Still, it took longer to have a great completion of spectroscopic surveys in the bulge area. Before APOGEE, many spectroscopic surveys were limited to pencil beams in the Baade's window[10] or at higher latitudes. Such spectroscopic surveys that were crucial in the chemo-dynamical characterization of the bulge are the **B**ulge **RA**dial **V**elocity **A**ssay (BRAVA; Rich et al. 2007), the **A**bundances and **R**adial velocity **G**alactic **O**rigins **S**urvey (ARGOS; Freeman et al. 2013), and The **GI**RAFFE **I**nner **B**ulge **S**urvey (GIBS; Zoccali et al. 2014).

The definition of "bulge" in our Galaxy is usually the region enclosing an area of ± 10° in both spherical galactocentric coordinates longitude and latitude (l, b). This definition is a bit confusing, as it does not define a Galactic component but a place in space; contrasting, a "classical bulge" observed in external galaxies is defined as the central spherical component of a galaxy with a steep brightness profile, pressure-supported kinematics, and high-velocity dispersions (Kormendy & Kennicutt 2004; Athanassoula 2005; Fisher & Drory 2016). A B/P bulge, or pseudo-bulge, is also a component observed in the centre of external galaxies but is flatter and characterised by rotation rather than dispersion. Both a classical and a pseudo-bulge can coexist (Erwin et al. 2015). We know that our Galaxy contains a B/P bulge that reflects the orbits of the bar component, but until the present day, it is a topic of discussion whether the MW has a classical bulge. In the following sections, we will summarize the main characteristics of the stellar populations in the inner Galaxy. For further reviews into this field, we recommend the reviews of Rich (2013), Gonzalez & Gadotti (2016), Zoccali & Valenti (2016), Barbuy et al. (2018), and Shen et al. (2010).

1.3.1 Dynamical properties

As we saw on Session 1.1.1 large photometric surveys uncovered the X-shape structure of the inner Galaxy, which a classical bulge formation scenario cannot explain. In dynamical models (Combes & Sanders 1981; Raha et al. 1991; Athanassoula 2005; Shen et al. 2010), the B/P bulge emerges as a natural outcome of bar formation. The bar forms through disk density instabilities, then weakens and thickens due to vertical buckling instabilities that trap stars in orbital resonances. Subsequently, the bar slowly increases in length and strength through secular evolution (Sellwood 1981; Debattista et al. 2006; Athanassoula et al. 2013; Cuomo et al. 2019). The B/P shape is formed during the buckling phase within Galactic disk populations trapped in it.

One of the first works studying the observational kinematics of bulge fields was performed by Minniti et al. (1992). The authors looked at two regions in l, b = (8°,7°), (12°, 3°) in Baade's

10 area of the sky with relatively low amounts of interstellar dust along the line of sight from Earth.

window and found an apparent increase of rotational velocity at the higher latitude field and that the velocity dispersion decreases drastically outward from the plane. Later more complete surveys, such as BRAVA with about 8 600 giants, demonstrated that stars in the B/P bulge rotate almost with the same velocity in the plane and at high latitude (Kunder et al. 2016), the so-called cylindrical rotation (Kormendy & Illingworth 1982). The cylindrical rotation was confirmed with a larger sample combining APOGEE to ARGOS in Ness et al. (2016), showing the bulge rotates cylindrically up until latitudes of 10°. In Ness et al. (2016), they also show that the velocity dispersion increases towards the centre with the highest values at $2-3°$ from the plane $\sigma_v = 130$ km/s. Extra-galactic observations also show cylindrical rotation in edge-on galaxies with a bar (Shaw et al. 1993). The rigid body rotation is a characteristic of a barred component of the Galaxy.

In Shen et al. (2010), they produce a self-consistent dynamical model of a bar that fits the data acquired by the BRAVA survey. The dynamical model of Shen et al. (2010) could fit the observations without any classical bulge component in the simulation. At this point, most of the kinematics would conclude that the MW has no classical bulge, but the picture still presents questions when works analyse chemistry with kinematics jointly. The measurement of the pattern speed of the bar $\Omega_{\rm bar}$ indicates the angular frequency with which the bar rotates around the GC and determines the orbital structure of the bar (Athanassoula 2003). The determination of the pattern speed helps to fix the position of the corotation radius which is where the centrifugal and gravitational forces cancel out in the bar rest frame. Most models indicate a pattern speed of $\Omega_{\rm bar} = 40$ kms$^{-1}kpc^{-1}$ for the MW (Shen et al. 2010; Portail et al. 2017). *Gaia* makes available proper motions for millions of stars in the bulge area, for example Sanders et al. (2019a) use the VVV combined with *Gaia* DR2 to measure a $\Omega_{\rm bar} = 41$ kms$^{-1}kpc^{-1}$, which puts the co-rotation radius of the bar at 5.7 kpc. Clarke et al. (2019) compared the kinematical data to the made-to-measure models of the findings of Portail et al. (2017) and found $\Omega_{\rm bar} = 37$ kms$^{-1}kpc^{-1}$. Recently, measurements of the bar length and pattern speed directly from orbit integration of *Gaia* and APOGEE combined gave consistent results only for a bar length of 3.5 kpc and a $\Omega_{\rm bar} = 39$ kms$^{-1}kpc^{-1}$ (Lucey et al. 2022).

1.3.2 Chemical composition

It is very clear from early estimates that the bulge contains a considerable amount of metal-rich stars (McWilliam & Rich 1994; Rich 1990). The metallicity distribution function (MDF) of the inner Galaxy presents multiple peaks, and depending on the survey and tracer it has different characteristics and numbers of peaks (Bensby et al. 2017; Johnson et al. 2013; Schultheis et al. 2017). In Zoccali et al. (2008) and Babusiaux et al. (2010) they show that there is a bimodality in the distribution metallicity of the bulge, where metal-rich stars are more concentrated in the plane and follow kinematics of a bar supporting the X-shape, while a more metal-poor population extends to higher distances from the plane and could be compatible with a primordial spheroidal component or a thick disk. In Zoccali et al. (2017) and Zoccali et al. (2018), they measured the MDF for 26 bulge fields in the GIBs surveys and weighed the bulge total mass fraction from contributions of the metal-rich (52%) and metal-poor 48% stars. They also found that the metal-poor stars produce a spherical distribution across the centre and that metal-rich stars form a square boxy shape. Recent studies using GES and APOGEE (Rojas-Arriagada et al. 2014, 2019, 2020) show that fitting Gaussians to the MDF at different latitudes results in two or three components, implying the possibility of more than two stellar populations. In Rojas-Arriagada et al. (2019) it was also starting to become clear that there is bimodality and discontinuity in the inner Galaxy between the high-α and low-α sequence as seen in the solar neighbourhood, a result not as evident in the analysis within the inner Galactocentric radii of Hayden et al. (2015). Analysis of α-process elements in the bulge show conflicting results, which is expected since treating abundances for different populations is already

complicated in the solar neighbourhood. The bulge area is not only complex because of the high extinction and crowding, but also because the superposition of different stellar populations such as the inner thin disk, inner thick disk, and inner halo stars. In Zoccali et al. (2006); Fulbright et al. (2007) the authors found bulge [O/Fe] values that are slightly higher than the local chemical thick disk, although other works have found no differences between oxygen abundances of the bulge and local thick disk samples (Alves-Brito et al. 2010; Meléndez et al. 2008). Odd-Z elements, such as sodium, show compelling results in the bulge that differ from the local samples; odd-Z elements are mainly produced together with *alpha* abundances in the last stages of the life of massive stars. The sodium in the bulge increases at the high metallicity end, and in Johnson et al. (2014) they showed this for high metallicity stars in the bulge, which differs from disk samples where [Na/Fe] has a more constant behaviour. For a more detailed chemical analysis of the bulge, see Barbuy et al. (2018). In summary, the bulge indicates a fast enrichment scenario portrayed by its abundances and this is the region of the Galaxy where we find the most metal-rich stars. A detailed and consistent analysis of the chemical abundances in the bulge and the local thin and thick disks is extremely important to reach a better comprehension of the Galactic disks and bulge formation.

1.3.3 RR lyrae tracers, metal-poor stars and a classical bulge

Although harder to detect, metal-poor stars can also be found in the bulge (Howes et al. 2015). Chemical simulations suggest that those could be the oldest stars in the Galaxy (Salvadori et al. 2010; El-Badry et al. 2018). The Pristine survey (Starkenburg et al. 2017) is a recent narrow-band photometric project focused on the metallicity-sensitive Ca H & K lines. The survey also maps the inner Galaxy, and in the recent works of Arentsen et al. (2020), they used follow-up spectroscopy to investigate the kinematics of a wide range of metal-poor stars from $-3 < [\mathrm{Fe/H}] < -0.5$. The authors show that the velocity dispersion is a function of metallicity. Interestingly, some metal-poor stars show signs of cylindrical rotation, but the rotation dissolves for the most metal-poor (with metallicities $[\mathrm{Fe/H}] < -1.5$) bins where velocity dispersion is the highest. Some of these stars from Pristine could belong to the halo; more accurate orbital analysis of metal-poor stars is still needed to better understand the complex orbital structure of the inner Galaxy. In Lucey et al. (2021), they calculated orbits for a sample of metal-poor stars from which they concluded only 14% has high confidence of being confined to the bulge. A large dataset of metal-poor stars was recently evaluated using the low-resolution spectra of the third data release of *Gaia*, about 2 million stars in a region of 30° for which ≈ 1.2 million have orbital parameters (Rix et al. 2022). The analysis of this large sample shows that there is a significant fraction of the metal-poor stars bound to bulge orbits at an extent of 2.7 kpc, although most of these stars have metallicities similar to the halo from the distribution of globular clusters (Geisler et al. 2022). RR lyr stars are very old low-mass variables which are found in a variety of regions of the Galaxy. One can determine very precise distances with their period-luminosity relation and therefore they are very good tracers of the structure of old populations in the Galaxy. The studies with RR lyr stars in the bulge also show the manifestation of two distinct kinematics (Pérez-Villegas et al. 2017a; Kunder et al. 2020; Kunder 2022). In Kunder et al. (2020) with orbital analysis, the authors cleaned the 25% contamination of halo and find the RR lyrae follow two distinct kinematics and structure: one group of stars does not present bar shape orbits and is concentrated to the centre while the other group is kinematically and spatially consistent with the bar structure.

All these studies show evidence of a non-negligible ancient population that could be tracing the pressure-supported component of the Galaxy. Although simulations can also explain a more spherically distributed metal-poor component without a classical bulge, this concentrated population is suggested then to be the outcome of the thick disk, which has a different radial distribution

than the thin disk (Debattista et al. 2017; Fragkoudi et al. 2018). Nonetheless, further analysis of metal-poor and metal-rich stars in the Galactic bulge/bar is necessary to clarify the existence of a pressure-supported component.

1.3.4 The bulge age

Primarily, stellar ages for the Galactic bulge were measured using CMD fitting procedures for high-resolution photometry, and proper motion cleaned. Studies have found the bulk of the bulge to be old, ≈ 10 Grys (Ortolani et al. 1995; Kuijken & Rich 2002; Clarkson et al. 2011; Valenti et al. 2013). In Bensby et al. (2017), they obtained spectra through micro-lensing events using a selection of subgiants, for which they found young ages: 35% of their sample have ages younger than 8 Gyrs. The results of Bensby et al. (2017) have been recently challenged in Joyce et al. (2022) where they argue that a different set of stellar evolutionary models and a more careful uncertainty analysis leads to very few stars with ages younger than 7 Gyrs, but a population that peaks at 8-9 Gyr at higher metallicities is a robust result. Ages of 8 Gyr at high metallicity align with a fast formation history of the bulge and agree with ages derived through learning machine algorithms and [C/N] abundances (Hasselquist et al. 2020, 2019). Unfortunately, there are no ages measured through asteroseismology in the bulge. Ages that are less model dependent and accurate will undoubtedly have an impact on understanding the stellar populations of the bulge area.

1.4 Open questions in Galactic archaeology

After this short review of the central observational science done across the last century to unravel the formation history of the Galaxy, we can define some critical open questions that will help us better understand the evolution of the Galactic disks and bulge. This thesis attempts to resolve most of these questions by analysing APOGEE and *Gaia* surveys. We give a brief summary here of how we intend to treat these questions in the following chapters.

- How do the high and low α-sequences vary across the Galaxy?
  Multiple works using APOGEE DR14 and SEGUE show that the chemically thick disk is coeval at different Galactic radii. However, until the completion of this thesis, there was still no good coverage of the inner Galaxy and outer Galaxy. We explore this question using *Gaia* and APOGEE DR16 together with the Bayesian code `StarHorse`.

- What is the chemo-dynamical structure of the Galactic bar and inner Galaxy?
  Kinematical data analysis of ARGOS, GIBS, and BRAVA have consistently shown that the metal-rich stars compose an X-shape and cylindrical velocity component. Still, some works with RR lyrae and metal-poor stars also show considerable rotation. The new data gave us the opportunity to investigate the interplay of metal-rich and metal-poor stars as a function of dynamical orbits in a well-defined (cleaned by foreground stars) sample of the inner Galaxy.

- Does the MW have a classical bulge component?
  With a statistically significant sample of the inner Galaxy, we break down the stellar populations into their chemo-orbital space, tracing the contribution of the internal thin and thick disks and the bar, and then analyse if there are stars consistent with a classical bulge.

- How to date the stellar populations in our Galaxy using large spectroscopic surveys?
  Ages are fundamental for the precise comparison with chemical evolutionary models that can describe the formation of the disks. We use the code `StarHorse` to compute reliable

ages for sub-giant branch stars and main sequence turn-off stars for a large sample of public spectroscopic surveys. We investigate chemical clock relations with those ages, as shown in Figure 1.5.

- How to distinguish between chemical populations in our Galaxy?
  We scrutinize the multidimensional chemical space available in various spectroscopic surveys, which derive abundances sampling different nucleosynthetic channels. In a new method, we use an unsupervised learning machine algorithm and combine chemical information with the ages of subgiants to cluster distinct chrono-chemical populations effectively.

1.5 Summary and thesis outlook

This thesis is divided into five Chapters, and three of these Chapters consist of publications in peer-review journals or in-review process. The time of this thesis is marked by the *Gaia* era, where parallaxes became available in 2018 for more than one billion stars. And it is also at this time that the APOGEE survey released observations from the southern hemisphere, reaching an area of the bulge that was poorly covered before. Although chapters 2, 3 and 4 are independent publications, they share as a central theme: the chemodynamical characterization of the disks and bulge. As a goal, we want to understand our Galaxy by breaking down the steps of evolution that formed the present chemically defined thick and thin disks and the Galactic bar and bulge. Chapter 2 presents a study using APOGEE and *Gaia* DR2 to chemically map the MW from its inner to the outer regions (0-20 kpc), as well as the derivation of distances and extinctions using `StarHorse` for about five million sources. These parameters are released to the community as value-added catalogues to projects such as SDSS. Chapter 3 focuses on a defined sample in the inner Galaxy. With precise orbital calculations, we explore for the first time the chemical orbital space of the stellar populations that coexist in this region. In Chapter 4, we derive ages for about four million stars in the solar neighbourhood, investigate their relations with chemical composition, and show a new method to delineate chemical age groups. Finally, in Chapter 5.7, we make our concluding remarks, future perspectives and explain the impact of this thesis discoveries on the field.

2 From the bulge to the outer disk: StarHorse stellar parameters, distances, and extinctions for stars in APOGEE DR16 and other spectroscopic surveys

A. B. A. Queiroz, F. Anders, C. Chiappini, A. Khalatyan, B. X. Santiago, M. Steinmetz, M. Valentini, A. Miglio, D. Bossini, B. Barbuy, I. Minchev, D. Minniti, D. A. García Hernández, M. Schultheis, R. L. Beaton, T. C. Beers, D. Bizyaev, J. R. Brownstein, K. Cunha, J. G. Fernández-Trincado, P. M. Frinchaboy, R. R. Lane, S. R. Majewski, D. Nataf, C. Nitschelm, K. Pan, A. Roman-Lopes, J. S. Sobeck, G. Stringfellow, O. Zamora

This chapter was published in Astronomy & Astrophysics, Volume 638, id.A76, 31 pp. Queiroz et al. 2020

Abstract

We combine high-resolution spectroscopic data from APOGEE-2 survey Data Release 16 (DR16) with broad-band photometric data from several sources as well as parallaxes from *Gaia* Data Release 2 (DR2). Using the Bayesian isochrone-fitting code `StarHorse`, we derived the distances, extinctions, and astrophysical parameters for around 388,815 APOGEE stars. We achieve typical distance uncertainties of $\sim$ 6% for APOGEE giants, $\sim$ 2% for APOGEE dwarfs, and extinction uncertainties of $\sim$ 0.07 mag, when all photometric information is available, and $\sim$ 0.17 magif optical photometry is missing. `StarHorse` uncertainties vary with the input spectroscopic catalogue, available photometry, and parallax uncertainties. To illustrate the impact of our results, we show that thanks to *Gaia* DR2 and the now larger sky coverage of APOGEE-2 (including APOGEE-South), we obtain an extended map of the Galactic plane. We thereby provide an unprecedented coverage of the disk close to the Galactic mid-plane ($|Z_{\rm Gal}| < 1$ kpc) from the Galactic centre out to $R_{\rm Gal} \sim 20$ kpc. The improvements in statistics as well as distance and extinction uncertainties unveil the presence of the bar in stellar density and the striking chemical duality in the innermost regions of the disc, which now clearly extend to the inner bulge. We complement this paper with distances and extinctions for stars in other public released spectroscopic surveys: 324,999 in GALAH DR2, 4,928,715 in LAMOST DR5, 408,894 in RAVE DR6, and 6,095 in GES DR3

2.1 Introduction

The second data release (DR2) of the astrometric flagship mission *Gaia* launched by ESA has added an invaluable wealth of astrometric and photometric data for more than a billion stars (Gaia Collaboration et al. 2018b). While the DR2 parallax uncertainties are still sufficiently large to hamper detailed tomographic views of the Galaxy beyond 2 – 3 kpc around the Sun from *Gaia* data alone, the combination of these data with spectroscopic and photometric measurements from various other surveys opens up the possibility of extending the 3D mapping of Galactic stellar populations as far as the Galactic centre and out to similar heliocentric distances towards the outer disk or directions perpendicular to the disk mid-plane. This enables detailed quantitative comparisons between observed properties in phase and chemical space to chemo-dynamical model predictions (e.g. Fragkoudi et al. 2018; Frankel et al. 2018). Additionally, for the first time, ages of large numbers of field stars are being determined with sufficient precision, at least within $\simeq$ 2 kpc, to impose strong direct constraints on the Galactic star formation history (Bensby et al. 2017; Ness et al. 2019).

In Queiroz et al. (2018, Q18), we presented the `StarHorse` code: a `python` tool that

uses Bayesian analysis of spectroscopic, photometric, and astrometric data to infer distances, extinction, ages, and masses of field stars. In that paper we illustrated the impact of *Gaia* DR1 parallaxes on improving our estimates of distances and extinctions. We also generated several value-added catalogues (VACs) for the spectroscopic datasets Apache Point Observatory Galaxy Evolution Experiment (APOGEE) DR14 (Abolfathi et al. 2018), Radial Velocity Experiment (RAVE) DR5 (Kunder et al. 2017), the Gaia-ESO spectroscopic survey (GES) DR3 (Gilmore et al. 2012), and The GALactic Archaeology with HERMES (GALAH) DR1 (Martell et al. 2017), thus extending the volume for which precise distances are available.

`StarHorse` has been applied in numerous studies concerning different fields of Galactic astrophysics, such as stellar populations in the local neighbourhood (e.g. Anders et al. 2018; Grieves et al. 2018; Minchev et al. 2018), the origin of the stellar halo (Fernández-Alvar et al. 2017, 2019), the physical carriers of diffuse interstellar bands (Elyajouri & Lallement 2019), Milky Way stellar population kinematics (e.g. Palicio et al. 2018; Monari et al. 2018; Carrillo et al. 2019; Minchev et al. 2019), or recently the chemo-dynamical study of N-rich stars (Fernández-Trincado et al. 2019a).

In Anders et al. (2019, A19), we used an updated version of `StarHorse`, combining *Gaia* DR2 parallaxes and optical photometry with other photometric bands from PanSTARRS-1, 2MASS, and AllWISE, to derive Bayesian distances and extinctions for around 300 million stars brighter than $G = 18$. We showed that the addition of complementary information to the *Gaia* parallaxes and photometry could lead to a breakthrough in which, with the best-quality data, we might start seeing structures such as the Galactic bar already in density stellar maps. However, as explained in that paper, the A19 photo-astrometric results were computed with a prior upper limit of 4 magin A_V extinction, resulting in a limited view of stellar populations towards the innermost regions.

We now have the opportunity to start dissecting the Milky Way, including the central region and the far side of the Galactic disc, by combining Gaia DR2 with the APOGEE DR16 release. The latter includes around 380 000 stars with precise radial velocities, stellar parameters, and chemistry from near-infrared (NIR) high-resolution spectra taken in both hemispheres (Ahumada et al. 2020). Compared to the earlier releases, the data now include many more targets in general, but especially towards the innermost kiloparsecs of the Galaxy.

In this paper we describe the first VACs generated from `StarHorse` using *Gaia* DR2 data in conjunction with APOGEE DR16 along with public releases of other spectroscopic surveys. We show the first high spatial-resolution chemical maps of our Galaxy covering the entire disc, from 0 to beyond 20 kpc in Galactocentric distance, complementing earlier maps shown in Anders et al. (2014), Hayden et al. (2015), and Weinberg et al. (2019), who used APOGEE DR10, DR12, and DR14, respectively. We presented distances and extinctions, and their associated uncertainties, study the robustness of these quantities to different choices of priors, parameter sets, and systematic corrections, and also compare these quantities to data from other sources.

The paper is organised as follows: In Sect. 2.2 we provide a brief description of the `StarHorse` code, focussing on the main improvements since Q18 and A19. Section 2.3 describes the input data (photometry, astrometry, and spectroscopy) used in the computations of distances and extinctions for APOGEE DR16. In Sect. 2.4 we describe the output parameters that resulted from the `StarHorse` calculation as well as their uncertainties. As an example of science application, in Sect. 2.5 we present the first density and chemical maps obtained over the entire Galactic plane and discuss the main science implications derived from these maps. In Sect. 2.6 we discuss the complementary catalogues GALAH, RAVE, GES, and the Large Sky Area Multi-Object Fiber Spectroscopic Telescope (LAMOST), and the distribution of the resulting parameters. The resulting catalogues are provided in machine-readable form: the data model can be found in Appendix 2.A, a set of validation tests that for our new `StarHorse`

APOGEE DR16 results can be found in Appendix 2.B, and summary plots for each survey are shown in Appendix 2.C. In Section 2.7 our main conclusions are summarised.

2.2 StarHorse code

StarHorse (sometimes abbreviated as SH in the resulting catalogues) is a Bayesian isochrone-fitting code that derives distances d, extinctions in the V band (at $\lambda = 542$ nm) A_V, ages τ, masses m_*, effective temperatures $T_{\rm eff}$, metallicities [M/H], and surface gravities $\log g$ for field stars. In order to do so, we use as input a set of spectroscopically measured stellar parameters (typically $T_{\rm eff}$, $\log g$, and metallicity [M/H]), photometric magnitudes m_λ, and, when available, parallax ϖ, to estimate how close a stellar evolutionary track is to the observed data. In this work we adopt the latest version of the PARSEC stellar evolutionary model tracks (Bressan et al. 2012; Marigo et al. 2017)[11]. For APOGEE DR16 we adopt a fine grid of models to compute the estimated parameters with steps of 0.01 dex in $\log\tau$ and 0.02 dex in metallicity [M/H], covering the ranges $7.5 < \log\tau < 10.13$, $-2.2 <$ [M/H] < 0.6.

To compute the posterior probability distribution function (PDF) for the model parameters given the observed data, we include priors about the geometry, metallicity, and age characteristics of the main Galactic components, following previous Bayesian methods to derive distances (e.g. Burnett & Binney 2010; Burnett et al. 2011; Binney et al. 2014). The priors adopted are the same as in Q18 and A19, namely: an initial mass function from Chabrier (2003) for all Galactic components; exponential spatial density profiles for thin and thick discs (see Section 5 for a discussion on the differences between the geometric and chemical definitions of the thick disc); a spherical halo and a triaxial (ellipsoid+spherical) bulge/bar component, and broad Gaussians for the age and MDF priors. The normalisation of each Galactic component, as well as the solar position, were taken from Bland-Hawthorn & Gerhard (2016).

The code was first described in Santiago et al. 2016, and later modified to use *Gaia* parallaxes and derive astrophysical stellar parameters in Queiroz et al. 2018. The latter paper also included extensive validation comparisons with simulations and independent high-quality distance determinations from asteroseismology, eclipsing binaries, and open clusters. Those samples showed precision of $\simeq$ 10% for distances, ages accurate to $\simeq$ 30%, and A_V errors of $\simeq$ 0.1 magfor stars out to $\simeq$ 1kpc, with a continuous worsening of accuracy and precision towards larger distances. Most recently, in A19, we used StarHorse to determine photo-astrometric (i.e. not using spectroscopy at all) distances, extinctions, and stellar parameters for *Gaia* DR2 stars down to magnitude $G = 18$.

More details about the method, priors, stellar evolutionary models, code validation, and previous released catalogues are provided in Q18. We have since updated the code in some important aspects briefly summarised in this work (for more details see A19). Namely, we improved the extinction treatment, which now considers the dependence of the extinction coefficient, A_λ, on effective temperature and extinction itself, as explained in Holtzman et al. (1995), and Girardi et al. (2008), for instance; and the latest version has migrated to python 3.6, which made the code faster and compatible with recent libraries. These and other small computational improvements are described in detail in A19, Sect. 3.2. In this paper, we use the high-quality spectroscopically determined stellar parameters from APOGEE spectra, in conjunction with *Gaia* DR2 parallaxes and broad-band photometric measurements.

11 Downloaded from http://stev.oapd.inaf.it/cgi-bin/cmd

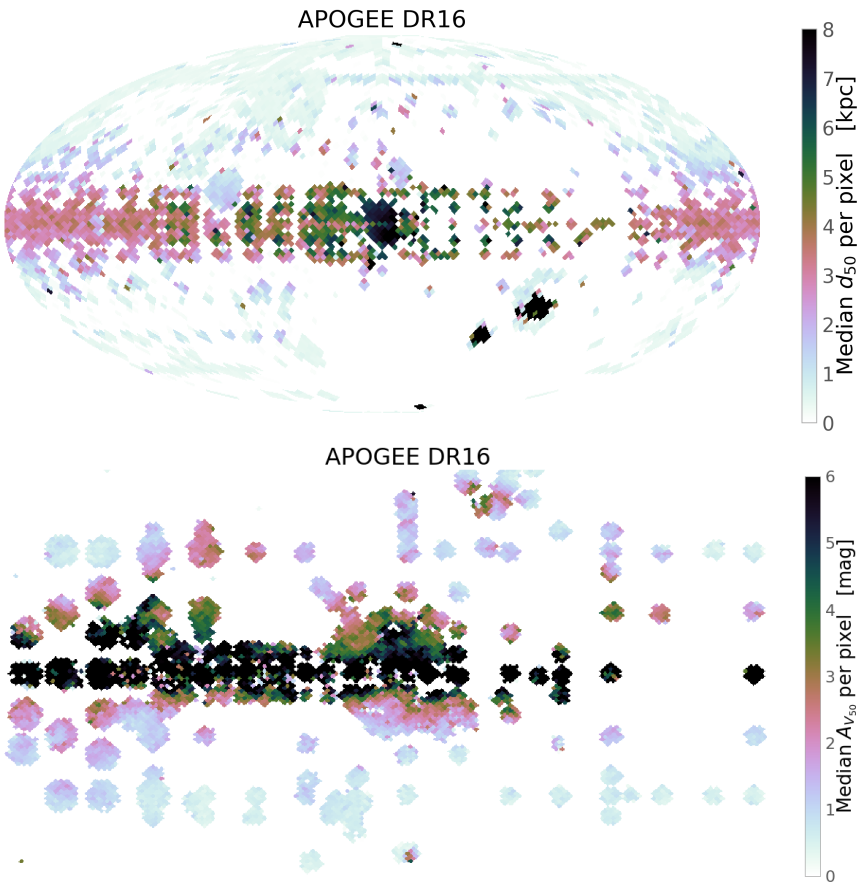

Figure 2.1: Overview of the coverage of the APOGEE DR16 `StarHorse` VAC. Top panel: Median `StarHorse` distance per HealPix cell as a function of Galactic coordinates. Bottom panel: Same as in previous panel, but now showing the median A_V as a function of direction in the sky, and zooming in on the innermost 40 x 20 degrees of the Galactic plane (the line spacing in the bottom panel is 10 degrees).

2.3 Input data

We followed a similar configuration to previous `StarHorse` runs (Queiroz et al. 2018; Anders et al. 2019) to complement the APOGEE DR16 `StarHorse` catalogue with parameters such as extinction and distances. We gathered parallaxes from *Gaia* DR2 (Gaia Collaboration et al. 2018b) and photometry from 2MASS (Cutri et al. 2003), WISE (Cutri et al. 2013), and PanSTARRS-1 (Chambers et al. 2016) and gathered this information with spectra from APOGEE DR16 (Ahumada et al. 2020). We introduced the input catalogues, the necessary adjustments in these data, and the `StarHorse` configuration to produce the final parameters.

2.3.1 APOGEE DR16

The spectroscopic survey APOGEE (Majewski et al. 2017) started in the third phase of the Sloan Digital Sky Survey (SDSS-III; Eisenstein et al. 2011). The APOGEE survey continues as part of SDSS-IV (Blanton et al. 2017). It is a spectroscopic survey conducted in the NIR, at high resolution ($R \sim 22,500$), and high signal-to-noise ($S/N > 100$) (Wilson et al. 2019). The data reduction pipeline is described in Nidever et al. (2015). As a NIR survey, APOGEE is capable to peer into the dusty areas of our Galaxy, such as the Galactic bulge and the central Galactic plane.

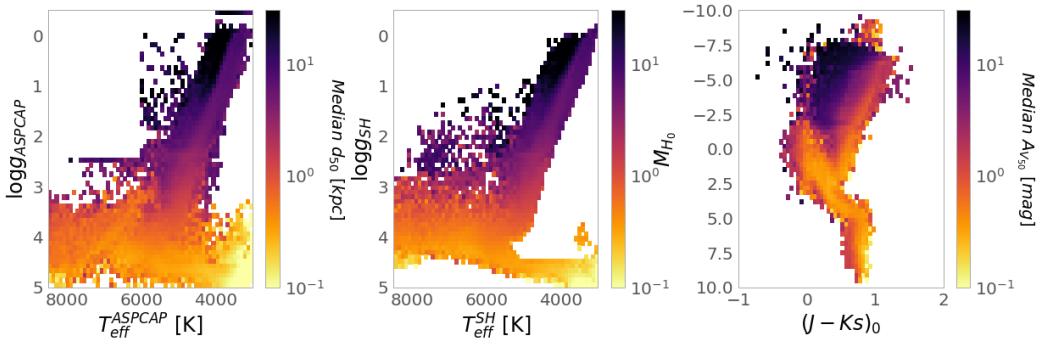

Figure 2.2: *Kiel* diagram colour coded by median `StarHorse` distance as a function of position on the input (left) and output (middle) effective temperatures and surface gravities. The right-most panel shows the colour magnitude diagram coloured by median `StarHorse` extinction; the colour is already corrected by `StarHorse` extinction.

The APOGEE survey has been collecting data in the northern hemisphere since 2011. Since 2015, APOGEE-2 data have also been collected in the southern hemisphere. Observations from both hemispheres use the twin NIR spectrographs (Wilson et al. 2019) on the SDSS 2.5 m telescope at APO (Gunn et al. 2006) and the 2.5 m du Pont telescope at Las Campanas Observatory (LCO; Bowen & Vaughan 1973), respectively. The DR16 is the first SDSS-IV data release that includes data from APOGEE-2 South: it contains a total of 473,307 sources with derived atmospheric parameters and abundances. The pre-processing of the APOGEE DR16 data in preparation for the `StarHorse` run presented in this work was very similar to the pre-processing of APOGEE DR14 described in Q18.

The APOGEE Stellar Parameter and Chemical Abundance Pipeline (ASPCAP; García Pérez et al. 2016) was optimised for red giant stars, since this is the main population targeted by the survey. However, we also computed `StarHorse` results for stars in APOGEE DR16 catalogue that fall outside the recommended calibration ranges of ASPCAP. For those stars we used inflated uncertainties of $\sigma_{\log g} = 0.3$ dex, $\sigma_{T_{\rm eff}} = 200$ K, $\sigma_{[\rm Fe/H]} = 0.15$ dex, and $\sigma_{[\alpha/\rm Fe]} = 0.1$ dex.

As in Q18 (and differently from A19 where no extinction prior was used), we used the APOGEE targeting extinction estimate $A_{K_s}^{\rm Targ}$ as a broad prior for the total line-of-sight extinction: $A_{V_{\rm prior}} = 0.11 \cdot A_{K_s}^{\rm Targ}$. `StarHorse` treats this extinction using Schlafly et al. (2016) extinction curve.

Finally, because we used PARSEC stellar models, which at present do not include non-solar $[\alpha/Fe]$ ratio models, we corrected for this effect in the input data. For that we used the Salaris et al. (1993) formula, which accounts for α-enhancement by a slight shift of the total metallicity [M/H] as follows:

$$[\rm M/H] = [\rm Fe/H] + \log\left[C \cdot 10^{[\alpha/\rm Fe]} + (1 - C)\right] \quad (2.1)$$

$$\sigma_{[\rm M/H]} \simeq \sqrt{\sigma^2_{[\rm Fe/H]} + \sigma^2_{[\alpha/\rm Fe]}}. \quad (2.2)$$

We chose $C = 0.66101$, in agreement with the scaled solar composition $Y = 0.2485 + 1.78 \cdot Z$ used in the PARSEC 1.2S models[12].

2.3.2 *Gaia* Data Release 2

The *Gaia* astrometric mission was launched in December 2013 and placed close to the L2 Lagrangian point, about 1.5 million km from the Earth, in July 2014. It is measuring positions, parallaxes, proper motions, and photometry for well over 10^9 sources down to $G \simeq 20.7$, and obtaining physical parameters and radial velocities for millions of brighter stars (Gaia Collaboration et al. 2016). Its recent Data Release 2 (

12 http://stev.oapd.inaf.it/cgi-bin/cmd_3.1

Gaia DR2; Gaia Collaboration et al. 2018b) covers the initial 22 months of data taking (from a predicted total of $>$ 5 years) and has positions and photometry for $1.7 \cdot 10^9$ sources, full astrometric solutions for $1.3 \cdot 10^9$ (Lindegren et al. 2018), $T_{\rm eff}$, extinction, stellar radii and luminosities for $8 \cdot 10^7$ stars (Andrae et al. 2018), and radial velocities for $7 \cdot 10^6$ of the sources (Katz et al. 2019). Particularly important for our purposes are the DR2 parallaxes, since they allow us to better disentangle dwarfs from giants for stars with more uncertain surface gravity measurements.

The *Gaia* DR2 parallax precision varies from < 0.03 mas for $G \leq 13$ to $\simeq 0.7$ mas for $G = 20$, and the parallax zero-point (accuracy) has been shown to be of similar order, and probably dependent on a combination of sky position, magnitude, and colour (e.g. Arenou et al. 2018; Stassun & Torres 2018; Zinn et al. 2019; Khan et al. 2019).

In this work, we adopted the mean zero-point correction of 52.8 μas to the *Gaia* DR2 parallaxes determined by Zinn et al. 2019 using red giants co-observed by APOGEE and the *Kepler* mission. This is somewhat midway between the quasar-derived correction advertised by Lindegren et al. (2018) and the zero-point shift estimated by Stassun & Torres 2018, which is 82 μas. In fact, Stassun & Torres 2018 find that their estimate of the offset may be 61 μas, which is much closer to that of Zinn et al. 2019, if they allow for a possible scale error in the parallaxes. They also note that the larger offset of 82 μas would be most applicable to the brightest stars, with $G \lesssim 11$, however only ~10% of the APOGEE sample is so bright. On the other hand, Khan et al. (2019) find that the parallax zero-point shift could be smaller: for two *K*2 fields analysed in their paper they find smaller discrepancies between asteroseismic and astrometric parallaxes than in the *Kepler* field.

Independent distances measurements using cepheids and quasars (Riess et al. 2018; Lindegren et al. 2018) also show that the *Gaia* DR2 parallax uncertainties are slightly underestimated, and can suffer from systematics as well as the parallax itself. To account for these effects we applied the suggested inflation of parallax uncertanties described in Lindegren et al. (2018). The inflated error can be written as

$$\sigma_{\rm ext} = \sqrt{k\sigma_{\rm in}^2 + \sigma_s^2}, \tag{2.3}$$

where $\sigma_{\rm ext}$ is the inflated uncertainty, $\sigma_{\rm in}$ the uncertainty from *Gaia* catalogue, $k = 1.08$ is a constant parameter, and σ_s is slightly different for different magnitude ranges. For the bright regime ($G < 13.0$ mag) we used $\sigma_s = 0.021$ and for the faint ($G > 15.0$ mag) we used $\sigma_s = 0.043$. In between these two regimes we interpolated linearly using $\sigma_s = 0.030$.

The *Gaia* DR2 catalogue also includes broadband photometry for about 10^9 sources, although in the case of APOGEE we decided not to include this photometry in the calculations. The reason for this choice is simply because most of APOGEE DR16 is targeting the Galactic plane, and in this region *Gaia* DR2 photometry partly suffers from crowding issues. In addition, it should be acknowledged that the *Gaia* DR2 photometry for the G_{BP} and G_{RP} bands is essentially aperture photometry, which has been shown to be problematic in regions of high stellar density and/or nebulous emission (e.g. Evans et al. 2018; Arenou et al. 2018). We therefore followed a conservative approach and did not use this photometry for the APOGEE sample.

2.3.3 Photometric catalogues

In all produced catalogues we use infrared photometry from 2MASS (Cutri et al. 2003) and WISE (Cutri et al. 2013). Both are all-sky photometric surveys, and 2MASS photometry has almost 100% coverage of the APOGEE catalogue. For that reason we used it as primary photometry when running `StarHorse` (see Q18 details). For both input catalogues, we applied a minimum photometric uncertainty of 0.03 mag. Finally, we assumed the uncertainty of the stars in 2MASS and WISE, which have no measured uncertainty to be 0.4 mag.

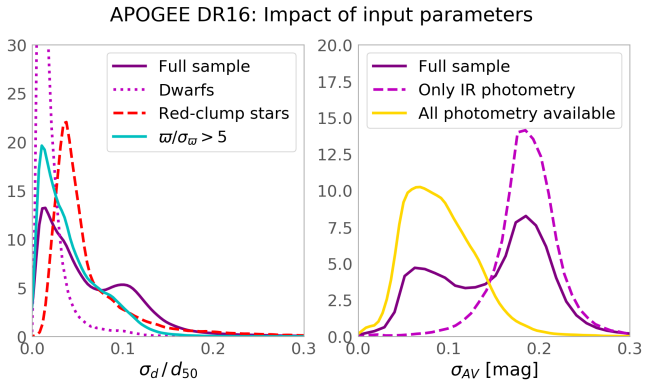

Figure 2.3: Kernel-density estimates of the uncertainty distributions for the distances (left panel) and A_V extinctions (right panel) in the APOGEE DR16 StarHorse VAC. The different curves show the distributions of distances and extinctions uncertainties for subsets of different data input quality. In the left panel, we highlight the higher distance precision achieved for a) stars with *Gaia* DR2 parallaxes more precise than 20%, b) dwarf stars ($\log g < 4$), and c) red-clump stars ($2.3 < \log g < 2.5$). In the right panel, we show how the (un-)availability of optical photometry drastically improves or worsens the precision of our A_V estimates.

For the optical regime we used PanSTARRS-1 photometry ($\lambda \sim 3943 - 10838$ Å) (Scolnic et al. 2015) with corrected zero points according to Scolnic et al. (2015) and minimum photometric uncertainties of 0.04 mag. Furthermore, we only used measurements with reported individual errors for stars fainter than $G = 14.5$. In constrast to Q18, we decided only to use PanSTARRS-1 photometry rather than APASS (Henden & Munari 2014) photometry. The motivation for this choice comes from reports that APASS photometry has a high percentage of sources (30 %) with a positional mismatch, especially in the faint regime ($g_{sloan} > 16$) (Marrese et al. 2019).

2.4 APOGEE DR16 StarHorse catalogue

The APOGEE DR16 StarHorse catalogue presented in this work was generated from the processed APOGEE DR16 data, explained in Sect. 2.3.1, cross-matched with *Gaia* DR2 (98%), PanSTARRS-1 (37%), 2MASS (100%), and AllWISE (95%). The final produced catalogue contains 388,815 unique stars with derived StarHorse parameters, along with their uncertainties. From the 473,307 APOGEE sources StarHorse has converged for 418,715, and after this we selected unique stars by the highest signal to noise.

Our catalogue will appear as a VAC of the SDSS DR16 (Ahumada et al. 2020). The catalogue can also be downloaded from Leibniz Institute for Astrophysics (AIP) webpage[13], similar to what was done in Q18. The description and format of the provided StarHorse products are listed in Table 2.B.1, while the description of the adopted input and output quality flags can be found in Table 2.B.2.

The StarHorse output provides the posterior distribution functions of masses, effective temperatures, surface gravity, metallicities, distances, and extinctions (see Table 2.B.1). The median value 50th percentile should be taken as the best estimate for that given quantity and the uncertainty can be determined using the 84th and 16th percentiles. The full distribution of the StarHorse median output parameters is shown in the left panel of Fig. 2.4.

In addition to the percentile values of the estimated parameters, all released VACs have columns that describe the StarHorse input data, SH_INPUTFLAGS, and the StarHorse output data, SH_OUTPUTFLAGS as specified in Table 2.B.1. The input flags describe which parameters were used in the likelihood calculation for each star. These flags also indicate if we used an A_V prior as the AVprior flag or if the A_V was determined using the parallax True option (See Q18). The meaning of each string in SH_INPUTFLAGS can be seen in Table 2.B.2. The output flags inform the number of models which have converged in the likelihood

13 https://data.aip.de/aqueiroz2020

calculation and also indicate the occurrence of problems in the estimated extinction (see also Table2.B.2).

In what follows we present some of the basic properties of the APOGEE-DR16 StarHorse catalogue (maps involving chemical abundances are discussed in the next section). In the following figures we applied a few quality cuts as follows: stars with signal-to-noise ratio greater than 50 (SNREV > 50), those with non-negative posterior extinction ($A_{V_{84}} > 0$), and those with a good ASPCAP fit (ASPCAP_CHI2 < 25). This corresponds to ≃ 95% of the converged stars.

Figure 2.1 shows Galactic maps colour coded by the median of the resulting APOGEE DR16 StarHorse distances (top panel) and extinctions (middle panel). By design, most of the APOGEE pointings are concentrated towards low Galactic latitudes (Zasowski et al. 2013, 2017), offering a much greater coverage of the thin disk than other surveys. The north-south equatorial asymmetry is also visible, since most of the data so far come from the northern spectrograph at Apache Point Observatory. Yet, the Magellanic Clouds are clearly visible on the distance map as the distant clumps of sampled stars. Because the density of stars increases towards the Galactic centre, there is also a clear trend of larger median distances in this direction. The A_V map in the bottom panel of Fig. 2.1 zooms into the central degrees of the Galactic plane, where the average extinction is higher, and patchy (also visible in this map).

Figure 2.2 shows the mean distance per pixel in the spectroscopic *Kiel* diagram, using the input parameters from APOGEE (ASPCAP; left panel) and using the StarHorse output spectroscopic parameters (middle panel). As expected, stars belonging to the giant branch (comprising most of the APOGEE sample) are found at larger distances than dwarfs since they have brighter absolute magnitude and are therefore detectable in a larger distance range. In the giants regime StarHorse seems to be detecting asymptotic giant branch stars (AGBs) at very large distances (at $T_{\rm eff} \sim 4500K$ and $\log g < 1.0$), as expected since those are very bright stars. However, those stars should be analysed with care since the ASPCAP pipeline does not perform well in this range (García Pérez et al. 2016). The third panel of Figure 2.2 also shows higher extinction for intrinsic brighter and therefore distant stars. The output spectroscopic parameters from StarHorse seem to be, as expected, very much in accordance with the input ASPCAP parameters. For the dwarfs stars, which are not ASPCAP calibrated stars and therefore have larger uncertainties, StarHorse seems to improve the results finding a smoother solution, as expected because of the use of stellar evolutionary models.

The distribution of distance and extinction uncertainties for the APOGEE DR16 StarHorse catalogue are shown in Fig. 2.3. Thanks to the availability of *Gaia* DR2 parallaxes, the distance uncertainties (left panel of Fig.2.3) are usually smaller than 10%. The three peaks at ≃ 2%, 4%, and ≃ 10% correspond to nearby dwarf stars within the *Gaia* DR2 parallax sphere, red-clump stars, and more distant giant stars, respectively. These distance uncertainties are slightly improved with respect to those from the DR14 APOGEE and Tycho-Gaia astrometric solution (TGAS) sample discussed in Q18, but now are available for a much larger number of stars, covering much larger volumes. Even for distant upper red-giant branch stars with more uncertain parallaxes (e.g. APOGEE targets near the Galactic centre), the achieved distance precision is typically within 10%.

The extinction uncertainty distribution (right panel of Fig. 2.3) is clearly double-peaked, at $A_V \simeq 0.07$ and $A_V \simeq 0.17$, as previously observed by Q18 for APOGEE DR14 combined with TGAS. As shown by the two subsets in the figure, the two peaks correspond to stars with and without available optical magnitudes, respectively. A more detailed discussion of the accuracy of the obtained parameters can be found in Appendix 2.B.

In Figure 2.4 we show the correlations between the output parameters and the correlations between the output uncertainties. We see the expected correlations between stellar parameters inherited from the isochrones (e.g. the $\log g$ versus $T_{\rm eff}$ diagram), as well as stel-

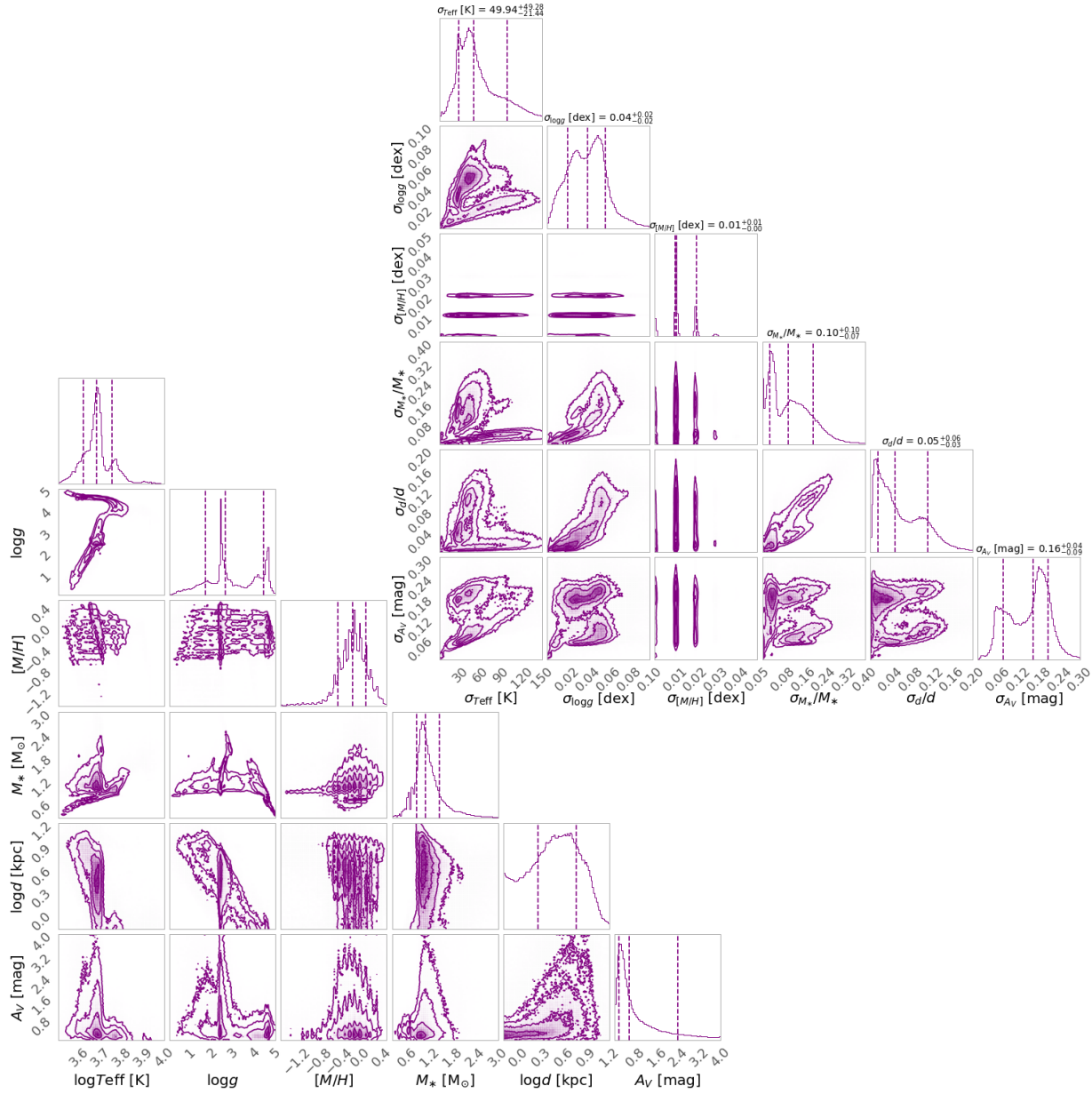

Figure 2.4: One-dimensional distributions and correlations between StarHorse output parameters (bottom left corner plot) and their corresponding uncertainties (top right corner plot) for the APOGEE DR16 sample.

lar population effects, such as the decrease of $\log g$ with increasing distance or a greater metallicity range for greater distances. Extinction is correlated with increasing mass, metallicity, and distance. The doubled-peaked uncertainty distribution in extinction is not explained by any other output parameter uncertainty apart from the completeness of the photometric set as seen in fig. 2.3. The uncertainties in the other parameters show approximately linear correlations between $\log g$ and mass, $\log g$ and distance, as well as mass and distance. The distribution of each parameter and its uncertainty can also be seen in the diagonal row of that plot, along with the uncertainty statistics for each of the `StarHorse` output parameters.

2.5 Extended chemical maps in the Galactic plane up to the bulge

In this section, we demonstrate the value of the APOGEE DR16 `StarHorse` results by presenting the most extensive and precise chemical-abundance map of the Milky Way disk and bulge to date. The unprecedented coverage of the APOGEE DR16 data can be appreciated in Fig. 2.5, in which we show the density distribution of all DR16 stars with StarHorse results in galactocentric coordinates. In this figure the colour represents the 3D local stellar density estimated via the smoothed-particle technique (Monaghan 1992) with Nngb = 35 neighbours; the maximum intensity projection rendering method implemented in pmviewer[14] is used.

Figure 2.5 shows very clearly that the APOGEE DR16 sample covers a large portion of the Galaxy with statistically significant samples; these now include the innermost regions with many more stars close to the Galactic mid-plane ($Z_{\rm Gal}$ <0.5 kpc) thanks to the southern observations taken at Las Campanas. This is an important improvement in the number of targets and in the quality of distances and extinction estimates with respect to previous releases.

To be more quantitative, the stellar density of the APOGEE DR16 sample amounts to over a thousand stars per kpc^2 in the complete $R_{\rm Gal} - Z_{\rm Gal}$ plane for $0 < R_{\rm Gal} < 15$ kpc and -1 kpc $< Z_{\rm Gal} < 1$ kpc (see Fig. 2.5), allowing for an unprecedented chemo-kinematic mapping of the inner and outer stellar disc. The top panel of Fig. 2.5 displays a top-down view of the Galactic disc, again demonstrating the exquisite spatial coverage of the APOGEE DR16 sample. The figure also shows a slight but distinct density enhancement in the region of the stellar bar, as observed for the full *Gaia* DR2 dataset in Anders et al. (2019), but with the canonical inclination angle of $\sim$ 25 degrees (e.g. Bland-Hawthorn & Gerhard 2016).

Since APOGEE traces around 20 chemical elements at high spectral resolution and provides radial velocities precise to $\sim$ 300 m/s (Majewski et al. 2017), this dataset will be a legacy for detailed chemo-dynamical studies of the Milky Way at least for several years.

To illustrate the impact of the APOGEE data released with the 16th SDSS Data Release in the field of Galactic archaeology, we focus on just a few examples of abundance-ratio maps in bins of galactocentric cylindrical coordinates ($R_{\rm Gal}, Z_{\rm Gal}$), in a similar manner as the maps presented by Hayden et al. (2015) using DR12 data: first, the standard relative-to-iron abundance diagrams (Figs. 2.7 and 2.8 for [α/Fe] versus [Fe/H] and Fig. 2.6 for [Al/Fe] versus [Fe/H]); and second, two examples of an abundance ratio as a function of an alpha-element ([Mg/O] versus [Mg/H] and [Al/Mg] versus [Mg/H], shown in Fig. 2.9). These figures show, for different bins of R_{Gal} and Z_{Gal}, diagrams of abundances colour coded by density estimation using a Gaussian kernel. The bandwidths of the kernel density estimates obey Scott's rule (Scott 1992). Figs. 2.7 and 2.8 also show, in the top plots, the uncertainty distributions in distance and extinction for each $R_{\rm Gal}$ bin.

Owing to the pencil-beam nature of the APOGEE survey, and the fact that metal-poor stars are brighter, the relative weight of the subpopulations in each plot may still be slightly affected by the selection function. Therefore,

14 http://pmviewer.sourceforge.net

a quantitative interpretation of these spatial chemical maps needs to take into account such biases and will be the subject of future work. The so-called α elements are produced by core-collapse supernovae and hence more directly connected with the star formation rate. Recently, Weinberg et al. (2019) discussed such abundance maps, but based on a much smaller sample of $\sim 20,000$ stars from APOGEE DR14, and not including data in the innermost radial bin (0-2kpc), which is now possible.

2.5.1 Map of [α/Fe] versus [Fe/H]

The [α/Fe] versus [Fe/H] diagram has long served as a tracer of the chemical enrichment timescales of the Milky Way (Matteucci 2012), which are a consequence of the star formation history. A pioneer work to demonstrate the direct connection of the high-[α/Fe] 'plateau' with old stars was realised by Fuhrmann (1998), and Fuhrmann (2011), who computed ages for a volume-complete sample of *Hipparcos* stars within 25 pc of the Sun. His work clearly showed the stars on the high-[α/Fe] plateau to be older than 10 Gyr, whereas stars along the chemical thin-disk sequence were found to be younger. The observed chemical discontinuity in the [α/Fe] versus [Fe/H] diagrams in the solar neighbourhood has important consequences on interpretations related to the assembly history of the Milky Way and similar galaxies (see e.g. Chiappini et al. 1997; Minchev et al. 2013; Mackereth et al. 2018; Buck 2020; Nuza et al. 2019; Spitoni et al. 2019 for discussions).

The mapping of the Milky Way in terms of the [α/Fe] vs. [Fe/H] diagram has quickly evolved since then. The first high-resolution spectroscopic samples outside the solar vicinity were small and without age information (e.g. Bensby et al. 2010, 2011; Alves-Brito et al. 2010 - see Figure 14 of Anders et al. 2014), but were already able to show the complexity and impact of such maps. For instance, the disappearance of high-[α/Fe] stars towards the outer disk could be interpreted as an indication that the (chemical) thick disk had a shorter scale length than the thin disk (Bensby et al. 2011; Cheng et al. 2012), contrary to what had been seen for the (geometrically defined) thick discs in other galaxies.

Extended maps, with a much better coverage along the Galactic mid-plane ($|Z_{\rm Gal}| < 0.5$ kpc) only appeared with APOGEE (Allende Prieto et al. 2008; Majewski et al. 2017), which in its first year of data (with around only 20,000 stars of sufficient quality) was already able to demonstrate that the chemical discontinuity observed by Fuhrmann was also present far outside the solar neighbourhood (Anders et al. 2014; Nidever et al. 2014), also confirming the short scale length of the chemical thick disc. These APOGEE results were complemented by other surveys at larger distances from the Galactic mid-plane (e.g. Bovy & Rix 2013; Mikolaitis et al. 2014, and references therein), but without such a good coverage of the inner Galaxy.

Shortly afterwards, Hayden et al. (2015) used a sample of around 70,000 red giants from APOGEE DR12 (Alam et al. 2015) to increase the sampled volume with respect to the 2014 maps, covering a Galactocentric distance range between 3 kpc and 15 kpc within 2 kpc of the Galactic plane. By that time it became clear that towards the outer parts of the disk we would see a flaring, in which the low-[α/Fe] would dominate even at large heights above the Galactic mid-plane (see Minchev et al. 2015, 2019 for discussions), implying that the term 'thick disc' should be used more carefully. The chemically defined thick disk (by separating populations in the [α/Fe versus [Fe/H] diagram) is indeed confined to the inner regions, whereas the geometrically defined thick disk (by a cut in $Z_{\rm Gal}$) is a mixture of flaring mono-age populations, and therefore would show an age gradient (see Martig et al. 2016a; Mackereth et al. 2017; Minchev et al. 2018).

The Hayden et al. (2015) chemical-abundance maps were limited by the still poor coverage of the innermost parts of the Milky Way.

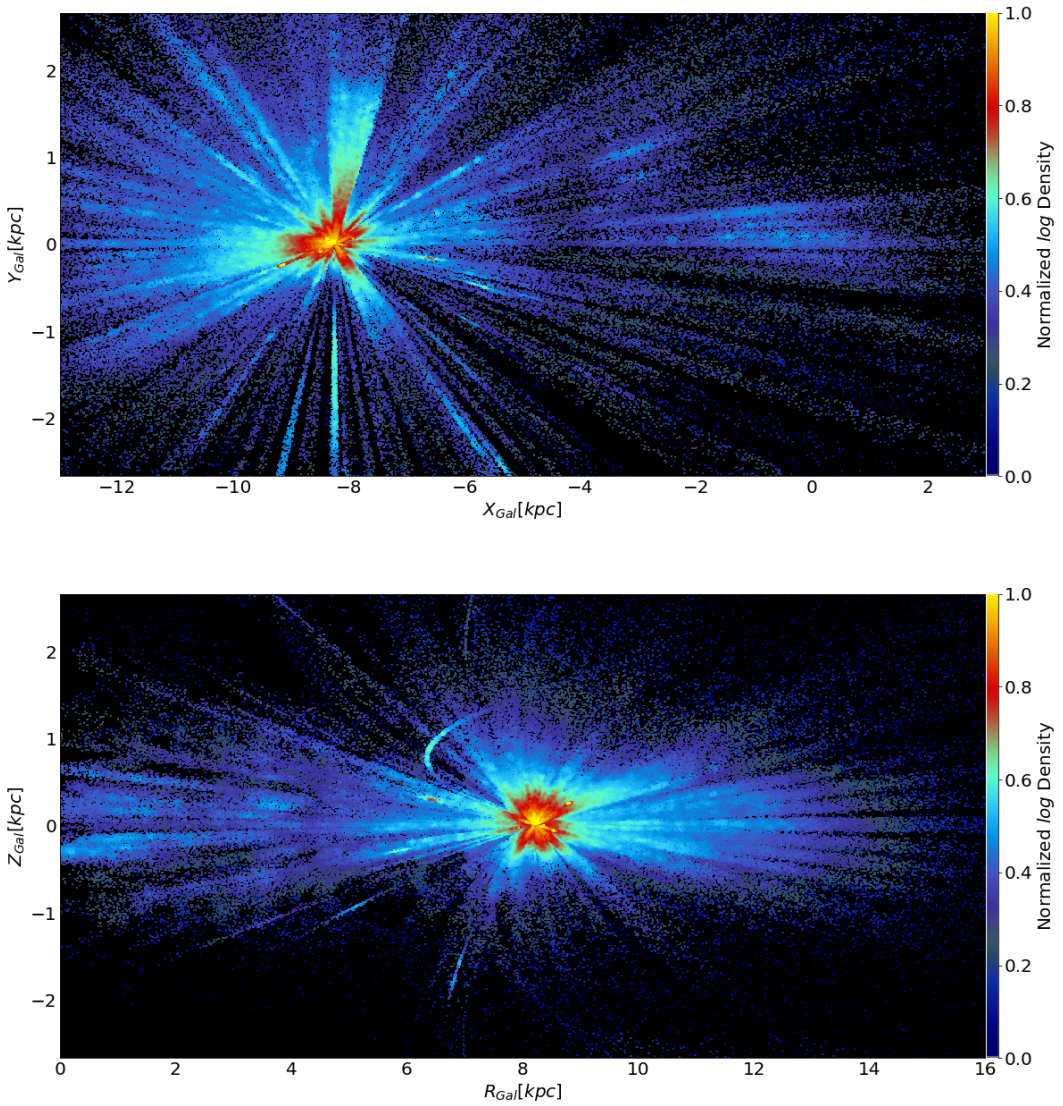

Figure 2.5: Top panel: Galactocentric Cartesian XY map of the APOGEE DR16 sample. Bottom panel: Density distribution in Galactocentric cylindrical RZ coordinates. Some distinct features of APOGEE targeting can be easily discerned: the high target density in the *Kepler* field, enhanced density distributions around open clusters. These are sometimes elongated when the distance precision is low, e.g. ($d \sim 5.2$ kpc); ω Cen appear around $R \simeq 6.5$ kpc, $Z \simeq 1$ kpc.

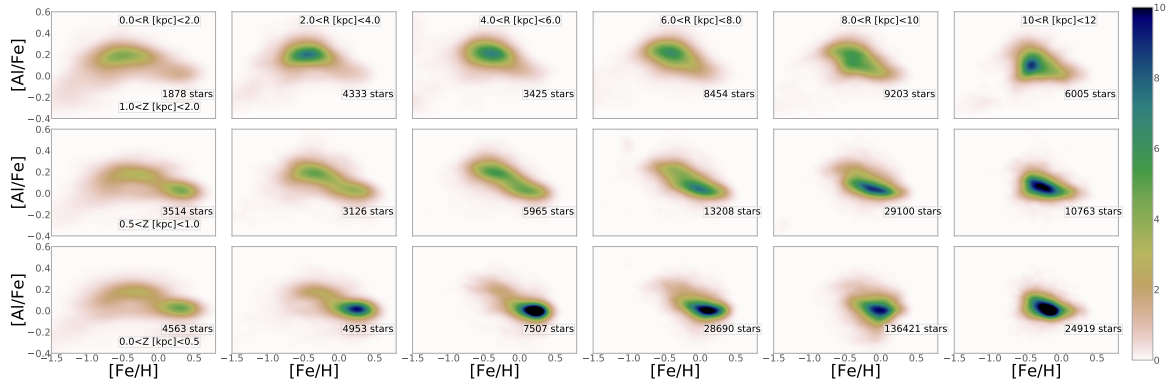

Figure 2.6: APOGEE DR16 [Al/Fe] vs. [Fe/H] diagrams in bins of galactocentric cylindrical coordinates out to $R_{\rm Gal}$ = 10 kpc, similar to Fig. 2.7.

That paper, along with following APOGEE publications (e.g. Zasowski et al. 2019 based on DR14) tentatively reported that stars with $R_{\rm Gal}$ < 5kpc seem to lie on a single track, whereas at larger radii two distinct sequences were observed (an observation later interpreted as the fundamental dichotomy between the inner and outer discs by Haywood et al. 2016, 2018a). Recio-Blanco et al. (2017), using a sample of GES spectra, report the existence of low-[α/Fe] in the bulge area. With the larger APOGEE sample available from SDSS DR14 (Abolfathi et al. 2018), Rojas-Arriagada et al. (2019) selected stars within 3.5 kpc from the Galactic centre and report the detection of a bimodal sequence in [Mg/Fe] versus [Fe/H], confirming the GES results. The authors also suggest the two sequences to merge above [Fe/H]$\sim$ 0.15 dex into a single sequence (see Barbuy, Chiappini, & Gerhard (2018) for a review of other chemical-abundance studies of the Galactic bulge previous to APOGEE DR14 and *Gaia* DR2).

Figures 2.7 and 2.8 present our updated [α/Fe] versus [Fe/H] diagrams in 2 kpc bins in width in $R_{\rm Gal}$ and three narrow bins in $|Z_{\rm Gal}|$, obtained from APOGEE DR16 in combination with *Gaia* DR2 and our `StarHorse` distances. These abundance-ratio maps now extend from $R_{\rm Gal}$ = 0 out to 20 kpc, with excellent statistics (more than 150 stars per bin) out to $R_{\rm Gal}$ = 18 kpc, where the target density drops dramatically. To avoid figures that are too crowded, we divided the chemical-abundance maps into two plots: Fig. 2.7 shows the [α/Fe] versus [Fe/H] diagrams for the inner-disk bins, while Fig. 2.8 shows the outer-disk bins. The distance and extinction uncertainties in each of the radial bins are shown in the top row of the two figures. These show that even in the innermost 2 kpc, `StarHorse` achieves precision of around 10% in distance and better than 0.1 magin A_V for most of the targets; the, unfortunately, less precise extinction estimates in regions closer to the solar position is due to our imposed bright limit for the Pan-STARRS1 photometry.

While the DR16 [α/Fe] versus [Fe/H] diagrams shown in Figs. 2.7 and 2.8 confirm most of the previous analyses, they also show some clear and important differences. Figure 2.7 now shows a much more complete view of the chemical-abundance distribution in the inner disc. Each of the innermost bins ($R_{\rm Gal}$ < 4 kpc) contains more than 1000 stars now, and especially very close to the Galactic mid-plane these numbers amount to > 5000 (see the two leftmost bottom panels), potentially also allowing for analyses of azimuthal abundance variations.

The bimodality reported by Rojas-Arriagada et al. (2019) is clearly confirmed in this improved map: we observe this bimodality in all [α/Fe]-[Fe/H] diagrams in the innermost regions ($R_{\rm Gal}$ < 4 kpc), but especially for stars closest to the Galactic plane ($|Z_{\rm Gal}|$ < 0.5 kpc). The single sequence reported in Hayden et al. (2015) and Zasowski et al. (2019) for the inner-

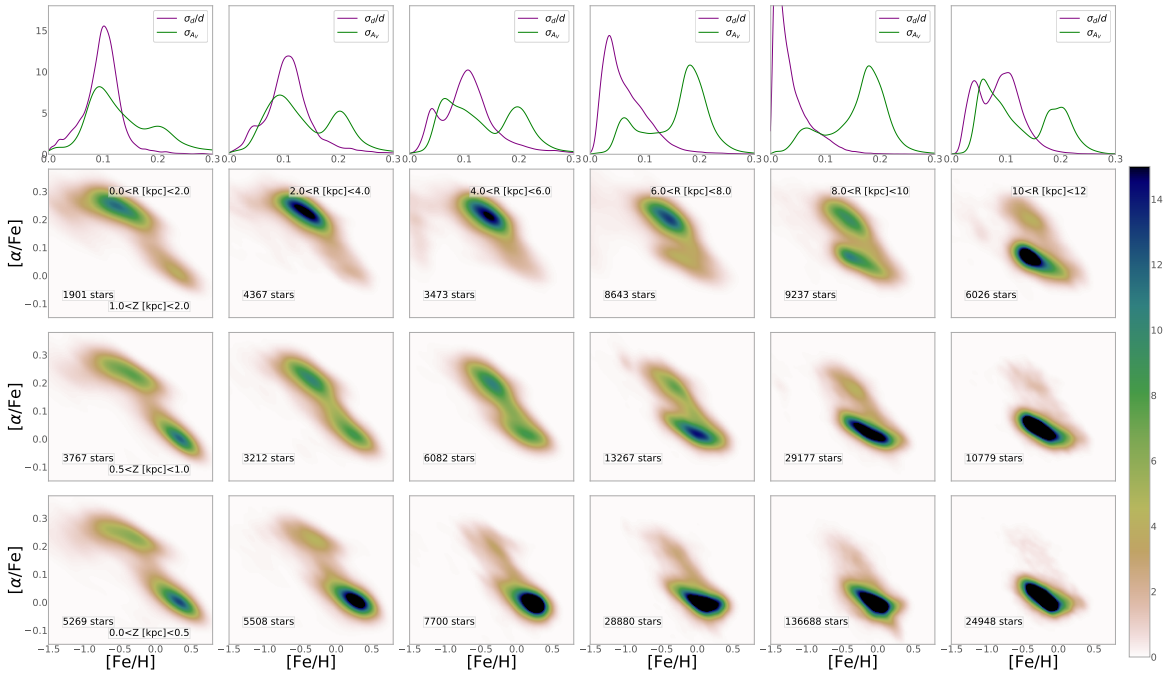

Figure 2.7: APOGEE DR16 [α/Fe] vs. [Fe/H] diagrams in bins of galactocentric cylindrical coordinates, similar to the chemical maps presented in Hayden et al. (2015), but extending further into the inner Galaxy. The top panels show kernel-density estimates of the uncertainties distributions in `StarHorse` extinctions and distances, for each galactocentric distance bin (including all $Z_{\rm Gal}$ bins).

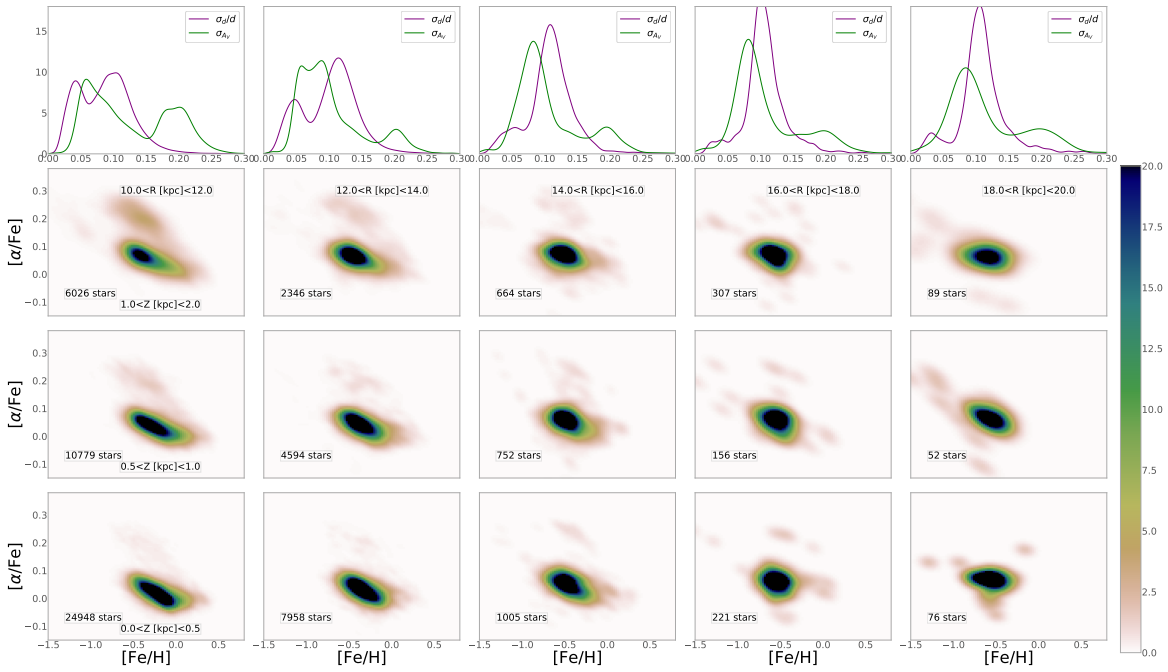

Figure 2.8: Same as previous figure, but now extending to the outer disc.

most regions is not confirmed now, as the bins at lower $|Z_{\rm Gal}|$ contain more data.

In contrast to Rojas-Arriagada et al. (2019), however, the two blobs completely define the detached sequences without merging, thus showing a true chemical discontinuity. The new maps show that the chemical discontinuity seen in the solar neighbourhood bin (mostly studied by other surveys; middle row, fourth column) extends towards the bulge and become completely separated; this is very similar to what was found by Fuhrmann (1998), and Fuhrmann (2011) within 25 pc but now extended to larger metallicities, as expected given the observed abundance gradients in the Galactic disc. The more detailed implications of these maps for chemo-dynamical models or the Milky Way will be discussed in future papers. We also caution that this chemical discontinuity is not seen in smaller samples of bulge stars (e.g. da Silveira et al. 2018). Biases in small samples, as well as large distance uncertainties, may contribute to the appearance/disappearance of the chemical discontinuity in the bulge. It is difficult, however, to invoke a bias in the APOGEE inner-Galaxy sample (comprised of many thousands of stars) that would artificially increase the chemical discontinuity.

Figure 2.8 shows the [α/Fe] versus [Fe/H] plane for the outermost bins in $R_{\rm Gal}$ (the bin 10-12 kpc is repeated from previous figure because the colour scale is slightly different from Fig. 2.7. Again we observe that for the more distant stars, the addition of the PanSTARRS-1 photometry improves the extinction estimates (compare uncertainty distributions in the top row of the figure). The diagram also clearly confirms the almost total disappearance of the high-[α/Fe] sequence around $\sim$ 14 kpc. Because the number of stars is small in the very outer disc, the noise in those plots increases, giving more visual weight to outliers.

Finally, we note two other important characteristics of the new maps presented both in Fig. 2.7 and Fig. 2.8, when focusing on stars near to the Galactic mid-plane ($|Z_{\rm Gal}| <$ 0.5 kpc). Firstly, the [α/Fe] centroid of the low-[α/Fe] distribution gradually shifts to larger values with increasing galactocentric distance (especially visible in Fig. 2.8), corresponding to a positive radial [α/Fe] gradient, continuing the trend observed at larger galactocentric distances (Anders et al. 2014; Hayden et al. 2014). Secondly, in the innermost bin ($R_{\rm Gal} <$ 2 kpc, and $|Z_{\rm Gal}| <$ 0.5 kpc) the [α/Fe] trend for the more metal-rich, low-[α/Fe] population ($\sim -0.2 <$ [Fe/H] < 0.5) is linearly decreasing, without any flattening at larger metallicities. This is in agreement with optical studies of the bulge (Friaça & Barbuy 2017; da Silveira et al. 2018 – see also Barbuy, Chiappini, & Gerhard (2018)), but remains in stark contrast to what is observed at larger galactocentric distances (see radial bins from $6 < R_{\rm Gal} < 12$ kpc, in the same row – $|Z_{\rm Gal}| < 0.5$ kpc), where the cloud of data bends, thereby showing a flattening of the abundance-ratio trend beyond solar metallicities. The reason for this bending is the migration of old metal-rich stars from the innermost bins towards the outer regions, populating mostly the 8 – 12 kpc bins.

Indeed, the high-metallicity thin disk stars in the outer regions are known to be migrated stars from the inner disk (e.g. Grenon 1989; Casagrande et al. 2011; Anders et al. 2017b). For example, according to the chemo-dynamical model of Minchev et al. (2013) and Minchev et al. (2014), the mixture of migrating stars from other galactocentric distances changes when moving from the inner to the outer disc, and even in the 8 – 12 kpc range there is are large number of migrators from the innermost disk regions. A large number of old inner disk stars can be found around the solar vicinity, according to the predictions of Minchev et al. (2014). This can also be clearly seen in Anders et al. (2017a, their Figure 1).

The larger statistics of the current maps, especially near the Galactic mid-plane, do not support the dichotomy between the inner and outer discs advertised by Haywood et al. (2019). This suggests instead an inside-out formation of the thin disc, a continuous variation in the chemical properties from the innermost regions towards the outer parts, and significant radial migration (e.g. Frankel et al. 2018).

At larger $|Z_{\rm Gal}|$ bins and in the outer disc, the combined effects of radial migration and disk flaring make interpretations more complex, and the multif-element abundance maps available from APOGEE offer a unique opportunity to finally quantify all these processes (see e.g. Frankel et al. 2018, 2020 for first attempts on constraining radial migration efficiency using APOGEE red-clump giants with statistical age estimates). In the innermost bins, going from low to large $|Z_{\rm Gal}|$, we also sees a smooth transition from a thin disc-like component to an old (i.e. [α/Fe]-enhanced) thick disc-like (or spheroidal) component.

Detailed future investigations should use forward simulations to properly take into account selection effects (see e.g. Miranda et al. 2014; Anders et al. 2016; Nandakumar et al. 2017; Fragkoudi et al. 2018; Frankel et al. 2019, for discussions). Moreover, the addition of age and kinematical information is also necessary to be able to disentangle the factors playing a role in these maps, namely, radial migration, population mixture, flaring, and details of the nucleosynthetic yields. An illustrative example is provided by the birth-radius estimation technique proposed by Minchev et al. (2018).

2.5.2 [Al/Fe] versus [Fe/H] diagram

Figure 2.6 shows the same type of plot as Fig. 2.7, but in this case for the [Al/Fe] abundance ratio instead of [α/Fe]. As an additional constraint, we only include stars with well-determined ASPCAP Al abundances (AL_FE_FLAG=0) in this plot. The maps are similar to those in Fig. 2.7, indicating that overall, Al (being an odd-Z element) behaves like an α element at disc-like metallicities; this was also previously shown to be the case in the bulge (for instance, see discussion in McWilliam 2016). The important difference of Fig. 2.6 with respect to the corresponding Fig. 2.7 is the almost complete absence of the bimodality in the abundance plane for galactocentric distances $R_{\rm Gal} > 2$ kpc.

However, the [α/Fe] versus [Fe/H] discontinuity seen in the very inner regions discussed above is also seen in the [Al/Fe] versus [Fe/H] diagram: in the $R_{\rm Gal} < 2$ kpc bin close to the Galactic plane we see essentially two detached [Al/Fe] sequences. This fact provides further evidence for the reality of the chemical discontinuity seen in the heart of the Galactic bulge.

The difference between [α/Fe] and [Al/Fe] for the most metal-poor stars is that, whereas the [α/Fe] seems to continue raising towards lower metallicities, the [Al/Fe] starts to bend down. This is a consequence of the metallicity-dependent Al yields in massive stars.

2.5.3 [Al/Mg] versus [Mg/H] and [Mg/O] versus [Mg/H] diagrams

As an example illustrating the wealth of new chemical-abundance information contained in DR16, we now discuss the behaviour of the ratios between two α-like elements that use magnesium rather than iron as a reference element. Because Mg is mainly a product of core collapse supernovae, its increase with time follows the star formation rate more closely than iron, which can keep increasing even if the star formation stops as a result of the contribution of type Ia supernovae released on longer timescales. From the observational side, magnesium is also a convenient element because the calibrated ASPCAP [Mg/H] abundances show small dispersions, very small trends with effective temperature, and they follow the expected trends in the abundance diagrams.

Fig. 2.9 shows both an [Al/Mg] versus [Mg/H] and an [O/Mg] versus [Mg/H] map of the Galaxy, focussing on the inner disk and bulge region ($R_{\rm Gal} < 8$ kpc). In both plots, we again only plot stars with high-quality DR16 ASPCAP abundances, by requiring the corresponding abundance flag entries (MG_FE_FLAG and, respectively, AL_FE_FLAG and O_FE_FLAG) to equal zero.

The main point of Fig. 2.9 is to showcase the vast amount of new high-quality APOGEE data, especially for the inner disc. To appreciate the increase of the sample with respect to DR14, Fig. 2.9 should be compared to Figs. 4 and 5 of Weinberg et al. (2019), which was based on a small sample of 20,000 stars with

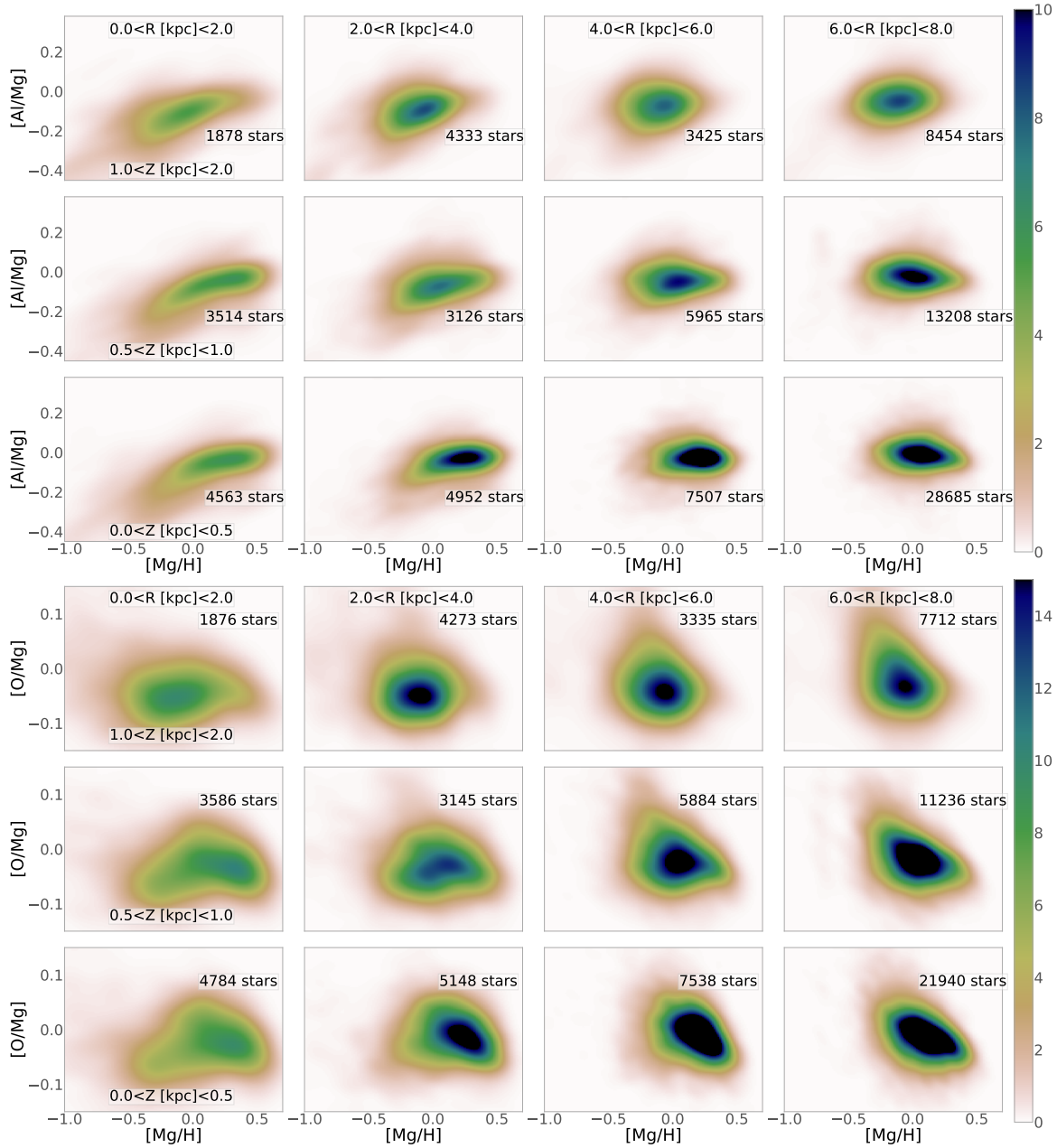

Figure 2.9: Top panel: APOGEE DR16 [Al/Mg] vs. [Mg/H] diagrams in bins of Galactocentric cylindrical coordinates, similar to Fig. 2.7, but only out to $R_{\rm Gal}$ = 8 kpc. Bottom panel: the same for [O/Mg] vs. [Mg/H].

only slightly stricter quality requirements (3700 K < $T_{\rm eff}$ < 4600 K, SNREV > 80, no "ASPCAP bad" flags, EXTRATARG=0). The new data clearly allow us to study the very heart of our Galaxy in much more detail, even when the same quality cuts are applied.

The main isotopes of both O and Mg are produced during the hydrostatic phases of high-mass stars. This ratio is then mostly sensitive to details of related to the stellar yields, such as mass loss and rotation in the case of oxygen and convection treatment in the case of Mg, but is expected to remain close to solar (Woosley et al. 2002; Sukhbold et al. 2016; Groh et al. 2019).

The following two things can be noted in the [O/Mg] versus [Mg/H] diagrams in the inner Galaxy (Fig. 2.9): a systematic slight increase of the [O/Mg] median value from the innermost regions towards the solar neighbourhood for stars in the top row (1 kpc < $|Z_{\rm Gal}|$ < 2 kpc) and a less pronounced presence of the low-[Mg/H] low-[O/Mg] population towards the mid-plane that remains visible only in the innermost bin.

In order to understand if this is due to O or Mg, we next checked the [Al/Mg] diagrams (bottom panel of Fig.2.9). Similarly, the median [Al/Mg] ratio in the top row (1 kpc < $|Z_{\rm Gal}|$ < 2 kpc) increases with galactocentric distance, reaching the solar value at the solar ring. Moreover, [Al/Mg] also increases with metallicity in the smallest galactocentric distance bins.

Taking both results at face value, without considering further biases that could be affecting proportions of stars in the different loci of these diagrams, the results suggest that there is an increase of Mg towards larger metallicities or a relative decrease of both O and Al (e.g. Groh et al. 2019).

2.6 StarHorse results for other publicly released spectroscopic surveys

In this paper we also provide distances and extinctions for different spectroscopic surveys, namely for GALAH DR2 (Buder et al. 2018), LAMOST DR5 (Xiang et al. 2019), RAVE DR6 (Steinmetz et al. 2020a), and GES DR3 (Gilmore 2012). We again used *Gaia* DR2 parallaxes (Gaia Collaboration et al. 2018b). Moreover, we also included photometry from APASS (Henden & Munari 2014) that was not included in the APOGEE run. Also, since none of these surveys extend to the very extincted regions, we used Gaia DR2 photometry in this case. *Gaia* contains three passbands G, G_{BP}, and G_{RP} in the respective wavelengths 320-1050 nm, 320-680 nm, and 610-1070 nm (Gaia Collaboration et al. 2016; Weiler 2018). Even though this photometry is very precise, there are some discrepancies between observations and the sensitivity curves published. To correct for this effect, we followed the recommendations of Maíz Apellániz & Weiler (2018); these are the same corrections as applied in Anders et al. (2019, see their Table 1).

We computed distances and extinctions in the same way as for APOGEE DR16, for which we present catalogues in the same format as before (Table 2.B.1). Fig. 2.10 shows the resulting spatial coverage of the surveys analysed in this work, and Fig. 2.11 shows the corresponding distance and distance uncertainty distributions. In addition, in Appendix 2.C we provide summary plots similar to Figs. 2.1, 2.2, and 2.4, demonstrating the sky coverage and the quality of the results for each of the surveys. In the following subsections we describe the assumptions made in each of these catalogues.

2.6.1 GALAH DR2

The spectroscopic survey GALAH (De Silva et al. 2015; Martell et al. 2017) aims to identify stellar groups that were born together, by searching for similarity on the chemical patterns of the stars. Therefore GALAH spectra were obtained with the high-resolution and multi-band spectrograph HERMES (Barden et al. 2010), which is capable to deliver abundances for up to 23 chemical elements. Its latest data release, GALAH DR2 release in April 2018, contains radial velocities, atmospheric parameters, and abundances for a total of 342,682 unique stars (Buder et al. 2018).

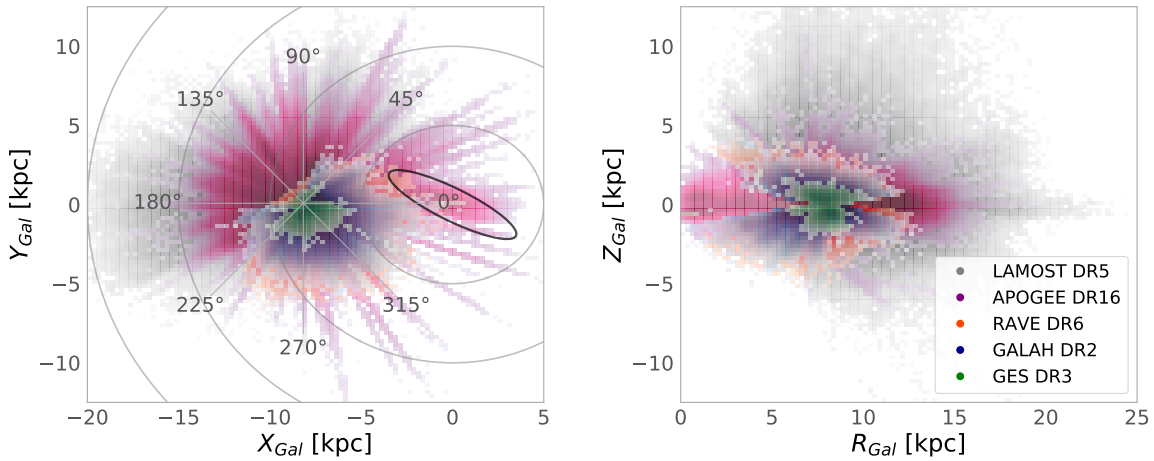

Figure 2.10: Survey coverage of the catalogues presented in this paper in galactocentric coordinates. In both panels, the colours indicate the different surveys (grey: LAMOST DR5; magenta: APOGEE DR16; red: RAVE DR6; blue: GALAH DR2; and green: GES DR3) and the relative density of observed stars (bins with less than five stars are left blank). To guide the eye, grey circles are placed in multiples of 5 kpc around the Galactic centre, the expected location of the Galactic bar (e.g. Bland-Hawthorn & Gerhard 2016) is indicated by the black ellipse, and a heliocentric Galactic longitude frame is over-plotted. Left panel: Cartesian XY coordinates. Right panel: Cylindrical RZ coordinates.

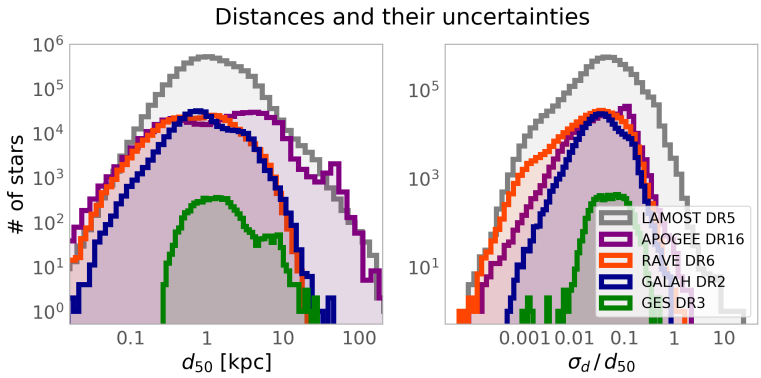

Figure 2.11: Distribution of posterior distances (left) and their corresponding relative uncertainties (right) for the catalogues presented in this paper. In both panels, the axes are logarithmic and the colours are the same as in Fig. 2.10 (grey: LAMOST DR5, magenta: APOGEE DR16, red: RAVE DR6, blue: GALAH DR2, and green: GES DR3).

The GALAH survey maps all stellar populations between magnitudes ($12 < V < 14$) and avoids the Galactic plane $|b| > 10$. In Q18 we computed distances and extinctions using the GALAH DR1 parameters combined with *Gaia* DR1. Now we have available much more data both in GALAH DR2 and *Gaia* DR2. We followed the same procedure in this work as in Q18 to run this latest public GALAH data. The atmospheric parameters were treated as they come in the catalogue. We again used the (Salaris et al. 1993) correction for stars that have [α/Fe] (see Section 2.3.1). For those without a reported [α/Fe] ratio, we assumed [M/H]=[Fe/H].

We chose to run GALAH with APASS photometry since its faint limits are still too bright to be able to use PanSTARRS-1 (due to saturation). We also ran StarHorse with parallax True mode (see Q18 section 3.2.1) since more than 90% of the catalogue contains parallaxes uncertainties better then 20%. From the input catalogue a total of 324,999 stars converged (94%) with solutions of distances, extinctions, and astrophysical parameters that can be downloaded via the CDS.

2.6.2 LAMOST DR5 DD-Payne VAC

The survey LAMOST (Cui et al. 2012; Zhao et al. 2012) is one of the largest scale spectroscopic

surveys and the first large astronomical device in China. This instrument has been collecting data since 2012, and now after about eight years the survey has released nine million spectra in the wavelength range of 3690-9100 Å and spectral resolution of $R \sim 1800$. These nine million spectra contain stars, galaxies, quasars, and non-classified sources.

We adopted the recently published DR5 DD-Payne VAC[15] (Xiang et al. 2019) catalogue. This catalague contains stellar parameters and individual elemental abundances for six million LAMOST DR5 stars, obtained with a data-driven approach incorporating constraints from theoretical spectra and trained on GALAH DR2 and APOGEE DR14 results.

From this catalogue we only selected stars with stellar parameters with uncertainties in gravity, surface temperature, metallicity, and [α/Fe] ratios smaller than $\sigma_{\log g} < 1$ dex, $\sigma_{T_{\rm eff}} < 800$ K, $\sigma_{[\rm Fe/H]} < 1.0$ dex, and $\sigma_{[\alpha/\rm Fe]} < 1.0$, respectively. The goal was to avoid stars with too large uncertainties and save computing time.

For LAMOST DR5 we combined the spectra again with *Gaia* parallaxes and photometry. We complemented the input data with photometry from PanSTARRS1, 2MASS, and WISE. We also ran LAMOST with parallax true mode since most parallaxes in LAMOST also have uncertainties better then 20%. From 5,651,710 sources with available parallaxes `StarHorse` converged for 4,928,715 stars (87%). One of the reasons for a smaller convergence in the case of LAMOST is the fact that we used a thicker spaced PARSEC model grid (0.05 Gyr in age and 0.05 dex in [M/H]). The solutions of distances, extinctions, and astrophysical parameters can be downloaded via the CDS.

2.6.3 RAVE DR6

We obtained the RAVE spectra with the multi-object spectrograph deployed on 1.2*m* UK Schmidt Telescope of the Australian Astronomical Observatory (AAO). The spectra have a medium resolution of ($R \sim 7.500$) and cover the CaII-triplet region (8410-8795Å). We used the final RAVE data release, DR6 (Steinmetz et al. 2020a), and in particular, the purely spectroscopically derived stellar atmospheric parameters subscripted `cal_madera` (Steinmetz et al. 2020b). The uncertainties that we use are, in general, the maximum between the calibrated and not calibrated parameters given in the catalogue or a fiducial maximum. These corrections are very similar to those applied to run RAVE DR5 combined with *Gaia* DR1 in Q18. We then combined RAVE DR6 with *Gaia* DR2 parallaxes and the photometric data used in this case is the same as for LAMOST. We configured `StarHorse` to use the `parallax=true` option and the same coarser isochrone grid we used for LAMOST, since the uncertainties of these surveys are larger. From the input catalogue of DR6 (488,233 unique objects), 408,894 stars converged, and we make their derived astrophysical stellar parameters available in this work. Because of the significantly smaller formal uncertainties of the DR6 MADERA stellar parameters compared to DR5, the number of stars for which `StarHorse` converged is slightly smaller than for DR5.

2.6.4 GES survey DR3

The large public spectroscopic survey GES (Gilmore 2012) has a high resolution that covers all Milky Way components and open star clusters of all ages and masses. The final GES release is expected to include about 10^5 stars. We downloaded the GES Data Release 3 (DR3) from the ESO catalogue facility. This catalogue contains a total of 25533 stars, including the Milky Way field, open clusters, and calibration stars. We selected only the stars in the Milky Way field to produce our `StarHorse`, which is about 7870 stars. In this case we also made a quality criteria cut, that is, $\sigma_{\log g} < 0.4$ dex, $\sigma_{T_{\rm eff}}/T_{\rm eff} < 0.05$ K, $\sigma_{[\rm Fe/H]} < 0.2$ dex. The final catalogue used as `StarHorse` input contains then 6316 stars, The complementary photometric data used in this case is the same as for LAMOST. We then ran the code again with parallax True mode, and `StarHorse` converged

15 http://dr5.lamost.org/doc/vac

for 6,095 stars. The StarHorse astrophysical parameters for the GES DR3 stars are also at the CDS.

2.7 Conclusions

With this paper we present a set of VACs derived from the stellar spectroscopic surveys APOGEE, GALAH, LAMOST, RAVE, and GES. In particular our APOGEE DR16 VAC, released as part of SDSS DR16 (Ahumada et al. 2020), was produced by running the StarHorse code, which is described in detail by Q18, in the DR16 ASPCAP catalogue matched to *Gaia* DR2 with the addition of photometry from PanSTARRS-1, 2MASS, and AllWISE. This VAC contains distance and extinction estimates for 388,815 unique stars out of a total of 437,485 unique objects contained in the DR16 catalogue. Our code was validated extensively in Santiago et al. (2016), and Queiroz et al. (2018), and Anders et al. (2019). In Appendix 2.B we provide some additional tests showing that the newly derived parameters for APOGEE DR16 generally compare well to results obtained from asteroseismology, open clusters, and other spectroscopic surveys. There is evidence for slightly overestimated extinctions for our APOGEE DR16 VAC, which we attribute in part to the missing reliable optical photometry for most of this sample, and in part to an offset in the ASPCAP temperature scale, especially outside the recommended calibration regime.

In Appendix 2.B we also show that our distances are less biased towards the inner Galactic disk than the neural-network based distances of Leung & Bovy (2019) (see Fig. 2.B.6). The typical uncertainties for the APOGEE DR16 sample are of the order of $\simeq$ 10% in distance and of 0.16 magin A_V. A clearly bimodal distribution of extinction uncertainties is observed with the peak at $\sigma_{A_V} \simeq 0.06$ found for stars with available optical magnitudes from PanSTARRS-1, while the peak at larger σ_{A_V} is made by stars with no such measurements. The typical distance uncertainties are also different for dwarfs ($\simeq$ 2%) and giants ($\simeq$ 5%). The scientifc results from the first analysis of the StarHorse APOGEE DR16 catalogue can be summarised as

- Using the StarHorse VAC we demonstrate that the APOGEE DR16 sample represents a major leap in terms of coverage of the Galactic disk with high-resolution spectra. The density of APOGEE targets exceeds a dozen stars per kiloparsec^2 everywhere in the $R_{\rm Gal} - Z_{\rm Gal}$ plane for $0 < R_{\rm Gal} < 18$ kpc and $-3{\rm kpc} < Z_{\rm Gal} < 3$ kpc, allowing for an unprecedented chemo-kinematic mapping of the inner and outer stellar discs with significant azimuthal coverage.

- From the improved APOGEE coverage and StarHorse distances we can see a bar signature in the density maps projected in XY Galactocentric coordinates; this is also found in A19. However the bar signature found in this work has a smaller angle with respect to the Galactic plane, which is more consistent with previous studies about the Galactic bar structure (Bland-Hawthorn & Gerhard 2016).

- The extended chemical-abundance maps in Fig. 2.7 confirms, for the first time with good statistics of thousands of stars, a chemical bimodality in the very inner Galaxy $0 < R_{\rm Gal} < 2$ kpc and $0 < |Z_{\rm Gal}| < 1$ kpc. This is different from previous analyses that reported a single sequence (Hayden et al. 2015; Zasowski et al. 2019), but with much less populated samples.

- The two groups visible in the [α/Fe]-[Fe/H] plane in the innermost bin completely define the detached sequences, implying a true chemical discontinuity. The larger statistics of the current maps, especially near the Galactic mid-plane, do not support the dichotomy between the inner and outer discs. On the other hand, it suggests the chemical discontinuity to be a clear property of the global chemical-enrichment history of the Milky Way.

- The chemical maps of [α/Fe]-[Fe/H] extend to the very outer disc, $R_{\rm Gal} > 20$ kpc,

and also show the complete disappearance of a high-alpha population further than $R_{\rm Gal} > 14$ kpc. This confirms the shorter scale length of the Galactic thick disk concerning the Galactic thin disc, following previous studies (Cheng et al. 2012; Anders et al. 2014).

- There is an indication for a positive radial $[\alpha/Fe]$ gradient, observed from the fact that the $[\alpha/Fe]$ centroid of the α-poor sequence in the inner Galaxy gradually shifts to larger values with increasing Galactocentric radius observed in Figures 2.7 and 2.8 continuing the trend reported by Anders et al. (2014), and Hayden et al. (2014).

- The maps of $[\alpha/Fe]$ show some evidence for radial migration of old metal-rich stars from the inner Galaxy to the outer Galaxy; this is shown by the flattening of the abundance-ratio trend beyond the solar metallicities.

- The chemical duality in the inner bins is also confirmed in maps using aluminium and iron, $[Al/Fe] - [Fe/H]$. This is not seen for larger Galactocentric distances, where the disk chemical bimodality disappears in this abundance regime. This indicates a strong chemical duality in the inner Galaxy. Those diagrams also show metallicity-dependent Al yields in massive stars, with $[Al/Fe]$ starting to bend down towards lower metallicities.

- The resulting maps using α-elements and magnesium as a reference instead of iron, show an increase of Mg with respect to Galactocentric distance. Since Mg follows the star formation more closely than iron, this suggests an inside-out formation.

The data produced in this work and made publicly available allow for much more sophisticated chemical-abundance studies over much larger disk volumes than previous data releases. New studies also gathering kinematic information will enable unprecedented constraints for chemo-dynamical models of the Milky Way, espetially in the inner-most and outer-most Galaxy.

All the newly produced `StarHorse` catalogues are available for download from https://data.aip.de/aqueiroz2020 please use the DOI to quote the data: doi : 10.17876/$data$/2020_2.

Acknowledgements The `StarHorse` code is written in python 3.6 and makes use of several community-developed python packages, among them `astropy` (Astropy Collaboration et al. 2013), `ezpadova`[16], `numpy` and `scipy` (Virtanen et al. 2019), and `matplotlib` (Hunter 2007). The code also makes use of the photometric filter database of VOSA (Bayo et al. 2008), developed under the Spanish Virtual Observatory project supported from the Spanish MICINN through grant AyA2011-24052.
Funding for the SDSS Brazilian Participation Group has been provided by the Ministério de Ciência e Tecnologia (MCT), Fundação Carlos Chagas Filho de Amparo à Pesquisa do Estado do Rio de Janeiro (FAPERJ), Conselho Nacional de Desenvolvimento Científico e Tecnológico (CNPq), and Financiadora de Estudos e Projetos (FINEP). Funding for the Sloan Digital Sky Survey IV has been provided by the Alfred P. Sloan Foundation, the U.S. Department of Energy Office of Science, and the Participating Institutions. SDSS-IV acknowledges support and resources from the Center for High-Performance Computing at the University of Utah. The SDSS web site is www.sdss.org.
SDSS-IV is managed by the Astrophysical Research Consortium for the Participating Institutions of the SDSS Collaboration including the Brazilian Participation Group, the Carnegie Institution for Science, Carnegie Mellon University, the Chilean Participation Group, the French Participation Group, Harvard-Smithsonian Center for Astrophysics, Instituto de Astrofísica de Canarias, The Johns Hopkins University, Kavli Institute for the Physics and Mathematics of the Universe (IPMU) / University of Tokyo, Lawrence Berkeley National Laboratory, Leibniz-Institut für Astrophysik Potsdam (AIP), Max-Planck-Institut für Astronomie (MPIA Heidelberg), Max-Planck-Institut für Astrophysik (MPA Garching), Max-Planck-Institut für Extraterrestrische Physik (MPE), National Astronomical Observatory of China, New Mexico State University, New York University, University of Notre Dame, Observatário Nacional / MCTI, The Ohio State University, Pennsylvania State University, Shanghai Astronomical Observatory, United Kingdom Participation Group, Universidad Nacional Autónoma de México, University of Arizona, University of Colorado Boulder, University of Oxford, University of Portsmouth, University of Utah, University of Virginia, University of Washington, University of Wisconsin, Vanderbilt University, and Yale University.

16 https://github.com/mfouesneau/ezpadova

Guoshoujing Telescope (the Large Sky Area Multi-Object Fiber Spectroscopic Telescope LAMOST) is a National Major Scientific Project built by the Chinese Academy of Sciences. Funding for the project has been provided by the National Development and Reform Commission. LAMOST is operated and managed by the National Astronomical Observatories, Chinese Academy of Sciences.
Funding for RAVE has been provided by: the Australian Astronomical Observatory; the Leibniz-Institut für Astrophysik Potsdam (AIP); the Australian National University; the Australian Research Council; the French National Research Agency; the German Research Foundation (SPP 1177 and SFB 881); the European Research Council (ERC-StG 240271 Galactica); the Istituto Nazionale di Astrofisica at Padova; The Johns Hopkins University; the National Science Foundation of the USA (AST-0908326); the W. M. Keck foundation; the Macquarie University; the Netherlands Research School for Astronomy; the Natural Sciences and Engineering Research Council of Canada; the Slovenian Research Agency; the Swiss National Science Foundation; the Science & Technology Facilities Council of the UK; Opticon; Strasbourg Observatory; and the Universities of Groningen, Heidelberg and Sydney. The RAVE web site is at https://www.rave-survey.org. This work has made use of data from the European Space Agency (ESA) mission *Gaia* (http://www.cosmos.esa.int/gaia), processed by the *Gaia* Data Processing and Analysis Consortium (DPAC, http://www.cosmos.esa.int/web/gaia/dpac/consortium). Funding for the DPAC has been provided by national institutions, in particular the institutions participating in the *Gaia* Multilateral Agreement.
This work has also made use of data from *Gaia*-ESO based on data products from observations made with ESO Telescopes at the La Silla Paranal Observatory under programme ID 188.B-3002.
FA is grateful for funding from the European Union's Horizon 2020 research and innovation programme under the Marie Skłodowska-Curie grant agreement No. 800502 H2020-MSCA-IF-EF-2017. CC acknowledges support from DFG Grant CH1188/2-1 and from the ChETEC COST Action (CA16117), supported by COST (European Cooperation in Science and Technology).
DAGH acknowledges support from the State Research Agency (AEI) of the Spanish Ministry of Science, Innovation and Universities (MCIU) and the European Regional Development Fund (FEDER) under grant AYA2017-88254-P. J.G.F-T is supported by FONDECYT No. 3180210.
DB is supported in the form of work contract FCT/MCTES through national funds and by FEDER through COMPETE2020 in connection to these grants: UID/FIS/04434/2019; PTDC/FIS-AST/30389/2017 & POCI-01-0145-FEDER-030389.
ABA thanks Cosmos

2.A StarHorse data model

The tables in this appendix describe our data model for the APOGEE DR16 StarHorse VAC (Table 2.B.1) and the meaning of the human-readable flags SH_INPUTFLAGS and SH_OUTPUTFLAGS (Table 2.B.2).

2.B Validation

At the level of spectroscopic stellar surveys, it is difficult to perform truly independent benchmark tests for the resulting distance, extinction, and stellar parameter scales (Jofré et al. 2019). Most comparison samples are themselves affected by significant systematic uncertainties. Especially for the APOGEE survey, meaningful comparisons with fundamental physical parameters such as interferometric temperatures or masses of detached eclipsing binaries are unavailable. In Santiago et al. (2016) and Q18 we performed fundamental accuracy and precision tests using simulated stars, nearby eclipsing binaries, astrometric distances, among others. In this section we therefore limit our

Table 2.B.1: Data model for the StarHorse catalogues described in this paper

Column	Description	Unit
ID	Unique object identifier	string
glon	Galactic longitude	deg
glat	Galactic latitude	deg
mass16	16th percentile of StarHorse stellar mass PDF	$M_\odot$
mass50	50th percentile of StarHorse stellar mass PDF	$M_\odot$
mass84	84th percentile of StarHorse stellar mass PDF	$M_\odot$
teff16	16th percentile of StarHorse effective temperature PDF	K
teff50	50th percentile of StarHorse effective temperature PDF	K
teff84	84th percentile of StarHorse effective temperature PDF	K
logg16	16th percentile of StarHorse surface gravity PDF	dex
logg50	50th percentile of StarHorse surface gravity PDF	dex
logg84	84th percentile of StarHorse surface gravity PDF	dex
met16	16th percentile of StarHorse metallicity PDF	dex
met50	50th percentile of StarHorse metallicity PDF	dex
met84	84th percentile of StarHorse metallicity PDF	dex
dist16	16th percentile of StarHorse distance PDF	kpc
dist50	50th percentile of StarHorse distance PDF	kpc
dist84	84th percentile of StarHorse distance PDF	kpc
AV16	16th percentile of StarHorse extinction in the V band PDF	mag
AV50	50th percentile of StarHorse extinction in the V band PDF	mag
AV84	84th percentile of StarHorse extinction in the V band PDF	mag
SH_INPUTFLAGS	StarHorse flags specifying catalogue input completeness and quality	string
SH_OUTPUTFLAGS	StarHorse flags specifying output quality	string

Table 2.B.2: Description of the contents of the `StarHorse` flags.

SH_INPUTFLAGS	Description
"TEFF.."	calibrated spectroscopic parameters (e.g. TEFF) were used
"uncalTEFF.."	uncalibrated spectroscopic parameters (e.g. TEFF) + inflated uncertainties were used
"PARALLAX"	*Gaia* DR2 parallaxes + recalibrated zeropoint and uncertainties were used
"JHKs"	2MASS photometry was used
"W1W2"	WISE photometry was used
"BVgri"	APASS photometry was used
"gps1_rps1.."	PanSTARRS-1 photometry was used
"AV_prior"	extinction prior (e.g. from APOGEE targeting) was used
SH_OUTPUTFLAGS	
"NEGATIVE_EXTINCTION"	bad extinction estimates
"NUMMODELS_HIGH"	high number of stellar models compatible with observations within 3σ
"NUMMODELS_LOW"	low number of stellar models compatible with observations within 3σ

validation to new, but slightly less fundamental tests: consistency with input parallaxes, asteroseismology (using the CoRoT-APOGEE sample), open clusters (using *Gaia* DR2 results), an inter-survey comparison, and a comparison with results obtained by Leung & Bovy (2019).

2.B.1 Comparison to input parallaxes

As a first simple consistency check, we show in Fig. 2.B.1 a comparison between our spectro-photo-astrometric distances with the recalibrated *Gaia* DR2 input parallaxes. We canonically allow `StarHorse` to converge to a solution that deviates from the input measurements by maximum 4σ, using trimmed Gaussians in the likelihood computation. We therefore expect an almost perfect agreement with the input parallaxes within the corresponding uncertainties. Fig. 2.B.1 shows that this expectation is fulfilled. The top panel compares our posterior estimates with the naive $1/\varpi$ distances (which is biased estimator of the true distance; see Luri et al. 2018), while the bottom panel demonstrates that there are minimal residuals between the input and the posterior parallaxes within the *Gaia* DR2 parallax sphere (the region where parallax uncertainties are within $10-15\%; d \lesssim 2.5$ kpc). We only see slight systematic trends appearing for distances $d \gtrsim 10$ kpc. In the regime in between, the parallax information is successfully complemented by APOGEE, delivering less biased and more precise `StarHorse` distances.

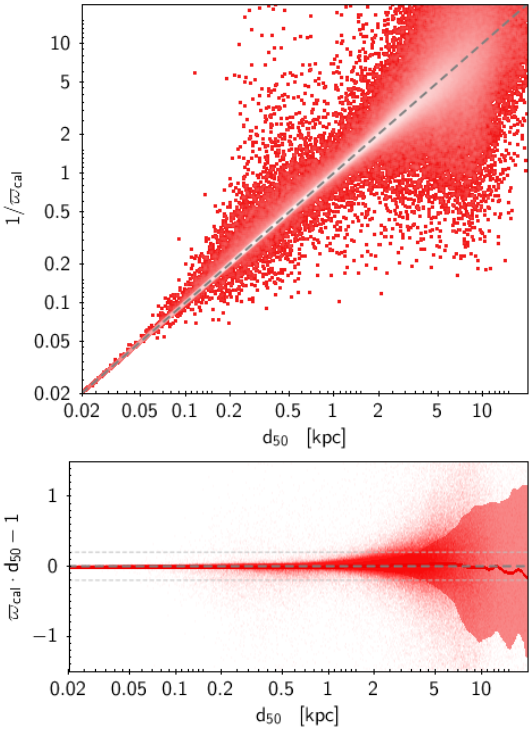

Figure 2.B.1: Comparison of `StarHorse` DR16 distances to naive distances obtained by inverting the recalibrated *Gaia DR2* parallaxes. Top panel: One-to-one comparison of posterior with naive $1/\varpi$ distances. Bottom panel: Residuals between pure astrometric and spectro-photo-astrometric ($1/d_{50}$) parallaxes. The red line shows the smoothed running median, while the shaded region shows the corresponding 1σ variations.

2.B.2 Asteroseismology: The CoRoT-APOGEE sample

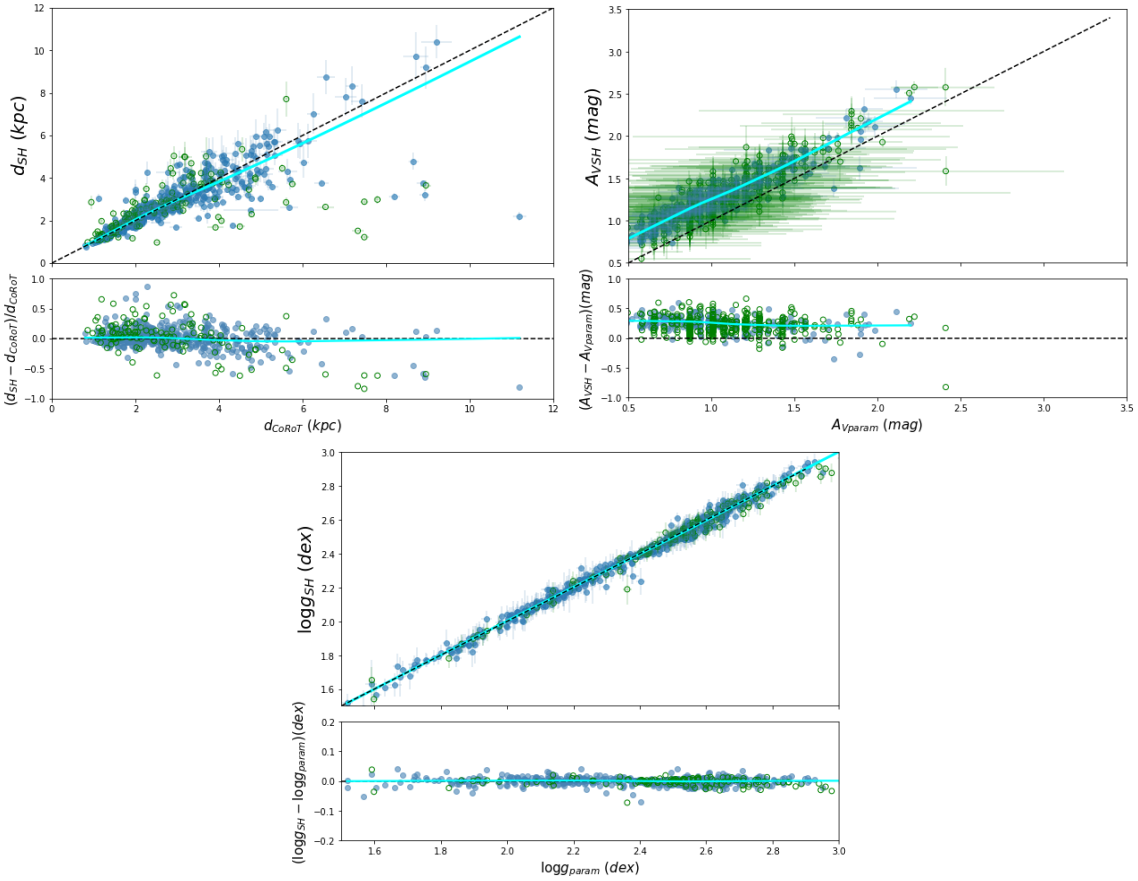

Figure 2.B.2: Comparison between distances and extinctions obtained in this work and those obtained from asteroseismology for CoRoT stars with APOGEE spectra (CoRoGEE sample) using an updated version of the PARAM code (Rodrigues et al. 2017). Blue filled dots are all stars with PARAM tension flags equal zero, for which the PDF of the estimated quantities does not contain multiple peaks. The cyan line indicates the locally linear adjust of the blue filled dots. In the case of extinction, right top panel, the blue dots represents the subset of PARAM tension flags equal zero and stars for which all photometric filters were available. Green open symbols indicate all stars that do not satisfy the conditions of the blue dots.

In Fig. 2.B.2 we show a direct comparison of the distances, A_V, and surface gravity for stars in common between the APOGEE DR16 `StarHorse` results and the CoRoGEE sample (Anders et al. 2017a), which contains stars observed by both APOGEE and the CoRoT space mission (Baglin et al. 2006). The CoRoT data allow us to determine stellar masses and radii from asteroseismology, thus also providing more precise distances outside the *Gaia* parallax sphere.

A similar comparison was shown in Sect. 5.2 of Q18, but the present comparison is significantly different in two ways: First, the CoRoGEE distances were obtained with an updated version of the PARAM code (Rodrigues et al. 2017), which has a configuration in which the input parameters were the two seismic parameters ($\Delta\nu$ and $\nu_{\rm max}$) and the APOGEE DR16 temperatures, metallicities, and [α/Fe] values. No *Gaia* parallaxes were used. Second, in contrast to the `StarHorse` run shown in Fig. 9 of Q18 (which used the PARAM distances as an input), we now compare to the `StarHorse` results obtained without any input from neither asteroseismology nor PARAM. In summary, we compare the result of two independent distance codes, one of which uses spectroscopy and asteroseismology (PARAM), and the other uses spectroscopy and astrometry (`StarHorse`).

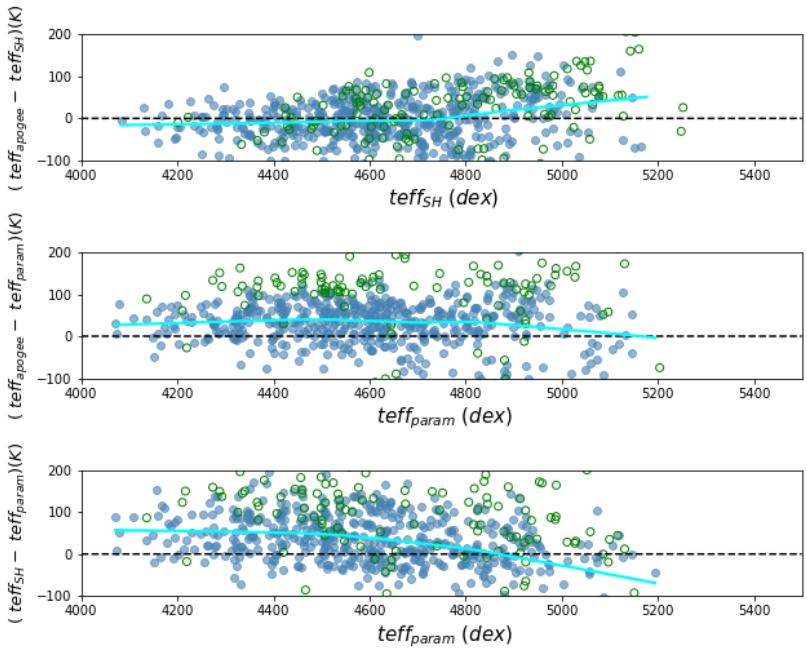

Figure 2.B.3: Comparison between temperatures from APOGEE DR16, the output PARAM code, and output `StarHorse`. Blue filled dots indicate all stars with PARAM tension flags equal zero, for which the PDF of the estimated quantities does not contain multiple peaks. The cyan line represents the locally linear adjust of the blue filled dots. Green open symbols indicate all stars that do not satisfy the conditions of the blue dots.

In Figure 2.B.3 we show the comparisons between the input temperatures from APOGEE DR16 and the output temperatures from PARAM and `StarHorse` codes. We see a systematic shift between PARAM and APOGEE DR16 temperatures even for PARAM tension flags equal zero. In contrast to PARAM, `StarHorse` output temperatures are very similar from the APOGEE input, since the spectroscopic errors are small and StarHorse does not rely on the seismic information. The systematic difference in temperatures between PARAM and APOGEE maybe due to the different calibration scales and model choices, which in the case of PARAM is MESA (Paxton et al. 2011).

Considering this systematic shift between PARAM output temperatures and APOGEE DR16, and looking at simulation tests with StarHorse (See Fig. 6 of Q18, bottom left panel), we expect a shift in the extinction itself, which is seen in the left top panel of Fig. 2.B.2. The magnitude of this shift in the extinction scale, however, exceeds our expectation: for a systematic +50 K shift in $T_{\rm eff}$ we would expect not more than 0.1 magdifference in extinction. We therefore tentatively attribute this difference to the missing reliable optical photometry for the APOGEE DR16 sample. Distances and superficial gravity are in very good agreement with those derived by PARAM using asteroseismic measurements.

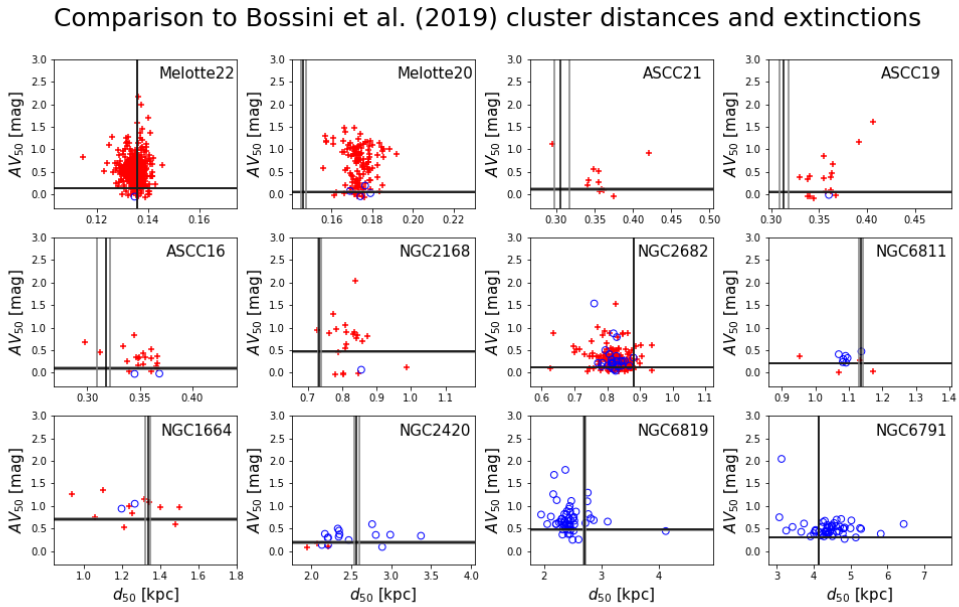

Figure 2.B.4: Comparison between distances and extinctions obtained in this paper with those obtained by Bossini et al. (2019), but in this case for the same input photometry as StarHorse and with PARSEC models, for open clusters. Each panel corresponds to an open cluster with more than ten member candidates observed by APOGEE. The median StarHorse results for individual stars in each cluster are shown as red crosses (dwarfs) and blue open circles (giants). The horizontal and vertical lines correspond to the median values and 1σ limits inferred by Bossini et al. (2019) through isochrone fitting.

2.B.3 Open clusters

In A19, we present a detailed comparison of StarHorse results (without using spectroscopic data) with open-cluster parameters derived from *Gaia* DR2 data (specifically, Cantat-Gaudin et al. 2018 and Bossini et al. 2019). Cantat-Gaudin et al. (2018) determine membership probabilities for 1229 Galactic open clusters, while Bossini et al. (2019) publish revised Bayesian cluster parameters for 269 of those clusters, based on the same membership list. In this work we again compare with the results obtained by Bossini et al. (2019), keeping in mind now that the APOGEE DR16 StarHorse results were obtained from higher-quality data.

In Fig. 2.B.4, we compare the APOGEE StarHorse results obtained for the most certain cluster members of Cantat-Gaudin et al. (2018) to the distances and extinctions determined similar to Bossini et al. (2019) with same input photometry as we use in StarHorse and using PARSEC models in the PARAM code. The figure shows a cluster-by-cluster comparison for the 12 most populated clusters observed by APOGEE, ordered by distance. In general, and in accordance with A19, we observe good agreement of the distance scales (within 20%). Some discrepancies are noticeable both in extinction and distance, which could be related to differential reddening, impure membership, and bad photometry, although this is mostly within the accuracy limits of the open cluster distance scale of Bossini et al. (2019). For the closest clusters, we see a very strong systematic difference in extinction estimates (up to > 1 mag). Its origin, however, is different from the shift seen in the comparison with the CoRoGEE sample: the ASPCAP $T_{\rm eff}$ scale of the M dwarf stars is offset from the PARSEC scale by over 200 K, thus forcing StarHorse to converge to a solution with higher extinction (see Q18, Fig. 6).

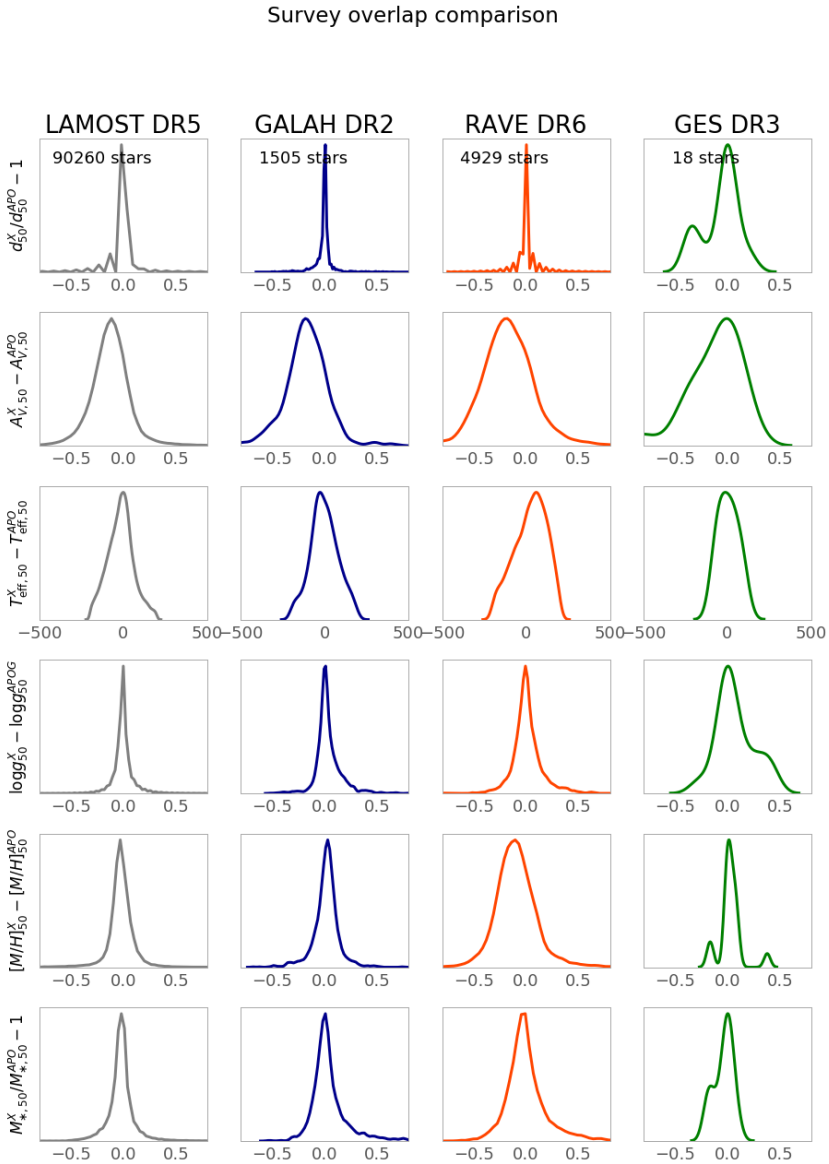

Figure 2.B.5: Inter-survey comparison of the derived `StarHorse` results using stars co-observed by APOGEE and LAMOST (left column), GALAH (second column), RAVE (third column), and GES (fourth column). Each panel shows a generalised histogram of differences of the posterior parameters obtained by `StarHorse` indicated in the y-axis of each row. For each survey, the number of stars in common with APOGEE DR16 is given in the top panel.

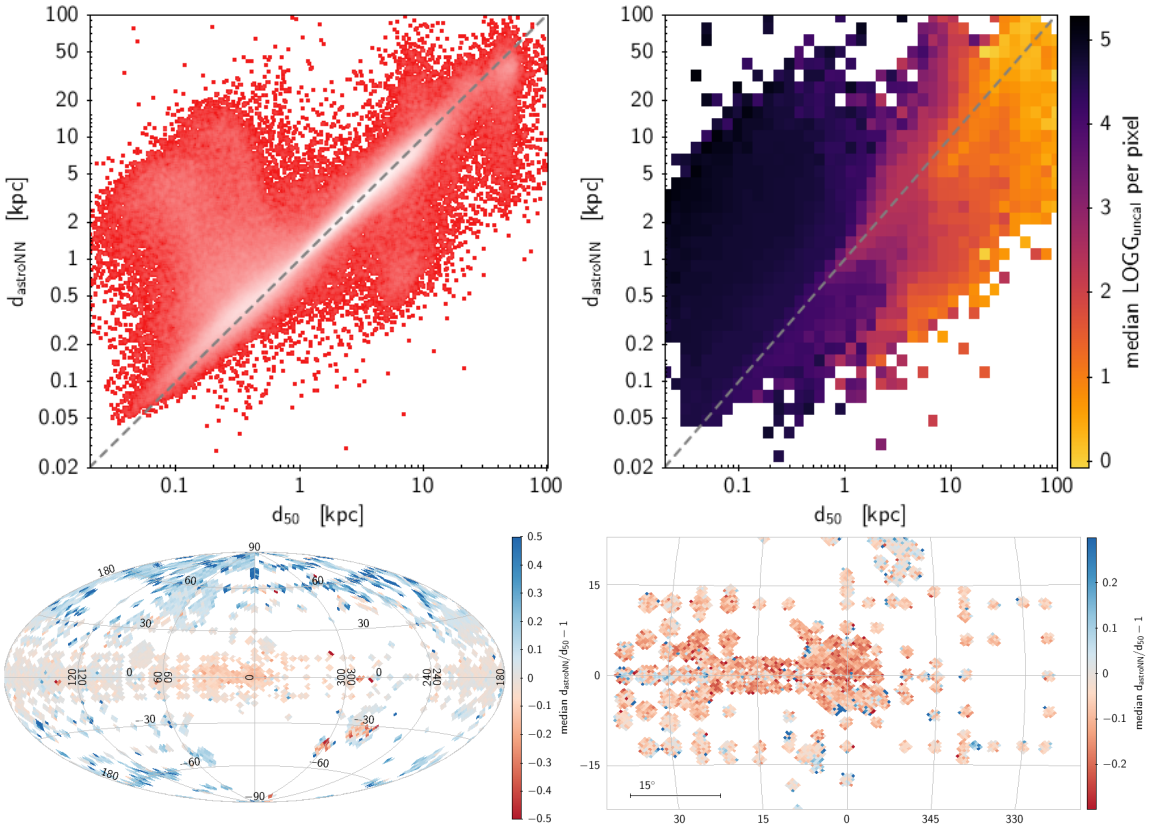

Figure 2.B.6: Comparison with `astroNN` distances presented by Leung & Bovy (2019). Top panel 1-to-1 comparison (left: density distribution; right: colour-coded by median uncalibrated surface gravity determined by ASPCAP, showing that `astroNN` is overstimating distances to dwarf stars). Bottom panels: Relative distance differences as a function of sky position (left: whole sky, right: zoom into the inner Galaxy).

2.B.4 Inter-survey comparison

Some of the stars observed by APOGEE have also been observed by other spectroscopic surveys, be it as a part of a dedicated cross-calibration effort or by chance. These stars are also useful to test the consistency of the StarHorse results. Therefore, in Fig. 2.B.5 we show the distribution of differences in StarHorse output parameters for stars co-observed by APOGEE DR16 and LAMOST DR5, GALAH DR2, RAVE DR6, and GES DR3, respectively (using simple cross-matches based on the *Gaia* DR2 source_id), colour-coded in the same way as Figs. 2.11 and 2.10. The distances obtained from the different input spectroscopic parameters show very satisfactory consistency (first row of Fig. 2.B.5), with systematics at the 1-2%-level, and standard deviations typically below the quoted uncertainties.

In accordance with the previous tests above, the extinction comparison for the survey overlap stars (second row of Fig. 2.B.5) shows that the APOGEE DR16 extinctions are on a slightly offset scale with respect to those obtained from LAMOST DR5, GALAH DR2, and RAVE DR6. As explained above, we suggest this to be due to a combination of a slight systematic offset of the ASPCAP $T_{\rm eff}$ scale with respect to that of the PARSEC models, and the missing reliable optical photometry for most of the DR16 sample.

The comparison of the other StarHorse output parameters ($T_{\rm eff}$, $\log g$, [M/H], and mass) is shown in the bottom rows of fig. 2.B.5, showing a very satisfactory agreement in the parameter scales of the different surveys.

2.B.5 astroNN distances

Finally, in Fig. 2.B.6 we compare our APOGEE DR16 distances with those obtained with the neural-network spectral analysis code astroNN (Leung & Bovy 2019). These authors claimed that "there is no doubt that our distances have higher precision and accuracy than those determined using stellar models and density priors, such as the BPG distances", based on a comparison with the pre- *Gaia* distances published in Santiago et al. (2016) prior to Gaia. In this appendix we repeat their comparison with our new results, now including Gaia DR2, revealing a more complex picture.

The top left panel of Fig. 2.B.6 shows that there is a generally very good agreement between the distances derived by the two codes for the bulk of the sample up to ~ 10 kpc (density colour coding in this plot is logarithmic). There are, however, groups of stars which deviate considerably from the one-to-one relation: First, dwarf stars located mostly at high latitudes (see $\log g$-coloured plot in the top right panel and sky distribution of distance residuals in the bottom left panel) for which astroNN determines too high distances (compare to Fig. 2.B.1), and second, giant stars in the inner Galaxy, for which systematic differences of the order of $10-20\%$ are visible (in the sense that the Leung & Bovy 2019 distances are significantly smaller; see bottom right panel).

The first group of stars can be explained by the limited training set used by Leung & Bovy (2019), which were comprised almost exclusively of red-giant stars. The second effect was indeed also noticed by Bovy et al. (2019) who corrected the systematic offset of the astroNN distances heuristically (see their Fig. 1).

2.C Summary plots for GALAH, RAVE, GES, and LAMOST

In this section, we show some summary figures illustrating the quality of our new StarHorse results for the surveys considered in this paper in addition to the APOGEE DR16 results. In particular, in Figs. 2.C.1 through 2.C.4 we provide sky plots and *Kiel* diagrams and CMDs for LAMOST DR5, GALAH DR2, RAVE DR6, and GES DR3, similar to Figs. 2.1 and 2.2. Figures 2.C.5 through 2.C.8 display summary corner plots of the StarHorse output parameters for each survey, as shown for APOGEE DR16 in Fig. 2.4. The colour in each of those plots coincides with the colours used in Figs. 2.10 and 2.11.

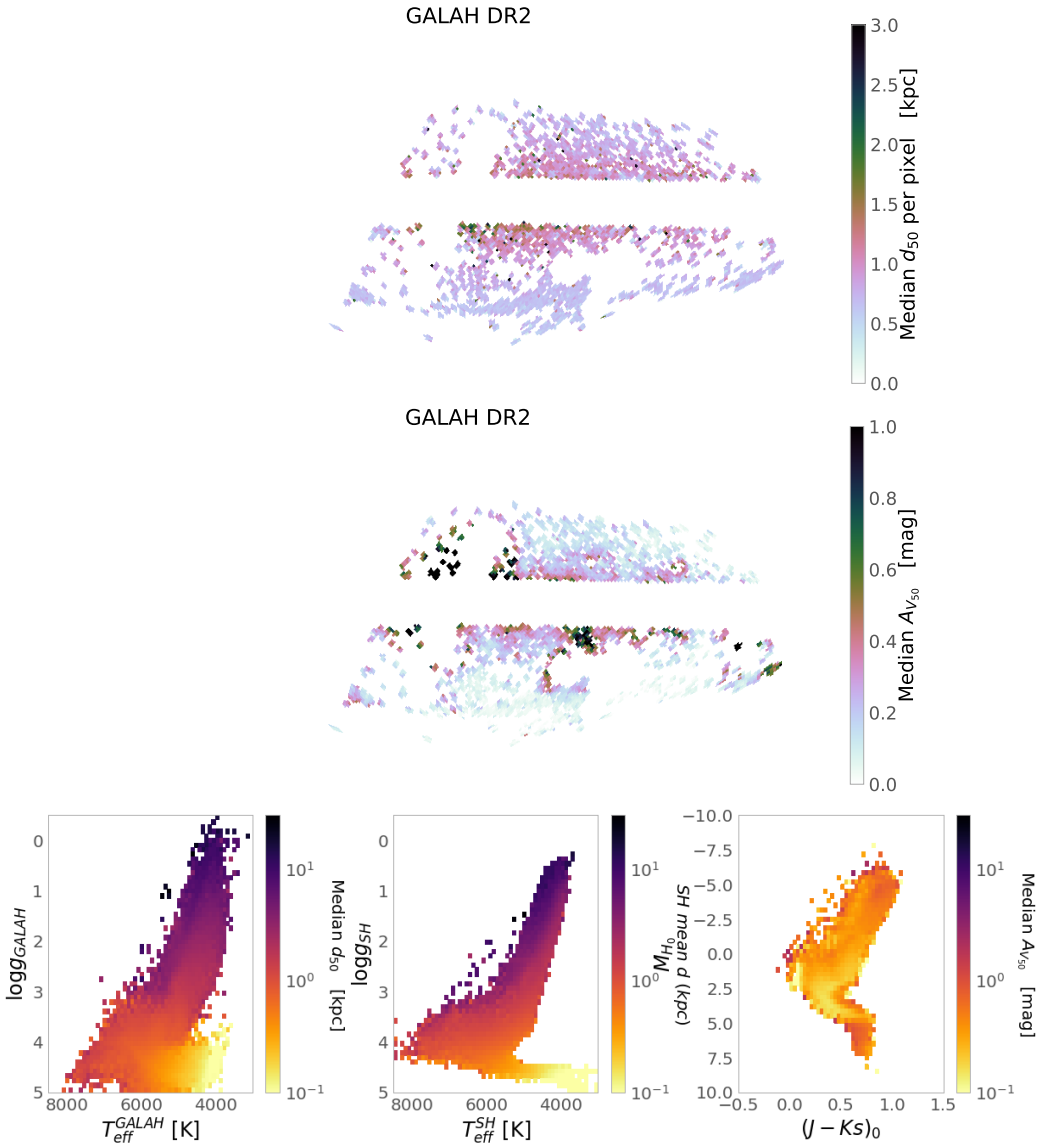

Figure 2.C.1: Similar to Figs. 2.1 and 2.2, but now for GALAH DR2.

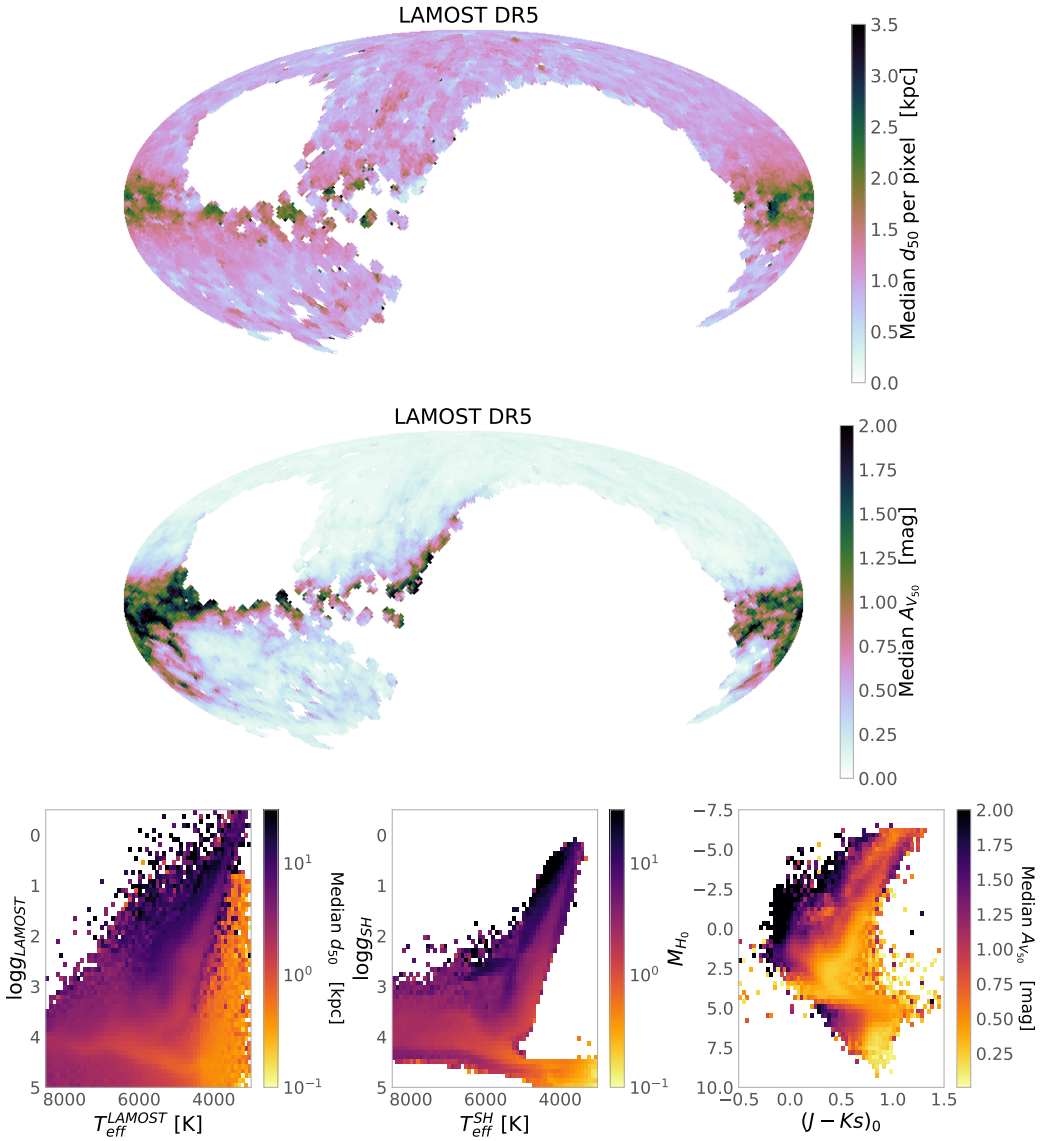

Figure 2.C.2: Similar to Figs. 2.1 and 2.2, but for LAMOST data. The CMD shown in the right panel does not include sources fainter than $K_s = 14.5$

.

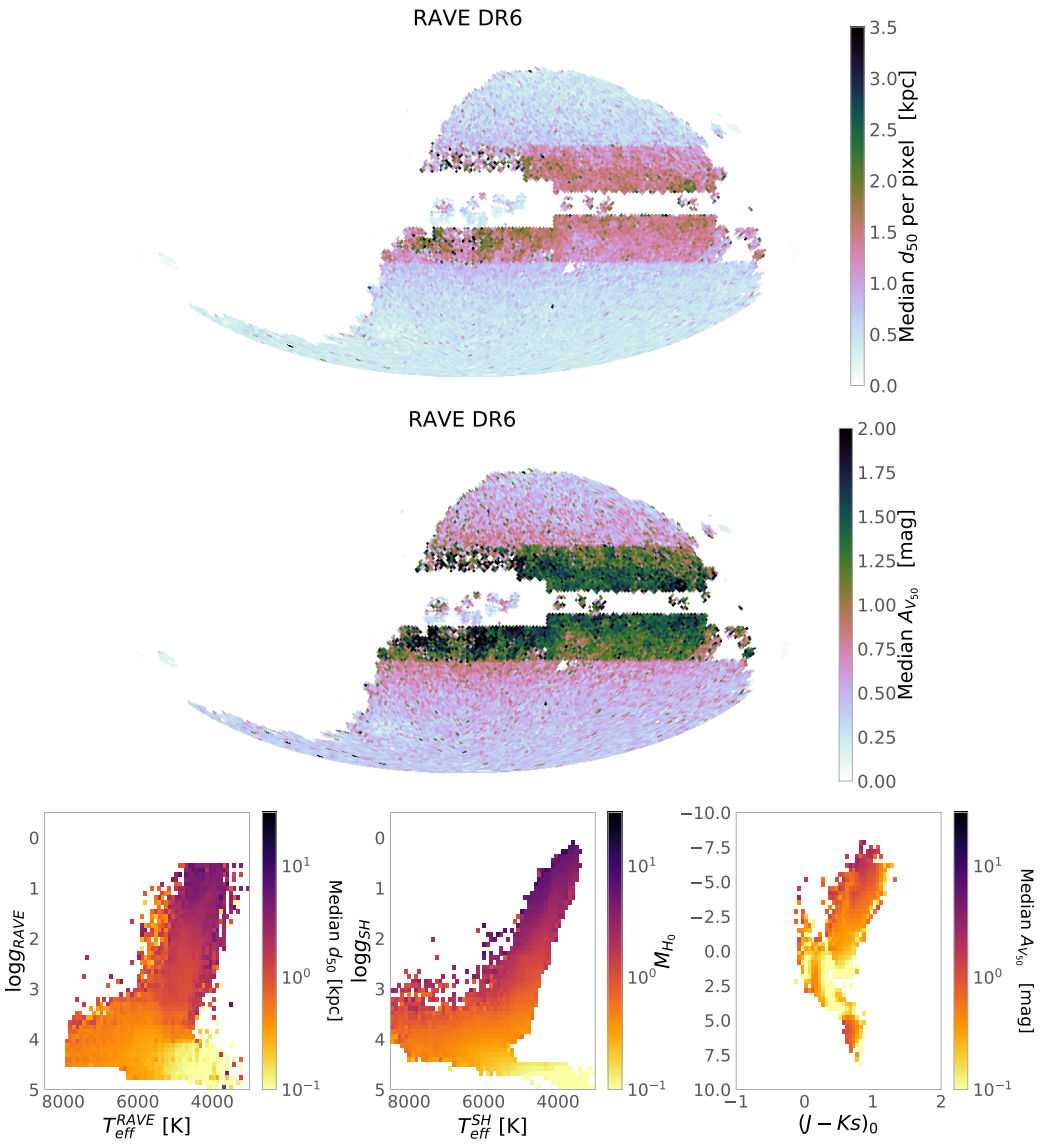

Figure 2.C.3: Similar to Figs. 2.1 and 2.2, but for RAVE DR6 data.

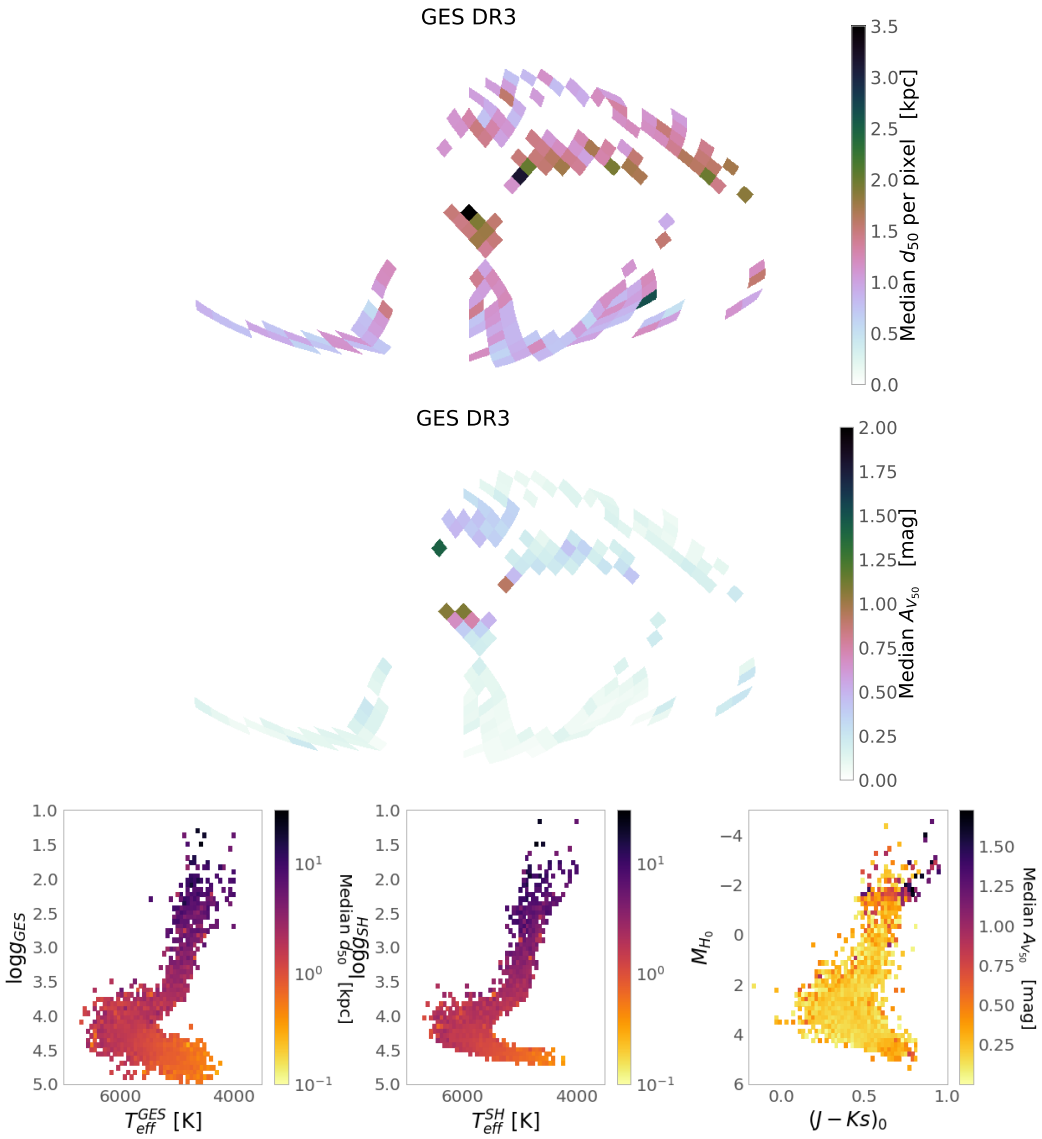

Figure 2.C.4: Similar to Figs. 2.1 and 2.2, but for GES DR3 data.

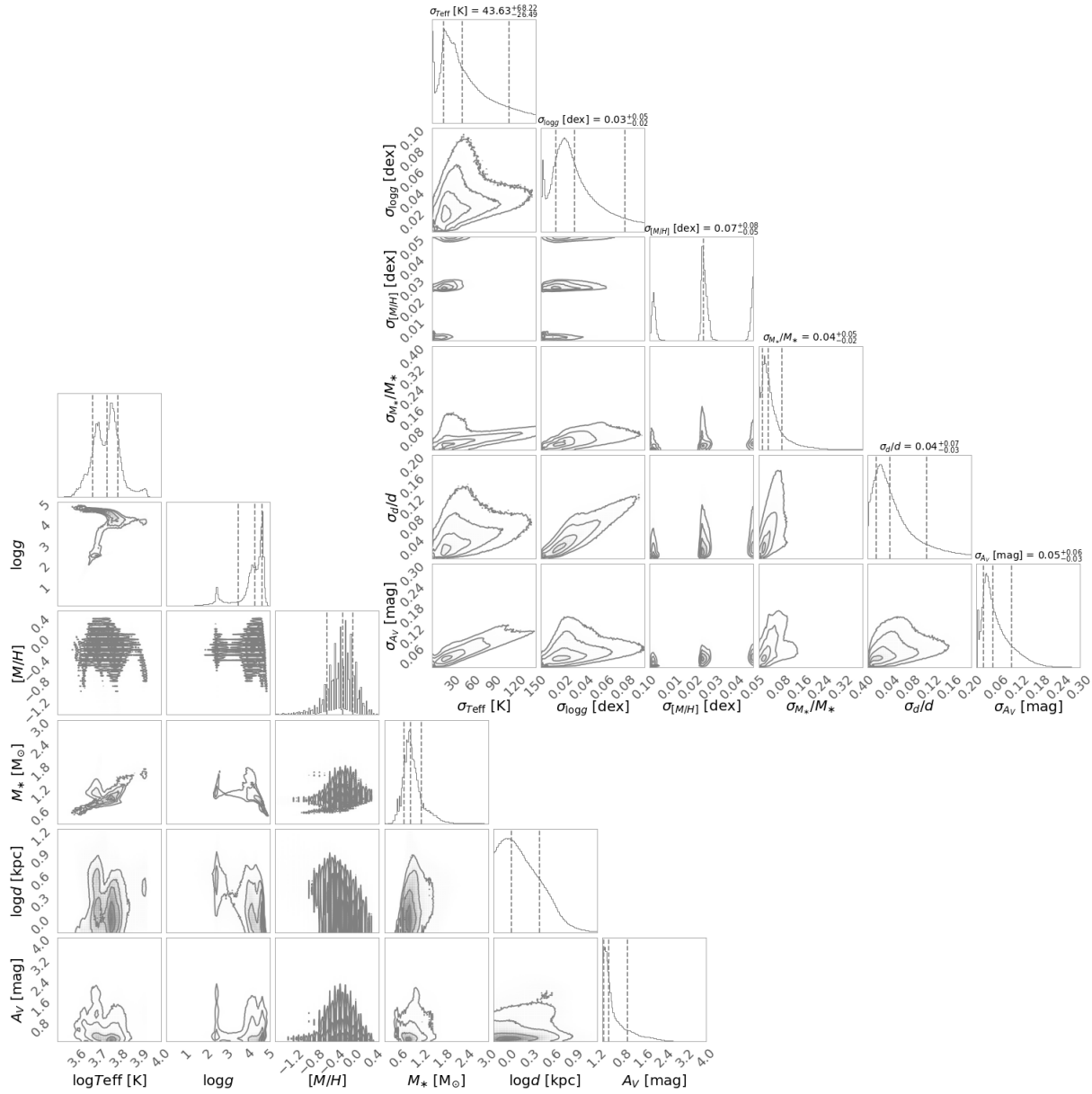

Figure 2.C.5: 1D distributions and correlations between `StarHorse` output parameters (bottom left corner plot) and their corresponding uncertainties (top right corner plot) for the LAMOST DR5 VAC sample.

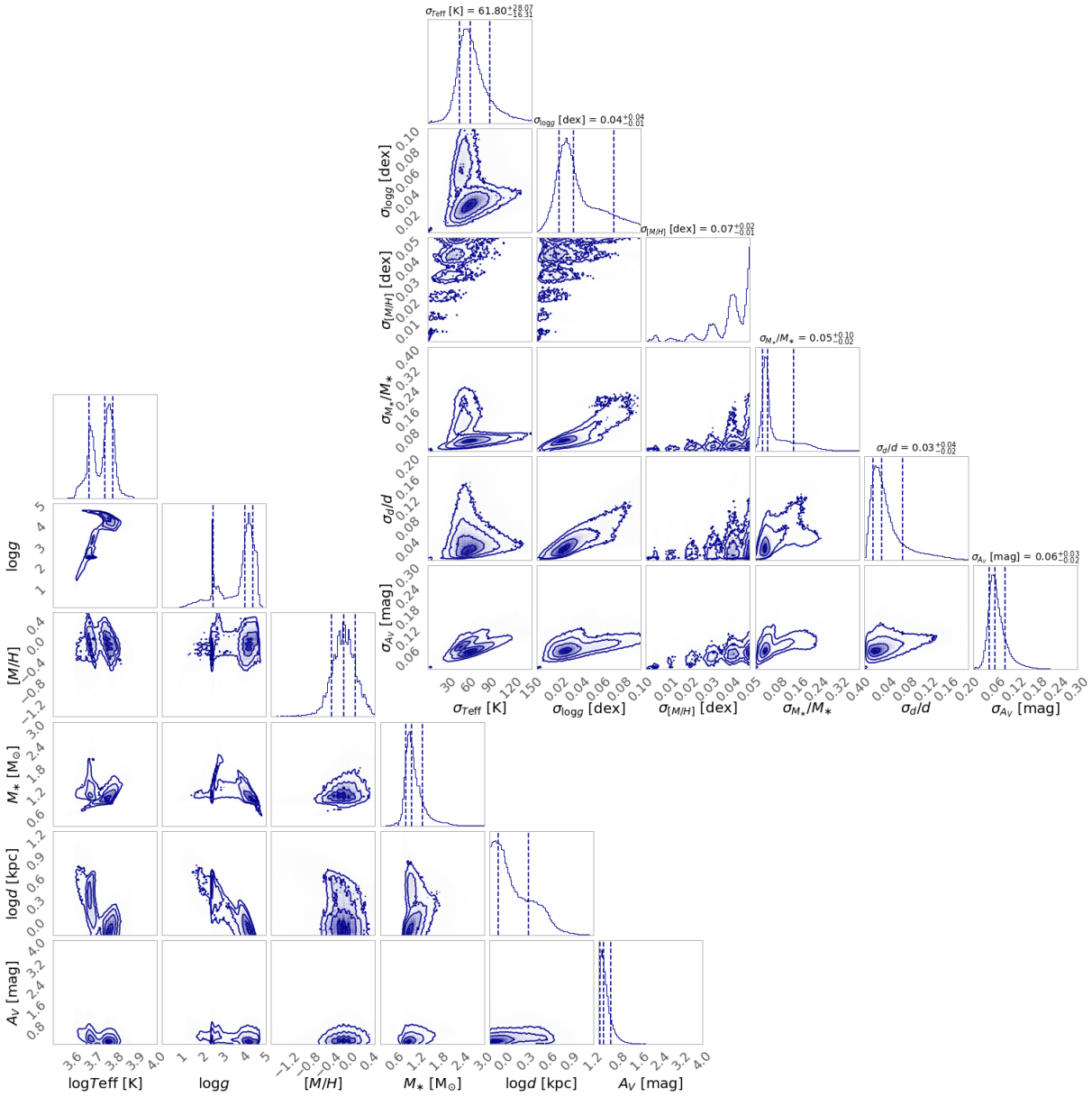

Figure 2.C.6: 1D distributions and correlations between `StarHorse` output parameters (bottom left corner plot) and their corresponding uncertainties (top right corner plot) for the GALAH DR2 sample.

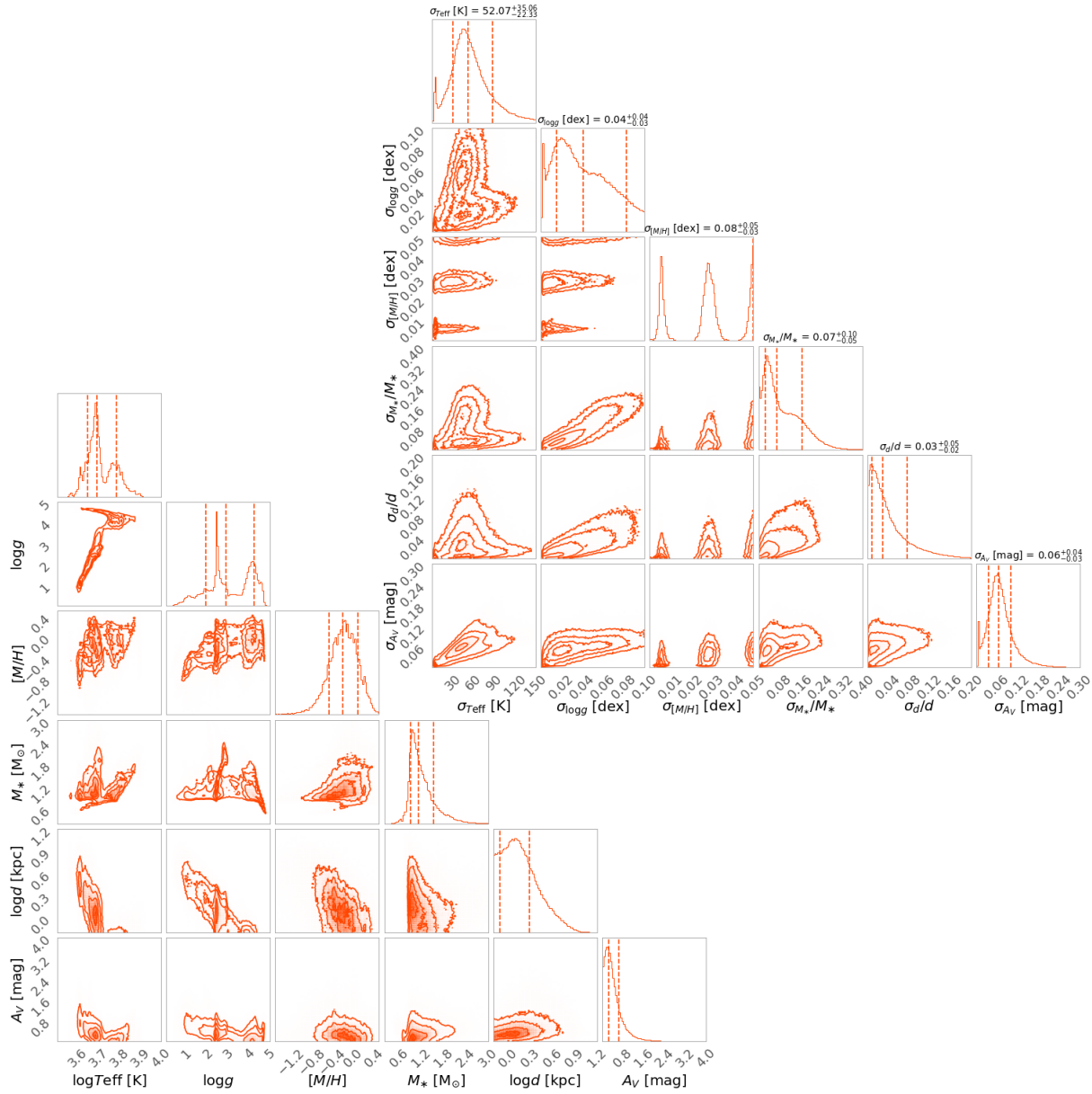

Figure 2.C.7: 1D distributions and correlations between `StarHorse` output parameters (bottom left corner plot) and their corresponding uncertainties (top right corner plot) for the RAVE DR6 sample.

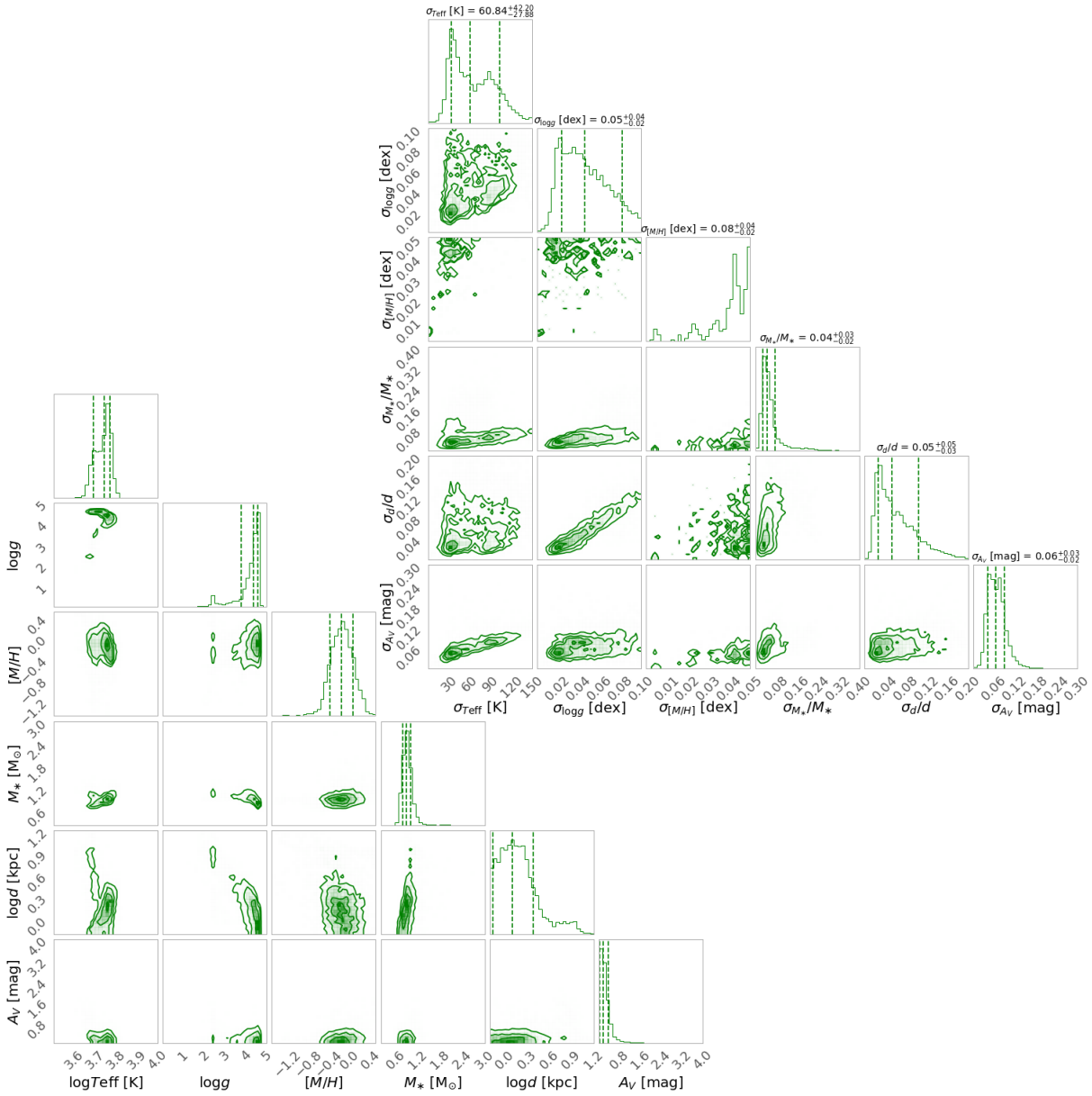

Figure 2.C.8: 1D distributions and correlations between `StarHorse` output parameters (bottom left corner plot) and their corresponding uncertainties (top right corner plot) for the GES DR3 sample.

3 The Milky Way bar and bulge revealed by APOGEE and *Gaia* EDR3

A. B. A. Queiroz, C. Chiappini, A. Perez-Villegas, A. Khalatyan, F. Anders, B. Barbuy, B. X. Santiago, M. Steinmetz, K. Cunha, M. Schultheis, S. R. Majewski, I. Minchev D. Minniti, R. L. Beaton, R. E. Cohen, L. N. da Costa, J. G. Fernández-Trincado, D. A. Garcia-Hernández, D. Geisler, S. Hasselquist, R. R. Lane, C. Nitschelm, A. Rojas-Arriagada, A. Roman-Lopes, V. Smith, G. Zasowski

This chapter was published in Astronomy & Astrophysics, Volume 656, id.A156, 27 pp. Queiroz et al. 2021

Abstract

We investigate the inner regions of the Milky Way using data from APOGEE and *Gaia* EDR3. Our inner Galactic sample has more than 26 500 stars within $|X_{\rm Gal}| < 5$ kpc, $|Y_{\rm Gal}| < 3.5$ kpc, $|Z_{\rm Gal}| < 1$ kpc, and we also carry out the analysis for a foreground-cleaned subsample of 8 000 stars that is more representative of the bulge–bar populations. These samples allow us to build chemo-dynamical maps of the stellar populations with vastly improved detail. The inner Galaxy shows an apparent chemical bimodality in key abundance ratios [α/Fe], [C/N], and [Mn/O], which probe different enrichment timescales, suggesting a star formation gap (quenching) between the high- and low-α populations. Using a joint analysis of the distributions of kinematics, metallicities, mean orbital radius, and chemical abundances, we can characterize the different populations coexisting in the innermost regions of the Galaxy for the first time. The chemo-kinematic data dissected on an eccentricity–$|Z|_{\rm max}$ plane reveal the chemical and kinematic signatures of the bar, the thin inner disc, and an inner thick disc, and a broad metallicity population with large velocity dispersion indicative of a pressure-supported component. The interplay between these different populations is mapped onto the different metallicity distributions seen in the eccentricity–$|Z|_{\rm max}$ diagram consistently with the mean orbital radius and V_ϕ distributions. A clear metallicity gradient as a function of $|Z|_{\rm max}$ is also found, which is consistent with the spatial overlapping of different populations. Additionally, we find and chemically and kinematically characterize a group of counter-rotating stars that could be the result of a gas-rich merger event or just the result of clumpy star formation during the earliest phases of the early disk that migrated into the bulge. Finally, based on 6D information, we assign stars a probability value of being on a bar orbit and find that most of the stars with large bar orbit probabilities come from the innermost 3 kpc, with a broad dispersion of metallicity. Even stars with a high probability of belonging to the bar show chemical bimodality in the [α/Fe] versus [Fe/H] diagram. This suggests bar trapping to be an efficient mechanism, explaining why stars on bar orbits do not show a significant, distinct chemical abundance ratio signature.

3.1 Introduction

The Milky Way bulge region, originally identified as a distinct Galactic component by Baade (1946) and Stebbins & Whitford (1947), has traditionally been very challenging to observe, because it is a crowded and extincted region (see Madore 2016 for a review). Photometric studies of the Galactic bulge towards low extinction windows suggest that the region is old in general (e.g., Zoccali et al. 2003; Renzini et al. 2018; Surot et al. 2019; Bernard et al. 2018). A spectroscopic sample of lensed dwarfs in the bulge was found to contain a significant population younger than 5 Gyr (Bensby et al. 2017). Optical spectroscopic surveys of the Milky Way

traditionally avoid low Galactic latitudes ($|b| \leq$ 5-10) because of the high levels of extinction, especially towards the inner regions. Gonzalez et al. (2013) used the VISTA Variables in the Via Lactea survey (VVV Minniti et al. 2010) to map the mean metallicity throughout the bulge using near-infrared (NIR) photometry, suggesting the existence of a gradient, with the most metal-rich populations concentrated to the innermost regions (Minniti et al. 1995).

Defining a complete sample of the stellar populations in the inner Galaxy has been a challenge. Available spectroscopic samples are traditionally very patchy and fragmented, especially toward the Galactic bulge where heavy extinction and crowding make this area hard to observe. Therefore, most of the spectroscopic data of the Milky Way bulge and bar were limited to a few low-extinction windows (e.g., Baade's Window), or slightly larger latitudes.

Since the pioneer works of Rich (1988) and Minniti et al. (1992), the bulge region has been explored by several spectroscopic surveys, such as BRAVA (Rich et al. 2007; Kunder et al. 2012), ARGOS (Ness 2012), GIBS (Zoccali et al. 2014), and GES (e.g., Rojas-Arriagada et al. 2014, 2017), as well as other smaller samples towards lower extinction windows (see Barbuy et al. 2018, for a review that summarises our knowledge on the Galactic bulge up to 2018). The bulge region was confirmed to be dominated by α-enhanced stars (McWilliam & Rich 1994; Cunha & Smith 2006; Fulbright et al. 2007; Friaça & Barbuy 2017), to have a broad metallicity distribution function (MDF; Rich 1988; Gonzalez et al. 2015; Ness & Freeman 2016), to show cylindrical rotation, which is especially contributed by the more metal-rich stars, and to have an X-shape structure which is the result of a buckling bar (e.g., Nataf et al. 2010; McWilliam & Zoccali 2010; Saito et al. 2012; Li & Shen 2012; Wegg et al. 2017). It has also been shown that the oldest bulge populations traced by RR Lyrae or very metal-poor stars do not follow the cylindrical rotation (Dékány et al. 2013; Gran et al. 2015; Kunder et al. 2016, 2020; Arentsen et al. 2020). A mix of stellar populations is detected in the Galactic bulge, inferred by the multi-peaked MDF (Zoccali et al. 2008; Johnson et al. 2013; Ness et al. 2013b), usually associated with different kinematics (Hill et al. 2011; Babusiaux et al. 2010, 2014); for a review see Babusiaux (2016); Barbuy et al. (2018). It has been suggested that the Galactic bulge harbours a more spheroidal, but still barred, metal-poor (with [Fe/H]~ -0.5) component formed by alpha-enhanced stars, and a more metal-rich ([Fe/H]~ 0.3) component that forms a boxy bar (Rojas-Arriagada et al. 2014; Zoccali et al. 2017), which can split into more components closer to the midplane (see Table 2 of Barbuy et al. 2018, for a summary).

The field of Galactic archaeology has been transformed in the last two years, firstly by the advent of the second and third early data release of *Gaia* (DR2, EDR3 Gaia Collaboration et al. 2018b, 2021), and secondly by the NIR survey (H-band) Apache Point Observatory Galactic Evolution Experiment (APOGEE-2 Majewski et al. 2017; Abolfathi et al. 2018) which is currently being extended to the Southern Hemisphere (Ahumada et al. 2020). In 2019, it finally became possible to probe the innermost regions of the Galaxy, much closer to the Galactic plane, with expanded samples of stars with full 6D phase-space information and detailed chemistry. This has opened the possibility for much more detailed studies of the innermost Galactic regions, extending the mapping of the mix of stellar populations to orbital–chemical space (i.e. García Pérez et al. 2018; Zasowski et al. 2019; Fernández-Trincado et al. 2019b; Rojas-Arriagada et al. 2019; Sanders et al. 2019a; Queiroz et al. 2020).

The latest *Gaia* dataset enables the Galactic community to tackle several outstanding questions, regarding for example the shape and kinematics of the Galactic halo (e.g., Helmi et al. 2018; Iorio & Belokurov 2019; Myeong et al. 2019), structures in the outer disk (Laporte et al. 2020), the Galactic warp (e.g., Romero-Gómez et al. 2019; Poggio et al. 2020; Cheng in prep.), the disk spiral structure (Poggio et al. 2021), and also the effect of bar resonances (Kawata et al. 2020). In Anders et al. (2019), we used the Bayesian `StarHorse` code (Queiroz et al. 2018; Santiago et al. 2016) to derive

photo-astrometric distances and extinctions for around 265 million *Gaia* DR2 stars down to magnitude $G < 18$. Our calculations allowed the direct detection of the Galactic bar from *Gaia* data and stellar density maps for the first time. Figure 3.1.1 shows a zoomed-in version of the the red clump (RC) density map presented by Anders et al. (see 2019, their Fig. 8). The breathtaking amount of data (almost 30 million stars with accurate distances and extinctions) shows the clear shape of an elongated structure around the Galactic centre (GC), associated with the Galactic bar. The map of Figure 3.1.1 shows the stellar density contours and an ellipse tilted by 45 deg with respect to the Sun–Galactocentric line (Sun–GC), adjusted by eye. This bar orientation is considerably greater than the ~ 30 degrees inferred by most other works (e.g. Wegg & Gerhard 2013; Cao et al. 2013; Rattenbury et al. 2007; Minchev et al. 2007; Sanders et al. 2019b), but is in the range of predictions from modelling of the velocity field of the solar neighbourhood (e.g. Dehnen 2000; Minchev & Famaey 2010). The higher density towards positive Y values is an effect of the lower extinction in that area.

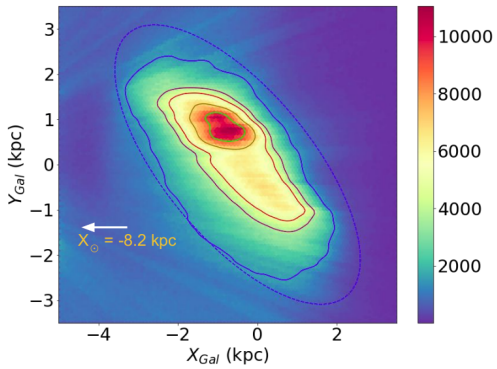

Figure 3.1.1: Magnified view of the Gaia DR2-derived map of the Galactic bar (Anders et al. 2019). The contours represent the four highest density levels. To guide the eye, an ellipse inclined by 45 deg is drawn in blue. Only RC stars with good `StarHorse` flags close to the Galactic plane ($|Z_{\rm Gal}| < 3$ kpc) are shown. The figure contains approximately 30 million stars.

Although a very clear image of the bar can be seen, the `StarHorse` catalogue of Anders et al. (2019) contains certain caveats that render profound exploration and characterisation of the bulge–bar population difficult. Firstly, the map was derived from parallaxes and photometry only, both of which have elevated uncertainties for the Galactic central region. Secondly, for this sample, `StarHorse` was run with a fixed range of possible extinction values ($A_V < 4$ mag), which is not a problem for most regions of the Galaxy, but in the central Galactic plane the extinction can be much higher than 4 mag (e.g. Gonzalez et al. 2012; Queiroz et al. 2020). To further characterise the bulge–bar populations, we need large samples of stars observed with IR spectroscopy, which is now becoming possible with APOGEE DR16.

In the present work, we use data from APOGEE which provides spectra for thousands of stars, including those at low latitudes where most of the Milky Way stellar mass is concentrated. The main challenge has been to determine precise distances in order to better define bulge samples with which to constrain, in turn, chemodynamical models. Thanks to the availability and improvements of *Gaia* EDR3 parallaxes in the APOGEE footprint, we derived precise distances and extinctions for the APOGEE stars using the `StarHorse` code (Queiroz et al. 2020), achieving individual distance uncertainties of typically 10% toward the centre of the Galaxy (see also Schultheis et al. 2019). This makes it finally possible to attempt to disentangle the complex mixture of stellar populations coexisting in the inner Galaxy, which is the goal of the present work.

Although the analysis presented in this paper is based on two much smaller samples than the one shown in Figure 3.1.1, the rich information provided by combining Gaia EDR3 and APOGEE allows an unprecedented view of the innermost regions of the Milky Way and the first complete analysis of the sample in orbital space. We are now in a position to offer much tighter observational constraints in chemodynamical simulations of the bulge–bar, contributing to clarifying the current debate over whether the Galactic bulge has a dispersion-dominated component resulting from mergers and/or dissipative collapse of gas (Minniti et al. 1992; Zoccali et al. 2008), or if

its properties can be completely accounted for by secular dynamical processes forming a buckling bar from pure disk evolution (Debattista et al. 2017; Buck 2020; Fragkoudi et al. 2020). So far, the broad range of available observational signatures seem to suggest a hybrid scenario in which the metal-poor and the metal-rich populations present in the bulge region would accommodate both the dispersion-dominated and secular-dominated scenarios, respectively (see also discussion in Section 4 of Barbuy et al. 2018). Recent results and discussions based on different kinematical populations of RR Lyrae (Kunder et al. 2020) also found evidence for bimodal distributions, as well as a small fraction of metal-poor stars and bulge globular clusters; see Fernández-Trincado et al. 2020c.

The paper is organised as follows. In Section 3.2 we describe the spectroscopic data. Section 3.3 describes the computation of velocities and orbital parameters. In Section 3.4 we describe our sample selection which consists of an inner-region sample (of around 26 500 stars) and a cleaned sample that avoids the foreground disk (with around 8 000 stars). The chemical and dynamical properties of both samples are described in Sections 3.5 (with particular focus on the observed chemical bimodality) and 3.6. In Section 3.7 we dissect the sample into families in the eccentricity–$|Z|_{\rm max}$ plane. The results and their implications are summarised and discussed in Section 3.8.

3.2 Data

The APOGEE survey is building a detailed chemo-dynamical map extending over all components of the Milky Way. Being the first large spectroscopic survey to explicitly target the central Galactic plane (Zasowski et al. 2013, 2017) thanks to its NIR spectral range (1.5 - 1.7μm; H-band), APOGEE allows us to determine precise line-of-sight velocities, atmospheric parameters, and chemical abundances, even in highly extincted areas.

APOGEE started as one of the Sloan Digital Sky Survey III (Eisenstein et al. 2011, SDSS-III) programs and is continuing as part of SDSS-IV (Blanton et al. 2017). The observations started in 2011 at the SDSS telescope (Gunn et al. 2006) with the northern high-resolution, high signal-to-noise ($R \sim 22\,500$, $S/N > 100$) APOGEE spectrograph (Wilson et al. 2010). Since 2017, southern observations have been conducted with a twin spectrograph mounted at the du Pont telescope at Las Campanas Observatory (Wilson et al. 2019).

The latest release of APOGEE data, SDSS DR16 (Ahumada et al. 2020), includes observations from the Southern Hemisphere and contains spectral observation for about 450 000 sources. Given the DR16 sky coverage and high-quality observations in the Galactic plane, we can study the Galactic bulge and bar both in the chemical and dynamical space with unprecedented completeness. Besides the data from APOGEE DR16, we also use the incremental DR16 internal data release which has about 150 000 additional stars observed in March 2020.

Spectral information is obtained through the APOGEE Stellar Parameters and Chemical Abundances Pipeline (ASPCAP García Pérez et al. 2016; Jönsson et al. 2020). This pipeline compares the observations with a large library of synthetic spectra, determining a best chi-squared fit. The first step in the process is to derive stellar atmospheric parameters and overall abundances of C and N alpha-elements. Then, the second step is to derive abundances from fits to windows tuned for each atomic element. Throughout this paper we use [M/H] (obtained in the first step in ASPCAP) as our metallicity. The studied elements in this paper are: [α/Fe], [Fe/H], [O/Fe], [Mg/Fe], [Mn/O], [Mn/Fe], [C/N], and, [Al/Fe]. The APOGEE internal data release has a slightly updated data reduction version (r13). From the APOGEE catalogue, we select only stars with high S/N, `SNREV` > 50, and a good spectral fit from the ASPCAP pipeline, `ASPCAP_CHI2` < 25.

Besides the APOGEE data, to define a bulge–bar sample we need precise distance measurements. To this end, we use `StarHorse` (Santiago et al. 2016; Queiroz et al. 2018) - a Bayesian tool capable of deriving distances, extinctions, and other astrophysical parameters based on

spectroscopic, astrometric, and photometric information. In Queiroz et al. (2020), we combined APOGEE DR16 spectroscopy with *Gaia* DR2 parallaxes corrected for a systematic −0.05 mas shift (Gaia Collaboration et al. 2018b; Arenou et al. 2018; Zinn et al. 2019) and photometry from 2MASS (Cutri et al. 2003), PanSTARRS-1 (Chambers et al. 2016), and AllWISE (Cutri et al. 2013) to produce spectro-photometric distances, extinctions, effective temperatures, masses, and surface gravities for around 388 000 stars. In Queiroz et al. (2020), we also make the same calculation for other major spectroscopic surveys, summing a total of 6 million stars with resulting `StarHorse` parameters.

For the data used throughout this paper, we follow the same procedure as in Queiroz et al. (2020) and run StarHorse for the APOGEE DR16 internal release + *Gaia* EDR3 parallaxes and the same set of photometry. Corrections were applied to parallaxes as recommended by Lindegren et al. (2021a). With *Gaia* EDR3, the resulting distance errors are greatly improved. The samples used along this work have distance uncertainties of around 7%, while previous computations using *Gaia* DR2 allowed us uncertainties of around 10%. However, the main difference is the improvement on proper motions, as we discuss in the following section.

3.3 Velocities and orbits

The combined catalogue APOGEE DR16 internal release + Gaia EDR3 + `StarHorse` gives us access to the 6D phase space of the stars with unprecedented precision. We use the *Gaia* EDR3 proper motions, the line-of-sight velocities (V_{los}) measured by APOGEE, and the `StarHorse` distances to calculate the space velocities in Galactocentric cylindrical coordinates. The cylindrical velocity transformations were performed using Astropy library coordinates (Price-Whelan et al. 2018), where we use a local standard of rest (LSR) of $v_{\,\mathrm{LSR}} = 241$ km/s (Reid et al. 2014), the distance of the Sun to the GC of $R_\odot = 8.2$ kpc, and height of the Sun from the Galactic plane of $Z_\odot = 0.0208$ kpc (Bennett & Bovy 2019). We also note that in all of our diagrams we use the Sun position at $X_{\mathrm{Gal}} = -8.2$ kpc.

We assume the peculiar motion of the Sun with respect to the LSR to be: $(U, V, W)_\odot$= (11.1, 12.24, 7.25) km/s (Schönrich et al. 2010). The resulting components of the velocity we use throughout this paper are the azimuthal velocity, V_ϕ, the radial velocity V_R, and the vertical velocity V_Z. All these components are with respect to the GC. We also note that $V_R \neq V_{\mathrm{los}}$.

As all bodies in the Milky Way move under the Galactic potential, many stars that we find nowadays with a present position at the GC may actually be in a disk or halo orbits. To identify if the stars are from disc, halo, or from bulge–bar components we proceed with the calculation of the orbital parameters. Our Galactic potential includes an exponential disk generated by the superposition of three Miyamoto-Nagai discs (Miyamoto & Nagai 1975; Smith et al. 2015), a dark matter halo modelled with an NFW density profile (Navarro et al. 1997), and a triaxial Ferrers bar (Ferrers 1877; Pfenniger 1984). The total bar mass is $1.2 \cdot 10^{10}$ $M_\odot$, the angle between the bar's major axis and the Sun–GC line is 25 deg, its pattern speed is 40 km s^{-1} kpc^{-1} (Portail et al. 2017; Pérez-Villegas et al. 2017b; Sanders et al. 2019a), and its half-length is 3.5 kpc. To consider the effect of the uncertainties associated with the observational data, we used a Monte Carlo method to generate 50 initial conditions for each star, taking into account the errors on distances, heliocentric line-of-sight velocities, and the absolute proper motion in both components. We integrate those initial conditions forward for 3 Gyr with the NIGO tool (Rossi 2015). From the Monte Carlo experiment, we calculated the median of the orbital parameters for each star: perigalactic distance R_{peri}, apogalactic distance R_{apo}, the maximum vertical excursion from the Galactic plane $|Z|_{\mathrm{max}}$, the eccentricity $e = (R_{\mathrm{apo}} - R_{\mathrm{peri}})/(R_{\mathrm{apo}} + R_{\mathrm{peri}})$ and the mean orbital radius, $R_{\mathrm{mean}} = (R_{\mathrm{apo}} + R_{\mathrm{peri}})/2$.

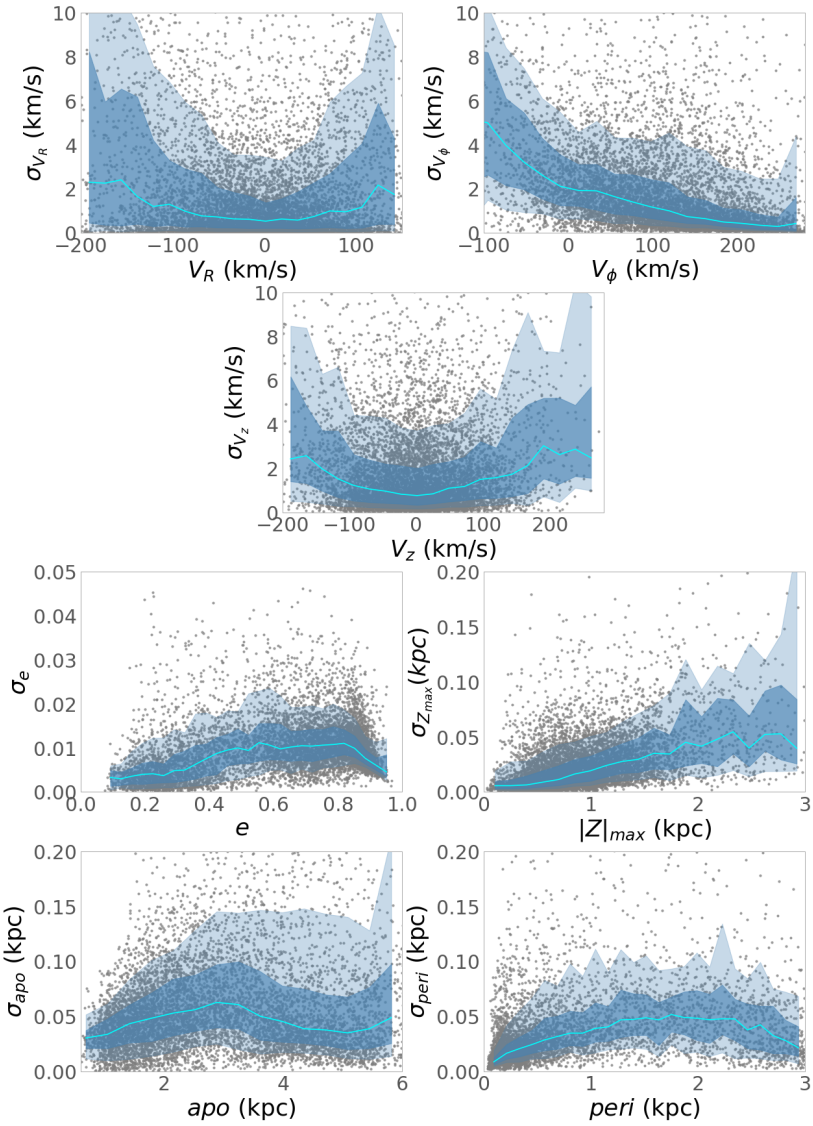

Figure 3.3.1: Standard error of the cylindrical velocities and orbital parameters. The blue line and shaded areas show the median and standard deviation of 1σ and 2σ for the distribution.

In the following sections, we use those orbital parameters when analysing the chemical patterns found in the innermost regions of the Galaxy. We show the uncertainties in the orbital parameters and cylindrical velocities in Figure 3.3.1. These distributions increase with increasing distance, which is expected because for larger distances we have larger StarHorse distance uncertainties. The uncertainties on velocity are larger for retrograde stars (negative v_ϕ) but are still usually around 5 km/s. The other components of the velocity show higher uncertainties for faster stars. One caveat in these calculations is that orbital parameters depend on the model employed. We integrated the orbits in a steady-state gravitational potential. In our model, we do not take into account dynamical friction and the secular evolution of the Galaxy (Hilmi et al. 2020). Also, we do not consider the dynamical effects due to the spiral arms. In Figure 3.B.2 of the Appendix, we show a comparison of the orbital parameters computed using different bar pattern speeds. The comparison gives relative differences of less than 20% for most of the stars.

3.4 Sample selection

In this paper we focus our analysis on the inner region of the Milky Way. In particular, we study a window that is symmetric about the GC in all three dimensions in Galactocentric Cartesian coordinates; see Figure 3.4.2 ($|X_{\rm Gal}| < 5$ kpc, $|Y_{\rm Gal}| < 3.5$ kpc, and $|Z_{\rm Gal}| < 1.0$ kpc).
Throughout the paper, we use two samples: (1) the full bulge-bar sample with the geometric cuts (detailed in Sect. 3.4.1), and (2) a cleaned subsample (see Sect. 3.4.2).

The uncertainties on distance and extinction are shown in Figure 3.4.1 for the two samples discussed in the following section, the bulge-bar sample and the reduced proper motion sample (RPM). Our stars can be seen to have uncertainties on distance of less than 15% which would translate to around 1.5 kpc for the stars with the largest errors. The distribution of distance uncertainties shows no big differences with quality cuts such as parallax relative errors > 20% or using only calibrated ASPCAP inputs. The extinction uncertainties from StarHorse has three main peaks at $A_V \sim 0.05$ mag, $A_V \sim 0.2$ mag, and $A_V \sim 0.3$ which are caused by the availability or not of one or more passbands from the full photometric set: {2MASS, AllWISE, PanSTARRS-1}. For a further discussion about the uncertainties on these parameters and their correlations please see Queiroz et al. (2018) and Queiroz et al. (2020).

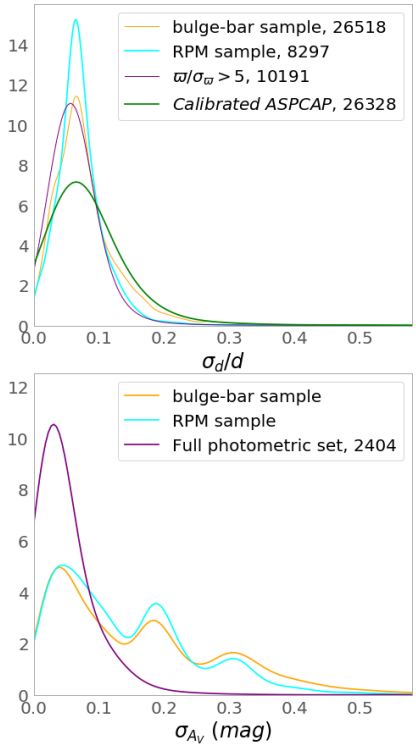

Figure 3.4.1: Upper panel: Distance uncertainty distributions for the bulge–bar (orange) and RPM (cyan) samples defined in Sections 3.4.1 and 3.4.2, respectively. Also shown are stars with parallax uncertainties smaller than 20% (magenta) and stars with calibrated ASPCAP parameters (green). Lower panel: Extinction uncertainty distribution for the bulge–bar (orange) and RPM (cyan) samples. Also shown are stars for which all photometric bands are available (magenta). This illustrates that the secondary and tertiary peaks at larger extinction uncertainties seen in our samples are due to stars for which the optical band is not available (see discussion in Queiroz et al. 2020).

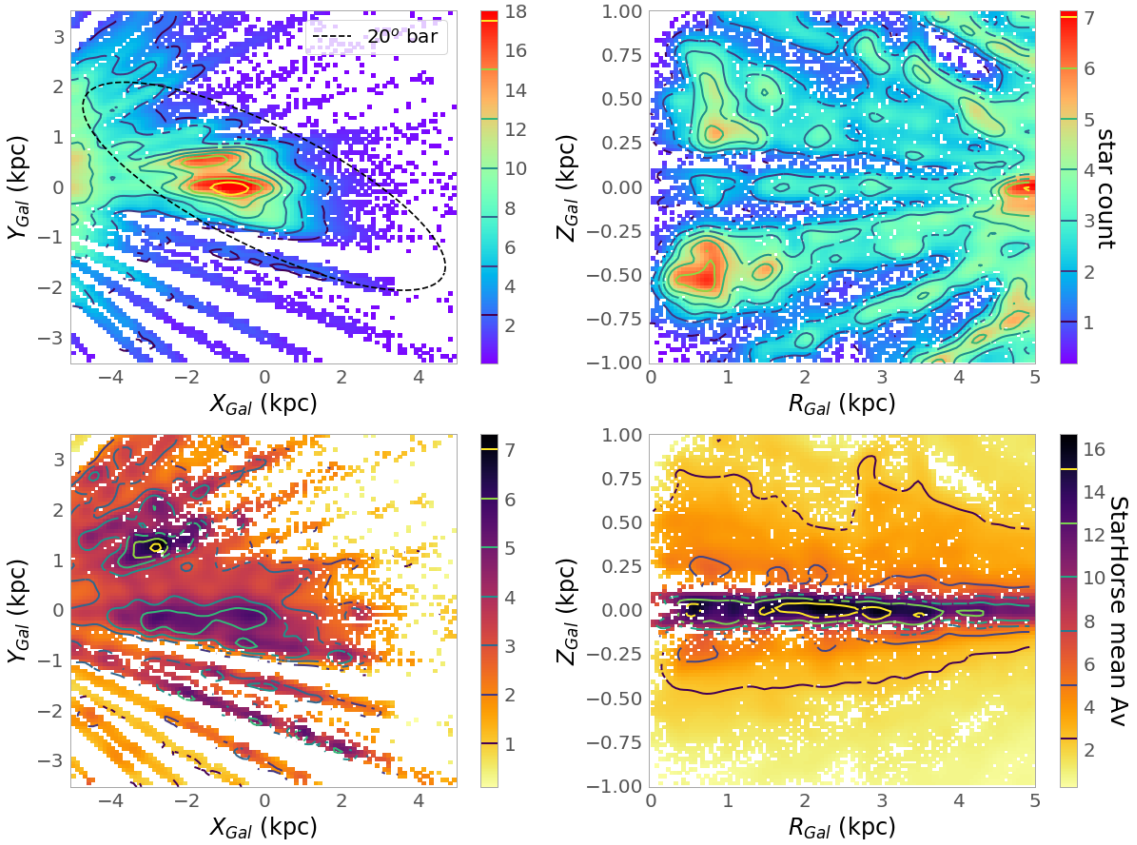

Figure 3.4.2: Cartesian (left panels) and cylindrical (right panels) projections of the GC using the APOGEE survey and `StarHorse` distances. Upper panels show the map colour-coded by the logarithmic number of stars and lower panels colour-coded by StarHorse extinction. Contours are shown for the densest regions as indicated by the colour bar. An ellipse is drawn in the first panel to indicate the approximate location of the Galactic bar.

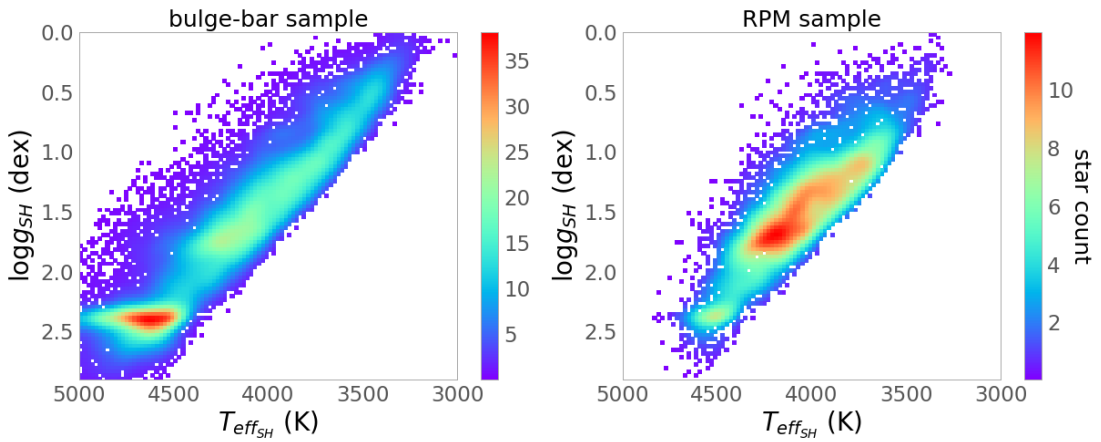

Figure 3.4.3: Kiel diagrams for the complete bulge–bar sample (left) and the RPM-selected sample (right). This figure illustrates that the innermost regions of the Galaxy are sampled by the more luminous stars. Because more luminous stars tend to be more metal poor, this bias needs to be considered during the analysis.

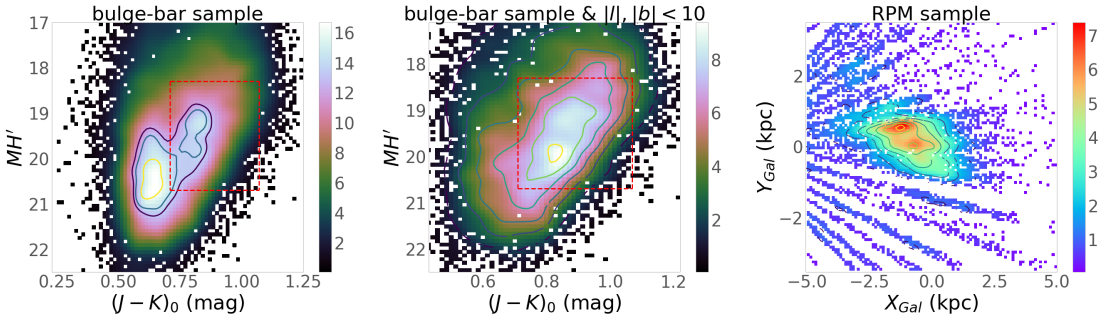

Figure 3.4.4: Illustration of our RPM selection. Left panel: RPM diagram. Contours show the most dense areas, highlighting two main density groups. Middle panel: Same as left panel, but for the central region ($|l|, |b| < 10$ deg). In both panels, the red dashed box indicates the boundaries of our RPM selection. Right panel: Cartesian density map of stars satisfying the RPM cut.

3.4.1 Bulge–bar sample

The full bulge–bar sample has a total of 26 518 stars, with typical distance uncertainties of around 7% (see below). This APOGEE DR16 inner Galactic sample has unprecedented coverage of thousands of stars that reach Galactic latitudes below $|b| < 5$. This low latitude range was not covered in previous dedicated surveys such as BRAVA and ARGOS, which were fundamental in revealing the peanut bar shape and in showing the rotation of the stars in the GC (Kunder et al. 2012; Ness et al. 2013b). The density and extinction distributions for the bulge–bar sample can be seen in Figure 3.4.2; the distribution is far less complete in terms of density than Figure 3.1.1, but the dense areas in the figure do seem to follow a bar-shaped pattern with higher density around the GC. If we again trace an ellipse by eye around the density contours, we obtain a much smaller inclination angle with respect to the Sun–GC line, of namely around 20 deg, which is much closer to the canonical value of ~ 27 deg (Bland-Hawthorn & Gerhard 2016). The angle from the ellipse fitted by eye is certainly not precise, but we see that the bar-shaped structure is less inclined than in Anders et al. (2019).

This seems to confirm the suspicion that the

photo-astrometric distances for the bar structure seen in Figure 3.1.1 are slightly overestimated because the extinction values get saturated at around $A_V = 4$. Figure 3.4.2 also shows that we still lack data very close to the Galactic plane, $|Z_{\rm Gal}|$ <0.2 kpc, as this area remains hidden by very high extinction (e.g. for $|Z_{\rm Gal}|$ <0.1 kpc we often observe large-scale extinction $A_V > 10$; Minniti et al. 2014). The Kiel diagram for this sample is shown in the first panel of Figure 3.4.3, showing that the population in this sample is mainly composed of red giant branch stars and RC stars.

3.4.2 Reduced-proper-motion diagram selection

There are different ways to select a cleaner and more homogeneous bulge–bar sample, avoiding foreground disk stars. Usually, studies of bulge stars select fields in the direction of Baade's window (Babusiaux et al. 2010; Hill et al. 2011) or fields in the direction of the GC (Zoccali et al. 2008; Kunder et al. 2012; Rich et al. 2012). We have a massive amount of information about the stars, and in addition to simply selecting the bulge-bar sample we can constrain an even 'cleaner' sample. One way to do this is to draw isocontours around the XY density maps. Another way is to look for similarities in the stellar composition. However, we could still be left with disk or halo stars and/or potentially important systematic abundance differences resulting from the fact that stars at different distances will have systematically different luminosities and stellar parameters. An additional abundance pre-selection would bias the study towards the chemical distribution of the bar–bulge components. For our definition of a clean bulge–bar sample, we therefore opt for a selection in the RPM diagram. Our goal with this selection is to clean the most apparent disk contamination without an abrupt cut in distances.

The RPM (Faherty et al. 2009; Gontcharov 2009; Smith et al. 2009) is a common tool used to distinguish between distinct kinematical populations. In the RPM diagram, $M_{H'}$ is defined analogously to the absolute magnitude, because the proper motions are also a proxy for the star's distance:

$$M_{H'} = H_{2mass} + 5.0 + \log_{10}(\sqrt{\mu^2_{\rm RA} + \mu^2_{\rm DEC}}). \tag{3.1}$$

In Figure 3.4.4 we show the RPM diagram, $(J - K_s)_0$ versus $M_{H'}$, for the bulge–bar sample defined above. The RPM diagram shows two agglomerations highlighted by the density contour levels, indicating distinct populations (e.g. Holtzman et al. 2018). A cut in $|l|, |b| < 10$ (middle panel of Figure 3.4.4) is analogous to a cut selecting the rightmost agglomeration, which is roughly indicated by the red rectangle, showing this cut represents the innermost population. The left-most agglomeration extends in colour, connecting with the rightmost stellar overdensity. In our selection, the tail of this population remains because we want to preserve completeness and a more symmetrical colour cut around the rightmost overdensity. The selection of stars inside the red rectangle also results in the exclusion of most of RC stars, as one can see in Figure 3.4.3. Our goal with this simple selection is to filter disk stars from our sample with the fewer biases possible to study chemistry and kinematics. We also highlight the fact that the cut in kinematics is minimal; we mostly cut the tails of the proper motion distribution, which have lower density bins. Therefore, the RPM cut is more consistent with a colour cut than a kinematic cut.

With this selection we maintain a relatively homogeneous coverage of the entire inner Galaxy, while removing background and foreground over-densities of disk RC stars. The RPM diagram selection shown in Fig. 3.4.4 results in a more smoothly distributed population around the GC and slightly distorts the density contours found for the purely geometric bulge–bar sample. The squared selection was chosen for simplicity, because the main purpose of this stricter sample is to distinguish whether the results found with the full sample are robust or if they may be significantly biased by the complex mix of stellar populations, the selection function of APOGEE, or systematic errors on abundance.

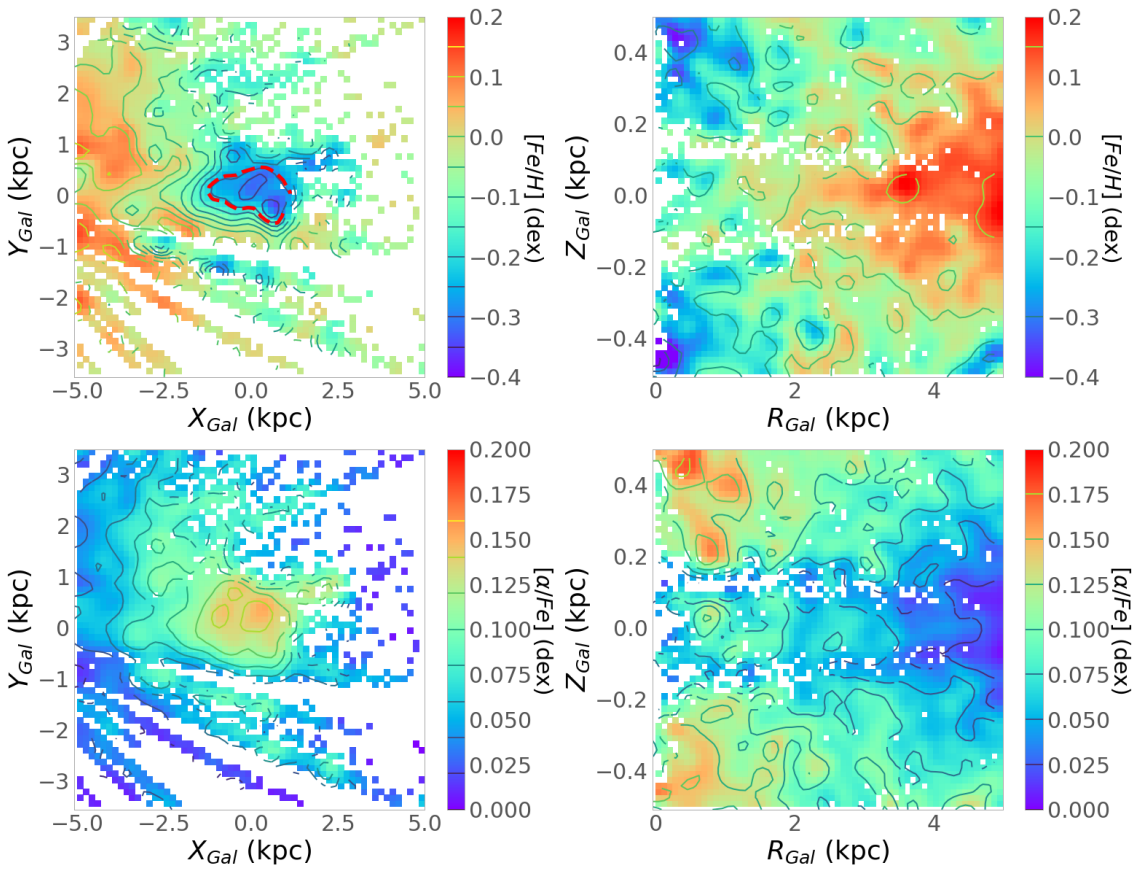

Figure 3.4.5: Cartesian (left panels) and cylindrical (right panels) Galactocentric projections of the bulge–bar sample with an extra cut of $|Z| < 0.5$ kpc. Bins are colour-coded according to their mean [Fe/H] (upper panels) and [α/Fe] (lower panels) content. A red contour is drawn around the metal poor area in the innermost regions of the Milky Way.

3.5 Chemical composition

3.5.1 The α-elements and metallicity

As mentioned in Section 3.1, the chemical composition of the bulge–bar region is fairly complex; for example its metallicity distribution has multiple peaks (e.g., Ness et al. 2013b; Rojas-Arriagada et al. 2014, 2017; Schultheis et al. 2017; García Pérez et al. 2018; Rojas-Arriagada et al. 2020), and the innermost regions of the Milky Way show not only the signature of a bar and a spheroid but also that of the stars from the halo and the thin and thick discs (Minniti 1996). In particular, it is still debated whether the thin and thick discs might have different chemical signatures in their inner regions from those of their local counterparts; see discussion in (Barbuy et al. 2018; Lian et al. 2020). This is especially the case for the thin disc, as shown by the metallicity gradients with Galactic radius (e.g. Hayden et al. 2014; Anders et al. 2014, 2017a). Moreover, debris from accreted globular clusters and dwarf galaxies is also expected to populate the central regions of the Milky Way (see Das et al. 2020; Horta et al. 2021; Fernández-Trincado et al. 2019a, 2020b, 2021).

In this section, we first focus on the main chemical characteristics of our inner Galactic samples as defined in the previous sections. It is important to keep in mind that we have used the ASPCAP [M/H] value as representative of metallicity, as explained in Section 3.2. No fundamental difference in results is seen when using [Fe/H] or [M/H] as the proxy for metallicity, but we retain a larger number of metal-rich stars

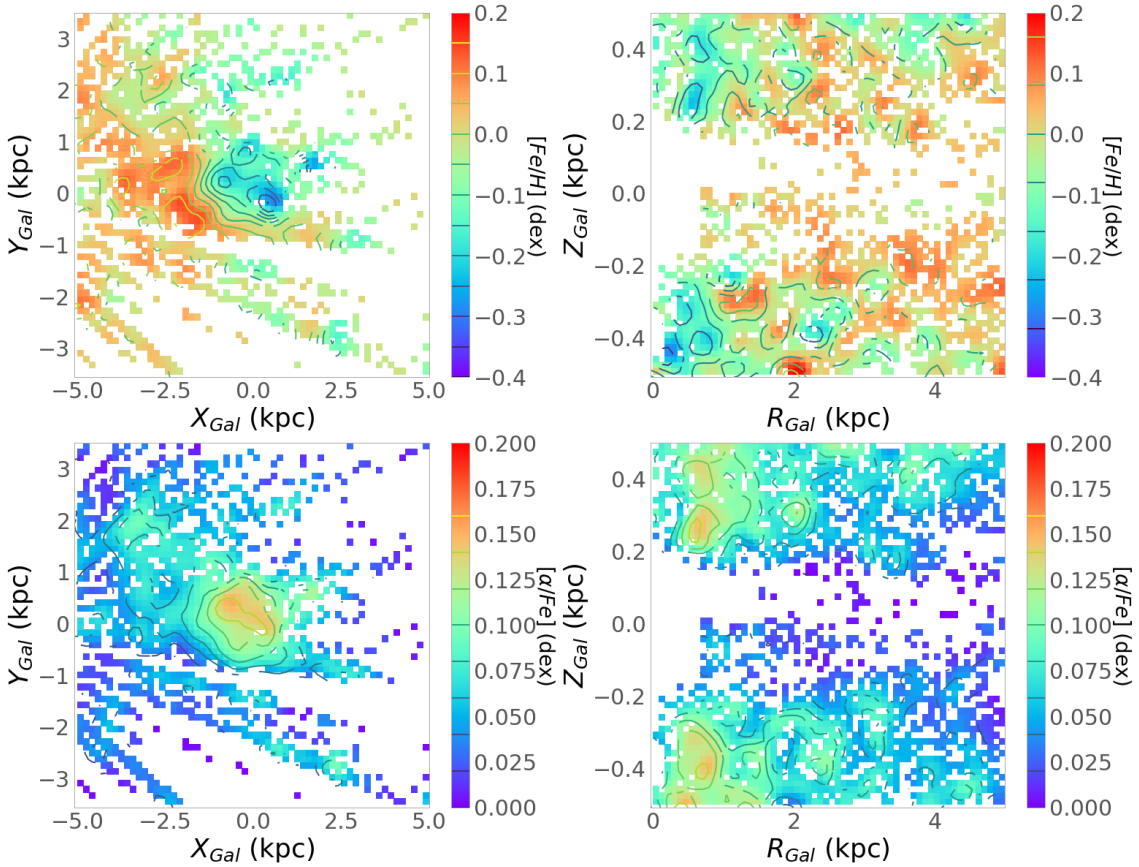

Figure 3.4.6: As in Fig. 3.4.5, but for the RPM sample, with around 3 800 stars. We note the lack of stars very close to the midplane, resulting from the fact we do not have *Gaia* proper motions for a considerable fraction of these stars.

of [M/H]>0.2 dex if [M/H] is used (see Section 3.7.2).

In the present work we have chosen to focus only on the following four abundance ratios: (a) the classical [α/Fe] ratio (as well as [O/Fe] and [Mg/Fe] for consistency checks, although for fewer stars), which is available for the whole sample and is a good tracer of the chemical enrichment timescales (e.g., Matteucci 1991; Haywood 2012; Miglio et al. 2021); (b) [C/N], which is used in the solar vicinity as a cosmic clock (Masseron & Gilmore 2015; Martig et al. 2016a; Hasselquist et al. 2019); and (c) the [Mn/O] and [O/H] ratios which also separate thick and thin disk stars (e.g. McWilliam et al. 2013; Barbuy et al. 2013, 2018).

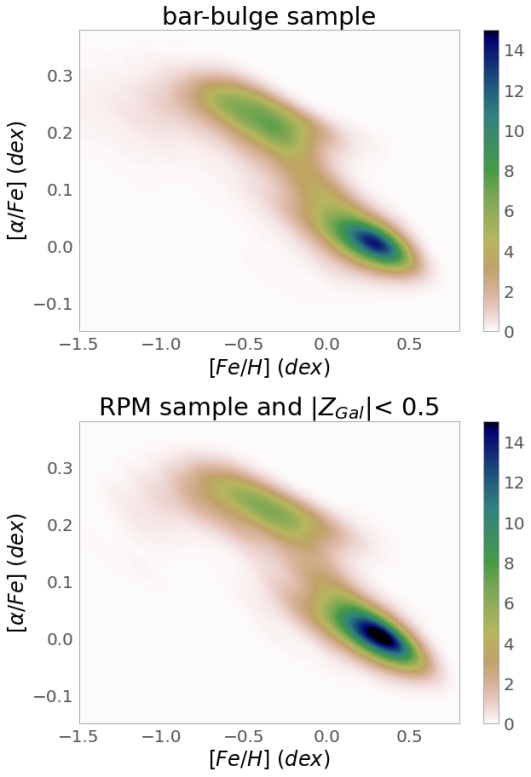

Figure 3.5.1: [α/Fe] vs. [Fe/H] distributions for the bar-bulge region (~ 26 500 stars) and RPM sample (~ 3 800 stars with $|Z_{\rm Gal}| < 0.5$ kpc), colour-coded according to probability density function.

Figure 3.4.5 shows the spatial chemical abundance maps in Cartesian (XY) and cylindrical (RZ) coordinates colour-coded according to [Fe/H] and [α/Fe] abundances for the bulge–bar sample with an extra cut in Galactic height $|Z|$ <0.5 kpc; this sample contains ~ 14 500 stars. The map shows an interesting spatial dependency of the metallicity, with a metal-poor (α-rich) component that seems to dominate the more central region, a feature that we can now see for the first time in the XY plane. We note that selection effects alone cannot explain this latter structure, because such effects are related to distance, and we can clearly see that the contribution from low-metallicity stars increases towards the GC, $X_{\rm Gal}$ ~0 kpc, heliocentric distance d ~ 8 kpc, and that at greater distances the metallicity starts do increase again (although more data are needed to confirm this point, especially in the Galactic southern hemisphere). In photometric samples of the bulge area as a whole, the metal-rich population seems to dominate, as photometric maps report an increase in the metallicity towards the innermost Galactic regions Gonzalez et al. (2013). The more detailed data discussed here enable us to see the spatial variations of the mean metallicity for stars closer to the Galactic midplane ($0.2 < |Z_{\rm Gal}| < 0.5$), showing a clear inversion of the radial metallicity gradient in the innermost 1 kpc. In the GC, the metallicity seems to be high again as shown by Schultheis et al. (2019).

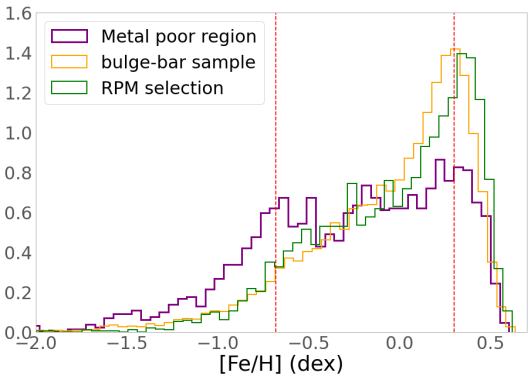

Figure 3.5.2: MDF for the bulge–bar field, RPM sample, and metal-poor region highlighted in Fig. 3.4.5. The prominent peaks of the distributions are indicated by the vertical dashed lines.

The RZ projection also shows large metallicity values (and lower [Mg/Fe]) closer to the Galactic midplane, becoming much less prominent at higher latitudes, a result already known from previous studies of the bulge MDF (e.g., Zoccali et al. 2008) inferred in the latitude, longitude space. The projection also shows

that the central metal-poor population extends to high $Z_{\rm Gal}$. In the very low Galactic plane, $Z_{\rm Gal}$ <0.2 kpc, there is a lack of data due to high extinction (e.g. Minniti et al. 2014; Queiroz et al. 2020), and therefore with the current sample we are not able to determine whether the innermost population is dominated by metal-rich or metal-poor stars.

It is beyond the scope of this paper to correct for selection effects, which we plan to do in a future work dedicated to the detailed comparison of our data with chemo-dynamical models. In the case of APOGEE, the lines of sight and magnitude determine the selection function, which can limit the populations in age or chemistry. In an upcoming paper (Queiroz et al. 2021) we will use mock simulations to study how these selection effects change our sample. However, the selection function seems to have a minor impact, as illustrated in recent work by Rojas-Arriagada et al. (2020) using APOGEE DR16, and also in work using DR14 (Nandakumar et al. 2017). There appears to be bias towards preferentially observing metal-poor (brighter) objects in the most reddened regions. Here we try to gauge this effect by investigating the RPM sample, which is shown in Figure 3.4.6. This figure shows a considerable lack of data in the most central regions of the Galaxy at $Z_{\rm Gal} < 0.2$ kpc compared to the bulge–bar sample. The absence of data in the low Galactic plane in the RPM sample results from the unavailability of *Gaia* EDR3 data for the high extinction and crowded areas such as the inner Galaxy. From the bulge–bar sample, around 3 000 stars have no *Gaia EDR3* proper motions. These are almost all located at low Galactic heights. Given this fact, there is no apparent shift to more metal-poor stars in the central regions sampled by the RPM selection than is seen when analysing the bulge–bar sample. We note that in the inner 200 pc regions, and in particular close to SgrA within the nuclear star cluster, we find a very metal-rich dominant population (Schultheis et al. 2019). In any case, these caveats should be kept in mind when discussing the results that relate chemistry with kinematics and orbital parameters in Sections 3.6 and 3.7, especially in the lower $Z_{\rm Gal}$ regions, and when extracting conclusions from 2D chemical abundance diagrams.

The [α/Fe] versus [Fe/H] plane is now shown for our two samples in Figure 3.5.1. In the figure we use a kernel density estimation from scipy (Virtanen et al. 2019) to estimate the probability density function. In both cases, the sequences show a bimodal distribution with an α-rich and α-poor populations, with the two subcomponents becoming better defined when we apply the proper motion selection to remove foreground stars, and confine the sample to near the Galactic midplane. This bimodality was also reported by Rojas-Arriagada et al. (2019) based on APOGEE DR14 data, though in the paper by Queiroz et al. (2020) and here the depression between the two peaks is significantly clearer, with the two sequences markedly separated.

The metallicity distribution of our two samples is shown in Figure 3.5.2. The Galactic bulge has long been reported to have multiple peak locations in the metallicity distribution (McWilliam 1997), but the peak metallicity values vary considerably according to the sample and technique used (see Table 2 of Barbuy et al. 2018). From Figure 3.4.5, we select all the stars that fall within the highlighted red-dashed contour line in the upper left panel, and we plot the resulting metallicity distribution in Figure 3.5.2. This region of stars has at least two peaks in the metallicity distribution: the most dominant peak at [Fe/H]= 0.30 and an intermediate peak at [Fe/H]=−0.68. This is in agreement with the peaks found by Rojas-Arriagada et al. (2020) −0.66, −0.17 and +0.32 dex, respectively. The multi-peaked metallicity distribution seen here can also be associated with different stellar populations in the Galactic bulge, as in Ness et al. (2013a). However, there is no requirement for a physically motivated population to have a Gaussian or narrow chemical composition. For a detailed study of the APOGEE DR16 MDF as a function of (l, b) we refer to Rojas-Arriagada et al. (2020). The MDF of our samples is discussed in Section 3.7 in the context of the chemo-orbital analysis.

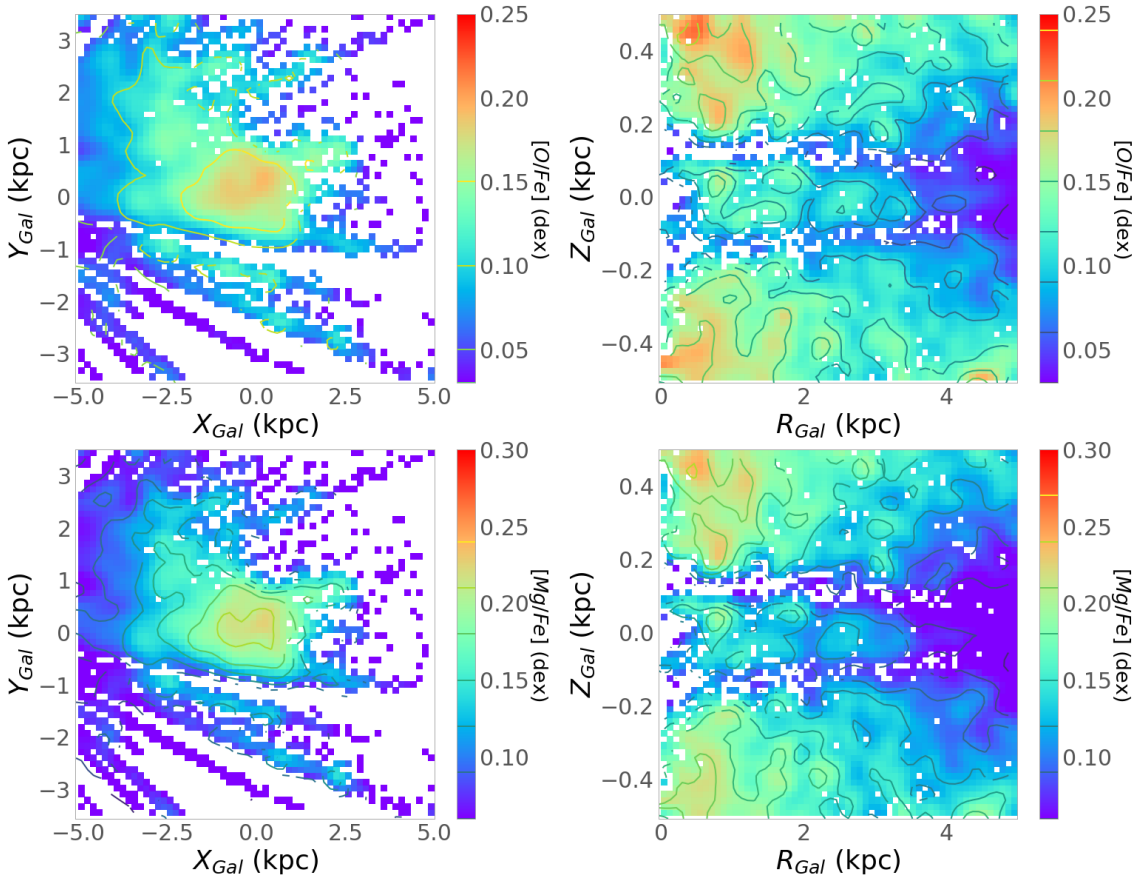

Figure 3.5.3: Same as Fig. 3.4.5 but now bins are colour-coded according to their mean [O/Fe] (upper panels) and [Mg/Fe] (lower panels). These maps are fully consistent with what was seen before when using the ASPCAP α instead of the individual alpha elements given by the pipeline.

Finally, we also looked at two individual α-elements, O and Mg, to ensure we obtain results that are consistent with what is found using the α values obtained from the ASPCAP pipeline. Figure 3.5.3 shows the [O/Fe] (with 13 421 stars) and [Mg/Fe] (with 13 473 stars) maps for the bulge–bar field sample. The results are consistent with the maps shown in Figure 3.4.5. In Figure 3.5.5, which is similar to Figure 3.5.1 but made using [O/Fe] and [Mg/Fe] and only for the RPM sample, the bimodality is still visible, though with a different morphology when Mg is used. The different morphologies are most probably partly a consequence of the details of the stellar pipelines. The APOGEE/ASPCAP dispersion in uncertainties for [Mg/Fe] is higher for colder, low- to intermediate-metallicity stars (Jönsson et al. 2020).

3.5.2 Checking for consistency with two other chemical clocks: [C/N] and [Mn/O]

Other important chemical clocks are the [C/N] and [Mn/O] abundance ratios. The [C/N] is broadly dependent on stellar mass, because the first and third dredge-up converts part of their C into N and thus decreasing the [C/N] ratio (see e.g. Masseron & Gilmore 2015). The dependency of the [C/N] ratio at the solar vicinity has been shown to indicate a correlation with stellar ages coming from APOKASC (Martig et al. 2016a) for stars in the 7 < R (kpc) < 9 Galactocentric range. The usage of this ratio and its link to stellar age has been extrapolated to larger disk regions by Ness et al. (2016) and more recently by Hasselquist et al. (2019, 2020), although the dependency of the [C/N] ratio on metallicity in giants

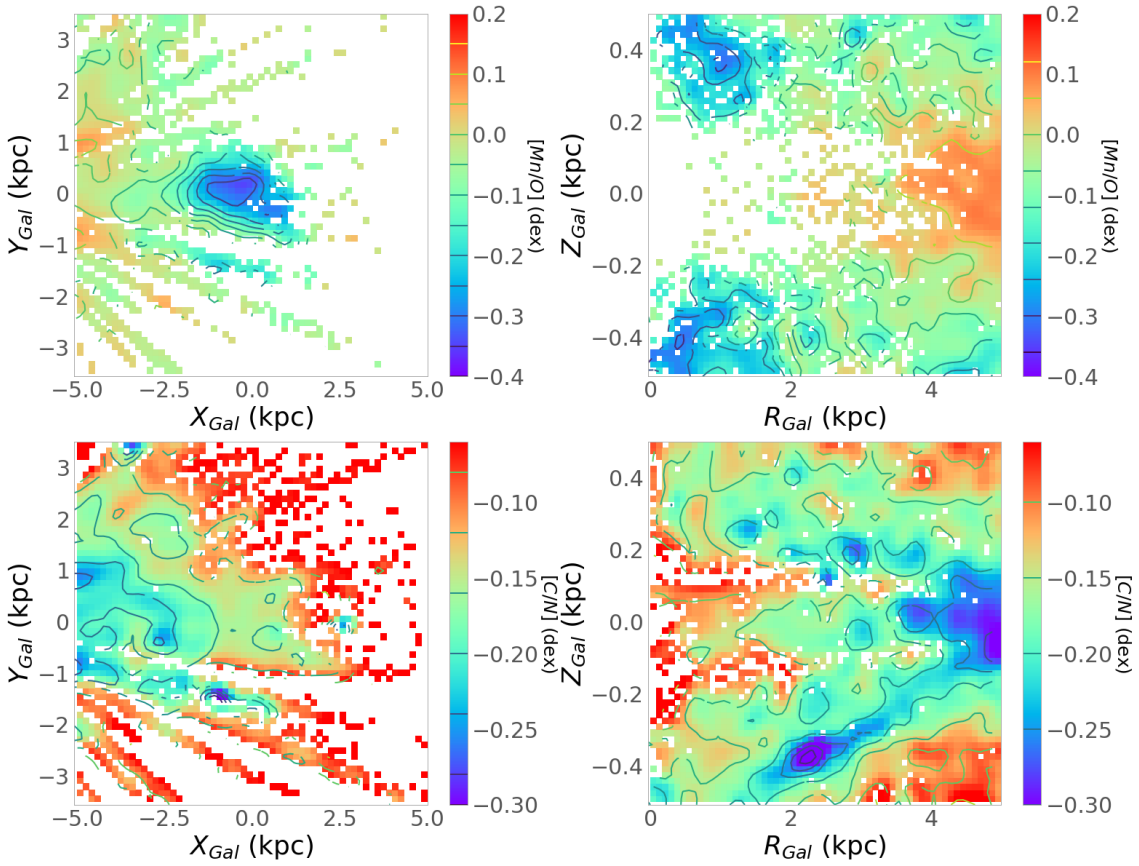

Figure 3.5.4: Same as Figure 3.4.5, now colour-coded by [Mn/O] (upper panels) and [C/N] (lower panels).

(both through hot bottom burning and stellar yields of C and N), and therefore on the chemical evolution of the Galaxy, makes these extrapolations very uncertain (see Lagarde et al. 2019, for a discussion). Despite these caveats, the [C/N] map in Figure 3.5.4 shows an encouraging agreement with previous maps based on the alpha elements, in the sense that larger [C/N] ratios correspond to high [α/Fe] ratios, as expected.

The [Mn/O] ratio is also a very promising population tracer (see Barbuy et al. 2018 for a discussion). This ratio should be low at earlier stages of chemical enrichment, when only core-collapse supernovae had time to pollute the ISM, increasing at later times due to the pollution by SNIa. However, its more complex nucleosynthesis (Chiappini et al. 2003; Barbuy et al. 2013) makes this elemental ratio behave differently from other iron-peak ratios (especially, and most importantly, at low metallicities), a fact that enhances differences between separate populations. An example is illustrated in Figure 3.5.4, where a nice correspondence between a low [Mn/O] ratio and the high [C/N] can again be observed. Nevertheless, our [Mn/Fe] distribution is biased against very cool stars, because the ASPCAP pipeline cannot properly measure Mn lines for stars with effective temperatures below 4000 K. This phenomenon is even more pronounced in the case of the RPM sample. Errors due to the assumption of local thermodynamic equilibrium (LTE) significantly affect data for Mn. Battistini & Bensby (2015) showed that Mn trends can change drastically if non-LTE corrections are taken into account (see also Schultheis et al. 2017).

The [Mn/O] and [C/N] ratios are projected in 2D diagrams in the panels of Figure 3.5.6. These panels still show hints of the bimodality observed in the α-elements, despite their more complex nucleosynthesis, the lower statistical significance of these plots, and the larger uncertainties on the measurements of these abundance ratios from APOGEE spectra.

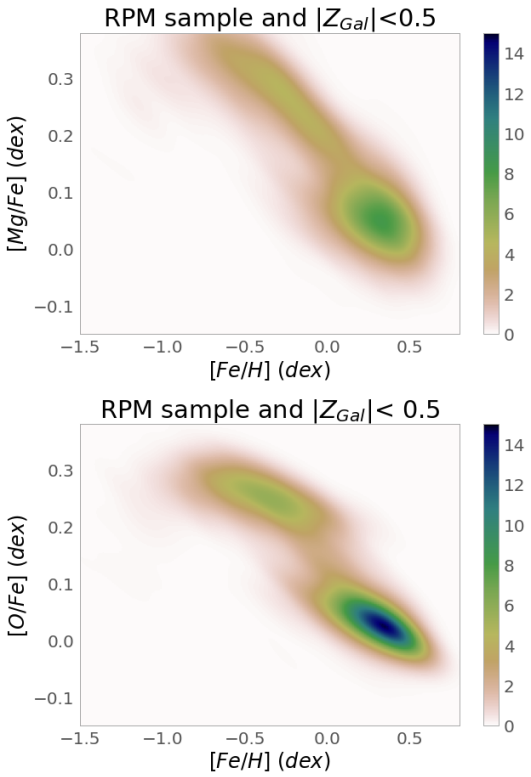

Figure 3.5.5: [O/Fe] vs. [Fe/H], and [Mg/Fe] vs. [Fe/H] for the RPM sample with an extra cut in $|Z_{\rm Gal}|$<0.5 kpc, respectively. Here too, the figures are colour-coded according to probability density function.

To summarise, in this section we confirm that the chemical bimodality previously observed in the alpha elements, is also present in the C/N and Mn/O ratios. From the standpoint of bulge-formation chemodynamical models, the implications differ if one considers that the bimodality is formed by a continuous or two distinct star formation paths. The results presented here suggest a bimodality with a well-defined depression between the two peaks which is more in agreement with a discontinuous star formation path.

Different approaches, from pure chemical evolution to chemodynamical models (either isolated or in the cosmological scenario), have been explored to understand the observed chemical bimodality first seen around the solar vicinity, and more recently shown to extended towards the whole inner disk (Queiroz et al. 2020) and bulge. These approaches are discussed in Section 3.8.

Finally, the chemical maps presented in this section show a consistent picture between the different tracers, and indicate the predominance of a moderately metal-poor (Barbuy et al. 2018; Savino et al. 2020) population in the innermost Galactocentric regions, which extends to larger $Z_{\rm Gal}$. This population could be an extension of the bulge RR Lyrae population —discussed in the recent literature (Kunder et al. 2020; Du et al. 2020)— to more intermediate metallicities. We return to this discussion in Sect.

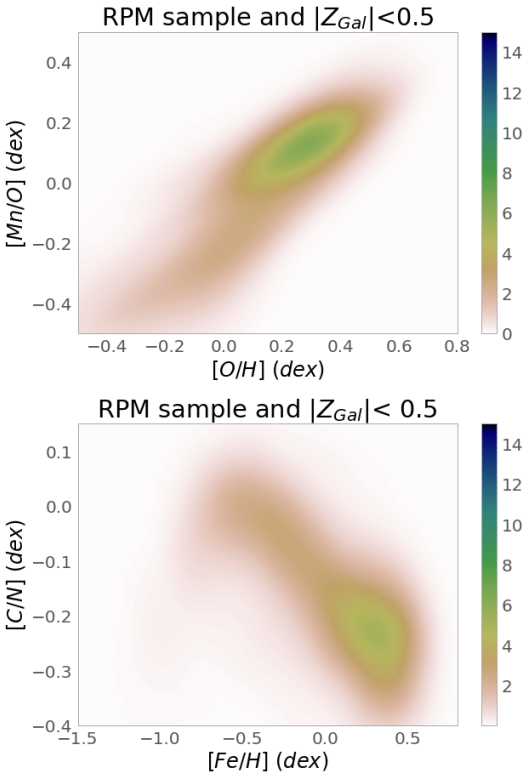

Figure 3.5.6: Two other chemical clocks projected into 2D diagrams for the RPM sample at $Z_{\rm Gal} > 0.5$ kpc. Upper panel: [Mn/O] vs. [O/H]. Lower panel: [C/N] vs. [Fe/H]. Here too, the figures are colour-coded according to probability density function.

3.8. Closer to the Galactic plane, $Z_{\rm Gal}$ <300 pc, the metal-poor population is mixed with a much more metal-rich (and alpha-poor) population, which is very probably related to the rearrangement of disk stars forming a buckling bar. We now proceed to the analysis of the kinematical properties in this region.

3.6 Kinematics

In Sect. 3.5 we present the chemical-abundance distributions of our bulge–bar samples. The clear dichotomy between [α/Fe]-rich/metal-poor and [α/Fe]-poor/metal-rich stars suggests that the GC region is inhabited by (at least) two very distinct populations. In this section, we analyse the 3D velocity space to establish whether the two distinct chemical populations also present different kinematical properties.

By combining *Gaia* EDR3 and APOGEE data, it has become possible to produce precise 3D kinematic maps that reach even the innermost parts of our Galaxy. Bovy et al. (2019) presented the first Cartesian maps of V_ϕ and V_R using data from APOGEE DR16 coupled with distances obtained using the neural-network algorithm by Leung & Bovy (2019). Figure 3.6.1 shows $X_{\rm Gal}$ versus $Y_{\rm Gal}$ maps colour coded according to the three velocity components in the Galactocentric cylindrical frame. The maps in Figure 3.6.1 cover the bulge–bar sample with a cut in $Z_{\rm Gal} < 0.5$kpc (lower panels) and an extended region surrounding the Galactic disk (upper panels).

The signature of bar rotation is noticeable in Figure 3.6.1. The first panel shows the Cartesian $X-Y$ map colour-coded according to V_R. A barred structure is expected to be characterised by a distribution of V_R that extends both inward and outward along the bar. This is seen in simulations of barred galaxies, as discussed by Bovy et al. (2019) and Fragkoudi et al. (2020). This effect is recognised in Figure 3.6.1 (first column, lower panel), where the resulting butterfly pattern of the V_R field is clearly observed. A second and more extended quadrupole is seen in the upper panel of Figure 3.6.1, indicating the presence of the spiral arms. By comparing the recent maps with simulations, it is possible to characterise the extent of the bar along both the major and minor axes, as well as its angle with Sun–GC line. A quantitative comparison with models is necessary to fully characterise the Galactic bar.

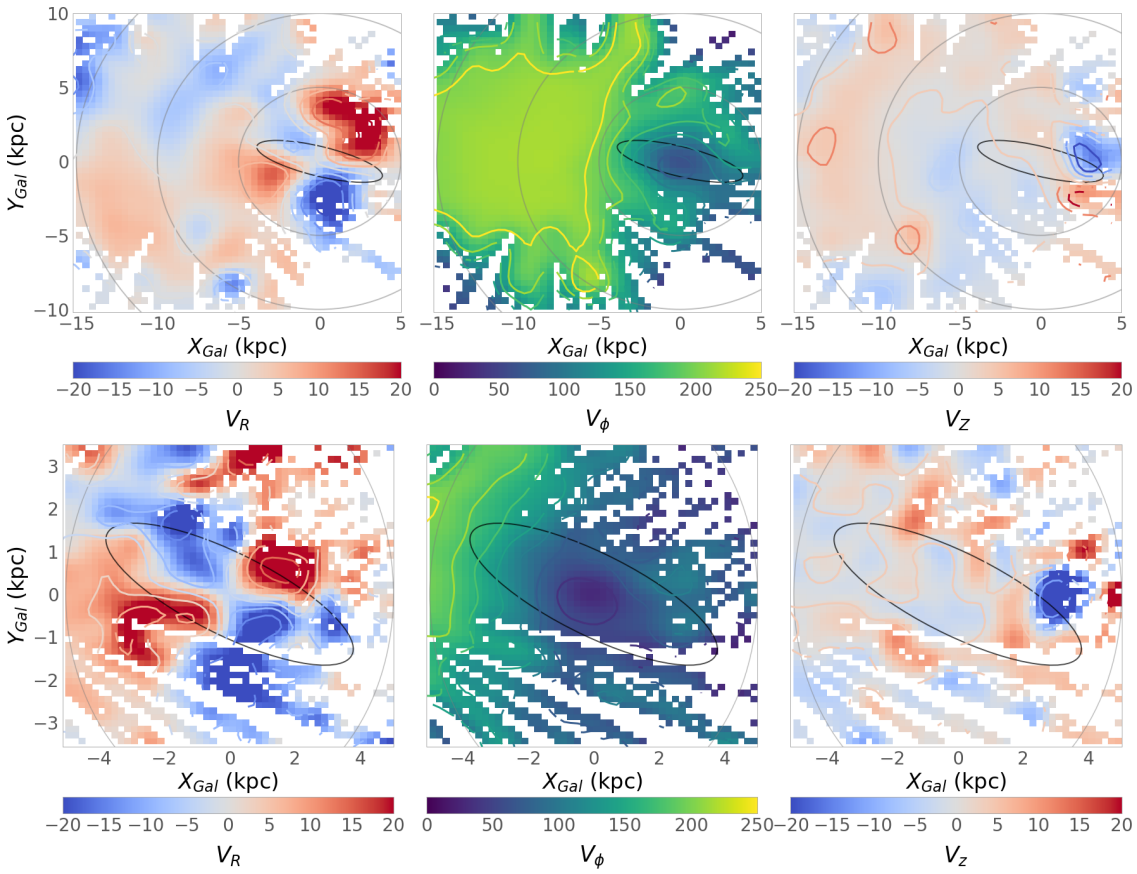

Figure 3.6.1: Cartesian projection of the Galactic disk using `StarHorse` distances. From left to right the maps are colour coded according to V_R (first panel), V_ϕ (second panel), and V_Z (last panel). Upper panels show the same region studied in Bovy et al. (2019), while the lower panels show a zoom into the innermost 5 kpc of the Galaxy (the grey circles illustrate the Galactocentric distances of 5, 10, and 15 kpc. To guide the eye, in the figures we draw an ellipse with an inclination of 20 degrees in relation to the Sun–GC line, 4 kpc semi-major axis length, and 1 kpc semi-minor axis length.

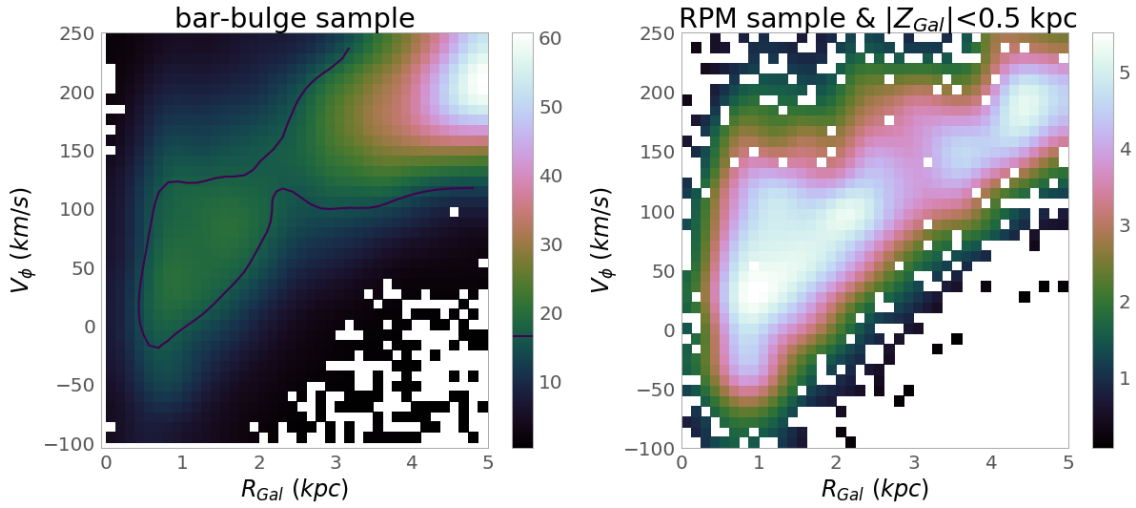

Figure 3.6.2: V_ϕ vs. Galactocentric radius for the inner Galaxy, the entire bulge–bar sample (left panel), and the RPM with an additional cut in Galactocentric height (right panel). The left panel shows contours of density indicated by the colour bar, highlighting the kinematical populations present in the sample.

The second panel of Figure 3.6.1, colour-coded according to V_ϕ, shows a more subtle elliptical shape extending in the $X_{\rm Gal}$ axis by ∼ 2 kpc and in the $Y_{\rm Gal}$ axis by ∼ 1 kpc, with the V_ϕ growing linearly from 0 to 150 km/s, which is a signature of the rigid body rotation of a barred structure. The elliptical structure in V_ϕ is not as extended and is also more spherical compared to Bovy et al. (2019).

Finally, in the third panel of Figure 3.6.1, we show V_Z. High positive V_Z characterises the region situated on the right side of the ellipse. In contrast, an area with negative V_Z is found at one end of the bar. In the extended velocity map (third column, upper panel) of Fig. 3.6.1 positive V_Z is seen in the outer disc, ∼ 10 − 12 kpc, which was also reported by Carrillo et al. (2019) based on *Gaia* DR2 and StarHorse data. The maps shown here show the wave structure in the disk much more clearly, extending the Carrillo et al. (2019) maps to a larger Galactocentric range.

In Figure 3.6.2, we plot the V_ϕ against Galactocentric radius for the bulge-bar sample and for the RPM selection with an extra cut in Galactic height ($|Z_{\rm Gal}| < 0.5$ kpc). These diagrams show the clear signature in the distinct stellar populations of a pressure-supported spheroid, a bar, and the Galactic discs. The first panel of Figure 3.6.2 shows a population that has a high dispersion in V_ϕ within $R_{\rm Gal} < 1$ kpc and then a structure in which V_ϕ increases linearly with radius, and a third structure with V_ϕ of the order of that of the thin disk population, i.e. ∼ 200 km/s. When we apply the RPM cut (second panel of Figure 3.6.2), stars with similar Galactic disk V_ϕ decrease significantly, indicating that our selection is indeed culling disk stars and leaving a purer bulge–bar sample. Biases must always be considered when analysing kinematics with a preceding selection in kinematics, but we would like to remind the reader that the cut in proper motions is subtle, and the velocity distributions of both samples do not change drastically apart from the clear decrease in stars at 200 km/s in $< V_\phi >$. The linear growth of $< V_\phi >$ with $R_{\rm Gal}$ extends up to ∼ 4 kpc where there is a conglomeration of stars that could belong to either the thick or the thin disc.

In order to confirm whether or not the kinematical structures seen in Figure 3.6.2 belong to different chemical populations, in Figure 3.6.3 we reproduce the same plot but colour-coded according to [Fe/H] and [α/Fe]. High-metallicity, low-α stars are mostly concentrated around V_ϕ ∼ 200 km/s, which is again very consistent with what is expected for thin-disk stars. Metal-poor, [α/Fe]-rich stars seem to be present in larger fractions inside $R_{\rm Gal} < 1$ kpc and to have

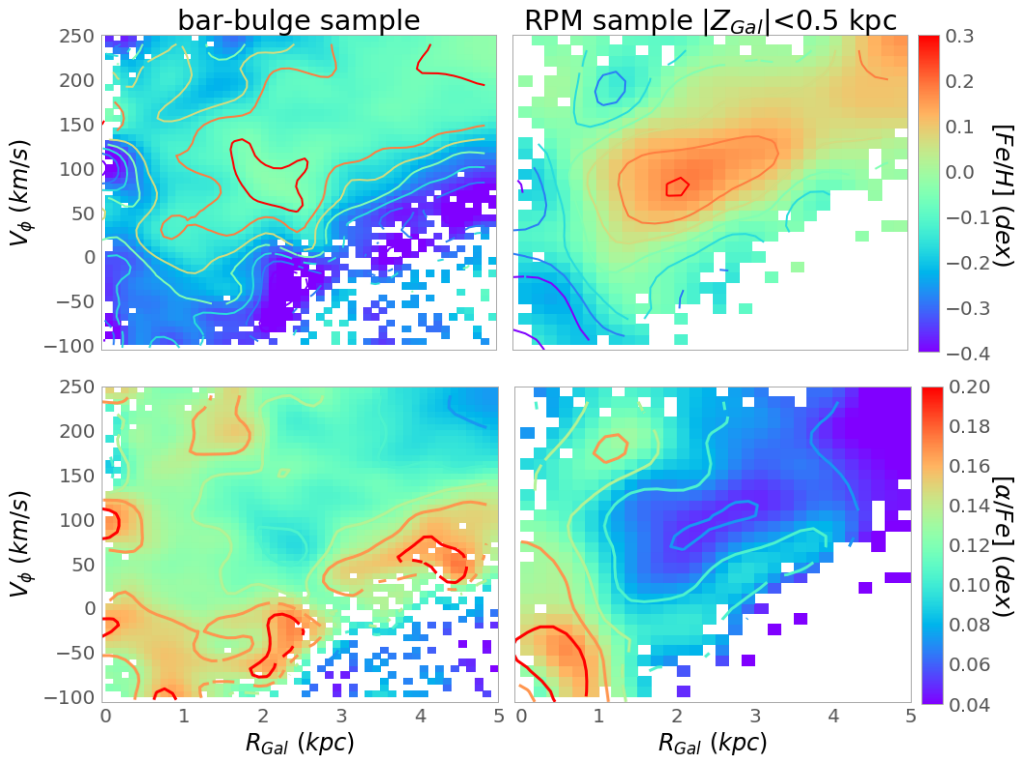

Figure 3.6.3: Same as Figure 3.6.2, but now with the panels colour-coded according to iron content (upper panels) and α-elements (lower panels).

a high V_ϕ dispersion, consistent with expectations for a pressure-supported spheroid. One may wonder from the figure what the two main concentrations of metal-poor stars are, one at negative V_ϕ and one around $V_\phi \sim 100$ km/s. This metal-poor V_ϕ bimodality in Figure 3.6.3 is mainly caused by the large contribution of stars at $V_\phi \sim 0$, (see Figure 3.6.2). At V_ϕ, $R_{\rm Gal} \sim 0$, a more metal-rich and higher density component dominates, causing the bimodal metal-poor distribution. A bar population signature, where the V_ϕ grows linearly with radius, seems to be complex and characterised by a mixture of both metal-rich and metal-poor populations. However, it has a more considerable contribution from metal-rich stars, in agreement with the findings of Wegg et al. (2019), but in contrast to those of Bovy et al. (2019) (see further discussion in Section 3.7.2). A lump (blob) of high-metallicity stars is observed in the right panels of Figure 3.6.3, between 10< V_ϕ <200 km/s and $R_{\rm Gal}$ ~3.5 kpc, which possibly represents the contribution of thin and thick disk stars in this region. The maps in this section show the present position of the stars, which means that stars in halo or disk orbits could well be passing close to the GC and be confused with the inner stellar populations. With this in mind, we proceed to the orbital analysis of the RPM sample and its relation to chemical composition.

3.7 Dissecting the mixed bulge populations in chemo-orbital parameters

To further disentangle the mixed bulge populations that became evident during both the chemical (see Section 3.5) and kinematic analyses (see Section 3.6), we turn to an analysis of the 6D phase space distribution (for a description of the orbital parameters, see Section 3.3) and its relation to stellar chemistry.

3.7.1 Counter-rotating stars

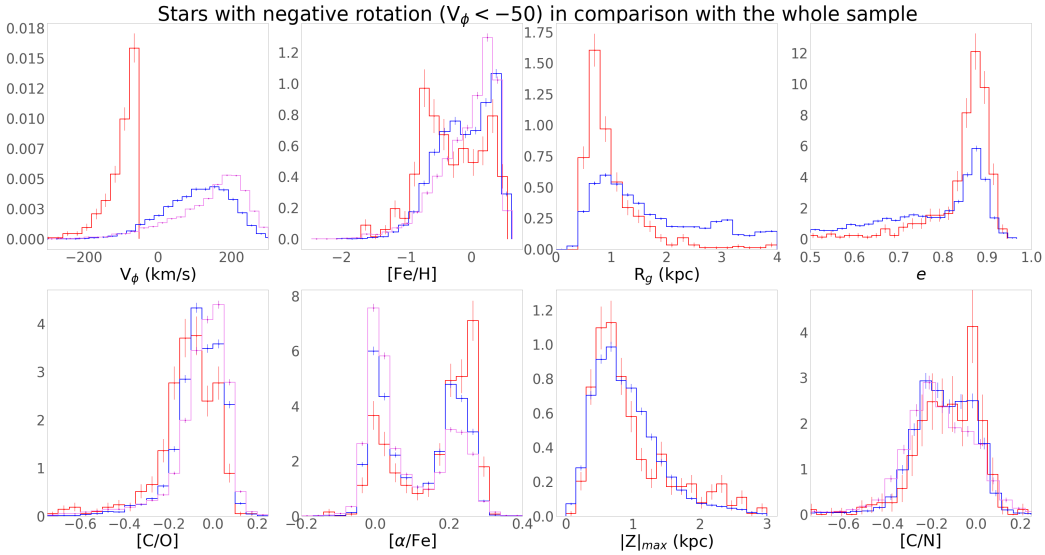

Figure 3.7.1: Distribution of all stars with V_ϕ <-50 km/s in the RPM sample shown in red as a function of many parameters, and compared to the same distribution for all stars in the RPM sample shown in dark blue, and all stars in the bulge–bar sample indicated by the violet lines.

In Figure 3.6.3, we notice a non-negligible contribution from stars with negative V_ϕ that are mostly metal poor. We selected stars with $V_\phi < -50$ from the RPM sample, representing about 600 stars. In Appendix 3.A, we use Monte Carlo realisations to show that simple errors could not reproduce this tail of counter-rotating stars. In Figure 3.7.1, we analyse the properties of these stars.

Figure 3.7.1 shows the distribution of parameters for stars in our RPM sample with $V_\phi < -50$ km/s in comparison with the full RPM and bulge–bar samples (limited always to $Z < 0.5$kpc). The main properties of this retrograde population are as follows.

- Stars with $V_\phi < -50$ km/s are predominantly metal-poor, but show a broad metallicity distribution. The distribution has its highest peak at around [Fe/H] ~ -0.7, compatible with the metal-poor peak we see in Figure 3.5.2 at the inner GC.
- The mean orbital radius distribution of the $V_\phi < -50$ km/s sample is confined to the innermost 1 kpc Galactocentric range, and the distribution has large eccentricities.
- Consistent with the fact that it is predominantly metal-poor, the retrograde population is [α/Fe]-rich and [C/O]-poor (i.e. typical of gas mostly polluted by core-collapse supernovae).
- The retrograde stars show larger [C/N] ratios, indicative of an older population (made of low-mass stars in which hot bottom burning does not take place, and therefore where C did not turn into N in these giants).
- Finally, we show an [Al/Fe] versus [Mg/Mn] diagram in Figure 3.7.2. Our RPM sample automatically excludes most of the more obviously accreted population (in contrast to the sample selection of Horta et al. 2021). According to this criterion, the accreted stars are 500 out of 26 500 stars in the bulge–bar sample, and only 80 out of 8 000 stars in the RPM sample). The blue dots in the right panel of Figure 3.7.2 show the locus in the [Mg/Mn], [α/Fe] plane of the counter-rotating stars. These blue dots are dispersed around the whole diagram and are not confined to the accreted location suggested by Hawkins et al. (2015). As seen

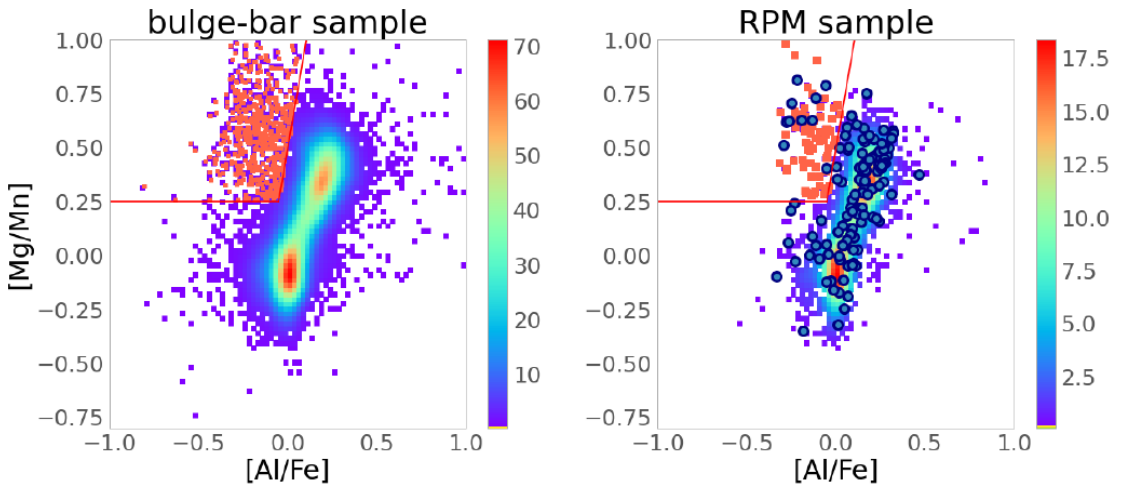

Figure 3.7.2: [Mg/Mn] vs. [Al/Fe] diagram for the bulge–bar sample and the RPM sample. The red line indicates the locus of the accreted stars as defined by Hawkins et al. (2015) (see also Das et al. 2020), and the stars that fall in this locus are indicated by the red squares. The blue dots represent the selection of counter-rotating stars, $V_\phi < -50$.

in the figure, we checked that the distribution of [Mg/Mn] for the retrograde component is shifted to larger values (~0.4), whereas a broader range in the values of [Al/Fe] is observed than that found for the accreted location defined by Hawkins et al. (2015).

The origin of this highly eccentric and counter-rotating population confined to the innermost kpc of the Galaxy is unclear. One possibility is that this is an accreted metal-poor population originated during a gas-rich accretion phase in the early formation of the bulge. The metallicity distribution of the retrograde stars includes a metal-rich hump, but this could be explained by some contamination by metal-rich stars. Another interesting possibility is that we are seeing the inner Galaxy counterpart of the Splash population identified in the solar vicinity by Belokurov et al. (2020). Splash stars have little to no angular momentum and many are on retrograde orbits and are slightly metal-poor, but can have a broad metallicity range. As explained by these latter authors, there are different theories for the origin of these stars, although the name Splash comes mainly from the idea that these are old stars that belonged to the proto-Galactic disk that were dispersed during the accretion event that created the Gaia Sausage. However, alternative explanations are also possible. Among them are two very interesting notions that are more directly associated with bulge: (a) these stars were formed within gaseous outflows resulting from a burst in star formation or AGN activity (Maiolino et al. 2017; Gallagher et al. 2019), or (b) such retrograde stars in the bulge could be the result of clumps of star formation that took place at early times in the early disk (high redshift) and migrated into the bulge, with some stars being driven to retrograde orbits by the bar (Amarante et al. 2020; Fiteni et al. 2021). In both cases, it is expected that a broad velocity dispersion is created, with some stars being on counter-rotating orbits. A recent study analysing the kinematics of metal-poor stars in the inner Galaxy also found an extended tail of counter-rotating stars that does not match their simulations (Lucey et al. 2021).

Figures 16-19 illustrate the complexity of the Galactic bulge region. In addition to this counter-rotating hot component and/or tail, we see the contributions of other populations, with properties suggestive of a bar, an inner thin disc, a thick disc, and what seems to be a pressure-supported component that cannot be attributed to the halo or thick disc.

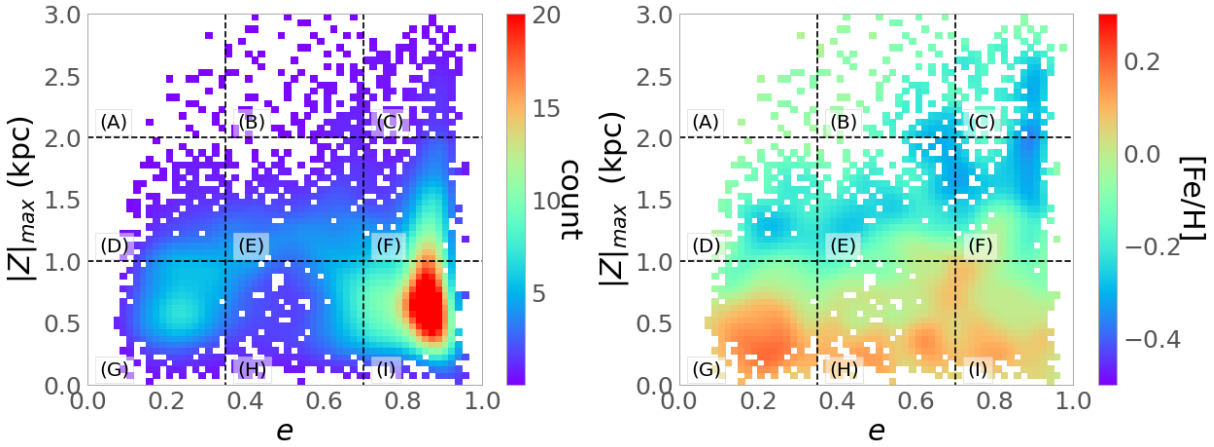

Figure 3.7.3: $|Z|_{\rm max}$ vs. eccentricity (e) diagram for the RPM sample. In the left panel, the colour shows the count of stars per bin and in the right panel the colour shows the mean [Fe/H] content per bin. We define nine windows in this diagram indicated by the letters (A) to (I).

As all these components overlap in the same region and parameter space, neither pure chemical nor kinematical criteria can be used to isolate these different populations. Therefore, we turn to a more detailed orbital–chemical analysis. Without pre-selections based on the classical definition of the local Galactic components, we can investigate the dominance of the different components around different parameter ranges.

3.7.2 The $|Z|_{\rm max}$–eccentricity plane

We now turn to the analyses of our RPM sample in the $|Z|_{\rm max}$–eccentricity plane, similarly to that found in Boeche et al. (2013) and Steinmetz et al. (2020a). These latter studies showed that this parameter space offers a powerful way to disentangle the coexisting populations in the region (avoiding the use of pre-define Galactic populations based on properties of the more local samples).

Figure 3.7.3 shows the distribution of stars in this plane colour-coded according to number density (left panel) and metallicity (right panel). We divide the $|Z|_{\rm max}$–eccentricity plane into nine cells (labelled alphabetically in the figure). From these diagrams we notice that most stars from our RPM sample have high eccentricity and low $|Z|_{\rm max}$. A second prominent population is concentrated at very low eccentricities and low $|Z|_{\rm max}$, being mostly composed of high-metallicity stars, which is consistent with classical disk populations. The right panel of Figure 3.7.3 is dominated by a metallicity gradient away from the midplane. On top of this, there is a population of less metal-rich stars on highly eccentric orbits that reaches ~ 1 kpc in $|Z|_{\rm max}$. A deficit of stars is also noticeable at intermediate eccentricities of ~ 0.48. Next, we analyse the composition distribution and orbital parameters for each cell.

Figure 3.7.4 shows [α/Fe] versus [Fe/H] for each cell defined in Fig. 3.7.3. We note that this is different from the usual diagram seen in bins of R, Z (e.g. Hayden et al. 2015; Queiroz et al. 2020). Here instead we are focusing on a very inner sample, and mapping the chemistry of stars sampling different orbital parameter space in that inner region. This approach shows that low-[α/Fe] stars are on low-inclination orbits, while high-alpha stars are on orbits of all types. Both populations are spread over orbits of every eccentricity.

Cell (I) shows a hot population (eccentricities > 0.7) that is thin-disc-like and low-[α/Fe] on top of a more metal-poor, high-alpha population. As we describe below, the stars in this cell are mostly stars on bar-shaped orbits. As we go to higher $|Z|_{\rm max}$ we lose most of the low-[α/Fe] stars, which results in the metallicity gradient seen in the right panels of Figure 3.7.3. The

separation between high-[α/Fe] and low-[α/Fe] is also clear in cell (I), whereas the bimodality becomes less clear for lower eccentricities and higher $|Z|_{\rm max}$.

The high-[α/Fe] population shows a broad range of metallicities for the cells at high eccentricity (especially at low $|Z|_{\rm max}$) that gradually becomes narrower towards low eccentricities. The cells (G) and (D) are consistent with predominantly thin and chemical-thick disk populations, respectively, with their distributions of $[\alpha/Fe]$ versus [Fe/H] appearing to be similar to those in Nidever et al. (2014); Hayden et al. (2015); Queiroz et al. (2020) for intermediate Galactocentric radii of $4 < R_{gal} < 10$ kpc. Note that when we refer to chemical-thick disc, we mean the definition of a thick disk by its high [α/Fe] content. However, for stars on more eccentric orbits (cells C, F, and I), the high-[α/Fe] populations become more extended in metallicity. One way of interpreting this is that the so-called knee moves to larger values for these stars. This is, for instance, the behaviour predicted for a spheroidal bulge (e.g. Matteucci et al. 2020). Moreover, these cells show slightly larger [α/Fe] than those from the chemically defined thick disk in the solar neighbourhood. We note that this is not in contradiction with earlier APOGEE results showing that the high-[α/Fe] chemical-thick-disk component has the same shape in different R_{gal}-Z_{gal} bins; it is simply that now we are able to see a spheroidal population confined to the smallest $R_{\rm mean}$ that stands out among the more eccentric stars. This suggests that the chemical-thick disk and spheroidal bulge have slightly different [α/Fe]-enhancements (see Barbuy et al. 2018, for a discussion). We also should keep in mind that cells (G), (H), and (I) may be incomplete, because of the selection outside the heavily reddened regions as seen in Sect. 3.2.

To understand where bar-like orbits would fall in these diagrams, we made Figure 3.7.5 which shows the [α/Fe] versus [Fe/H] similarly to Figure 3.7.4, but now colour-coded according to the probability of the star moving on a bar-shaped orbit. To estimate this probability, we used the Monte Carlo sample of each star (50 orbits, see Sect. 3.3) and calculated the fraction of orbits classified as bar-shaped. To classify each orbit, we follow the definition from Portail et al. (2015) which uses frequency analysis. We compute the main frequencies of each orbit in the Cartesian coordinate x and the cylindrical radius R in the bar frame. The orbits for which the frequency ratio fR/fx = 2 +/- 0.1 are in a bar-shaped orbit. The orbits that are not bar-shaped have a frequency ratio fR/fx $\neq$ 2 +/- 0.1.

Figure 3.7.5 shows that the stars most likely to be on bar-shaped orbits are in cell (I), with an important contribution also found in cell (H). As expected, the stars on the bar show eccentric and low-$|Z|_{\rm max}$ orbits. One very important finding is that the stars following bar-shaped orbits in cells (I) and (H) are seen in both low- and high-α populations. This suggests that stellar trapping has been an efficient mechanism throughout the lifetime of the bar, bringing stars to the bar that had previously belonged to Galactic components formed even before the bar was formed. There is a clear dearth of stars on bar-shaped orbits at high $|Z|_{\rm max}$ and with low eccentricity.

Figures 3.7.6 and 3.7.7 show the distributions of metallicity and $R_{\rm mean}$ for each $|Z|_{\rm max}$–eccentricity cell. These figures show very interesting features that are related to what we see in the [α/Fe]–[Fe/H] relationship discussed above.

In Fig. 3.7.6 we see two populations, one with a narrow [Fe/H] centred on $\approx$ 0.2 and another, broader distribution centred on $\approx$ -0.7. Comparison of Figures 3.7.4 and 3.7.6 tell us that the former is the low-alpha population and the latter the high-alpha population. The high [α/Fe] cells (I), (F), and (C) span the widest range of metallicities, but a narrower range in $R_{\rm mean}$, with most stars showing $R_{\rm mean} < 3$ kpc. The sampled $R_{\rm mean}$ go from $R_{\rm mean} < 2$ kpc (I) to $1 < R_{\rm mean} < 3$ kpc, as we go up in $|Z|_{\rm max}$. This is expected, but what is interesting is that this is accompanied by a low-metallicity component that starts to become more prominent (going from cells I to C). As we show below, these high-eccentricity stars are composed of a mix of bar and spheroid populations, giving the impression of a metallicity

gradient with $|Z|_{\rm max}$. The peak in the metallicity of cell (C) is consistent with the metal-poor peak seen in Figure 3.5.2. The metallicity distribution clearly becomes narrower towards lower eccentricities, while the distribution in $R_{\rm mean}$ is now broader, and with fewer stars coming from the innermost kiloparsecs. In the bottom row ($|Z|_{\rm max} < 1$), the prominent high-metallicity peak goes from [Fe/H] ~ 0.25 in cell (I) to 0.2 in cells (G) and (H). Progressively, going from (I) to (G), the metal-poor population around -0.7 dex appears to get weaker (with fewer and fewer stars from the pressure-supported component, which is mostly composed of stars with $R_{\rm mean} <$ 3 kpc). This is the population that is very dominant in cells (I), (F), and (C) as discussed before. Still in the bottom row, going from (I) to (G), a peak at [Fe/H] ~ -0.3 gets more prominent. This peak will increase for intermediate eccentricities as $|Z|_{\rm max} < 1$ increases. As seen here, this corresponds mostly to stars with 2 kpc $< R_{\rm mean} < 3$ kpc.

For low-eccentricity stars (left columns in Figures 3.7.6 and 3.7.7), the mean orbital radius distributions get broader, with $R_{\rm mean} > 2$ kpc. This suggests that the inner disk stars were not born in the innermost 2 kpc of the Galaxy, a result reminiscent of that of Matsunaga et al. (2016) based on classical Cepheids (see discussion in Section 7). The metallicity distribution is now dominated by stars in the 3 kpc $< R_{\rm mean} < 4$ kpc mean orbital radius range, and a peak around -0.27 dex starts to appear. In cell (G), the contribution of three peaks is visible at [Fe/H] $\sim$ 0.2,-0.27, and -0.33 dex. Toward larger $|Z|_{\rm max}$ values, the metal-rich peak at ~ 0.2 disappears, and the other two peaks begin to dominate, consistent with a transition from a thin-disc-like population to a thick disk population.

By analysing Figures 3.7.6 and 3.7.7 together with the V_ϕ distributions (Figure 3.7.8), we can more quantitatively relate the populations discussed previously. It is possible to see the contributions from the inner thin and thick discs in Figures 3.7.7 and 3.7.8 in cells (G),(D), and (A) (left column of the $|Z|_{\rm max}$–eccentricity diagram). The first column of the diagram is mostly dominated by inner thin-disk stars (stars with a V_ϕ peak at around 200 km/s and a low V_ϕ dispersion). The second column of the $|Z|_{\rm max}$–eccentricity diagram (intermediate eccentricities) contains mostly thick disc-like stars, which become more dominant towards larger $|Z|_{\rm max}$ values (also confirmed by the metallicity distribution in Figure 3.7.6). The last column of the $|Z|_{\rm max}$–eccentricity diagram (highly eccentric orbits) selects a pressure-supported component with lower rotation and larger V_ϕ dispersion (with small angular momentum and therefore small R_g range), which we saw in Fig. 3.7.4 to be a metal-poor, high-[α/Fe] population.

At low $|Z|_{\rm max}$ and high eccentricity (cell I), the bar population begins to dominate over the spheroid (pressure-supported population described in the previous paragraph), increasing the metallicity (as we also see in the bar probability figure). The last column of Fig. 3.7.8 also reveals, superposed on the spheroid and bar populations (both having large eccentricities), the counter-rotating, metal-poor population discussed in Section 7.1. Here, it is more prominent at the highest $|Z|_{\rm max}$ cell, probably because at lower $|Z|_{\rm max}$ it gets buried in the much more dominant metal-rich population of the bar. The counter-rotating population could also just be an extended tail of the spheroid. In Appendix 3.A, we show that the errors are not likely to form an asymmetric structure in V_ϕ; significantly, that structure would extend to high negative rates such as -50 km/s. We also notice positive tails in the three central panels of Figure 3.7.8. The canonical V_ϕ distribution of an exponential disk has a sharp cutoff at high V_ϕ, suggesting a slow outward decline in σ_R.

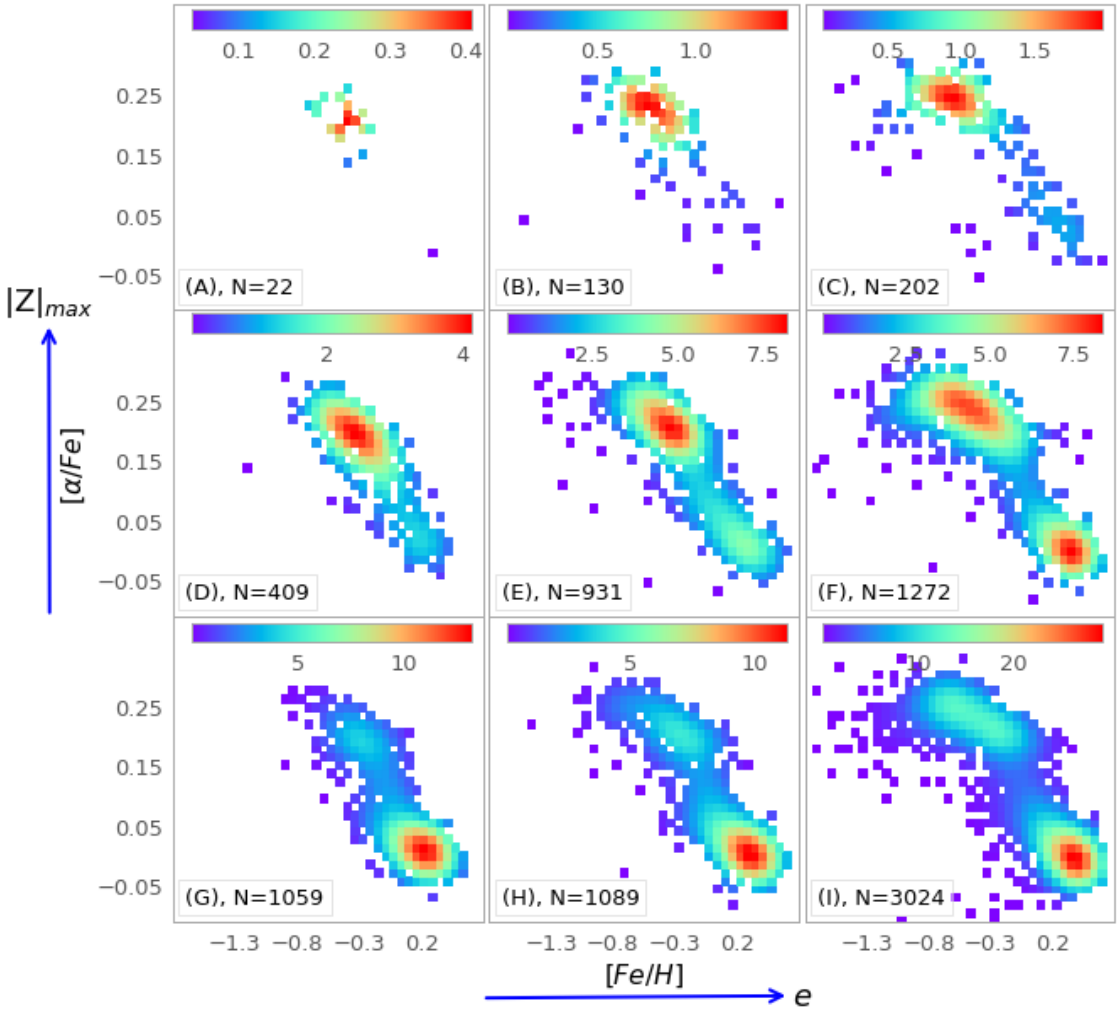

Figure 3.7.4: [α/Fe] vs. [Fe/H] for each cell defined in Fig. 3.7.3. The number of stars for each cell is indicated next to the panel labels. The rightmost columns, dominated by large eccentricity stars (pressure-supported component), show larger alpha-enhancement ([α/Fe] $\sim$ 0.25) than what is seen among the low-eccentricity stars. The (inner) thin-disk contribution is seen mostly in the lower row, with a low, near-solar [α/Fe] ratio, which peaks at [Fe/H] = 0.2 in cells (G) and (H), and at 0.25 in cell (I).

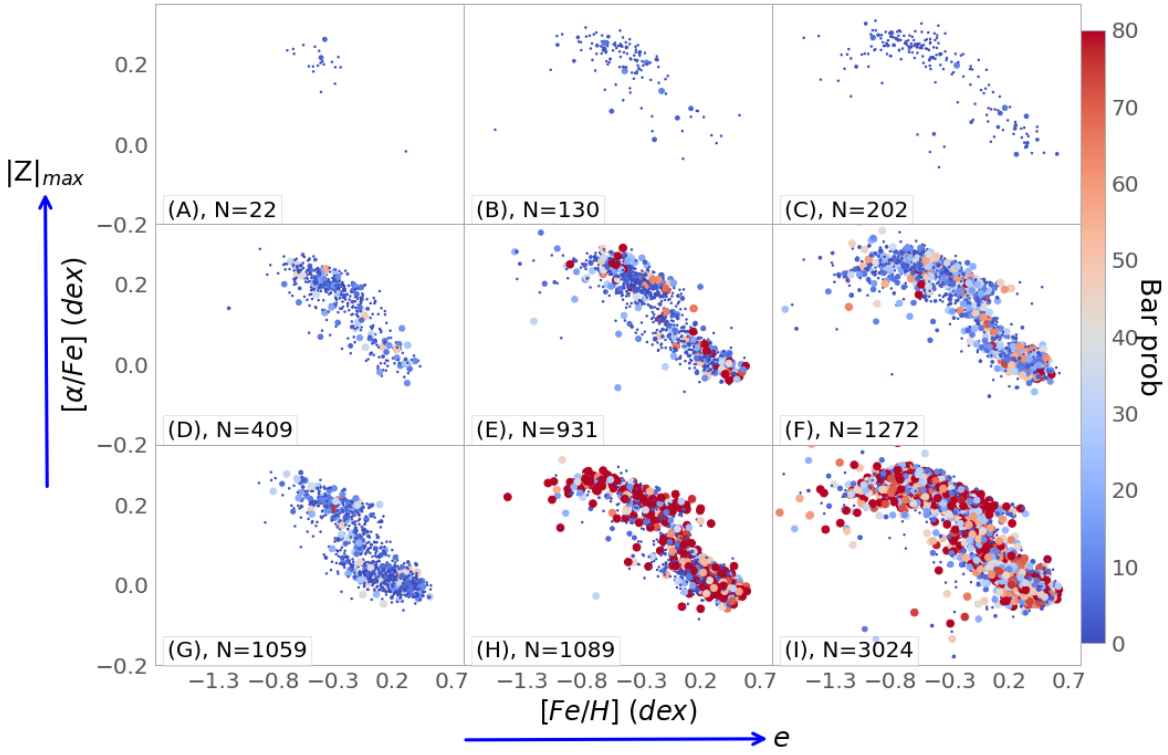

Figure 3.7.5: [α/Fe] vs. [Fe/H] for each cell defined in Figure 3.7.3 now colour-coded according to the probability that a star follows a bar-shaped orbit (see text). Stars with the largest bar-shaped orbit probabilities populate cells (H) and (I), and are found both among high- and low-[α/Fe] populations.

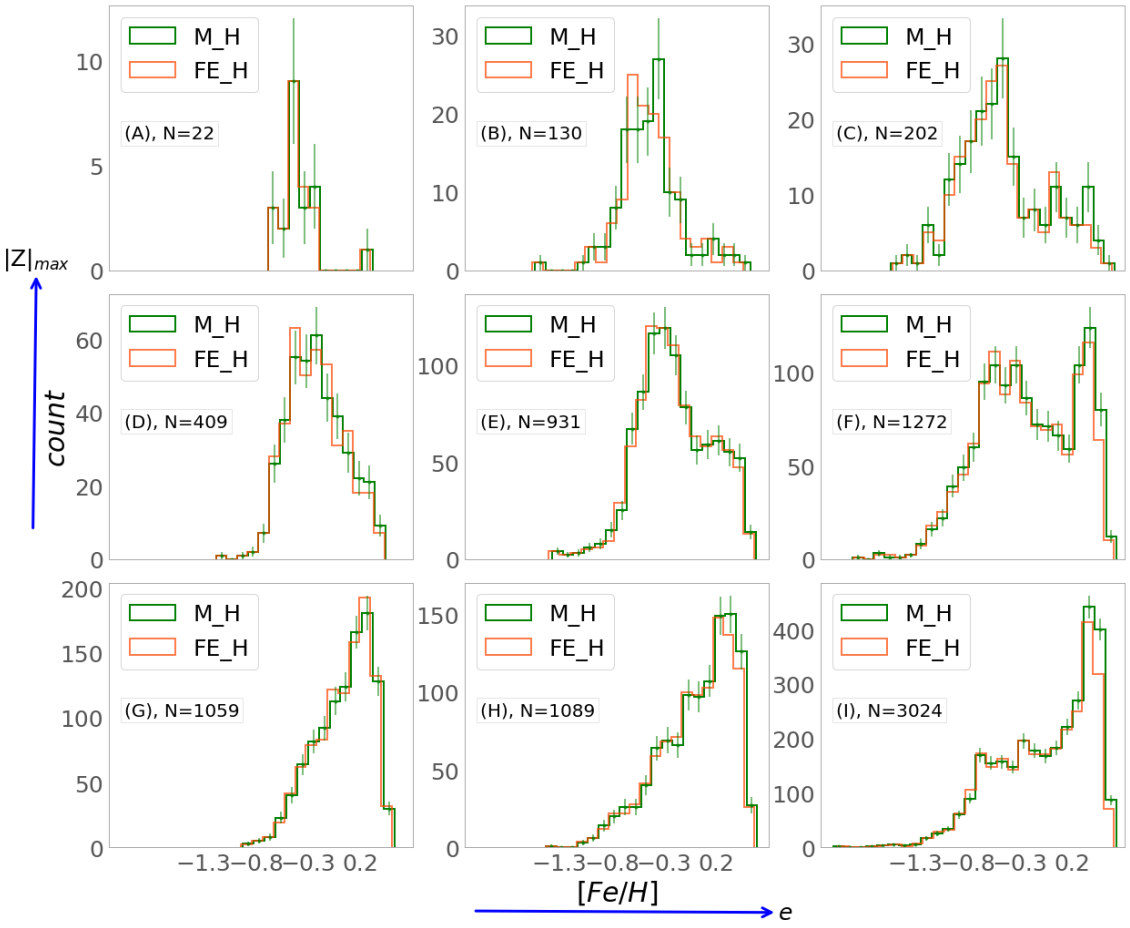

Figure 3.7.6: MDF for each cell defined in Fig. 3.7.3. We show the distributions of [Fe/H] (orange line) and [M/H] (green line) coming from ASPCAP.

In summary, the analysis performed in this section shows, for the first time, a detailed dissection of the innermost parts of the Milky Way. We show that the several peaks in the metallicity distribution correspond to populations of different eccentricities and $|Z|_{\rm max}$ distributions. The metal-rich population (with a peak at 0.2 dex) is made of inner thin disk stars, mostly formed outside the innermost 1-2 kpc. Some of the metal-rich stars are from the bar, which is populated by stars with $R_{\rm mean}$ within the 0-3 kpc range. These populations sit on top of a broader metallicity component extending from around −0.8 to above solar, which resembles a classical bulge (Cescutti et al. 2018; Matteucci et al. 2019) made of mostly high-[α/Fe] stars (most probably old; see Miglio et al. 2021). Meanwhile, with increasing $|Z|_{\rm max}$ we start to probe even more of the inner thick disc, and the metallicity distribution is increasingly dominated by stars with metallicities around −0.5 dex, which is similar to the peak of the local thick disk metallicity distribution (emerging in cell (B)).

3.8 Summary and implications

In this paper, we analyse the inner regions of our Galaxy using APOGEE post-DR16 internal release data combined with *Gaia* EDR3 and the `StarHorse` distances and extinctions. This latter addition provides us with an unprecedented catalogue of the Galactic innermost regions, with thousands of stars with distance uncertainties of less than 1 kpc.

We analyse two distinct samples: (a) one sample of more than 26 500 stars spatially selected in

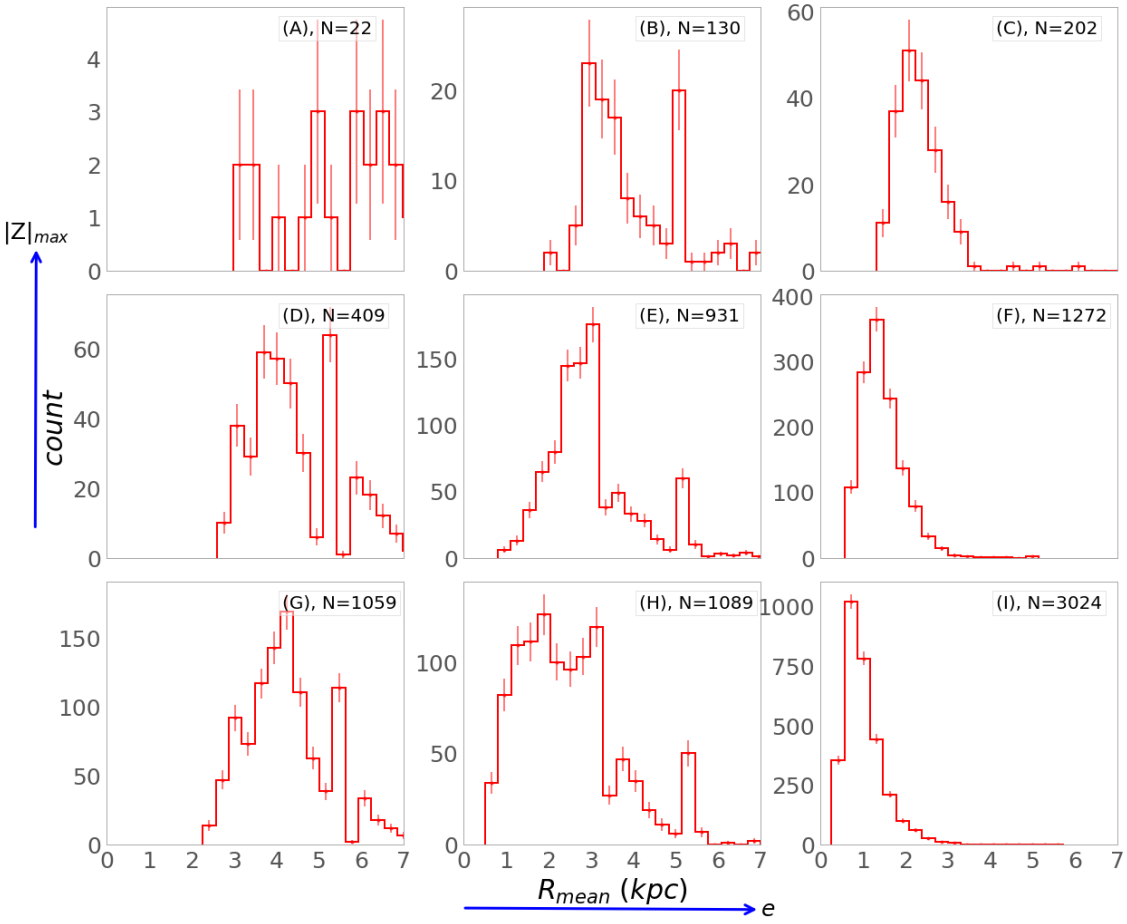

Figure 3.7.7: Mean orbital radius distribution for each cell defined in Figure 3.7.3. The more eccentric population has $R_{\rm mean}$ confined to the innermost (1-3 kpc) regions of the Galaxy, whereas the thin-disk stars have $R_{\rm mean}$ larger than 2-2.5 kpc.

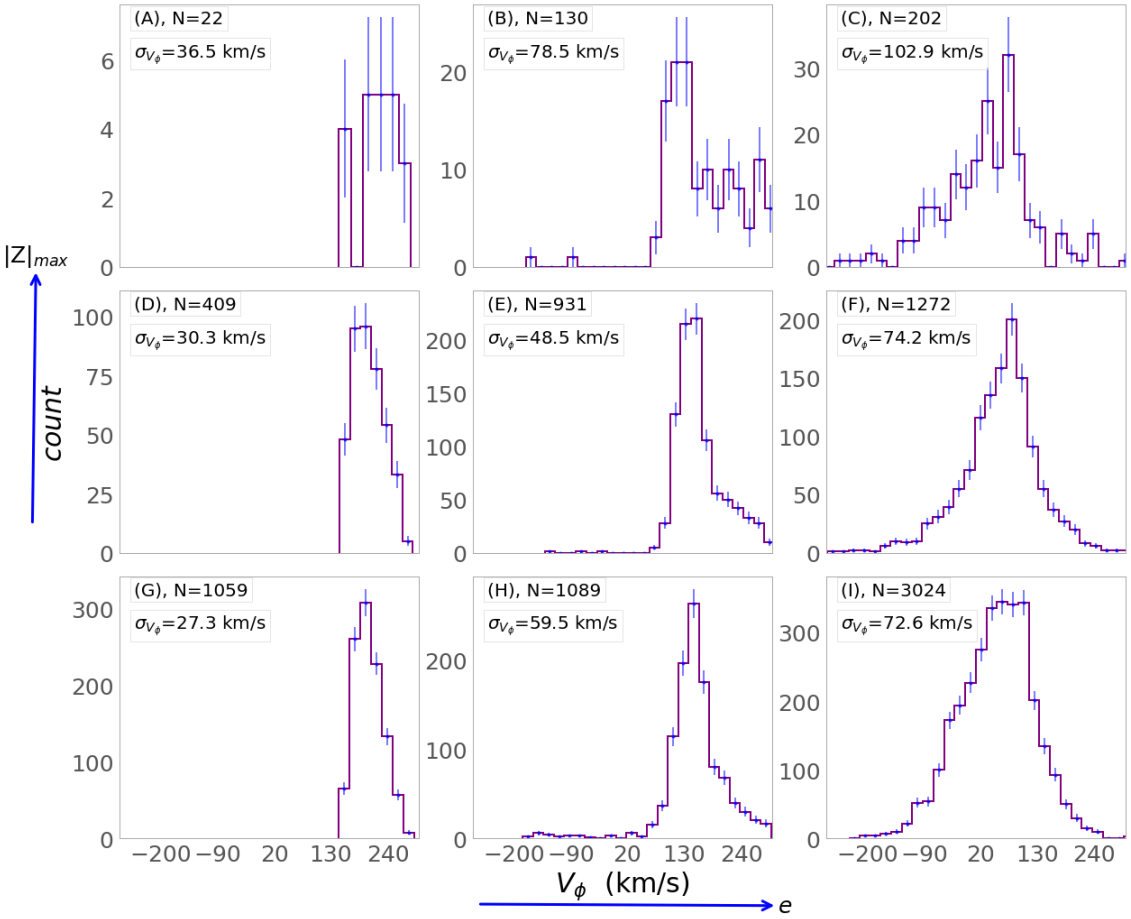

Figure 3.7.8: V_ϕ distribution for each cell defined in Figure 3.7.3. The value of the dispersion in V_ϕ is also shown for each cell. Thick disk stars with $V_\phi \sim 140$ km/s are seen in panels H and E where there is less contamination by thin disk stars (with V_ϕ around 200 k/ms - cells G and D) and the spheroidal component (with V_ϕ around 80 km/s cells I, F, and C). A counter-rotating tail is noticeable in cell C.

Cartesian coordinates X and Y, and (b) a sample of around 8 000 stars that are more confined to the inner Galaxy and cleaned from foreground stars using the RPM method, which becomes possible thanks to the very precise proper motions of Gaia EDR3. Most of this sample is outside the locus for accreted stars defined by Hawkins et al. (2015); Das et al. (2020) on the [Mg/Mn]–[Al/Fe] plane (but see discussion in Horta et al. 2021). Despite this, we see a counter-rotating population the origin of which requires further investigated (see discussion in Section 7.1).

With our larger sample, we were able to build exquisite chemical and kinematical maps of the innermost regions of the Galaxy. Furthermore, our analysis of the chemical data reveals a clear chemical bimodality in the [α/Fe] versus [Fe/H] diagram for the full sample of 26 500 stars. The separation becomes more evident when we apply a proper-motion cut to clean the sample for foreground disk stars. Although the bimodality has also been detected in previous works (Rojas-Arriagada et al. 2019; Queiroz et al. 2020) it is much more clearly seen here. We also confirm that similar results are obtained when we adopt [Mg/Fe] or [O/Fe]. This shows the level of precision and consistency obtained by the APOGEE ASPCAP pipeline (García Pérez et al. 2016; Jönsson et al. 2020).

In chemical evolution, it is expected that a bimodality seen in [α/Fe] versus [Fe/H] is also seen in other chemical abundance ratios that trace similar enrichment timescales. Here we illustrate this using the [C/N] and [Mn/O] ratios. Indeed, double densities are also seen when they are plotted as a function of metallicity. For the C/N ratio, the interpretation is complex as both elements can be modified during the evolution of the star on the giant branch. For [Mn/O], difficulties arise in the abundance measures because the pipeline processing does not estimate Mn for stars cooler than 4000 K. Broadly the results remain consistent with the bimodality seen in alpha-elements.

The chemical maps show a spatial dependency on the metallicity, with the predominance of a metal-poor (α-rich) component that is located in the central region. This feature can now be seen in the XY plane. This component is also seen on the [C/N] and [Mn/O] maps, again in agreement with nucleosynthetic sites of production of these different elements, and their release timescales to the interstellar medium.

The XY spatial maps of cylindrical velocities exhibit an elliptical but almost circular form in V_ϕ and a butterfly pattern in V_R, indicating the rotation of a barred structure, which is the kinematical signature of a bar. This is similar to what has been seen by Bovy et al. (2019), also using DR16 data but with fewer stars and a completely different way of estimating distances. The velocity maps are in agreement with the expectation from simulations of barred galaxies, for example as discussed by several authors (Debattista et al. 2017; Bovy et al. 2019; Carrillo et al. 2019; Fragkoudi et al. 2020), where the butterfly pattern of the V_R field is one example of the expected features. These maps suggest an inclination of the bar with respect to the Sun–GC line of 20 degrees, and a spatial extent of around 4 kpc in the semi-major axis and 1 kpc in the semi-minor axis. A more detailed comparison with models is required to provide a more quantitative characterisation of the properties of the Milky Way bar.

The V_ϕ versus Galactocentric radius (mapped both in [α/Fe] and [Fe/H]) for the two samples studied here shows the signature of the distinct stellar populations coexisting in these samples, suggesting the presence of a pressure-supported spheroid, a bar, and the Galactic discs. These diagrams also show a counter-rotating population of metal-poor stars or an extended tail of negative V_ϕ, which we then characterise in detail. In particular, the dispersion in V_ϕ of the innermost metal-poor component is too large to be attributed to thick-disk stars (around 120 km/s), strongly suggesting the presence of an underlying spheroid, as predicted by Minniti (1996).

After the chemical and the velocity analysis we further dissect the innermost regions thanks to a sample of approximately 8 000 stars for which we computed stellar orbits. The populations are then characterised on a $|Z|_{\max}$–

eccentricity plane (and in this way we avoid any pre-selection based on chemistry or kinematics). We pursue a joint analysis of the distributions of metallicity, [α/Fe] abundance ratios, mean orbital radii ($R_{\rm mean}$)[17], and the V_ϕ and its dispersion. This comprehensive analysis is needed in order to map the parameter space where each of the different populations dominates, thus avoiding the use of artificial sharp boundary definitions. In this way, we identify and better characterise the chemical properties of the following populations inhabiting the innermost parts of the Milky Way close to the Galactic midplane:

- Inner thin-disk and the bar:

  Most of the low-eccentricity, high-V_ϕ stars show low [α/Fe]. This inner thin-disk population has a metallicity peak at [Fe/H] = +0.2. This metallicity shifts to larger values for more eccentric stars, still close to the Galactic midplane, reaching a peak of [Fe/H] = +0.25. However, these metallicities are seen only in the (1-2) kpc mean orbital radius range, suggesting that the most metal-rich stars are part of the bar component (in agreement with Wegg et al. (2019)). This suggests that the bar is slightly more enriched than the inner thin disk stars, most probably due to residual star formation in the innermost 2 kpc that form stars that enter bar orbits. Bars at high redshift could induce bursts of star formation due to gas trapping and gas funneling, especially toward the centre. The inner thin-disk stars in our sample have $R_{\rm mean}$ larger than 3 kpc, consistent with the fact that the thin disk does not extend all the way to the GC (although this conclusion could be affected by the non-optimal coverage of the innermost regions). This is in agreement with a similar suggestion made by Matsunaga et al. (2016) who reported that no Cepheid was found in the innermost 2.5 kpc of the Milky Way.

- Pressure-supported component and the bar: Underneath the bar population mostly found at large eccentricities and low heights from the plane (confirmed by the large fraction of stars with bar-shaped orbits in this part of the parameter space; see Figure 3.7.5), there is another component that is much broader in metallicity and that becomes more apparent towards larger distances from the Galactic midplane (where the bar component fades in). This large velocity dispersion component has a non-negligible contribution of metal-poor stars, which makes the metallicity distribution broad. This pressure-supported spheroid shows high-[α/Fe] ratios. Part of these spheroid stars that have orbits that are more confined to lower heights from the Galactic midplane also get trapped by the bar. Indeed, as shown in Figure 3.7.5, we find stars with a high probability of being in bar-shaped orbits among the high-[α/Fe] stars. This figure suggests that bar stars have eccentricities in the 0.5-0.8 range and metallicities above solar (explaining the shift to larger metallicities in cell (I) of Figure 3.7.6). Therefore, we find the bar to be composed mostly of metal-rich stars, with some additional contribution of stars with a similar chemical pattern to those in the spheroidal component. The latter were most probably trapped into the bar potential. It seems that the bar traps the more metal-rich component of the spheroid, while the more metal-poor component is able to escape the bar. The mechanisms that explain how this happens need to be investigated using proper dynamical models. This also explains the details of the shape of the [α/Fe] versus [Fe/H] distribution closer to the Galac-

17 $R_{\rm mean}$ represents the mean Galactocentric distance a star has in its orbit, that is, the mean between its apocentric and pericentric distances. This is taken here as being close to the birthplace of the stars, except for effects due to radial migration.

tic midplane, which becomes more metal rich both in high and low-alpha populations.

- Inner chemical-thick disc: Stars of intermediate eccentricities with V_ϕ compatible with the local thick disk population dominate cell (E) (Fig. 3.7.6 and Fig. 3.7.8). These stars show typical local thick disk metallicity distribution (Fig. 3.7.6) and [α/Fe] enhancement. The majority of these stars are not on bar-shaped orbits. Local thick discs stars were recently shown to be a very old and coeval population (thanks to the very precise ages from asteroseismology (see Miglio et al. 2021; Montalbán et al. 2021)). Therefore, the same is expected to be true for the inner-thick disk population discussed here. If that is the case, it would suggest this component to have formed before the bar.

- Counter-rotating stars or the tail of the pressure-supported (spheroid) component: We find, superposed on the two components populating the high-eccentricity orbits (the bar and the pressure-supported spheroid), a population with negative V_ϕ in highly eccentric orbits, confined to the innermost kiloparsec of the Galaxy. This population is seen as a tail in the V_ϕ distribution shown in cell C of Figure 3.7.8, and its properties are shown in Figure 3.7.1. Given the low statistics of stars in cell C, a more robust characterisation of this population is deferred to future work when larger samples will be available.

- The spheroid and the thick disc: The conclusion that we have a non-negligible contribution from a spheroid (on top of the thick-disc-like component)is strengthened by the shape of the high-alpha populations in Figure 3.7.4. The high-[α/Fe] population can be seen to be shifted to slightly larger values of [α/Fe] in the last column of Fig. 21 (spheroid-dominated) compared to the two other columns (more thick-disk dominated). The extent of the high-alpha population is also different, going to larger metallicities for the spheroid-dominated population, suggesting a higher star formation rate (and efficiency) in the spheroidal bulge than in the thick disc. The caveat here is that this could also be the result of low statistics in the thick-disc-dominated cells. A more detailed comparison between these two populations, with more data, will be the topic of a forthcoming paper.

The existence of a spheroidal bulge in which star formation has been vigorous would be in agreement with what is expected from chemical evolution models (see a discussion in Section 4 of Barbuy et al. (2018), and Matteucci et al. (2019)). In a scenario of fast enrichment, very old stars can be found already at metallicities [Fe/H] ~ -1 (see Chiappini et al. (2011); Wise et al. (2012); Cescutti et al. (2018) and Section 3.2.4 of Barbuy et al. (2018) for a discussion). Indeed, some of the oldest objects known in our Galaxy are located in the bulge and have metallicities around one-tenth of solar. For instance, the Galactic bulge has a system of globular clusters (Minniti 1995) that are now known to be among the oldest in our Galaxy (Barbuy et al. 2009; Chiappini et al. 2011; Barbuy et al. 2014; Kerber et al. 2018, 2019; Ortolani et al. 2019); these can be as old as the RR Lyrae. These stars were born around 400 000 years after the big bang, and are thus relics of the earliest chemical enrichment of the Universe.

The properties of the pressure-supported metal-poor, α-enhanced stars we find in the bulge are consistent with the RR Lyrae stars in the same region. A debate over the origin of the RR Lyrae population in the bulge is ongoing, and the conclusions are very dependent on the samples analysed and models employed. Some of the suggestions in the literature are that these RR Lyrae could be the extension of the stellar halo in the inner Galaxy (Minniti 1996; Pérez-Villegas et al. 2017a), have a bar distribution (Pietrukowicz et al. 2015), or show evidence of being a more spheroidal, concentrated, pressure-

supported structure (Dékány et al. 2013; Kunder et al. 2016; Contreras Ramos et al. 2018). To break this dichotomy, Kunder et al. (2020) recently suggest the existence of two components of RR Lyrae in the inner Galaxy. One RR Lyrae component is spatially and kinematically consistent with the bar, and the second component is more centrally concentrated and does not trace the bar structure. This agrees with the results shown here, where we see that the bar seems to trap mostly thin-disk stars, but also the more metal-rich part of the α-enhanced spheroidal component.

The pressure-supported component could be the result of an accreted event or strong gas flows at the early stage of the formation of the Galaxy, and this is consistent with an age for the RR Lyrae stars in the bulge of 13.41 ± 0.54 Gyr (Savino et al. 2020). Du et al. (2020) use OGLE IV photometry and Gaia DR2 proper motions to analyse metal-poor ([Fe/H]< -1) and metal-rich ([Fe/H]> -1) RR Lyrae stars in the bulge. These authors concluded that the angular velocities and spatial distribution are different for metal-rich and metal-poor RR Lyrae stars. These results are in agreement with the findings of Wegg et al. (2019) and Kunder et al. (2020).

The results presented here also offer some insight into the conundrum of the age of the bulge, namely: the old ages from colour magnitude diagrams proper-motion-cleaned towards low extinction bulge windows versus the non-negligible contribution of stars younger than 5 Gyr suggested by the microlensed dwarfs (Bensby et al. 2017). After the analysis shown here, it is clear that each of the techniques leads to a different mixture of stars, with Baade's window CMD probing more of the spheroidal component mostly occurring in the inner 2-3 kpc of the Galaxy, whereas in the other case the stars are sampling a mix of spheroid and inner thin-disk stars, as confirmed by their multi-peak metallicity distribution (see also Rojas-Arriagada et al. 2020).

The clear bimodality in the chemical diagrams for stars closer to the Galactic midplane and the existence of a dearth of stars in between the two overdensities (Fig. 3.5.5) offer an important new observational constraint to chemodynamic models of the Galaxy. There has been considerable debate over the origin of this bimodality based on data for stars closer to the solar vicinity, and since the proposition made more than 20 years ago by Chiappini et al. (1997) that this would reflect two main star formation paths, with a quenching of the star formation in between. More recently, this scenario has been revived both by chemical evolution models and numerical simulations (e.g. Anders et al. 2017a, 2018; Weinberg et al. 2019; Spitoni et al. 2021; Grand et al. 2020) as well as by the indication of an age dichotomy between the high- and low-α populations (Miglio et al. 2021; Rendle et al. 2019; Lian et al. 2020; Das et al. 2020). Cosmological simulations are particularly important to identify the reasons for this quenching, which can be manyfold, as discussed in the literature (e.g. Weinberg et al. 2019; Grand et al. 2020; Agertz et al. 2020; Ciuca & Hernández 2020; Buck 2020; Vincenzo & Kobayashi 2020). Alternative views, explaining the observed dichotomy as being the result of internal processes such as radial migration were also put forward (Schönrich & Binney 2009; Sharma et al. 2020), but difficulties in forming a hot thick-disc-like component by radial migration alone have been pointed out (see Minchev et al. 2013; Martig et al. 2016b; Aumer et al. 2016, for a discussion). The data presented here for the innermost regions now show the dichotomy to also be present in the innermost regions. The properties of the different populations show the dichotomy to be mainly a result of the mix of different populations. The upper [α/Fe] sequence is dominated by a spheroidal, pressure-supported component (the bulge) in the innermost 2-3 kpc, whereas it is dominated by thick disk stars beyond that distance. The lower sequence is formed by the bar in the innermost 2-3 kpc, and then by thin-disk stars not in the bar. Further out, the lower alpha-sequence is then the result of the thin disk mixture caused by radial migration from stars born at different Galactocentric distances (Friedli et al. 1994; Minchev et al. 2013, 2014). Stars born at different distances have different chemistry due to the

inside-out formation of the disc. We note however that the chemical bimodality is less clear in the high-resolution data towards Baade's window (as can be seen in Barbuy et al. (2018)). However, in a recent study by Thorsbro et al. (2020) a chemical bimodality was also detected. Accurate distances are necessary to put these findings into a more robust context. One caveat we still have to consider is that even though `StarHorse` provides a large improvement in distance and extinction estimates, it still does not take into account variations in the extinction law, which are potentially important in the bulge region. Improvements in this direction are also part of our future plans.

Finally, we also see a population of counter-rotating stars, which needs to be further investigated and confirmed. This population could be the remnant of an early accretion event, or the coalescence into the forming bulge of a clump of star formation formed by disk instabilities (Elmegreen et al. 2008; Huertas-Company et al. 2020) like those commonly observed in the discs of star-forming galaxies at redshift z ∼ 2-3. Otherwise it could simply be the tail of the large dispersion spheroid.

APOGEE plus Gaia have been transformative in our understanding of the innermost parts of the Milky Way. The picture emerging from our results is in much better agreement with high-redshift observations, which show early spheroids being formed due to massive amounts of highly dissipative gas accretion and mergers as suggested by simulations (e.g. Tacchella et al. 2015; Bournaud 2016; Renzini et al. 2018).

Acknowledgements The authors thank the referee, Prof. James Binney, for all the valuable suggestions. The authors thank R. Schiavon for helpful discussions. CC acknowledges support from DFG Grant CH1188/2-1 and from the ChETEC COST Action (CA16117), supported by COST (European Cooperation in Science and Technology). FA is grateful for funding from the European Union's Horizon 2020 research and innovation programme under the Marie Skłodowska-Curie grant agreement No. 800502 H2020-MSCA-IF-EF-2017. BB acknowledges partial financial support from FAPESP, CNPq, and CAPES - Finance Code 001. APV acknowledges the FAPESP postdoctoral fellowship no. 2017/15893-1 and the DGAPA-PAPIIT grant IG100319. DAGH acknowledges support from the State Research Agency (AEI) of the Spanish Ministry of Science, Innovation and Universities (MCIU) and the European Regional Development Fund (FEDER) under grant AYA2017-88254-P. ARA acknowledges partial support from FONDECYT through grant 3180203. J.G.F-T is supported by FONDECYT No. 3180210 and Becas Iberoamérica Investigador 2019, Banco Santander Chile. S.H. is supported by an NSF Astronomy and Astrophysics Postdoctoral Fellowship under award AST-1801940. SH is supported by an NSF Astronomy and Astrophysics Postdoctoral Fellowship under award AST-1801940. ABAQ, CC, FA, BX, BB acknowledges support from Laboratório Interinstitucional de e-Astronomia (LIneA). This work has made use of data from the European Space Agency (ESA) mission *Gaia* (http://www.cosmos.esa.int/gaia), processed by the *Gaia* Data Processing and Analysis Consortium (DPAC, http://www.cosmos.esa.int/web/gaia/dpac/consortium). Funding for the DPAC has been provided by national institutions, in particular the institutions participating in the *Gaia* Multilateral Agreement.

The `StarHorse` code is written in python 3.6 and makes use of several community-developed python packages, among them `astropy` (Astropy Collaboration et al. 2013), `ezpadova`, `numpy` and `scipy` (Virtanen et al. 2019), and `matplotlib` (Hunter 2007). The code also makes use of the photometric filter database of VOSA (Bayo et al. 2008), developed under the Spanish Virtual Observatory project supported from the Spanish MICINN through grant AyA2011-24052.

Funding for the SDSS Brazilian Participation Group has been provided by the Ministério de Ciência e Tecnologia (MCT), Fundação Carlos Chagas Filho de Amparo à Pesquisa do Estado do Rio de Janeiro (FAPERJ), Conselho Nacional de Desenvolvimento Científico e Tecnológico (CNPq), and Financiadora de Estudos e Projetos (FINEP). Funding for the Sloan Digital Sky Survey IV has been provided by the Alfred P. Sloan Foundation, the U.S. Department of Energy Office of Science, and the Participating Institutions. SDSS-IV acknowledges support and resources from the Center for High-Performance Computing at the University of Utah. The SDSS web site is www.sdss.org. SDSS-IV is managed by the Astrophysical Research Consortium for the Participating Institutions of the SDSS Collaboration including the Brazilian Participation Group, the Carnegie Institution for Science, Carnegie Mellon University, the Chilean Participation Group, the French Participation Group, Harvard-Smithsonian Center for Astrophysics, Instituto de Astrofísica de Canarias, The Johns Hopkins University, Kavli Institute for the Physics and Mathematics of the Universe (IPMU) / University of Tokyo, Lawrence Berkeley National Laboratory, Leibniz-Institut für Astrophysik Potsdam (AIP), Max-Planck-Institut für Astronomie (MPIA Heidelberg), Max-Planck-Institut für Astrophysik (MPA Garching), Max-Planck-Institut für Extraterrestrische Physik (MPE), National Astronomical Observatory of China, New Mexico State University, New York University, University of Notre Dame, Observatário Nacional / MCTI, The Ohio State University, Pennsylvania State University, Shanghai Astronomical Observatory, United Kingdom Participation Group, Universidad Nacional Autónoma de México, Univity of Arizona

3.A Probabilities of flipping the velocity

Here we decipher whether or not the errors in velocity would produce inconsistent results in our analysis, especially the case where errors can cause the measured parameter to flip its original sign. This situation could fabricate the counter-rotating bump we observe in Section 3.7.1.

To prove this is not the case in our data, we performed 1000 Monte Carlo realisations, considering the errors in the distance, the line-of-sight velocity, and the proper motions to calculate the probability of the star flipping its velocity. The parameter that most influences the error in velocities is the distance. Figure 3.B.1 shows the median velocity component against Galactocentric distance colour coded according to the probability of flipping the sign. As can be seen in the figure, this probability is higher for small velocities, in the case of V_ϕ < -50 km/s. For V_ϕ we have that 61% of the stars in the RPM sample will never change sign; from the ~ 8 000 stars, ~ 1 000 have more than 50% probability of changing direction. If we split the stars with > 50% of changing sign in positive and negative, we have 559 (~ 7%) that go from positive to negative and 458(~ 6%) that go from positive to negative. This shows that the errors in V_ϕ are symmetric and would not likely produce the extended tail in velocities $< -50 km/s$ we see in Section 3.7.1. The flipping probabilities are also symmetric in the other components of the velocity, as one can see from Figure 3.B.1.

3.B Orbits comparison

Here we show the differences in the orbital parameters if they were calculated with different pattern speeds for the bar potential. We verified that using a different pattern speed does not lead to any inconsistency in the presented results; Figure 3.B.2 shows the relative errors between eccentricity, $|Z|_{\max}$, pericentre, and apocentre for two different pattern speeds of 35 and 50. The relative errors are generally not higher than 25%. Errors are more significant for low-eccentricity stars and pericenter determination.

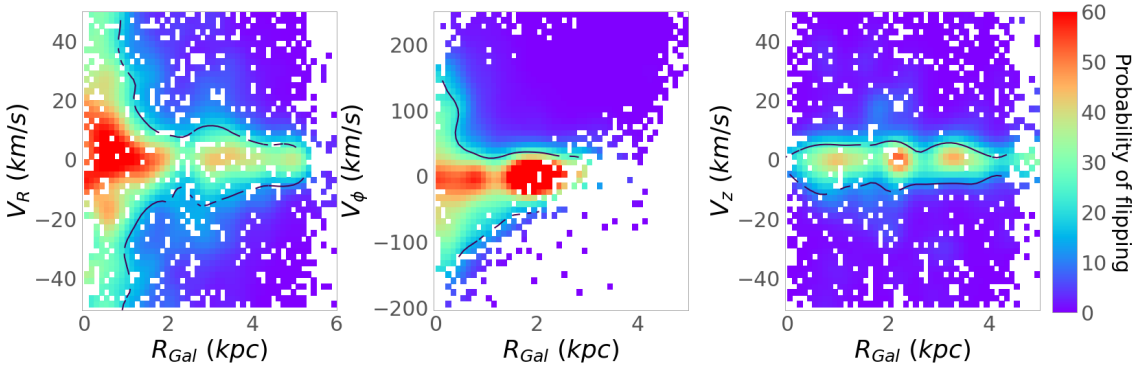

Figure 3.B.1: From left to right: Radial, azimuthal, and vertical velocities against Galactocentric radius. The diagrams are colour coded according to the probability that velocity will flip sign.

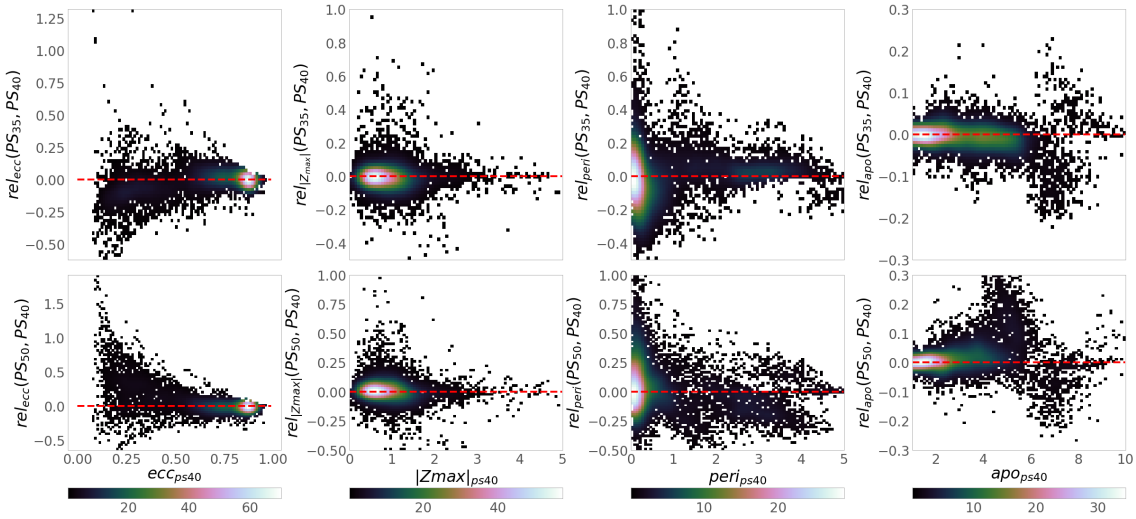

Figure 3.B.2: Comparison between orbits with the same bar potential but with varying pattern speeds. From left to right relative errors for eccentricity, $Z_{\max}$, pericentre, apocentre. The upper panels compare pattern speeds of 40 and 35; lower panels pattern speeds 40 and 50.

4 StarHorse results for spectroscopic surveys + *Gaia* DR3: Chrono-chemical structures in the solar vicinity, the genuine thick disk, and young-alpha rich stars

A. B. A. Queiroz, F. Anders, C. Chiappini, A. Khalatyan, B. X. Santiago, S. Nepal, M. Steinmetz, C. Gallart, M. Valentini, M. Dal Ponte, B. Barbuy, A. Pérez-Villegas, T. Masseron, José G. Fernández-Trincado, S. Khoperskov, I. Minchev, E. Fernández-Alvar, Richard R. Lane, C. Nitschelm

This chapter has been submitted to Astronomy & Astrophysics

Abstract

The *Gaia* mission provided an invaluable wealth of astrometric data for more than a billion stars in our Galaxy. The synergy between *Gaia* astrometry, photometry, and spectroscopic surveys give us comprehensive information about the Milky Way. Using the Bayesian isochrone-fitting code StarHorse, we derive distances and extinctions for more than 10 million unique stars observed by both *Gaia* Data Release 3 as well as public spectroscopic surveys: 557 559 in GALAH+ DR3, 4 531 028 in LAMOST DR7 LRS, 347 535 in LAMOST DR7 MRS, 562 424 in APOGEE DR17, 471 490 in RAVE DR6, 249 991 in SDSS DR12 (optical spectra from BOSS and SEGUE), 67 562 in the *Gaia*-ESO DR3 survey, and 4 211 087 in the *Gaia* RVS part of *Gaia* DR3 release. StarHorse can extend the precision of distances and extinctions measurements where *Gaia* parallaxes alone would be uncertain. We use StarHorse for the first time to derive stellar age for main-sequence turnoff and subgiant branch stars (MSTO-SGB), around 4 million stars with age uncertainties typically around 30%, 15% for only SGB stars, depending on the resolution of the survey. With the derived ages in hand, we investigate the chemical-age relations. In particular, the α and neutron-capture element ratios versus age in the solar neighbourhood show trends similar to previous works, validating our ages. We use the chemical abundances from local subgiant samples of GALAH DR3, APOGEE DR17 and LAMOST MRS DR7 to map groups with similar chemical compositions and StarHorse ages with the dimensionality reduction technique t-SNE and the clustering algorithm HDBSCAN. We identify three distinct groups in all three samples. Their kinematic properties confirm them to be the genuine chemical thick disk, the thin disk and a considerable amount of young alpha-rich stars (427), which are also a part of the delivered catalogues. We confirm that the genuine thick disk's kinematics and age properties are radically different from those of the thin disk and compatible with high-redshift (z≈2) star-forming disks with high dispersion velocities. We also find a few extra substructures in the GALAH DR3, thanks to the availability of neutron-capture elements.

4.1 Introduction

The European Space Agency satellite *Gaia* mission (Gaia Collaboration et al. 2016) is continuing to revolutionize and transform Galactic astrophysics in many areas (Brown 2021). The latest release from the *Gaia*-mission, (*Gaia* DR3; Gaia Collaboration et al. 2022) is built upon the Early Data Release 3 (EDR3 Gaia Collaboration et al. 2021) which includes 36 months of observations, with positions and photometry for $1.7 \cdot 10^9$ sources, and full astrometric solutions, (Lindegren et al. 2021b), for $1.3 \cdot 10^9$ objects. *Gaia* DR3 extends EDR3 by delivering multiple data products, for example, low-resolution BP/RP spectra and astrophysical parameters for about 400 million sources (Andrae et al. 2022) and about 5 million sources with medium resolution spectra observed with the Radial Velocity Spectrometer (RVS) instrument (Recio-Blanco et al. 2022).

Combining astrometric solutions from *Gaia* with large-scale spectroscopic surveys is fundamental for Galactic archaeology because it enables us to access the full phase space and the chemical composition of millions of stars. Such rich information gives us essential clues to the formation and evolution history of the Milky Way (Freeman & Bland-Hawthorn 2002; Matteucci 2001, 2021; Pagel 2009), disentangling the multiple overlapping processes that once took place in our Galaxy, such as mergers, secular evolution and gas accretion flows.

The synergy between astrometry and spectroscopy resulted in many important discoveries in the different components of our Galaxy. As proof of that, we have the characterization of the halo and the discovery of several accreted dwarf galaxies (e.g. Koppelman et al. 2018; Mackereth et al. 2019; Myeong et al. 2019; Limberg et al. 2021; Fernández-Trincado et al. 2020b,a, 2022; Horta et al. 2021; Ruiz-Lara et al. 2022) and the massive *Gaia*-Enceladus merger event (Haywood et al. 2018b; Helmi et al. 2018; Belokurov et al. 2018). These structures substantially influence the formation of the thick disk and halo (for a review, see Belokurov et al. 2018; Di Matteo et al. 2019; Helmi 2020). The chemical duality of the Galactic disk, which was primarily evident in [α/Fe] vs. [Fe/H] in the solar neighbourhood, was shown by several authors to designate the thin and thick disks (Adibekyan et al. 2011; Bensby et al. 2014; Anders et al. 2014; Hayden et al. 2015). Further, Rojas-Arriagada et al. (2019); Queiroz et al. (2020) show that the same chemical bimodality extends to the inner Galaxy, indicating populations with different formation paths. Finally, the characterization of the Galactic bulge and bar (Lian et al. 2020; Rojas-Arriagada et al. 2020; Queiroz et al. 2021) into its chemo-orbital space reveals a diversity of populations coexisting in the inner Galaxy. Recently works that studied the inner Galaxy's metal-poor counterpart show evidence of a pressure-supported component which follows a more spherical distribution than the disk and little to no rotation (Kunder et al. 2020; Queiroz et al. 2021; Arentsen et al. 2020; Lucey et al. 2021; Rix et al. 2022).

To achieve all the aforementioned scientific results is essential to calculate precise distances from the astrometric solutions provided by *Gaia*. As shown by Bailer-Jones (2015) it is a limited and dangerous approach to determine distances by inverting the parallax, especially for high astrometric uncertainties and large volumes of the Galaxy. In Queiroz et al. (2018, hereafter Q18), we first presented the StarHorse code: a Bayesian isochrone fitting tool that makes versatile use of spectroscopic, photometric, and astrometric data to determine distances, extinctions, and stellar parameters of field stars. The method was then extensively validated using simulations and external catalogues of asteroseismology, open clusters and binaries. Therefore, in Queiroz et al. (2020, hereafter Q20) many efforts were put together to provide catalogues generated from StarHorse using *Gaia* DR2 data with APOGEE DR16 and other spectroscopic surveys, resulting in an important leap in stellar parameter precision.

In this paper, we provide updated StarHorse stellar parameters, distances, and extinctions for major spectroscopic surveys (see Table 4.2.1) combined with the *Gaia* DR3 data. The StarHorse results for APOGEE DR17 (Abdurro'uf et al. 2022) are already published in the form of a value-added catalogue jointly with SDSS DR17, except for the ages, which are published here for the first time. The paper focuses on science enabled by sub-samples for which StarHorse delivers reasonable age estimates thanks to the exquisite quality of the *Gaia* parallaxes. However, the results are limited to a local volume bubble of d< 2kpc since ages derived by isochronal matching can only be reliable for the main sequence turn-off (MSTO), and subgiant branch (SGB) regimes, the degeneracies between neighbouring isochrones in the Hertzsprung-Rusell diagram are much smaller for these cases.

In this work we take advantage of the rich chemical information delivered by spectroscopic surveys combined with StarHorse ages to explore the detection of (known and new) chrono-chemical sub groups more in the line of classical "chemical tagging"; see, e.g.

Table 4.2.1: Summary of the datasets for which we deliver StarHorse parameters in this work. Upper rows show the main numbers of input catalog sources, those that survived the quality cuts, those for which the code converged to a solution, and the number of MSTO and subgiants selected on the output. The lower rows show the model configuration and parallax coverage for the final input catalogues.

Survey	$N^{\text{cat}}_{\text{objects}}$	$N^{\text{Quality cuts}}_{\text{objects}}$	$N^{\text{Converged}}_{\text{stars}}$	N^{MSTO}_{stars}	$N^{\text{subgiants}}_{\text{stars}}$
LAMOST DR7 LRS	6 179 327	4 803 496	4 531 028	2 278 480	241 319
LAMOST DR7 MRS	738 025	457 359	425 281	224 876	29 215
SDSS DR12 (optical)	503 967	258 194	249 991	96 615	13 584
GALAH+ DR3	588 571	581 149	557 559	290 475	47 594
RAVE DR6	517 095	515 800	471 490	157 251	30 220
APOGEE DR17	733 901	720 970	562 424	100 956	18 966
GES DR5	114 324	75 008	67 562	24 620	4 539
Gaia DR3 RVS	5 594 205	4 833 548	4 211 087	1 405 199	258 131

Survey	Model Resolution	bestfilter	parallaxes
LAMOST DR7 LRS	age_{step} = 0.1 ; met_{step} = 0.05	Ks_{2MASS}	99%
LAMOST DR7 MRS	age_{step} = 0.05 ; met_{step} = 0.02	Ks_{2MASS}	77%
SDSS DR12 (optical)	age_{step} = 0.1 ; met_{step} = 0.05	parallax	100%
GALAH+DR3	age_{step} = 0.05 ; met_{step} = 0.02	Ks_{2MASS}	98%
RAVE DR6	age_{step} = 0.1 ; met_{step} = 0.05	Ks_{2MASS}	86%
APOGEE DR17	age_{step} = 0.05 ; met_{step} = 0.02	H_{2MASS}	75%
GES DR5	age_{step} = 0.05 ; met_{step} = 0.02	H_{2MASS}	97%
Gaia DR3 RVS	age_{step} = 0.1 ; met_{step} = 0.05	G_{Gaia}	100%

Freeman & Bland-Hawthorn 2002; Anders et al. 2018; Buder et al. 2022. To this aim, we use three different survey samples to map groups with similar chemical compositions.

This paper is outlined as follows. In section 4.2, we summarize the Bayesian technique StarHorse, the references for its newest implementations and main configuration. In section 4.3, we describe all datasets we used as input to the StarHorse code, astrometric, photometric and spectroscopic data. In section 4.4, we discuss the main parameters derived with our method, the new released StarHorse catalogues, which contain more than 10 million stars and 4 million nearby stars with ages, and a few validations of the parameters. In section 4.5, we show relations between the derived ages and some chemical relations. In section 4.6, we show our results using the chemo-age multi-dimension in the t-sne and HDBSCAN technique. Finally in section 4.7, we present our new conclusions and summarize our main results. All the catalogues used in this work are made public in the Leibniz Instititute für Astrophysik (AIP) database[18].

4.2 Method

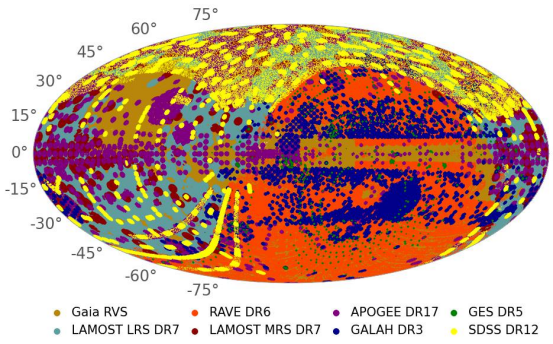

Figure 4.2.1: Sky distribution of all public spectroscopic surveys for which we derive StarHorse parameters

18 data.aip.de

Isochrone fitting has been extensively used in astronomy to indirectly derive unknown stellar parameters by using known measured stellar properties (e.g. Pont & Eyer 2004; Jørgensen & Lindegren 2005; da Silva et al. 2006; Naylor & Jeffries 2006). A diversity of methods can be applied to the fitting procedure, (e.g. Burnett & Binney 2010; Rodrigues et al. 2014; Santiago et al. 2016; Mints & Hekker 2018; Das & Sanders 2019; Lebreton & Reese 2020; Souza et al. 2020). Here we use StarHorse (S16; Q18; Q20, Anders et al. 2019, 2022), a Bayesian isochrone-fitting code that has been optimised for heterogeneous input data (including spectroscopy, photometry, and astrometry). Its results are limited only by observational errors and the accuracy of the adopted stellar evolution models.

StarHorse is able to derive distances d, extinctions A_V (at λ = 542 nm), ages τ, masses m_*, effective temperatures $T_{\rm eff}$, metallicities [M/H], and surface gravities $\log g$. The resulting parameter's uncertainties are directly linked with the set of observables used as input. A complete set of observables comprises multi-band photometry (from blue to mid-infrared wavelengths), parallax, $\log g$, $T_{\rm eff}$, $[M/H]$, and an extinction prior A_v. In this work we use all this information by combining data from public spectroscopic surveys with photometric surveys and *Gaia* parallaxes. We then execute the Bayesian technique to quantitatively match the observable set with stellar evolutionary models from the PAdova and TRiestre Stellar Evolution Code (PARSEC Bressan et al. 2012), ranging from 0.025 to 13.73 Gyr in age and −2.2 to +0.6 in metallicity.

Since Q20, StarHorse has seen several upgrades that are explained in Section 3 of Anders et al. (2022). These upgrades include the implementation of extragalactic and globular cluster priors, a change in the bar-angle prior (to the canonical value of 27 degrees; e.g. Bland-Hawthorn & Gerhard 2016), a new 3D extinction prior, and updated evolutionary models that include difusion (especially important during the evolutionary phases close to the MSTO). Finally, the new catalogues presented here also take advantage of the more precise and additional data products of *Gaia* DR3.

4.3 Input data

The large set of available spectroscopic surveys gives us detailed information about individual stars, such as chemical abundances, atmospheric parameters and radial velocities. By combining this information with photometry and astrometry, we can constrain models by a small range of limits and effectively derive the best fitting StarHorse parameters with low uncertainties.

We follow a very similar approach to previous StarHorse papers (Q18; Q20). In Table 4.2.1, we summarize the input numbers of stars for each spectroscopic survey, the stars remaining after applying a few quality cuts, the resulting number of converged stars, and the following amount of MSTO and SBG stars with available StarHorse ages. The quality cuts applied before executing StarHorse vary from survey to survey, and a more detailed explanation is given in the following sub-sections. As regard to model grid resolution and the photometric passband that we used as the "master filter" are also described in the lower rows of Table 4.2.1. The $\rm age_{step}$ and $\rm met_{step}$ represent the spacing between age and metallicity in the models we use in the StarHore method; for higher resolution surveys, we use a thinner model grid. The "master filter" is the primary choice from which we draw the possible distance values. For more information, see section 3.2.1 of Q18.

In Figure 4.2.1 we show the sky distribution for all public spectroscopic surveys for which derive StarHorse parameters, the area coverage of the surveys is very complementary and focous on the different components of our Galaxy. Below, we summarize the configurations and calibrations done to all input data, the spectroscopic surveys and the photometric and astrometric catalogues used in this work.

4.3.1 Astrometric and photometric input

Gaia is an astrometric and photometric space mission from ESA launched in 2013 and which since then has delivered parallaxes and proper motions for more than 1 billion sources. Its early third release EDR3 (Gaia Collaboration et al. 2021) has astrometric solutions with uncertainties twice as better than its previous DR2 release. All resulting catalogues given in this paper were produced by combining the spectroscopic surveys with parallaxes from *Gaia* EDR3, which is an important new ingredient for the resulting `StarHorse` distances. We use the parallax corrections advertised by Lindegren et al. (2021b), and the most conservative parallax uncertainty inflation factor derived in the analysis of Fabricius et al. (2021), see their from Figure 19. Besides these corrections, we crossmatched our catalogues with the *fidelity_v1* column from Rybizki et al. (2022), which provides a scalar indicator for astrometric quality. For fidelities < 0.5, we do not use any parallax information. In the last column of the lower rows of Table 4.2.1 we show the coverage percentage of available parallaxes for the input catalogues that pass this condition.

As photometric input we use infra-red photometry from 2MASS *JHKs* (Cutri et al. 2003) and unWISE $W1W2$ (Schlafly et al. 2019), optical data from PanSTARRS-1 *grizy* (Scolnic et al. 2015), and SkyMapper DR2 *griz* (Onken et al. 2019), adopting generous minimum photometric uncertainties (between 0.03 and 0.08 mag). Magnitude shifts were applied to PanSTARRS-1 as in Q20 using the values from (Scolnic et al. 2015) and shift corrections were also applied to SkyMapper passbands according to Huang et al. (2021).

4.3.2 Spectroscopic catalogues

We compute posterior ages, masses, temperatures, surface gravities, distances, and extinctions for eight spectroscopic stellar surveys. All datasets were preprocessed to check for missing values or inconsistencies in the spectroscopic catalogues, crossmatched with *Gaia* EDR3 (epoch J2000.0, search radius 1.5 arcsec), with the photometric surveys described in the previous section, as well as with the *Gaia* EDR3 *fidelity_v1* column from Rybizki et al. (2022). For all catalogues we use the Salaris et al. (1993) transformation between [Fe/H] and [M/H] for stars with valid [α/Fe] values. For those without a reported [α/Fe] ratio, we assumed [M/H]≃[Fe/H]. The data curation applied for each survey is explained in the following subsections and the resulting numbers of stars are given in Table 4.2.1. We want to clarify that from each survey's uncertainty distribution, we usually remove a small fraction with substantial input observable uncertainties compared to the full distribution. We do so because it is computationally very costly to calculate the likelihood for many models inside an extensive uncertainty range. The threshold of acceptable uncertainties to `StarHorse` changes with the choice of the model grid - high-resolution surveys typically have minor uncertainties, requiring a denser model grid.

APOGEE DR17

DR17 Abdurro'uf et al. (2022) is the final data release of the fourth phase of the Sloan Digital Sky Survey (SDSS IV Blanton et al. 2017). It contains the complete catalogue of the Apache Point Observatory Galactic Evolution Experiment (APOGEE; Majewski et al. 2017) survey, which in December 2021 publicly released near infra-red spectra of over 650,000 stars. The APOGEE survey has been collecting data in the northern hemisphere since 2011 and south hemisphere since 2015. Both hemispheres observations use the twin NIR spectrographs with high resolution (R≈22 500) (Wilson et al. 2019) on the SDSS 2.5-m telescope at Apache Point Observatory (Gunn et al. 2006) and the 2.5-m du Pont telescope at Las Campanas Observatory (LCO Bowen & Vaughan 1973). The data reduction pipeline is described in (Nidever et al. 2015). The processed products of APOGEE DR17 are similar to the previous releases (Abolfathi et al. 2018; Holtzman et al. 2018; Jönsson et al. 2020). We use the temperature, surface gravity and

metallicity results from the ASPCAP pipeline (García Pérez et al. 2016; Jönsson et al. 2020) to produce a new StarHorse catalogue as in Q20. We use primarly the calibrated parameters indicated in the pipeline, when those are not available we use spectroscopic parameters. For DR17 new synthetic spectral grids were added in ASPCAP, which also account for non-local thermodynamic equilibrium in some elements. This led to the adoption of a different spectral synthesis code Synspec (Hubeny & Lanz 2017). Parameters reduction is also available with the previous spectral systhesis code TurboSpec (Alvarez & Plez 1998) but in StarHorse we only used the given parameters from Synspec. In the appendix 4.B we show some differences between the derived abundances in Synspec and Turbospec, which are discussed later in the analysis.

As an input to StarHorse, we selected only stars with available H_{2MASS} passband and spectral parameters (FPARAM[0,1,3])[19], which reduces the total number of objects in the initial catalogue from 733 901 to 720 970. We then run StarHorse with a spacely fine model grid (see lower rows of Table 4.2.1). 22% of the input did not converge to a solution, meaning that these stars were not compatible with any stellar evolutionary model in our grid. The results for StarHorse using the data from APOGEE DR17 are also published in form of a value-added catalogue (VAC) in Abdurro'uf et al. (2022).

GALAH DR3

The Galactic Archaeology with HERMES survey (GALAH, De Silva et al. 2015; Martell et al. 2017) is a high resolution spectroscopic survey that covers mostly a local volume, $d <\approx 2kpc$. Their latest data release, GALAH DR3, was published in November 2020. GALAH data are acquired with the High Efficiency and Resolution Multi-Element Spectrograph (HERMES), where the light is dispersed at $R \approx 28\,000$, coupled to the 3.9-metre Anglo-Australian Telescope (AAT). HERMES observes in four different wavelengths simultaneously: Blue: 471.5 - 490.0 nm; Green: 564.9 - 587.3 nm; Red: 647.8 - 673.7 nm; IR: 758.5 - 788.7 nm. We use the recommended catalogue, which contains radial velocities, atmospheric parameters and abundances for a total of 588,571 stars (Buder et al. 2021). The stellar parameters are derived using the spectrum synthesis code Spectroscopy Made Easy (SME) and 1D marcs model atmospheres (Piskunov & Valenti 2017). GALAH makes available abundances for around 30 different elements, which cover five different nucleosynthetic pathways (α-process elements mostly formed by core-collapse supernovae, iron-peak elements formed mainly in type-Ia supernovae, s-process elements formed in the late life stage of low mass stars, r-process elements formed by the merging of neutron stars, as well as lithium (created by the Big Bang and both created and destroyed in stars; Kobayashi et al. 2020). To derive StarHorse parameters, we selected only stars with mutually available $T_{\rm eff}$, $\log g$ and K_{2mass} passband as input. The coverage of high quality *Gaia* parallaxes for this sample is very high since most stars are nearby. Therefore, the resulting distances have very low uncertainties, as seen in Figure 4.3.1. For GALAH, we run StarHorse with a fine model grid, given the high resolution of the survey, and only 5% of the input catalogue did not converge.

LAMOST DR7

The Large Sky Area Multi-Object Fiber Spectroscopic Telescope (LAMOST, Cui et al. 2012; Zhao et al. 2012) is a spectroscopic survey covering a large area of the northern hemisphere, including stars and galaxies. LAMOST stellar parameter catalogues can be divided into LAMOST low-resolution (LRS) and medium-resolution (MRS). LAMOST, DR7, has been publicly available since March 2020 and includes the spectra obtained from the pilot survey through the seventh-year regular survey. We downloaded the stellar parameter catalogues both for LRS (6 179 327) and MRS (738 025)[20]. A new LAM-

19 Output parameter array from ASPCAP stellar parameters fit, where 0, 1, 3 correspond to $T_{\rm eff}$, logg and [M/H]
20 http://dr7.lamost.org/catalogue

OST data release, DR8, is available since September 2022 and contains circa 500 thousand new observations in LRS and more 500 thousand in MRS. We will also make StarHorse parameters publicly available for this data release in the near future, but LAMOST DR8 is not part of the analysis in this paper.

Both MRS and LRS stellar parameter catalogues provide atmospheric parameters, metallicity, and projected rotation velocity estimated by the LAMOST Stellar Parameter pipeline (LASP Wu et al. 2014), as well as an estimate of alpha abundances by the method of template matching based on the MARCS synthetic spectra (Decin et al. 2004). For LAMOST MRS, coadd and single exposure spectra have a resolution of $R \approx 7\,500$. The label-transfer method gives twelve individual element abundances based on a convolutional neural network (CNN). For MRS stellar parameter catalogue we selected all-stars with mutually available $\log g$, $T_{\rm eff}$, and 2MASS K_s photometry, and made the following cuts in uncertainty: $\sigma_{T_{\rm eff}} < 300K$; $\sigma_{\log g} < 0.5K$; $\sigma_{[Fe/H]} < 0.3K$. This leaves us with 457 359 stars as StarHorse input. As we did for the high-resolution surveys, we ran LAMOST MRS with the fine model grid, which leads to a convergence rate of 93%. The LAMOST LRS parameter catalogue, the largest dataset in this work, consists of A, F, G and K type stars. We selected stars with available $\log g$, T_eff, 2MASS Ks passband and made the following cuts in uncertainty: $\sigma_{T_{\rm eff}} < 500K$; $\sigma_{\log g} < 0.8K$; $\sigma_{[Fe/H]} < 0.5K$, resulting in 4 803 496 stars as input. Using a coarsely spaced grid of models for LAMOST LRS, StarHorse was able to deliver results for 80% of this input catalogue.

SDSS DR12/SEGUE

The Sloan Extension for Galactic Understanding and Exploration (SEGUE Yanny et al. 2009) is a spectroscopic survey that was conducted with the Sloan Foundation 2.5m Telescope (Gunn et al. 2006) using the two original low-resolution SDSS fiber spectrographs ($R \approx 2\,000$, Smee et al. 2013). The surveys targeted mostly metal-poor halo and disk stars. The stellar parameters from optical stellar spectra collected with SDSS/SEGUE were processed through the SEGUE Stellar Parameter Pipeline (SSPP), which reports three primary stellar parameters, $T_{\rm eff}$, $\log g$, and metallicity. Most stars have $T_{\rm eff}$ in the range between 4 000 and 10 000 K and spectral signal-to-noise ratios greater than 10 (Lee et al. 2008; Allende-Prieto et al. 2008). In the final data release (SDSS DR12; Alam et al. 2015), the pipeline also provided [α/Fe] abundance ratios (Lee et al. 2011). From this catalogue we use the recommended adopted values for $T_{\rm eff}$, $\log g$ and [Fe/H], selecting only stars with signal-to-noise ratios greater than 20 and that have all of these parameters available.

GES DR5

The *Gaia*-ESO survey (Gilmore 2012) targets $> 10^5$ stars in all major components of the Milky Way and open clusters of all ages and masses. The survey conducted its observations with the Fibre Large Array Multi Element Spectrograph (FLAMES; Pasquini et al. 2002), which feeds two different instruments covering the whole visual spectral range. The fifth and final data release of GES was made public in May 2022 (Randich et al. 2022). It has significantly increased the number of observed stars, 114 324, about four times the size of the previous public release, and it also increased the number of derived abundances and cluster parameters. Several working groups focussing on different types of stars and evolutionary stages analysed the GES spectra (Heiter et al. 2021). We downloaded the full catalogue[21], and used the recommended homogenised atmospheric parameters as StarHorse input. We only use entries with errors smaller than 300 K in temperature, 0.5 dex in surface gravity, and 0.6 dex in iron abundance. To correct the metallicities for the solar scale using the Salaris et al. (1993) formula, we have calculated a global [α/Fe] estimate based on the abundances of Si, Ca, and Mg, available for about 58% of the stars in the catalogue.

21 https://www.gaia-eso.eu/data-products/public-data-releases/gaia-eso-data-release-dr50

Compared to the previous StarHorse run on GES data, this is an important update because there are many more stars, and we do not exclude the open clusters from our analysis any longer.

RAVE DR6

The final data release of the RAdial Velocity Experiment (RAVE; Steinmetz et al. 2006) survey, DR6 (Steinmetz et al. 2020a) became public in 2020. The spectra from RAVE is acquired with the multi-object spectrograph deployed on 1.2-m UK Schmidt Telescope of the Australian Astronomical Observatory (AAO). The spectra have a medium resolution of R $\approx$ 7500 and cover the CaII-triplet region (8410-8795). We use the final RAVE data release and in particular, the purely spectroscopically derived stellar atmospheric parameters subscripted cal_madera. In Q20 we explain the processing of this final RAVE data release in detail and we follow the same procedure for pre-processing this catalogue. The only difference is that this catalogue is now cross-matched with *Gaia* EDR3 instead of DR2.

Gaia DR3 RVS

Besides its photometric and astrometric instruments, *Gaia* also features a spectroscopic facility, the Radial Velocity Spectrometer (RVS). The instrument observes in the near-infrared (845-872 nm) and has a resolution of $\lambda/\Delta\lambda \approx$11 500 (Cropper et al. 2018). The third data release of *Gaia* contains data of the first 36 months of RVS observations, obtained with the General Stellar Parametriser from the Spectroscopy (GSP-Spec; Recio-Blanco et al. 2022) module of the Astrophysical parameters inference system (Apsis; Creevey et al. 2022). There are two analysis workflows to process these data: the MatisseGauguin pipeline, and an artificial neural network (Recio-Blanco et al. 2016). We work here only with the data analysed by MatisseGauguin, which provides the stellar atmospheric parameters and individual chemical abundances of N, Mg, Si, S, Ca, Ti, Cr, Fe I, Fe II, Ni, Zr, Ce, and Nd for about 5.6 million stars (Recio-Blanco et al. 2022). We downloaded the data from the *Gaia* archive's DR3 table of astrophysical parameters. Following a similar procedure to the other spectroscopic surveys, we combine the data with zeropoint-corrected parallaxes from *Gaia* EDR3, and with broad-band photometric data. We do not apply any quality flag cuts when running StarHorse, but we only select stars with acceptably small nominal uncertainties ($\sigma_{T_{\rm eff}} < 700$ K, $\sigma_{\log g} < 1.0$ dex, $\sigma_{\rm [Fe\_H]} < 0.6$ dex). We also removed stars with [Fe_H]<-3, since those fall outside the metallicity range covered by the PARSEC stellar model grid used. Regarding parameter calibrations, we applied the suggestions for the calibration of $\log g$, [M/H] and [α/Fe] detailed in Recio-Blanco et al. (2022).

4.4 New StarHorse catalogues

We present a new catalogue set derived from the stellar spectroscopic surveys described in Section 4.3.2 combined with photometry and *Gaia* EDR3 parallaxes (Section 4.3.1). We provide percentiles of the posterior distribution functions of masses, effective temperatures, surface gravities, metallicities, distances, and extinctions for each successful converged source according to Table 4.2.1. We deliver the final data in the same format as in Q20 Table A.1 for each spectroscopic survey used as input. The median value, 50th percentile, should be taken as the best estimate for that given quantity, and the uncertainty can be determined using the 84th and 16th percentiles. In this release, we also make for the first time age determinations for a selection of main-sequence turn-off and sub-giant branch (MSTO+SGB) stars. The given ages follow the same format as the other StarHorse parameters, but we flag everything outside our MSTO+SGB selection as -999. All the newly produced StarHorse catalogues are available for download from data.aip.de and through VizieR. Some of the results of StarHorse for APOGEE, GALAH and SDSS12 have already been analysed by recent publications on the study of halo debris (Limberg et al. 2021; Perottoni et al. 2022; Limberg et al. 2022a).

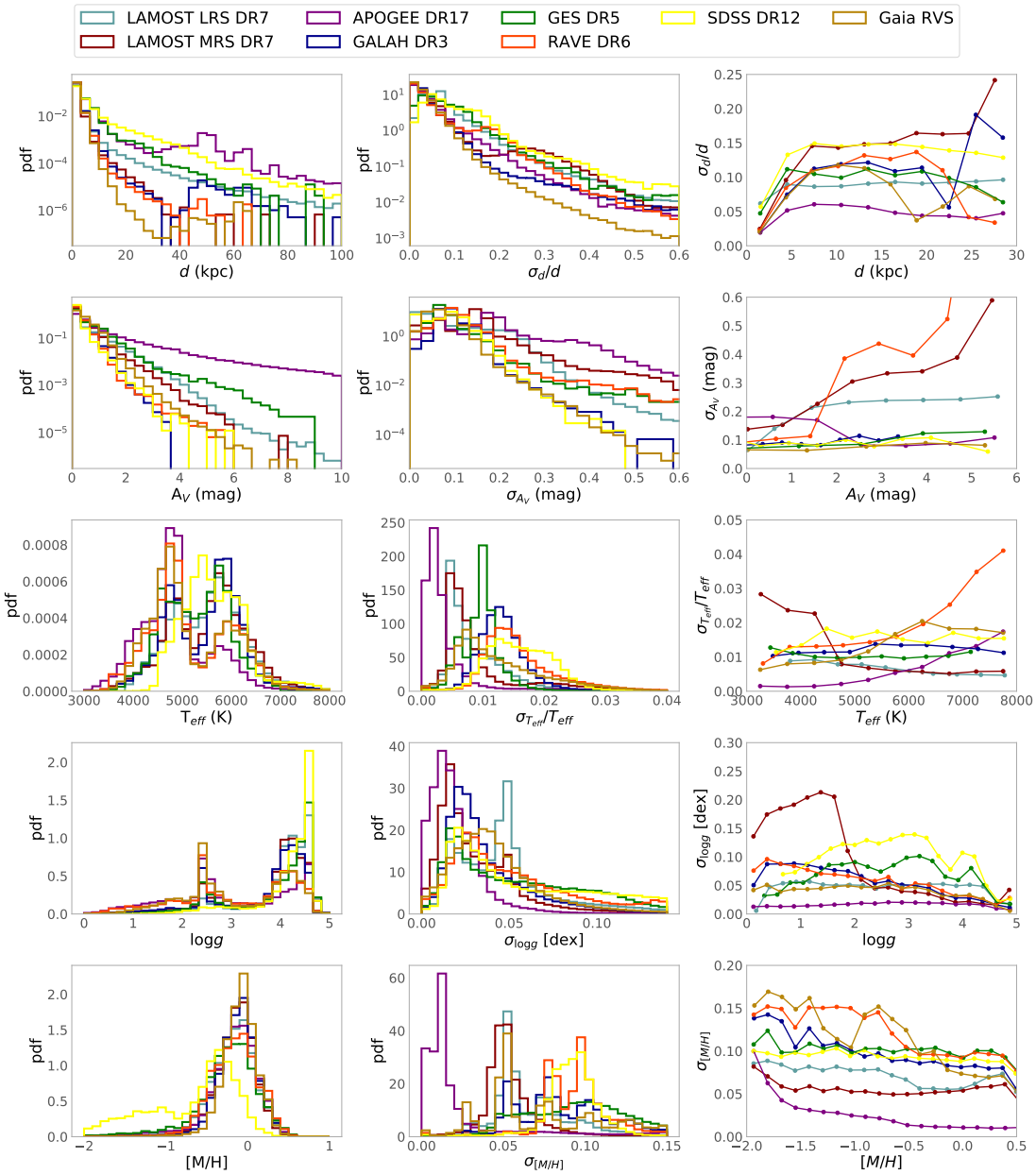

Figure 4.3.1: Left and middle panels: probability density functions of StarHorse output parameters and their respective uncertainties. The distributions are shown for each spectroscopic survey separately, as indicated in the legend. The upper panels for distance and extinction have their y-axis in logarithm scale to show the extent to larger values. Right panels show the median trend of the dependence of each parameter with it's associated uncertainty.

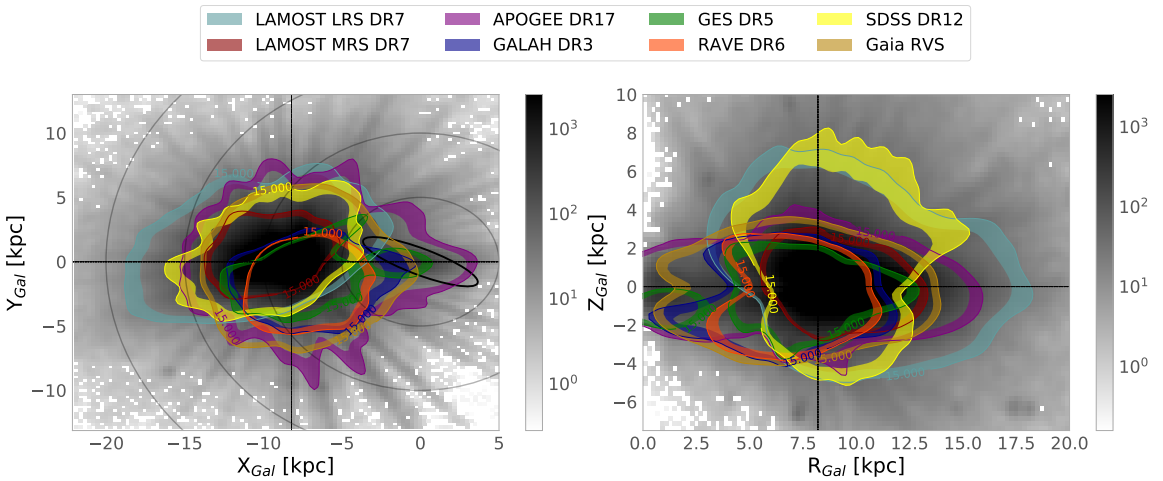

Figure 4.4.1: Galactic distribution of all spectroscopic surveys for which we present StarHorse results in this paper. The gray background density shows the star counts for all surveys combined, while the coloured bands trace the region between iso-contours of 25 000 and 15 000 stars per pixel for each survey. To guide the eye, gray circles are placed in multiples of 5 kpc around the Galactic centre in the left panel. The approximate location and extent of the Galactic bar is indicated by the black ellipse (minor axis = 2kpc; major axis = 8kpc, inclination = 25°), and the solar position is marked by the dashed lines. Left panel: Cartesian XY projection. Right panel: Cylindrical RZ projection.

Table 4.4.1: Mean relative error or uncertainty per StarHorse output parameter per spectroscopic survey

Survey	σ_d/d (%)	σ_{A_V} (mag)	$\sigma_{T_{\rm eff}}/T_{\rm eff}$ (%)	$\sigma_{\rm [M/H]}$ (dex)	$\sigma_{\log g}$ (dex)	σ_{m_*}/m_* (%)	$\sigma_{age}/age_{MSTO+SGB}$ (%)	σ_{age}/age_{SGB} (%)
LAMOST DR7 LRS	7.5	0.082	0.8	0.067	0.053	9.6	19.9	16.3
LAMOST DR7 MRS	4.9	0.129	0.9	0.072	0.042	11.2	18.3	9.4
SDSS DR12 optical	10	0.075	1.6	0.093	0.080	8.0	21.8	12.0
GALAH+ DR3	3.6	0.092	1.3	0.092	0.041	12.1	28.2	12.8
RAVE DR6	5.1	0.099	1.6	0.099	0.058	8.0	34.8	18.5
APOGEE DR17	4.3	0.178	0.4	0.029	0.021	12.6	28.9	8.3
GES DR5	5.8	0.099	1.2	0.076	0.053	11.2	25.7	13.5
Gaia DR3 RVS	3.1	0.069	1.3	0.172	0.044	17.3	51.4	21.7

4.4.1 StarHorse distances and extinctions

Precise distances and extinctions are fundamental for Galactic archaeology (Helmi 2020). By combining spectroscopic and *Gaia* data, StarHorse achieves precise distances from the inner to the outer Galaxy. As seen in the left panels of Figure 4.3.1 we get relative errors in the distance of only 15% for distances as far as 20 kpc, and a mean extinction uncertainty of about 0.2 (mag). Distances and extinctions have also been extensively validated with simulations and external methods in Q18 and Q20, showing internal precision in the distance and extinctions of about 8% and 0.04 mag, respectively. In Figure 4.4.1 we show the distribution of stars for all surveys for which we compute distances in Galactocentric Cartesian coordinates. This map expresses the extent and capability of the resulting data, which samples very well the solar vicinity, reaches the inner parts of the Galaxy, covers the outer disk beyond $R_{\rm Gal} = 20$ kpc and extends to $|Z_{\rm Gal}| > 10$ kpc. We display the distribution of parameters and their uncertainties in Figure 4.3.1, and we show the mean uncertainty in each parameter for each survey in Table 4.4.1. The mean relative distance uncertainty for all surveys lies below 10%, while for GALAH, APOGEE, LAMOST MRS and Gaia

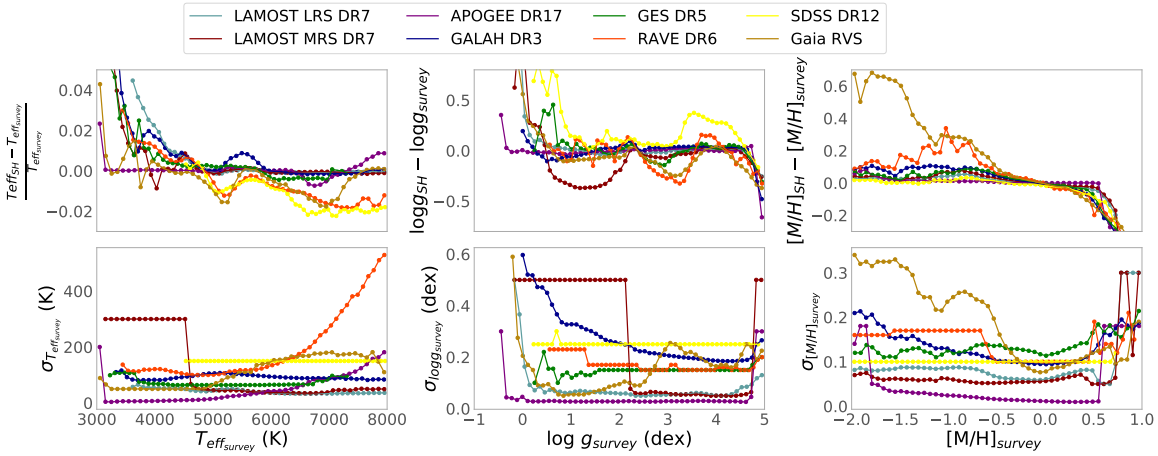

Figure 4.4.2: Consistency of StarHorse input and output parameters. Top panels: Median of the relative discrepancy between input parameters and StarHorse output parameters for each survey. Bottom panels: Median of the dependency between input uncertainties versus input parameters.

DR3 RVS, it is below 5%. It is noticeable from Figure 4.3.1 that with the new prior implementation (Anders et al. 2022), some survey distances extend to other galaxies, e.g. APOGEE reaches the Magellanic Clouds, the Sagittarius dwarf galaxy, and some globular clusters. A_V varies primarily according to each survey's selection function, and its uncertainty is strongly correlated with photometry, but on average below 0.2 mag. For the most precise determinations of A_V, one can select the stars with the complete photometry input set (detailed in the StarHorse input flags).

4.4.2 StarHorse $T_{\rm eff}$, log g and metallicity

Surface temperatures and gravities are also present in the output from the StarHorse catalogues. The code uses these parameters as input from the spectroscopic surveys. Therefore these are just slight improvements to the measurements, but this is especially useful for the atmospherical parameters that were not initially calibrated by surveys or have significant uncertainties and caveats. In Figure 4.4.2 we show a comparison between the atmospheric input parameters and the output StarHorse parameters for each spectroscopic survey, as well as their input uncertainties. The differences between the high-resolution surveys are minor since their uncertainties are well constrained. Most surveys show differences in effective temperature between cold stars and hot stars, respectively with $T_{\rm eff} < 4000$ K and $T_{\rm eff} > 7000$ K. SDSS DR12 and RAVE show the most significant deviation in input temperature for hot stars, which are usually overestimated with respect to the models by 5%. The surface gravity is the most deviating parameter. There are considerable differences between input and output for the whole log g range; LAMOST MRS has 0.5 dex overestimation against StarHorse output for giant stars, while SDSS shows the same amplitude but underestimation of logg for dwarf stars. The metallicities have excellent agreement with input differing only by 0.1 dex for most surveys except for RAVE DR6 which shows a difference up to 0.3 dex compared with StarHorse metallicities, but they also present one of the largest uncertainties in metallicities.

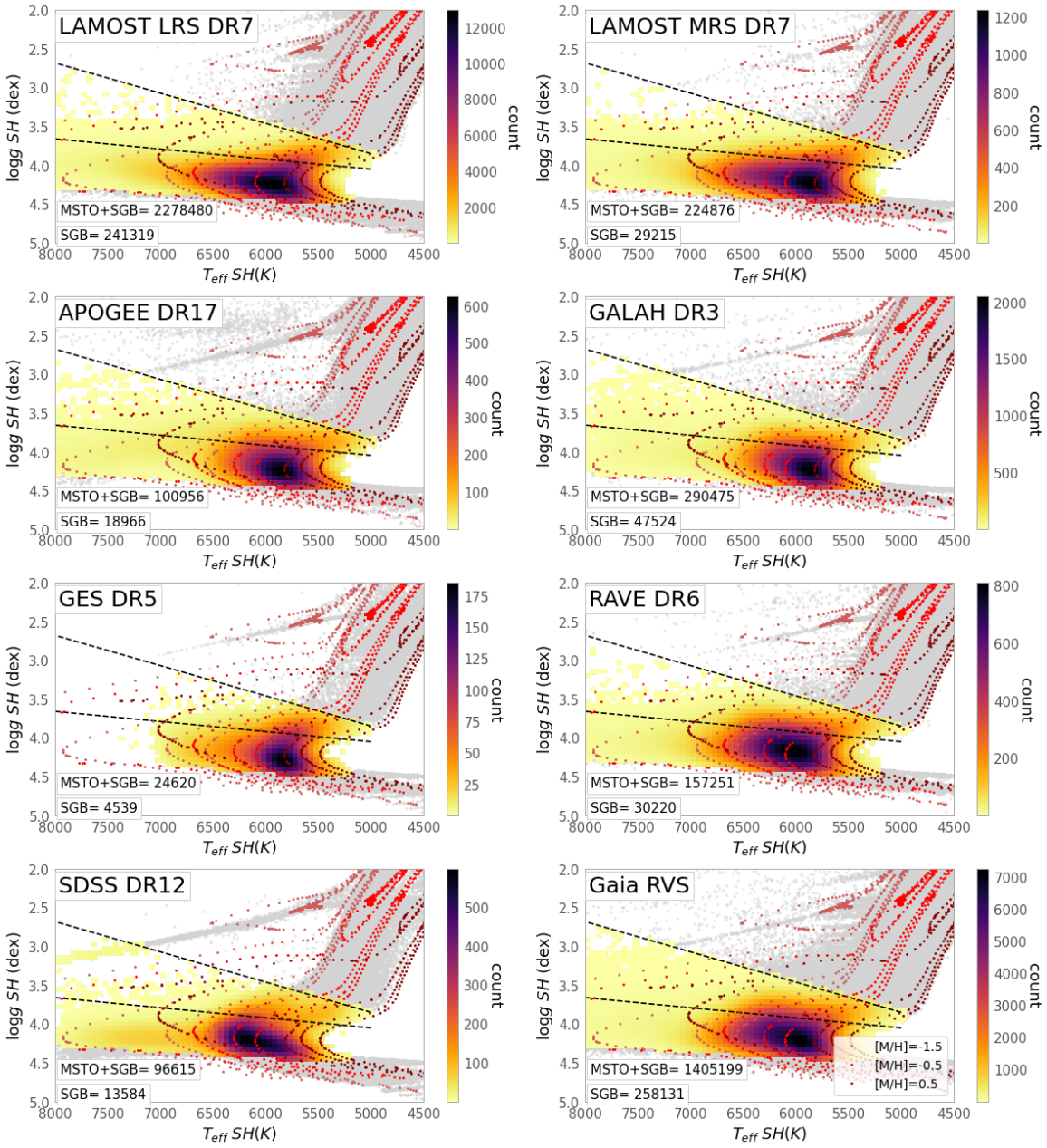

Figure 4.4.3: StarHorse *Kiel* diagram for the samples studied in this work. The grey dots in the background of each panel show all the stars in the respective survey, while the colour coded histograms highlight the MSTO+SGB regime for which we deliver StarHorse ages. The dashed lines limit the SGB, for which the computed ages are most precise. PARSEC isochrones are overplotted in red for three different metallicities, as indicated in the lower right corner of the Figure. For each metallicity four different ages are shown for 1, 4, 7 and 10 Gyr.

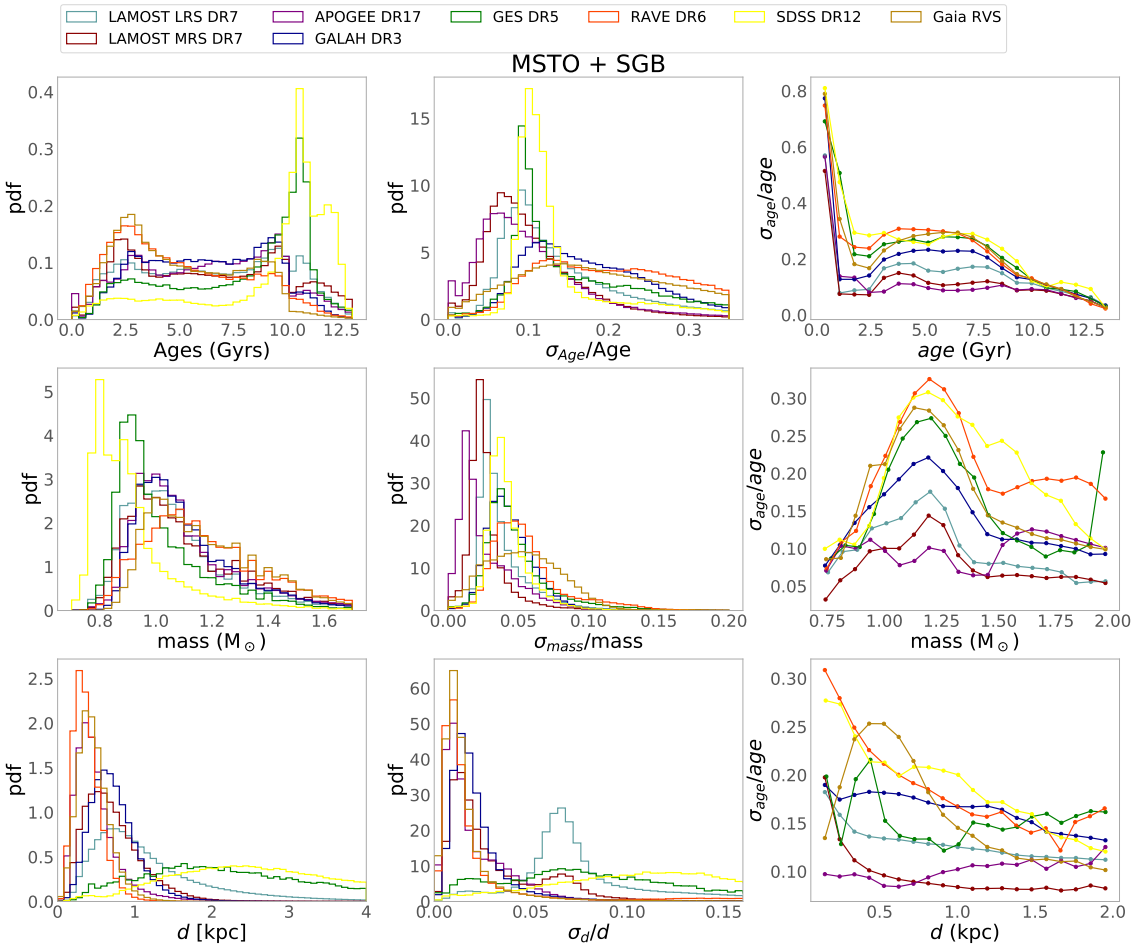

Figure 4.4.4: Distributions of ages, masses, distances and their uncertainties for the MSTO+SGB samples. The y-axis shows the probability density. All histograms are normalised so that the area under the histogram integrates to 1. The right panels show the mean age uncertainty per bin of age, mass and distance for each survey.

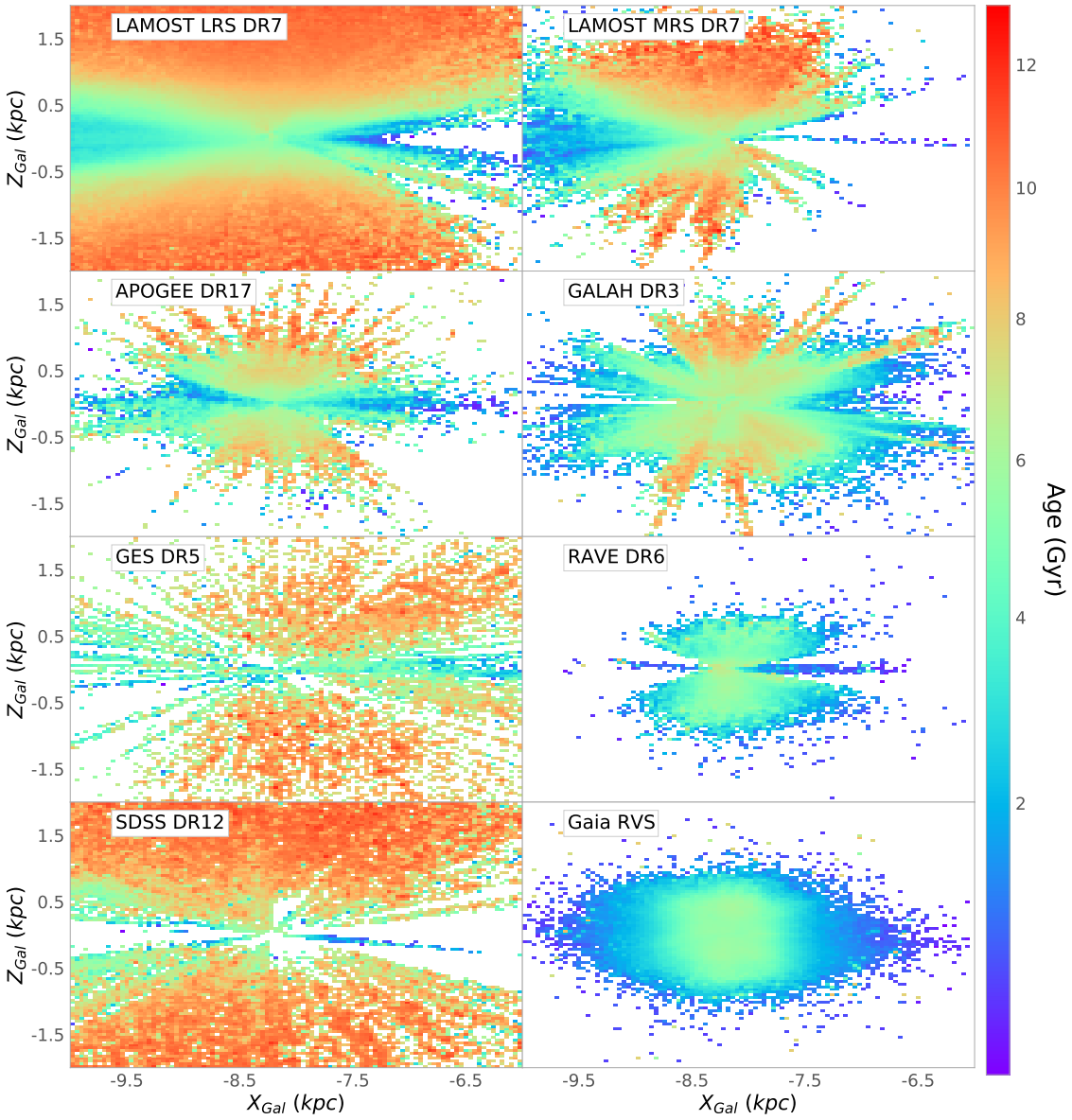

Figure 4.4.5: Galactocentric X and Z projection of MSTO+SGB samples colour coded by StarHorse ages, the colourbar is in power law scale with γ=0.7.

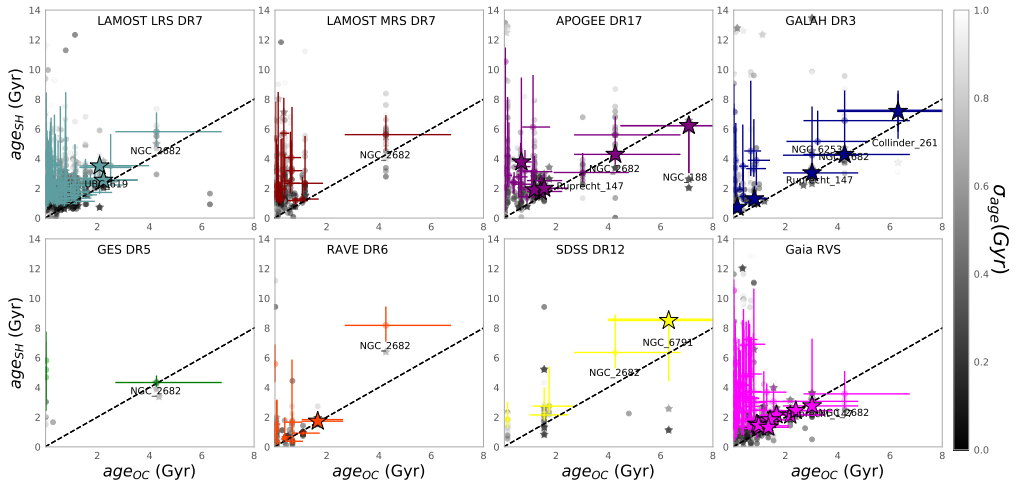

Figure 4.4.6: Comparison of our MSTO+SGB age estimates with open cluster ages from Cantat-Gaudin et al. (2020). In each panel, grey dots are individual OC member MSTO stars (membership probability > 95%), colour-coded by their posterior age uncertainty. For OCs that contain more than 3 MSTO cluster members, the uniform coloured points and errorbars indicate the median age and the 1σ quantiles. We indicate as a star symbol only the SGB sample which has smaller StarHorse uncertainties. The horizontal errorbars reflect the 0.2 dex uncertainties quoted by Cantat-Gaudin et al. (2020). The only OC that was observed by all surveys is M67 (NGC 2682).

4.4.3 StarHorse MSTO-SGB ages and masses

For the first time, we publish ages derived with StarHorse. Ages (and also masses) for individual stars are challenging to derive through isochrone fitting when only spectroscopic, astrometric, and photometric data are available (e.g. Joyce et al. 2022). In the absence of spectroscopic data, meaningful age estimates are even more complicated (Howes et al. 2019). More sophisticated methods such as asteroseismology or eclipsing binaries (where an additional constraint on the stellar mass becomes available) are much more reliable for deriving ages, and these methods can achieve uncertainties below 10% (Valle et al. 2015; Silva Aguirre et al. 2018; Anders et al. 2017b; Valentini et al. 2019; Miglio et al. 2021). The downside is that the samples with asteroseismic and eclipsing binaries are still limited in size and pencil beams compared to spectroscopic surveys. We can achieve a more considerable statistical significance by measuring less precise ages but for larger sets. Here we do so, but we restrain ourselves to the MSTO-SGB. In these evolutionary stages, isochrone fitting methods can be much more reliable since the shape and duration of this stage varies strongly with the stellar mass and, therefore, the age. For SGB stars, the luminosity correlates directly with age, which makes this stage specially suitable for isochrone-based age determinations (e.g. Xiang & Rix 2022). In Q18, e.g. Figure 4 we have also shown with simulations that StarHorse ages can achieve relative statistical uncertainties of 20% for SGB stars.

We display our MSTO-SGB selection in Figure 4.4.3. We opt to use the output StarHorse $T_{\rm eff}$ and $\log g$, since we saw in the previous Section 4.4.2 that for some surveys there are systematic differences between input and output parameters (especially in $T_{\rm eff}$ and $\log g$). Therefore a selection using the StarHorse parameters is more homogeneous and, to some extent, helps eliminate systematics between the different spectroscopic surveys. StarHorse

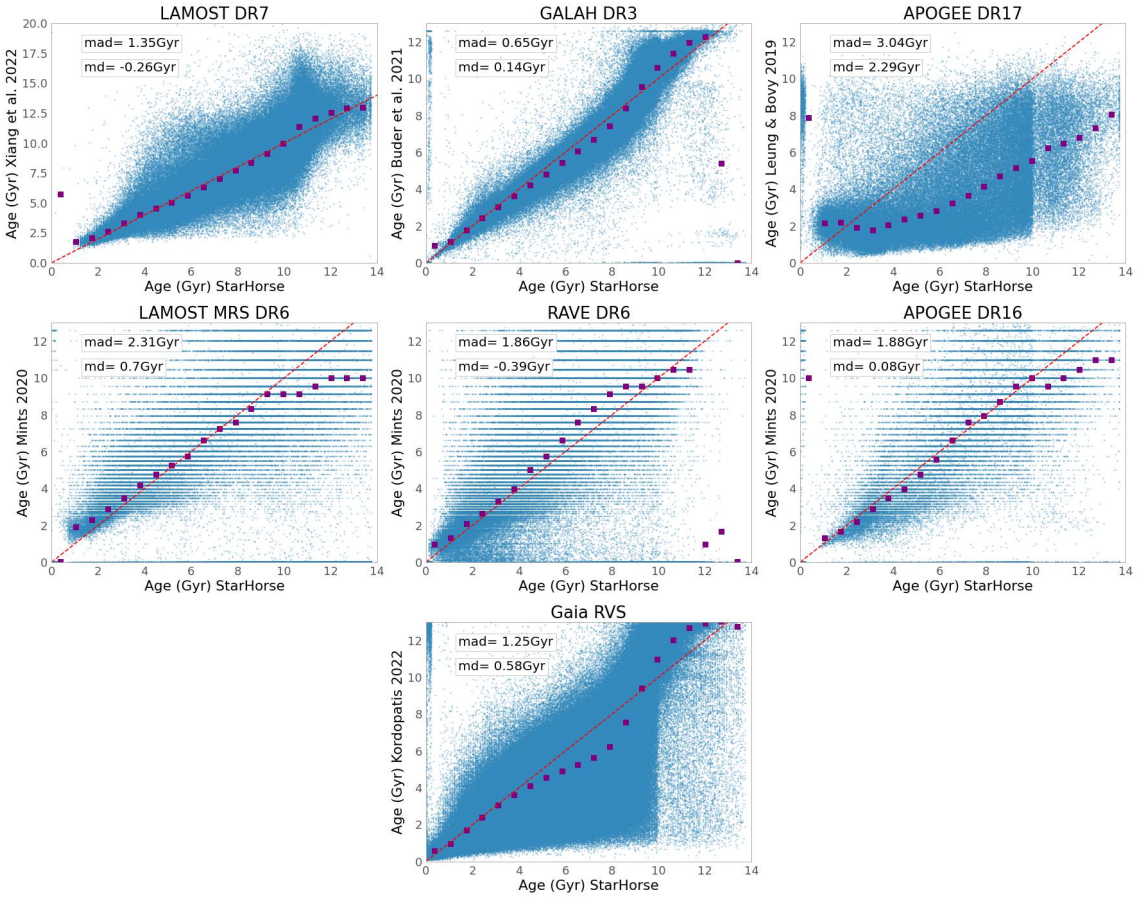

Figure 4.4.7: Comparison of our MSTO+SGB age estimates with values from the recent literature. Top row: comparison to the LAMOST DR7 ages of Xiang & Rix (2022), the GALAH DR3 ages of Buder et al. (2021), and the APOGEE-astroNN DR17 catalogue (Leung & Bovy 2019). Middle row: comparison to the LAMOST, RAVE, and APOGEE age estimates of Mints (2020). Bottom row: comparison to the ages calculated by Kordopatis et al. (2022) for *Gaia* RVS sample. In each panel, the small blue dots are individual stars, the magenta points indicate the median trends. The global spread for each comparison is shown as the mean absolute deviation, mad, and the global shift as mean deviation, md.

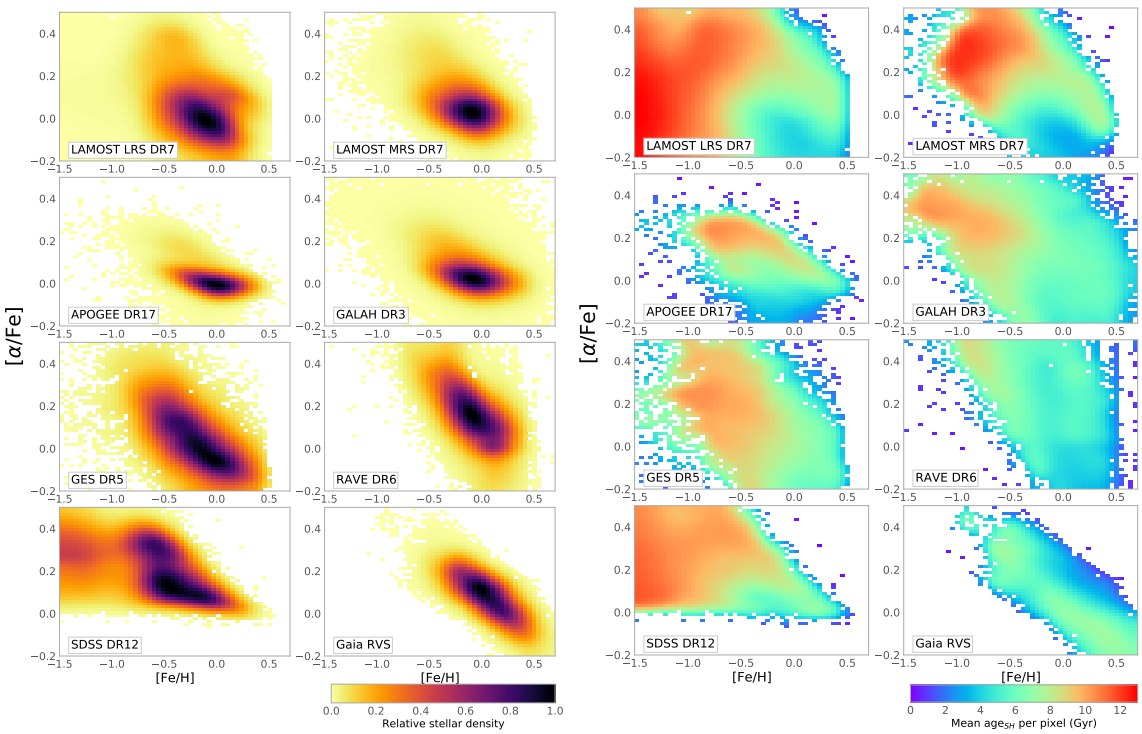

Figure 4.4.8: [α/Fe] vs. [Fe/H] distributions for the MSTO+SGB samples of the analysed surveys. Left: Density distributions (relative to the maximum count in each survey). Right: The same, but coloured by the mean age per pixel.

can break degeneracies by accessing the extra information from photometry and astrometry. The selections are perfomed using the following equations adjusted by eye to comprise the MSTO and SGB regime:

$$\begin{aligned} \log g_{SH} &< -0.000008 T_{eff_{SH}} + 5.8 \\ \log g_{SH} &> -0.00039 T_{eff_{SH}} + 4.9 \\ T_{eff_{SH}} &> 500 \log g_{SH} + 3000; T_{eff_{SH}} < 8000 \end{aligned} \tag{4.1}$$

And only for the SGB selection:

$$\begin{aligned} \log g_{SH} &< -0.00013 T_{eff_{SH}} + 4.7 \\ \log g_{SH} &> -0.00039 T_{eff_{SH}} + 4.9 \\ T_{eff_{SH}} &> 500 \log g_{SH} + 3000; T_{eff_{SH}} < 8000 \end{aligned} \tag{4.2}$$

In Figure 4.4.4 we show the distributions and uncertainties in ages and masses for the selected MSTO-SGB stars. Most age distributions display two peaks: one at intermediate ages ($\approx$ 3 Gyr) and one containing an older generation ($\approx$ 9-11 Gyr). There is a noticeable depression at 10 Gyr for the higher-resolution surveys APOGEE, LAMOST MRS, and GALAH. Since the SDSS/SEGUE survey preferentially targeted the Galactic halo, the age distribution for this survey is highly skewed towards old ages, and presents a double peak at 11 and 12 Gyr. GES and LAMOST LRS only show a rise at 11 Gyr. 90% of the MSTO stars have relative age uncertainties smaller than 50%, and their average is below 34% (see Table 4.4.1). For SGB stars, this average decreases below 20%. From all the spectroscopic releases, APOGEE and LAMOST MRS have the smallest nominal uncertainties in age (below 10%), although this is strongly driven by the input parameter uncertainties of the surveys.

Apart from ages, we also deliver mass estimates for the complete catalogues, not only the MSTO-SGB, but we remind the user to be cautious when using these values, since both

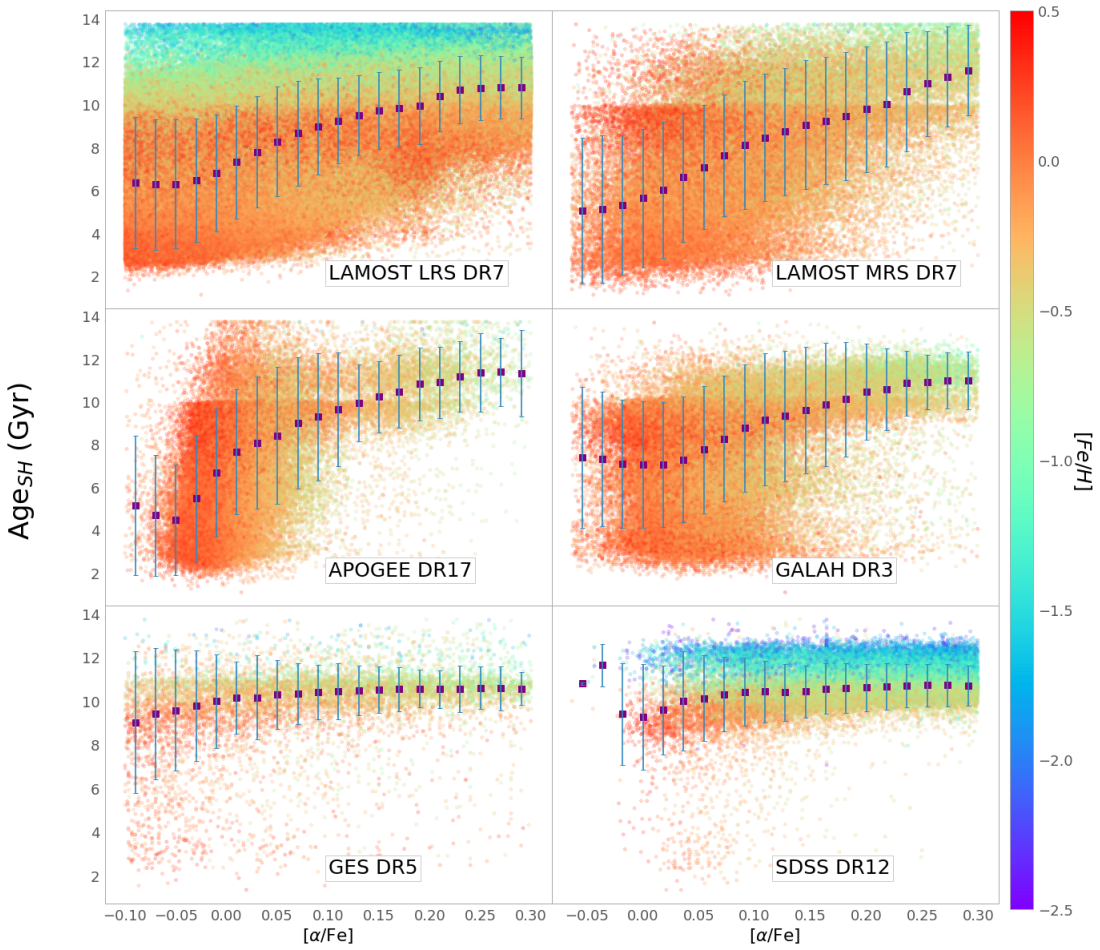

Figure 4.4.9: [α/Fe] vs age distribution for the MSTO+SGB samples of each survey. A cleaning per signal to noise and suggested flags was performed. The purple squares show the median trend per bin in [α/Fe] while the error bars show its one σ deviation. We only display the surveys that have mean statistical uncertainty in age < 30% according to Table 4.4.1

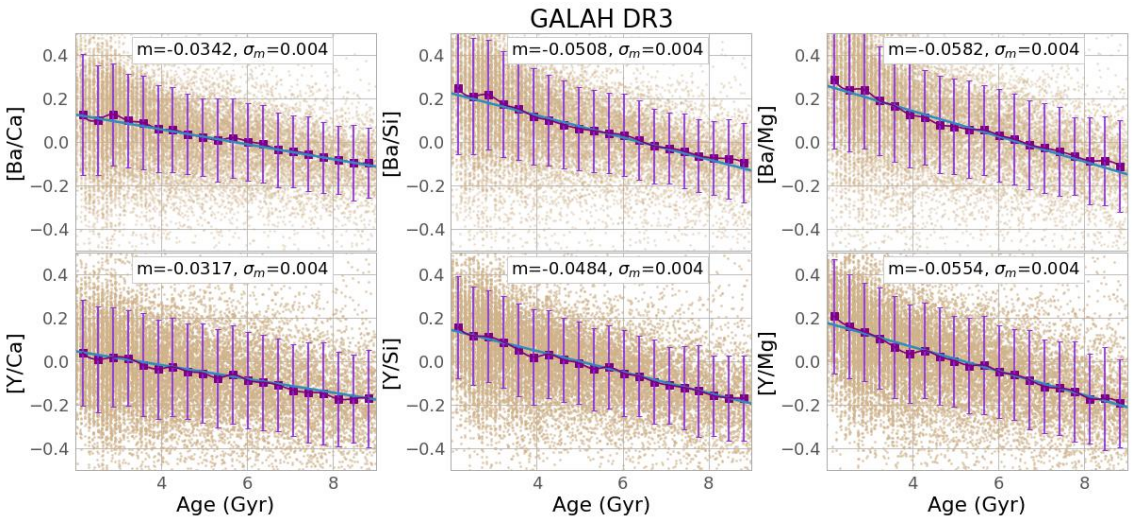

Figure 4.4.10: [s/α] abundance ratios vs. age for GALAH. The purple line shows the median abundance per age bin and the error bar represents one sigma deviation from the median.

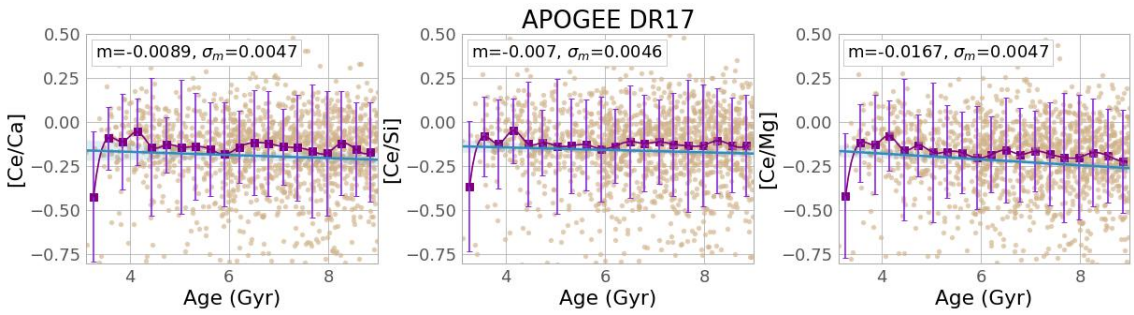

Figure 4.4.11: [s/α] abundance ratios vs. age for APOGEE. The purple line shows the median abundance per age bin and the error bar represents one sigma deviation from the median.

statistical and systematic uncertainties can be very high (depending on the class of stars). The posterior mass distributions do not show considerable differences between surveys, besides the higher content of low mass stars in SDSS and GES. Our mass estimates have been previously validated in earlier StarHorse versions, Q18, against asteroseismic and binaries samples, which yielded relative deviations of $\approx$ 12% and 25%.

In Figure 4.4.4, we also show the extent of heliocentric distances for the MSTO-SGB samples, which is mainly confined to an extended solar neighbourhood (0.1-3 kpc), surveys targetting the halo as GES and SDSS do reach farther distances even inside the MSTO-SGB selection. In the right panels of Figure 4.4.4 we see the dependence of the relative age uncertainty with age, mass and distance. StarHorse ages are more uncertain for younger, intermediate-mass stars. There is also a trend of decreasing age uncertainty with distance, which is related to older stars being found far from the disk. This effect is evident in Figure 4.4.5. For all surveys, we see dependence of age and Galactic height (Z_{gal}) more explicitly in LAMOST LRS, which has the most significant number of stars. The increasing age with Z_{gal} shows the consequence of transiting between the young, thin disk (confined to the Galactic plane) to the older thick disk and halo components.

Validation of age estimates

Since age estimates for field stars are highly dependent on stellar evolutionary models, it is important to identify (and, when possible, quantify) systematic biases. Although also not model-independent, asteroseismic and open cluster ages (OCs) are still our best anchor for validating field-star age estimates. Since solar-like oscillations in MSTO-SGB stars are much weaker than for the red-giant branch, large samples of MSTO-SGB benchmark ages from asteroseismology are still missing. In Figure 4.4.6 we therefore compare our age estimates to the OC ages derived by Cantat-Gaudin et al. (2020). Thankfully, all considered spectroscopic surveys have observed at least some OCs with MSTO-SGB members. The results of the test shown in Figure 4.4.6 can only be described as humbling. While the results are on average in good agreement for older OCs ($age \gtrsim 2$ Gyr), and for the SGB sample only, the ages of younger OC MSTO-SGB members are systematically overestimated, often by a factor of several billions of years. We suggest that the reason for this is the dominance of the initial-mass function prior, which for massive stars will result in the preference of lower-mass (and consequently, older-age) posterior solutions. We insist, however, that this is not a genuine problem of the StarHorse code, but a generic problem of one-fits-all isochrone-fitting codes.

A proof of this statement (and also a secondary sanity check) is delivered in Figure 4.4.7, which compares our age estimates to field-star ages in the recent literature (Xiang & Rix 2022; Buder et al. 2021; Leung & Bovy 2019; Mints 2020). The figure demonstrates that our age estimates compare well with other recent attempts

to derive isochrone ages, especially with the ages derived by Buder et al. (2021) for GALAH DR3 and, to a slightly lesser degree, with the results obtained by Xiang & Rix (2022) for LAMOST and Mints (2020) for APOGEE, RAVE, and LAMOST. The horizontal streaks in the comparison figures for the latter reference (lower panels of Figure 4.4.7) stem from the fact that Mints (2020) used a PARSEC grid with equal spacing in log age rather than linear age (as done in this StarHorse run). The significant scatter seen in each of the panels of Figure 4.4.7 demonstrates that, even when similar techniques and the same input data are used, results vary systematically. To give an extreme example, some of the GALAH DR3 stars that StarHorse indicates to be young (< 500 Myr) are found to be old by Buder et al. (2021), which is very likely to be a combination of a grid-edge effect and poor stochastic sampling of the posterior.

The only method that delivers significantly systematically different results from ours is the astroNN APOGEE DR17 catalogue (based on a convolutional neural network trained directly on APOGEE spectra; Leung & Bovy 2019). This is likely a consequence of the training set used by those authors: their method focuses primarily on red-giant stars and thus is likely to produce biased results for MSTO-SGBs.

4.5 Age-abundance relations

The advantages of combining *Gaia* with spectroscopic data are not limited to more precise distances and stellar parameters, but also opens the possibility to study detailed chemical abundances as a function of these parameters. Certain abundance ratios are strongly correlated with age in our Galaxy and can indicate the formation of different populations (Chiappini et al. 1997; Tucci Maia et al. 2016; Miglio et al. 2021; Morel et al. 2021). These relations between age and chemistry are potentially of great value for understanding and constraining Galaxy evolutionary models (Chiappini et al. 2014; Nissen 2015; Miglio et al. 2017). In this section, we investigate if we can recover some of the known age-chemical correlations between the StarHorse ages, metallicity, α-process and as *s*-process elements. This exercise also serves as an additional validation for the new StarHorse MSTO-SGB ages.

4.5.1 α abundances and metallicities

Since α elements are known to be produced mainly by dying massive stars, in type-II supernovae (SNe), those elements had a larger relative contribution to the chemical evolution of the Milky Way in the past. On the other hand, the content of elements produced by type-Ia SNe increases slowly with the enrichment of the interstellar medium. Therefore ratio of α-capture content with iron can be broadly associated with the temporal evolution of stellar populations (Tinsley 1980; Matteucci & Francois 1989; Chiappini et al. 1997; Woosley et al. 2002).

Diagrams of [α/Fe] vs. [Fe/H] have also been generally used as a classification of the stellar components of our Galaxy: the chemical thick disk is designated as the high-[α/Fe] sequence, while the thin disk can be chemically selected as the low-[α/Fe] sequence (Edvardsson et al. 1993; Fuhrmann 1998; Adibekyan et al. 2012). Although geometrically the thin and thick disks do not exactly match the chemical definitions (Minchev et al. 2015). The high-[α/Fe] sequence is mostly assumed to be old, while the low-[α/Fe] sequence is younger, but the position and shape of these sequences is know to vary across the Galaxy (Bensby et al. 2011; Anders et al. 2014). The inner disc, for example, shows a more prominent bimodality indicating different star formation paths and evolution across the Galaxy (Q20). The picture also gets more complex with the detection of young-α-rich stars (Chiappini et al. 2015). Therefore we expect a clear correlation between [α/Fe] and age but also a large spread due to the mixing of populations (Anders et al. 2017b, 2018; Miglio et al. 2021). In Figs. 4.4.8 and 4.4.9 we show that most of the old stars populate the high-[α/Fe] sequence, and we confirm a relation of increasing [α/Fe] for increasing StarHorse age for most spectroscopic surveys, but also a signifi-

cant scatter (as expected). Older ages are also visible in Figure 4.4.8, especially on APOGEE and the LAMOST survey, at high metallicities and low-α linking the formation of the chemical thick disk and the inner thin disk in a knee where the [α/Fe] ratio decreases at a constant rate as a function of [Fe/H] when SNIa contribution becomes important. Another set of old stars is seen in almost all surveys at low metallicity and low [α/Fe], which is compatible with the chemical characteristics of dwarf Galaxies and the most outer parts of the Galactic thin disk. Although the age and α scatter is high in Figure 4.4.9 for most surveys, one can notice that spread in age is considerably smaller for high-α populations, suggesting that the old high α sequence was formed in shorter time scale. This result is also seen by Miglio et al. (2021), using precise asteroseismology from red giant stars with Kepler and APOGEE spectra, which showed that the old thick disk has a spread smaller than 1.2 Gyr.

4.5.2 *s*-process abundances

The slow neutron-capture process (*s*-process) elements are produced in the asymptotic giant-branch (AGB) phase of low- and intermediate-mass stars, hence their contribution to the interstellar medium increases steadily with time (Busso et al. 1999; Sneden et al. 2008; Kobayashi et al. 2020). Studies of low-metallicity AGBs also show a strong component of *s*-process elements in the Galactic halo (Sneden et al. 2008; Bisterzo et al. 2014). Among the spectroscopic surveys considered in this work, APOGEE and GALAH have measured precise high-resolution abundances for a few neutron-capture elements for a significant number of stars in the MSTO-SGB regime. We choose these two surveys to explore the ratio between *s*-process (ytrium, barium and cerium) and α-elements with age.

In Figure 4.4.10 the ratios between [Ba/α] and [Y/α] show a linear dependence with age. The data points in Figure 4.4.10 are fitted with a non-linear least mean square method, and its uncertainty is taken as a square root from the covariance matrix. It is worth mentioning that the uncertainty associated to the fits done here are probably understimated due to the large data sets and the noise it contains, which are not variables in the fitting procedure (Hogg & Villar 2021), but doing a full Bayesian fit is out of the scope of the paper. In the GALAH data, both [Ba/α] and [Y/α] show strong relations with age. The [Y/Mg] chemical clock has been extensively studied in other works, from solar twins to clusters (Spina et al. 2018; Maia et al. 2019; Nissen et al. 2020; Casamiquela et al. 2021b). This relation has no apparent variation with metallicity (Nissen et al. 2020). In Table 4.5.1, we compare our resulting relations for different chemical clocks with previous works. For [Y/Mg], the linear trend with age agrees very much well with Casamiquela et al. (2021b), which is a higher value compared to the other works but still close to the values found by Spina et al. (2018); Jofré et al. (2020). For [Ba/Si] and [Ba/Mg], our results lay in between the different relations found in the literature, overall more in agreement with Jofré et al. (2020). This shows that `StarHorse` ages are, at least, meaningful in population studies and do reproduce expected chemical-clock relations. The differences between slopes found in the literature can be attributed to the different ranges in metallicity (Horta et al. 2022; Viscasillas Vazquez et al. 2022), the overabundance in neutron capture elements in open clusters compared to dwarf field stars (Sales-Silva et al. 2022) or still the different spectroscopic pipelines. In section 4.A we show the same Figures 4.4.10 and 4.4.11 colour-coded by temperature and metallicity. In Figure 4.4.11 we show yet another *s*-process element, Cerium, derived by the ASPCAP synspec pipeline (Jönsson et al. 2020). The precision for Cerium in APOGEE is much lower than the previously discussed *s*-process abundances in GALAH. It is noticeable from the figure that there is a high spread in [Ce/α] vs age and that most of the cerium abundances are below the solar value. In fact, a considerable shift between the Cerium derived by APOGEE and other surveys has been reported for giant stars in the Galactic bulge (Razera et al. 2022) and when compared to *Gaia* DR3 RVS spectra (Contursi et al. 2022).

Table 4.5.1: Chemical clock slopes, m_{age}, for several abundance ratios in this study (using GALAH DR3 data; see Figure 4.4.10) and the literature.

Publication	[Y/Mg]	[Ba/Si]	[Ba/Mg]	[Ce/Mg]
This work	-0.055±0.004	-0.050±0.004	-0.0582±0.004	-0.017±0.005
Spina et al. (2018)	-0.045±0.002	-	-	-
Nissen et al. (2020)	-0.038±0.001	-	-	-
Jofré et al. (2020)	-0.042±0.002	-0.040±0.002	-0.047±0.002	-0.037±0.002
Casamiquela et al. (2021b)	-0.055±0.007	-	-0.098±0.003	-
Viscasillas Vazquez et al. (2022)	-0.036±0.011	-0.061±0.009	-0.103±0.006	-

In a recent work, Sales-Silva et al. (2022) shows, also using APOGEE, that [Ce/α] has a strong dependence in metallicity and does not work as a universal chemical-clock. In light of these complexities, the relations between [Ce/α] abundances and age derived in this work are almost flat and have lower values than other studies in the literature (Jofré et al. 2020).

4.6 Analysing chemo-age groups of local SGB samples

As an example science case for our new catalogues, we choose three spectroscopic surveys (GALAH DR3, APOGEE DR17, and LAMOST MRS DR7) to map different populations with high-/medium-resolution spectroscopic abundances in the local sample of SGB stars. We choose only to use the SGB since this is a fast evolutionary stage where ages have an explicit dependence on its luminosity resulting in smaller StarHorse uncertainties, see Table 4.4.1. We see in section 4.4.3 that there is a better agreement for OCs in the case of SGB. In section 4.5, there is a clear relation between [Ba/α], [Y/α] and age for these stars, which all substantiate the robustness of the StarHorse derived ages for the SGB regime. The three surveys were chosen due to their higher-quality abundances and completeness. In this section we use the dimensionality reduction visualization technique t-distributed Stochastic Neighbor Embedding (t-SNE; Hinton & Roweis 2003; van der Maaten & Hinton 2008), in synergy with the Hierarchical Density-Based Spatial Clustering of Applications with Noise (HDBSCAN; Campello et al. 2013; McInnes et al. 2017). In the following subsections we describe t-SNE and HDBSCAN as well as their application to the SGB samples.

4.6.1 Methodology: t-SNE and HDBSCAN

Finding groups of chemically similar stars aids our understanding of the formation and evolution of the Milky Way (Freeman & Bland-Hawthorn 2002). Stellar chemical abundances of most elements remain constant during most of stellar evolution, while a star's orbit can be changed radically depending on the gravitational perturbation it suffers. The composition of a star's birth cloud dictates its chemical composition, making it possible to identify stars born in similar conditions through weak chemical tagging (e.g. Hogg et al. 2016). However, differences in chemical abundances can be very subtle and become masked by their observational uncertainties making strong chemical tagging or finding co-natal stars very difficult (Casamiquela et al. 2021a). It is also impotant to take into account the radial migration due to the dynamical effects produce by the non-axisymmetric structures (bar and spiral amrs).

One way to explore this problem is by visualizing the entire complex multi-dimensional chemical abundance and age space at once to find patterns in an easier manner. t-SNE is a statistical method for visualizing high-dimensional data by giving each datapoint a location in a two or three-dimensional map (van der Maaten & Hinton 2008). These maps are iteratively created by minimizing the Kullback–Leibler divergence between the similarity distributions

of the data in the original space and the low-dimensional map, and thus preserve the proximity between similar data points. For a slightly deeper introduction focussed on a similar science case, we refer to Section 2 in Anders et al. (2018). As in that paper, we use the python implementation of t-SNE included in *scikit-learn* (Pedregosa et al. 2012).

t-SNE has demonstrated to be an effective tool to help identify peculiar groups in different parameter spaces, and has wide applications in astronomy; e.g., stellar spectral classification (Matijevič et al. 2017; Traven et al. 2017; Valentini et al. 2017; Verma et al. 2021; Hughes et al. 2022), similarities between planetary systems (Alibert 2019), galaxies classification (Zhang et al. 2020; Rim et al. 2022). Finally, Anders et al. (2018); Kos et al. (2018), and et al. (in prep.) show that applying t-SNE to the abundance space to perform chemical tagging confirms cluster, stream membership and different stellar populations that compose the Galactic disk. Inspired by those works, we follow a similar approach but with a few differences; we apply t-SNE to a set of chemical abundances combined with the age information of APOGEE, GALAH, and LAMOST MRS and then, instead of looking for separations in the t-SNE by eye, we apply a clustering method to identify different chemical-age groups.

Clustering algorithms have been extensively used in astronomy to find stellar groups in the kinematical or chemodynamical space (Koppelman et al. 2019; Limberg et al. 2021; Gudin et al. 2021; Hunt & Reffert 2021; Shank et al. 2022). For example, HDBSCAN is an extension of the DBSCAN (Ester et al. 1996) clustering method. It converts DBSCAN into an Hierarchical method by extracting flat clustering based on the stability of the clusters, which leads to the detection of high-density clusters, and it is, therefore, less prone to noise clustering than DBSCAN.

The configuration of t-SNE+ HDBSCAN for each of the samples we discuss in the following sections is displayed in Table 4.6.1.The main hyperparameter of t-SNE is called perplexity and controls the number of nearest neighbours. We made several tests with different values for the perplexity parameter and the random state, which can influence the local minima of the cost function (Wattenberg et al. 2016). These tests are summarized in the appendix 4.C. We always choose the t-SNE configuration that visually splits the groups more clearly.

We then apply HDBSCAN to the t-SNE projections. The three relevant hyparameters described in table 4.6.1 were optimized to obtain the "best" clustering in the sense of weak chemical tagging i.e. a configuration that does not split the data into too many small groups. Since we are searching for a more global picture of the chemistry and age distribution of stellar populations, we know that a large group should be found by the method as the "thin disk" since it should dominates our samples. The HDBSCAN hyperparameter "min_cluster_size" controls the minimum number of stars allowed to be considered a cluster; this parameter depends on the sample size (see e.g. McInnes et al. 2017, and Appendix 4.C). The hyperparameter "min_samples" defines how conservatively the method treats noisy data. Finally, the hyperparameter "cluster_selection_epsilon" controls the distance between the clusters, which can change with the t-SNE projection. We also always set HDBSCAN to "eom" as cluster_selection_method which is optimized for larger groupings.

4.6.2 SGB samples

In this subsection we detail the exact selection of the elemental abundances and ages used for the following t-SNE and HDBSCAN analysis, separately for the APOGEE, GALAH, and LAMOST MRS samples. While this is important to understand the differences in the results for the three surveys, readers mainly interested in the overall results may consider to move on straight to Section 4.6.3 in which we discuss the chrono-chemical groups found in our analysis.

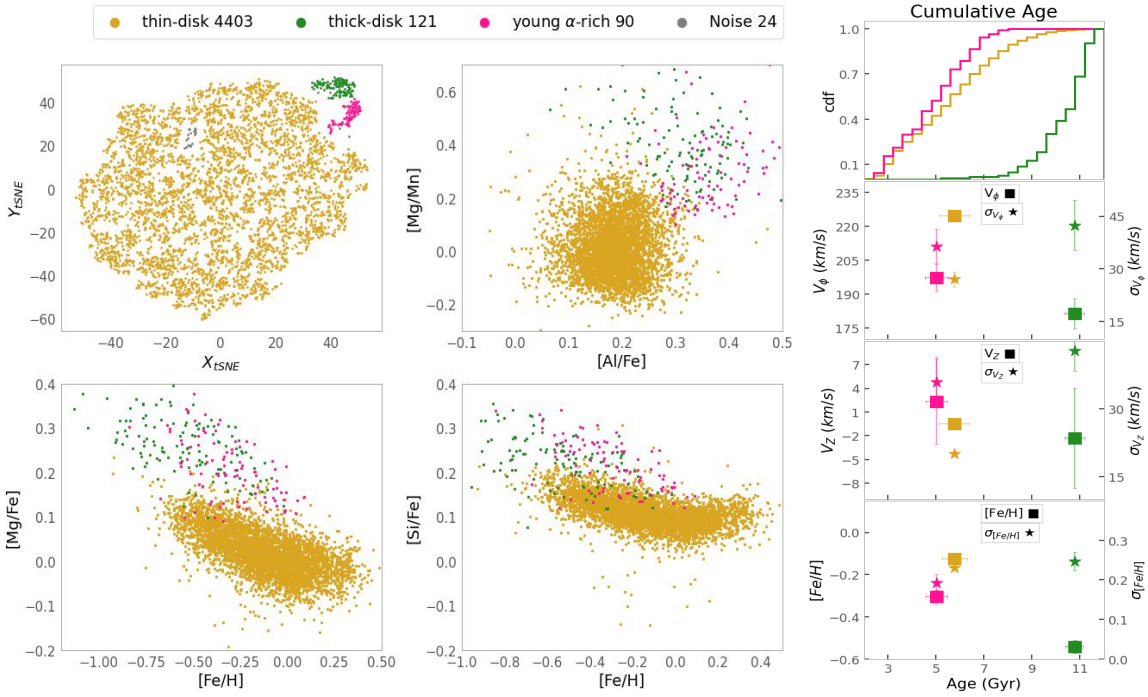

Figure 4.6.1: Upper left panel: t-SNE projection for SGB stars in APOGEE DR17. Colours correspond to different groups found by t-SNE+HDBSCAN on the data. Lower-left and middle panels: abundance ratios of α elements to those of iron group plotted against metallicity using the same colours for each identified group. Right panels from top to bottom: i) upper panel: cummulative ages distribution for each group; ii) upper middle panel: for each group we show mean azimuthal velocity (left y-axis and square symbol) and the mean dispersion in azimuthal velocity (right y-axis and star symbol) as a function of age. iii) lower middle panel: for each group we show mean vertical velocity (left y-axis and square symbol) and the mean dispersion in vertical velocity (right y-axis and star symbol) as a function of age. iv) bottom panel: for each group we show the mean metallicity (left y-axis and square symbol) and the mean dispersion in metallicity (right y-axis and star symbol) as a function of age. The error bars in the right panels represent the 95% confidence interval of a bootstrap resampling.

Table 4.6.1: Configuration and input parameters of t-SNE+HDBSCAN

t-SNE configuration

Survey	input	perplexity	random state
APOGEE DR17	[(Mg, Mn, Al, Si)/Fe] + Age_{SH}	80	50
GALAH DR3	[(Mg, Al, Si, Ni, Zn, Y, Ba)/Fe] +Age_{SH}	100	30
LAMOST DR7	[(C, Mg, Si)/Fe]+ Age_{SH}	50	80

HDBSCAN configuration

Survey	min_cluster_size	min_samples	cluster_selection_epsilon
APOGEE DR17	38	1	0.6
GALAH DR3	45	15	1.7
LAMOST DR7	207	8	1.95

APOGEE DR17

We use APOGEE DR17 abundances from the SGB sample to find groups in the t-SNE projection with HDBSCAN. We apply the following quality cuts before executing t-SNE: SNREV > 70, ASPCAP_CHI2 < 25, VSCATTER<1, ASPCAPFLAG=0, STARFLAG=0, "NEGATIVE" not in StarHorse_OUTPUTFLAGS, and "CLUSTER", "SERENDIPITOUS", "TELLURIC" not in TARGFLAGS. And finally, we also make a strict cut in temperature 5500 K < $T_{\rm eff}$ < 6000 K.

In Table 4.6.1, we list the abundance ratios chosen as input for the t-SNE method, we only select elements with relatively small uncertainty, as seen in Figure 4.B.3. In the abundance group, we have iron-peak, odd-Z, and α elements. The *s*-process element cerium is not included because of the large uncertainties and poor statistics for the SGB sample. We need to be cautious when using APOGEE abundances since its pipeline is optimized for giants (Jönsson et al. 2020). In the case of subgiants, there might still be many artifacts (e.g. Souto et al. 2021, 2022; Sales-Silva et al. 2022) that could possibly lead t-SNE and HDBSCAN to find an unphysical clustering in the chemo-age space. In Figure 4.B.3, we see some drastic differences when one uses different spectral analysis codes in the APOGEE pipeline. Even for abundances with minimal errors like [Al/Fe] and [Si/Fe], there is a significant difference at temperatures below $T_{\rm eff}$ <5500 K, thus our strict temperature cut. After a further cleaning per each abundance flag, elem_flag=0, we are left with 4 638 stars to which we apply t-SNE and HDBSCAN.

In the case of APOGEE the method finds at least three different groups (see Fig. 4.6.1 and tests with t-SNE parameters in Figure 4.C.3). To check if there is any dependence of the t-SNE clustering with the abundance pipeline, we also show in the appendix Figure 4.C.4, which displays the final t-SNE projections colour-coded by $T_{\rm eff}$, $\log g$, [Fe/H] and signal-to-noise ratio. Some areas of the resulting projections are predominantly found at a metallicity and $T_{\rm eff}$ range. This indicates that the clustered groups have a certain dependence on those parameters. The groups differ in [α/Fe] content, metallicity, and also in their age distribution. While most of the stars belong to a (chemically defined) "thin-disk" component ≈ with high dispersion in metallicity and age, two other groups are found with chemical characteristics of "thick disk" and "transition"/"high-α metal-rich" stars (Fuhrmann 2008; Adibekyan et al. 2011; Anders et al. 2018; Ciucă et al. 2021). We discuss these groups in more detail together with the ones found in GALAH and LAMOST in Sect. 4.6.3 and in Appendix 4.C.

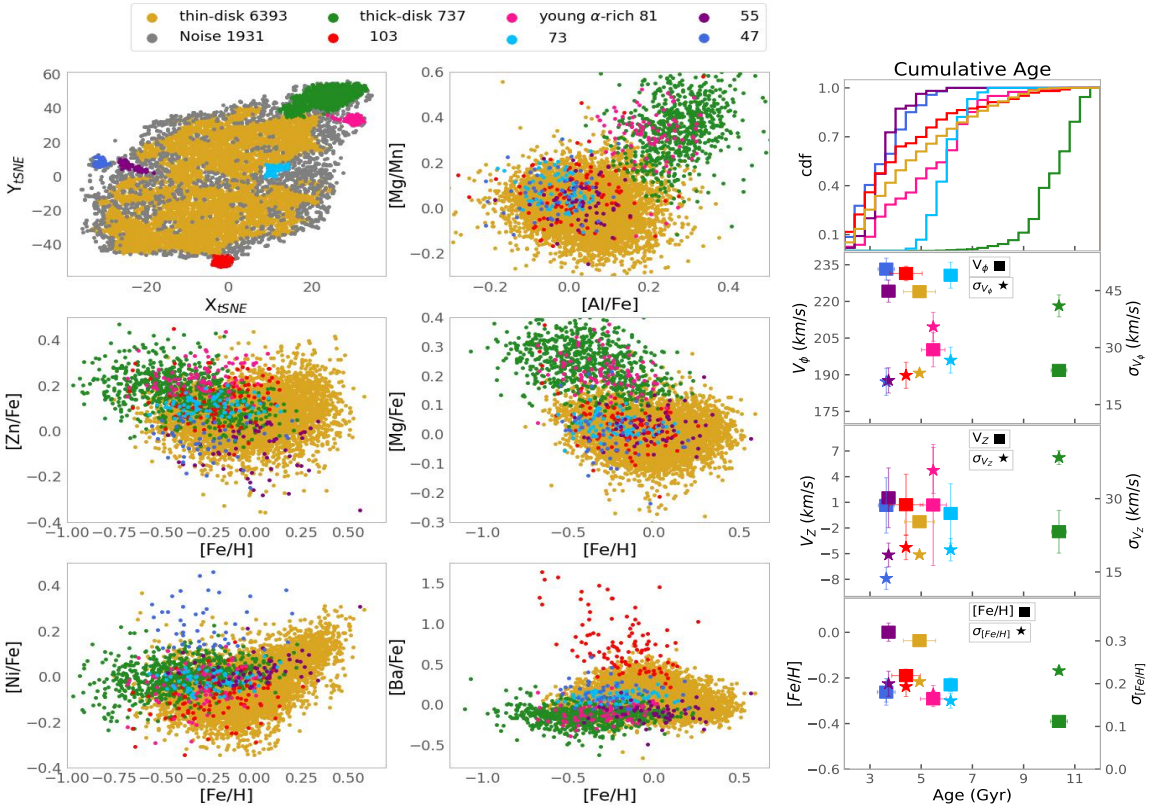

Figure 4.6.2: t-SNE projection for SGB stars in GALAH DR3, colours show the groups that the HDBSCAN method identified. Abundance ratios are also show coloured by the same groups.Colours correspond to each group found by t-SNE+HDBSCAN on GALAH data. Upper pannel: Cummulative ages distibuion for each group; middle panel left axis squares: mean azimuthal velocity for each group; middle panel right axis stars: mean dispersion in azimuthal velocity for each group; lower panel left axis squares: mean vertical velocity for each group; lower panel right axis stars: mean dispersion in vertical velocity for each group. The error bars in the right panels represent the 95% confidence interval of a bootstrap resampling.

GALAH DR3

Similarly to APOGEE, we use GALAH DR3 abundances for the SGB sample to find groups in the t-SNE projection with HDBSCAN. Before performing the analysis we made the quality cuts suggested by Buder et al. (2021): snr_c3_iraf<30, flag_sp=0, flag_fe_h=0 and 'other' not in survey_name, as well as anything with negative extinctions in StarHorse. The chemical abundances that we choose for the analysis are described in Table 4.6.1. The set contains iron peak elements as well as α and neutron capture elements, covering different nucleosynthetic paths. From this group of abundances we select only stars for which the flag_elem = 0. The GALAH DR3 SGB sample that satisfy all the mentioned flag conditions is reduced from 47 524 to 9 420 stars. We did not choose all abundances available in GALAH since this reduces the sample size even more drastically. We then combine the chosen abundance ratios from Table 4.6.1 together with the ages from StarHorse as t-SNE input. Here we also experiment with the different test parameters on t-SNE seen on Figure 4.C.1. For the GALAH sample we select the case for perplexity = 100 and random state=30. To check if there is any dependence of the t-SNE clustering with the abundance pipeline we also show in the appendix Figure 4.C.2 the final projections colour-coded by $T_{\rm eff}$, $\log g$, $[Fe/H]$ and Signal to noise, again here as expected there are some dependencies in temperature and therefore metallicity.

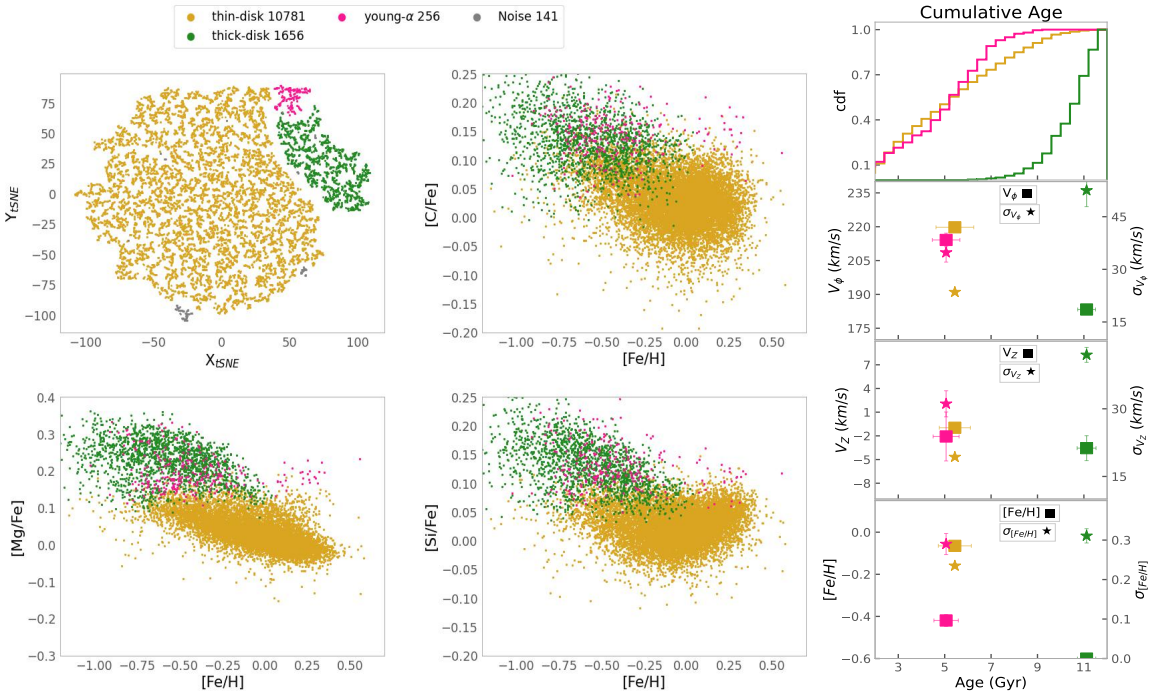

Figure 4.6.3: t-SNE projection for SGB stars in LAMOST MRS. Same as Figure 4.6.1 for LAMOST MRS data.

We then apply HDBSCAN to the t-SNE projection, with the parameters described in table 4.6.1. The results from the t-SNE projection and HBDSCAN clustering groups are shown in Figure 4.6.2 along with various abundance relations for the different coloured groups. We discuss a possible interpretation for each of the groups in 4.6.3, with a particular focus on the chemical thick disc.

LAMOST MRS

As a final exploration of the t-SNE+HDBSCAN method, we choose the medium resolution survey from LAMOST. It is essential to keep in mind that this has a lower resolution than the previously discussed surveys APOGEE and GALAH. LAMOST MRS has 12 individual element abundances, derived through a label-transfer method based on convolutional neural network (CNN) using as training set APOGEE spectra (Xiang et al. 2019). There are many caveats in such methodologies, e.g. incompleteness and noise in the training data and unavailability of uncertainties. Therefore, we must be aware of these problems when analysing the results. To proceed with the method, we made the following quality cuts to LAMOST MRS SGB sample: S/N > 30, fibermask=0 and 3500< $T_{\rm eff}$ <6500. We decide on the chemical abundances from LAMOST shown in table 4.6.1. The choice is mostly based on the mutual availability of the abundances since we do not have uncertainties or flags to control in this sample. With these choices we are left with 12 834 stars in LAMOST DR7 SGB sample. Combining the set of abundances with ages into the multi-dimensional space t-SNE+HDBSCAN can find three different groups as seen in Figure 4.6.3 together with some abundance ratios, age and kinematical properties. We discuss a possible interpretation in the next subsections.

4.6.3 Chrono-chemical groups

Thin disk stars (dark yellow)

Traditionally the disk in the Milky Way and in external galaxies (Dalcanton & Bernstein 2002) can be divided into geometric thin and thick disks. The thin disk dominates in density in the solar neighbourhood since its geometrical

component is denser and mostly confined to the Galactic plane. In contrast, the thick disk has a more extensive scale height (Jurić et al. 2008). Since our selection of SGB stars is limited to the solar neighbourhood, we expect that our samples have a strong dominance of thin-disk-like stellar populations. However, the disks defined chemically and geometrically are not identical (Kawata & Chiappini See 2016; Minchev et al. See 2015; Anders et al. See 2018 for a discussion). Our method for recovering chrono-chemical groups finds mostly stars similar to a chemical thin-disk highlighted with the dark yellow colour on Figures 4.6.1, 4.6.2 and 4.6.3. Chemically, the thin disk is much more complex and less well mixed than the chemically defined thick disk. A metallicity gradient with radius has been long reported as a characteristic of the thin-disk (Anders et al. 2014; Hayden et al. 2015) and radial migration is efficient in circular orbits, which can bring stars born in a certain inner radius to the solar neighbourhood (Minchev et al. 2011, 2013). With all these complexities, we expect that a technique to search chrono-chemical groups could find multiple systems in the thin disk. Our results show that the thin-disk population has a broad age and metallicity distribution, and multiple systems are found in the GALAH DR3 sample. The chemical composition of the thin disk does not extend much beyond 0.1 dex in α-abundances, and their enrichment in *s*-process elements is higher than the detected thick disk (green dots), but there is also considerable overlap. The thin disk has orderly rotation, with smaller velocity dispersion and high rotational velocities, as seen in the right panels of Figures 4.6.1, 4.6.2 and 4.6.3. All those characteristics are consistent with the chemical and kinematical "thin disk" populations defined in multiple works in the literature (e.g. Adibekyan et al. 2013; Anders et al. 2018). The mean age of the thin disk detected in this work lies between 5 to 6 Gyr, depending on the survey. We notice from Figure 4.6.4 that the thin disk age distributions have slight differences from survey to survey; all surveys show a prominent peak at about 3 Gyr, with GALAH having a higher proportion of those young stars. While in GALAH, the thin disk stars steadily decrease in proportion with age, APOGEE shows a secondary peak at 6 Gyr, and LAMOST mainly presents a flat distribution from four to eight Gyr. Curiously on APOGEE and LAMOST, the thin-disk extends to ages larger than ten Gyr; these stars are older than one would expect for standard thin-disk formation scenarios, even though recently Prudil et al. (2020) also found evidence for a population of RR Lyrae stars older than 10 Gyr with chemo-kinematical thin disk characteristics. We can attribute the cause of the differences in the thin disk's age distribution between surveys due to their different selection functions or the breakage into subpopulations, another issue is the case for the different solar scales utilized through the suveys which can led to differences in the chemical distributions. Furthermore, the consistent result of a broad age distribution throughout the surveys is in line with a slow and inside out formation of the chemical thin-disk component (e.g. Chiappini et al. 1997, 2001; Minchev et al. 2013, 2014). In Figure 4.6.5, we show the thin disk's age vs. metallicity in the three surveys. We see that for the thin disk populations, there is a clear relation of increasing ages to decreasing metallicities until about 3 Gyr, which corresponds to the prominent young peak seen in the age distributions of Figure 4.6.4. After 3 Gyr, the relation between age and metallicity becomes more complex. Still, there is an apparent change in the relation, suggesting an overall flat relation in age with metallicity but with high dispersion. As other works have shown it is complicated to reach strong conclusions from currently available age-metallicity relations, still affected by substantial age errors and important and difficult to corrrect selection effects. (Feltzing et al. 2001; Casagrande et al. 2011; Bergemann et al. 2014). Even though we can separate the thin disk via the chrono-age groups, we need to correct for selection effects, which is out of the scope of this paper. We refer to future works for a proper analysis of the age metallicity relation of these samples.

Genuine thick disk stars (green)

We find stars compatible with the abundance pattern of chemically defined thick disk stars (Reddy et al. 2006; Adibekyan et al. 2011; Bensby et al. 2014; Anders et al. 2014; Nidever et al. 2014; Mikolaitis et al. 2014; Hayden et al. 2015), which present high alpha abundances in the three different SGB samples for which we run t-SNE+HDBSCAN. Here we will refer to this population as the "genuine thick disc". These stars clearly occupy the high-[Mg/Fe] sequence in the classical Tinsley-Wallerstein diagram (Wallerstein 1962) (lower left panel of Figures 4.6.1 ; 4.6.3 and central panel of Figure 4.6.2) and show elevated [Mg/Mn] and [Al/Fe] abundances (Das et al. 2020). In the GALAH sample, where we have the *s*-process abundance ratios like [Ba/Fe], shows a slightly lower location than the bulk of the populations. At the same time, [Zn/Fe] is mildly enhanced compared to the thin disk at the same metallicity in agreement with previous measurements (Delgado Mena et al. 2017; Friaça & Barbuy 2017). In the right panels of Figs. 4.6.2,4.6.1 and 4.6.3 we show the cumulative age distribution as well as the age-V_Φ, age-σ_{V_Φ}, age-V_Z age-σ_{V_Z} relations, binned by HDBSCAN population. These plots show that the genuine thick disk is relatively old ($\gtrsim$ 10.9 Gyr), has lower rotation and is kinematically hotter than the thin disk populations, in line with the recent analysis of Rendle et al. (2019); Miglio et al. (2021). This result also agrees with observations of disk galaxies at redshifts $\approx$ 2, Übler et al. (2019) measured velocity dispersions of about 45 km/s for thick disks observed at that look-back time. Is also very clear that the genuine thick disk found by t-SNE+HDBSCAN has a contrasting mean age difference and a noticeable jump in velocity dispersion compared with all the other populations in the SGB samples, suggesting that it has indeed a very different formation path in agreement with Chiappini et al. 1997, 2001; Reddy et al. 2006; Miglio et al. 2021. Recent self consistent dynamical models of the Milky Way, also show distinctive characteristics in the kinematics and composition of the thin and thick disks (Robin et al. 2022).

The age distribution of genuine thick disk stars in Figure 4.6.4 shows a double peak. The second prominent peak at ages between 9-10 Gyr (very clear in the GALAH sample) is possibly the contribution of transition or bridge stars, previously detected by other works (Anders et al. 2018; Ciucă et al. 2021). The transition stars were probably formed in the inner Galaxy and extend from the high α abundances to low α and high metallicities, filling the gap between the thin and thick disks [α/Fe] diagram. Further analysis of bridge stars with t-SNE+HDBSCAN is a matter for a forthcoming paper (et al. in prep.). The metallicity distribution shown in the left panels of Figure 4.6.4 is reasonably similar for the three samples of SGB stars, ranging from -1.5 to 0.0 and with a clear peak at around -0.5 dex. For APOGEE and LAMOST the metallicity distribution shows a second prominent peak at -0.8 dex. The [Mg/Fe] distribution is also analogous throughout the different surveys showing a smooth distribution from 0.1 to 0.4 dex. In Table 4.6.2 we compare the mean age, azimuthal velocity and their dispersion values. We see that the age values agree very well between the surveys, varying from 10.4-10.9 Gyr, and the highest age dispersion being that of LAMOST DR7, of 1.35 Gyr. The age and age dispersion might be higher for LAMOST and APOGEE due to minor debris contamination as we see some stars in the green group to extend to the very metal-poor side.

Young α-rich (magenta)

Although young α-enhanced stars cannot be explained by standard chemical evolution models, a significant number of them have been previously detected by diverse works in the literature (Chiappini et al. 2015; Martig et al. 2015; Jofré et al. 2016; Silva Aguirre et al. 2018; Ciucă et al. 2021; Miglio et al. 2021). Our method also recovers stars with such characteristics in the SGB samples of GALAH, APOGEE and LAMOST, which we indicate by the magenta colour in Figures 4.6.1, 4.6.2, 4.6.3, and 4.6.4. In Figure 4.6.6, we show that most of the stars detected as the magenta group fall in the area delimited by the

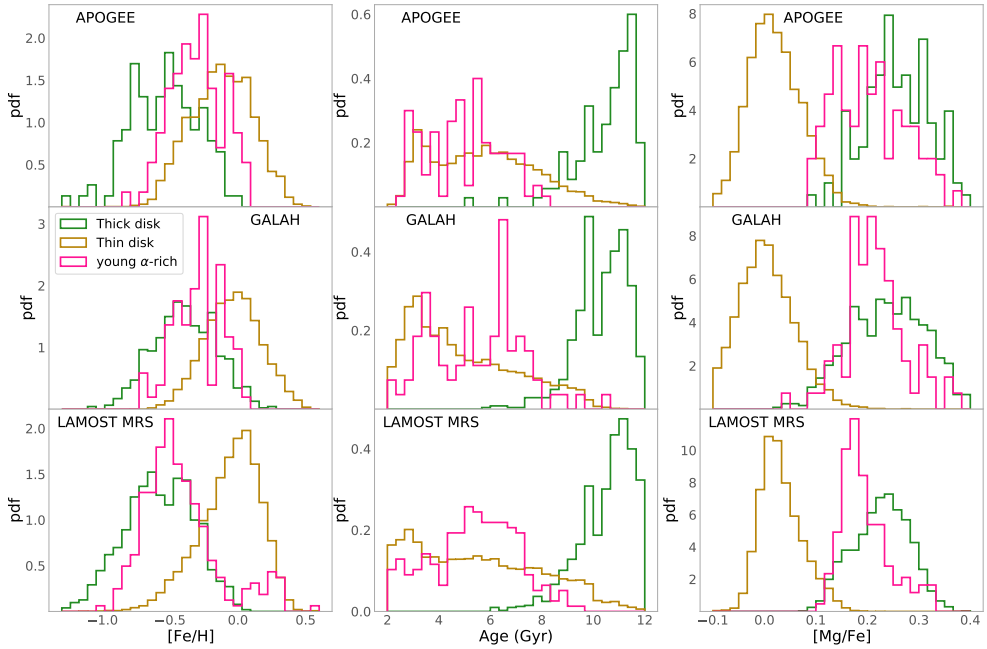

Figure 4.6.4: Probability density function of metallicity, age and [Mg/Fe] for the main populations founded in APOGEE, GALAH and LAMOST with t-SNE HDBSCAN.

black curves. It is hard to explain with chemo-evolutionary models of the Milky Way stars that fall in this area (Chiappini et al. 2015). The young α-rich populations detected here show a mean age of about 5 Gyr for the three different surveys. The cumulative age distributions have truncation at about 7 Gyr, but we see an extension to older ages in GALAH and LAMOST. Those older stars could perhaps again be part of the transition or bridge stars which have intermediate chemical characteristics between thin and thick disks (Anders et al. 2018). The range of abundances of the young-α-rich stars is similar to the genuine-thick-disk (green-dots), except that their metallicity and [α/Fe] distribution is more concentrated at intermediate values between thin-disk (dark yellow) and genuine-thick disk stars, see Figure 4.6.4. For LAMOST the metallicity distribution of the magenta stars is overall poorer than in APOGEE and GALAH although their [Mg/Fe] is lower which could classify some of those stars as debris (Hasselquist et al. 2021; Limberg et al. 2022b), outer disk or a pipeline problem. Is worth mentioning that the [Mg/Fe] measure through CNN algorithm in LAMOST DR7 MRS is not always consistent with the [α/Fe] measured from LASP pipeline (Wu et al. 2014). We also notice differences between the green and magenta stars in the [Mg/Mn] vs [Al/Fe] diagram: contradictorily in APOGEE these stars are richer in [Al/Fe], ranging from 0.2 to 0.5 dex, while in GALAH they range in [Al/Fe] from 0 to 0.2 dex. The kinematics of the young-α-rich stars is mostly hot from the right panels of Figures 4.6.1; 4.6.2; 4.6.3 the magenta groups show velocities dispersion both vertically and azimuthally of about 35 km/s. Although their mean V_ϕ is similar to the one of the thin disk, the hot kinematics agrees with previous works (Silva Aguirre et al. 2018; Miglio et al. 2021; Ciucă et al. 2021) suggesting that these stars formed from the same gas as the genuine-thick disk but they appear young because they are probably mergers from binary stars (Jofré et al. 2016).

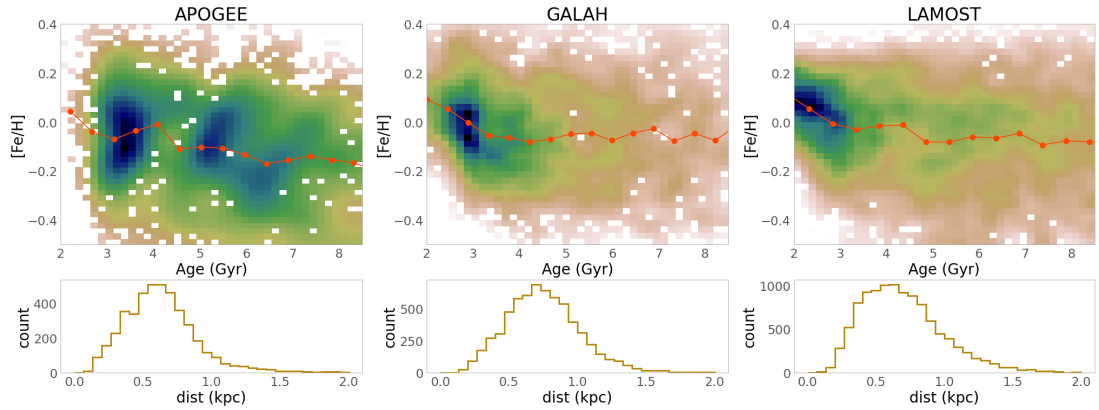

Figure 4.6.5: Upper panels: metallicity vs age for the detected thin-disk component in three surveys. The map shows the mean density per pixel where we have also applied gaussian smoothing. The red dotted line represents the median metallicity for the given age. The lower panels show the heliocentric distance coverage for each sample.

Other populations found in Galah DR3

Enriched s-process stars (red):

For the GALAH SGB sample, we can identify enhanced *s*-process stars since [Ba/Fe] is available and input to t-SNE. This chrono-chemical group shares very similar properties to the thin disk, showing low-α enhancement and a large dispersion in age and iron-peak elements, but a significant difference in barium enhancement , [Ba/Fe]> 0.5. The right panels of Figure 4.6.2 show that these stars are slightly younger than the thin disk group, with a mean age of about 4.5 Gyr. Their rotation is similar to the thin disk, showing high azimuthal velocities and low-velocity dispersion. Despite broad distribution in [Fe/H], these stars almost do not present any higher metallicities than Solar, and the most barium enhanced stars are on the metal-poor side. One can also notice a considerable fall of [Ba/Fe] for metal-rich in the thin-disk (Israelian et al. 2014; Bensby et al. 2014). However, it could be challenging to measure barium at higher metallicities as mentioned before in Delgado Mena et al. (2017); Buder et al. (2019). We also checked that the high [Ba/Fe] stars are also enriched in [Y/Fe] and [Zr/Fe]. The stars detected here do not belong to the enhanced barium stars seen as Am/Fm stars (Fossati et al. 2007; Xiang et al. 2020; Buder et al. 2021), since those are much younger, with high temperatures, $T_{\rm eff}$ > 6500 K and extremely low α abundances. These enriched *s*-process stars could be the outcome of binary stars systems that have accreted mass from a dim white dwarf companion enriching them with heavy elements (McClure 1983). Two of the 103 stars detected here are also in the binary catalogue from Traven et al. (2020). Another possibility is that these stars come from an accretted dwarf galaxy, since in those systems stars can present a different chemical evolution than in the Milky Way.

Outer thin disk (Cyan):

The stars marked as cyan are mainly concentrated at the metal-poor end of the chemical thin disk, occupying the locus of outer disk stars in an [alpha/Fe] and [Fe/H] plot (Hayden et al. 2015; Queiroz et al. 2020). The different populations overlap in [Zn/Fe] and [Ni/Fe]. The cyan points show systematically larger [Ba/Fe] ratios than the thick disk stars (green), but also lower than the rest of thin disk stars. This is into slight contradiction with the inside out picture formation (Chiappini et al. 2001) in which the outer disk star formation history proceeds on longer timescales than the in the inner parts of the Galaxy leading to a larger Ba enrichment by low and intermediate mass stars. Perhaps this population is related to recent works finding metal-poor stars with thin disk rotation

Fernández-Alvar et al. (2021). We see from the right panels of Figure 4.6.2, that the cyan population presents a steep age distribution at about 6.0 Gyr and has an older mean age than the thin disk. The [Mg/Mn] vs. [Al/Fe] diagram, upper panel second column of Figure 4.6.2, shows that the cyan population is at low [Al/Fe] and intermediate [Mg/Mn] borderline to the region occupied by dwarf galaxies (e.g. Limberg et al. 2022b; Hawkins et al. 2015; Das et al. 2020). The chemical characteristics and the older age attributed to this group could also indicate that these stars have been formed by gas polluted by the accretion of a dwarf Galaxy, e.g. *Gaia*-Enceladus dwarf, similar to what Myeong et al. (2022) recently suggests as *EoS* system which would chemically evolve to resemble the outer thin disk. Another possible interpretation for the characteristics of the cyan group is that they are the outcome of the perturbation caused by one of the passages of the Sagittarius Dwarf. In the star formation history reconstructed by Ruiz-Lara et al. (2020) there is a clear peak at about 5.7 Gyr which coincides with the mean age of the cyan group found by the t-SNE+HDBSCAN method. As Ruiz-Lara et al. (2020) suggests, these stars were possibly formed by a pericenter passage of the Sagittarius dwarf about 6.0 Gyr ago. The robustesness of this group is not very strong when we introduce noise to the t-SNE method as seen in appendix 4.C, which means this populations has a weak signal in the data and needs further investigation.

Young chemically peculiar stars (Navy blue, purple):

These two groups of stars are amongst the youngest stars detected by our method. They present high rotational velocities and very low dispersion indicating these stars were probably formed within the thin disk. The navy-coloured stars show high [Ni/Fe] and low [Zn/Fe] content and are also at hotter temperatures, T_{eff}>6100K see Figure 4.C.2. The metallicity of the navy stars is concentrated in the metal-poor end of the thin disk, not extending further than Solar metallicities, similar to the previously discussed outer disk but significantly younger. The contribution of nickel is higher than iron in supernova (SNe) type Ia (Tsujimoto et al. 1995; Sneden et al. 1991). As we see in the left lower panel of Figure 4.6.2 thin disk stars gradually become more [Ni/Fe] enriched for higher metallicities where SNe type Ia contribution dominates the interstellar medium. Therefore is puzzling that the stars rich in [Ni/Fe] have metallicities lower than solar. Since these stars are at a similar temperature range, it could also indicate a problem in the pipeline. In contrast, the purple stars cover almost the whole range of metallicities as the thin disk, but they present low [Ba/Fe], similar to thick disk stars and very low [Zn/Fe]. Trends of low [Zn/Fe] for higher metallicities are seen in the direction of the Galactic bulge (Barbuy et al. 2015; Duffau et al. 2017), although the stars that we discuss here appear too young to have migrated from the Galactic centre. It is also true that for this populations the robustesness of the groups is heavily perturbed when we introduce noise to the t-SNE as seen in appendix 4.C.

Table 4.6.2: Mean parameters of the genuine thick disk found in the different surveys

Survey	*age* (Gyr)	σ_{age} (Gyr)	V_ϕ (km/s)	σ_{V_ϕ} (km/s)
LAMOST DR7 MRS	11.12	1.35	192.66	52.50
GALAH DR3	10.38	1.03	191.78	40.98
APOGEE DR17	10.77	1.33	181.31	42.37

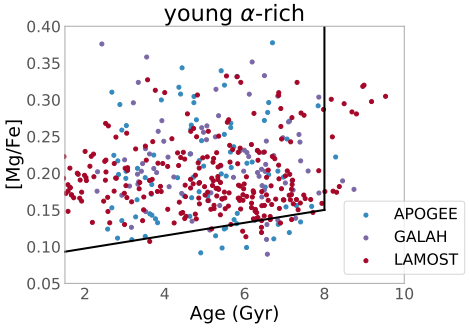

Figure 4.6.6: Age vs. [Mg/Fe] for the young α-rich groups found in APOGEE, GALAH and LAMOST. The black delineation shows the region where chemical evolutionary models cannot explain, as in Chiappini et al. (2014).

4.7 Conclusions

We present new StarHorse catalogues for eight (past and ongoing) spectroscopic surveys, coupled with *Gaia* DR3 and multi-wavelength photometry. We deliver a total of 10 998 676 distances, extinctions, masses, temperatures, surface gravity, metallicities, as well as ≈ 4 million age estimates for MSTO+SGB stars. For APOGEE DR17 results are also available, except for the ages, as a value added catalogue of the survey (Abdurro'uf et al. 2022).

Compared to the Q20- StarHorse release, we have included new results for more than 4 million stars from *Gaia* RVS spectra and additional data from LAMOST, GALAH, APOGEE and GES. For RAVE DR6 and SDSS/SEGUE we have updated our results to include *Gaia* DR3 parallaxes. We also make available StarHorse ages for the first time by selecting stars in the MSTO+SGB evolutionary stages, since the age determination by isochrone fitting methods is not reliable outside of this regime.

A validation against other methods (Xiang & Rix 2022; Buder et al. 2022; Mints 2020) and OCs (Cantat-Gaudin et al. 2020) have shown that our ages are trustworthy for stars older than 2 Gyr. StarHorse parameters have also been extensively validated in S16; Q18; Q20.

We deliver typical distance uncertainties of about 4-10% and SGB age uncertainties of about 8-20%, depending on the survey's spectroscopic resolution. For distances our results are about 5 to 10% better than when spectroscopic information is not used (Anders et al. 2022; Bailer-Jones et al. 2021). The inclusion of *Gaia* DR3 astrometry, along with improvements in the spectroscopic pipelines of GALAH, APOGEE, LAMOST and GES, allowed us to determine more precise parameters than in our earlier papers (Q18; Q20).

By combining the chemical abundances and radial velocities from the spectroscopic releases with the final StarHorse data products we were able to make the following findings:

- We have shown classical diagrams of [α/Fe] vs [Fe/H] colour-coded by age for each of the eight spectroscopic surveys. The results manifest the old thick disk population at high [α/Fe], the old acreted metal-poor stars with low α abundances, and a transition population extending from the thick disk to the high metallicity inner thin disk stars with intermediate ages (Anders et al. 2018; Ciucă et al. 2021; et al. in prep.). We see a non-linear relation between α abundances and age for surveys with typical uncertainties below 30%. We also notice in Figure 4.4.9 that the age dispersion decreases with increasing [α/Fe], in LAMOST LRS, the age dispersion is of about 3 Gyr for an $[\alpha/Fe]$ = -0.1 and of only 1.4 Gyr for an [α/Fe]$\sim$ 0.3. The statistics are similar for the other surveys, indicating that old stars (mostly thick disk high-α) had a fast formation history (Miglio et al. 2021).;
- The dependence of *s*-process/α-process abundances ratios against age (chemical-clocks) for the local sample of SGB stars reveals a linear correlation in most cases. The correspondence is strong for several abundance ratios, especially for [Ba/α]. A comparison with literature results of Spina et al. (2018); Jofré et al. (2020); Casamiquela et al. (2021b) for the same chemical clocks shows a similar effect, demonstrating that the StarHorse ages are sensitive enough to the abundance variations. The chemical clock's determination also covers a large number of stars in the local volume of GALAH DR3 (≈ 18 000 stars).
- Using an unsupervised machine learning approach coupled with a clustering algorithm, we can map different populations into their unique chemical age properties. For this exercise, we have collected a set of abundances spanning distinct nucleosynthetic paths and the SGB ages for three different surveys APOGEE DR17, GALAH DR3 and LAMOST MRS. In all samples, we recovered the same three populations: chemical thin disk,

genuine thick disk and young-α-rich stars corroborating the method's robustness. We stress that our method avoids pre-assumptions on the chemistry or kinematics of the thick and thin disk components of the Milky Way.

- Our results show that the stars we obtained from t-SNE+HDBSCAN cluster method and that follow the chemical pattern of thin disk have low α abundances, span a broad distribution in metallicity, have a mean age of about 5.0 Gyr, prominent peaks at 3 Gyr and a flattened distribution from 4 to 9 Gyr. These chemical characteristics and the flattened distribution of ages are in line with the slow and inside-out formation of the thin disk (Chiappini et al. 1997; Minchev et al. 2013). At the same time, the younger counterpart shows the influence of mergers in the star formation history of the thin disk (Ruiz-Lara et al. 2020). In APOGEE and LAMOST, a small portion of stars also extends to ages larger than 10 Gyr, indicating clumpy star formation scenarios in the early disk (Beraldo e Silva et al. 2021).;

- Stars marked as green in Figures 4.6.1, 4.6.2, and 4.6.3 represent genuine thick disk stars. They have high [α/Fe] and lower metallicity, as seen by many works in the literature (Adibekyan et al. 2011; Bensby et al. 2014; Anders et al. 2014). We find mean age values in this group ranging from 10.38-11.77 Gyr depending on the survey, although all age distributions exhibit a double peak at $\approx$ 11.5 Gyr and $\approx$ 9.5 Gyr. The younger counterpart of the genuine thick disk is probably a contribution of another population described in the literature as transition or bridge stars (Anders et al. 2014; Ciucă et al. 2021), further analysis of transition stars with high-resolution samples is part of a forthcoming paper (et al. in prep.). These results corroborate a formation scenario for the thick disk that happened at lookback times of z $\approx$ 2 (lookback time of 10-12 Gyr), and according to it, the small age dispersion of 1.05-1.35 Gyr indicates that the thick disk was fully formed before the interaction with *Gaia* Enceladus (Miglio et al. 2021; Montalbán et al. 2021).;

- The genuine thick disk dispersion in velocity is strikingly different from the thin disk, with values of standard deviation in vertical and azimuthal velocity of about 50 km/s which is in agreement with recent self consistent dynamical models of the Milky Way (Robin et al. 2022). This result also agrees with the kinematics of extragalactic thick disks at redshift $\approx$ 2. Based on KMOST integral field spectroscopy Übler et al. (2019); Förster Schreiber & Wuyts (2020) suggest that gravitational instabilities power the large velocity dispersions observed in thick disks. This suggests the chemical bimodality (Queiroz et al. 2020) to be linked to a kinematical bimodality (Miglio et al. 2021), a clear signature of stellar populations formed during different star formation regimes.

- We find a significant number of young α-rich stars in all surveys studied with t-SNE and HDBSCAN (427 stars). These stars have chemical enrichment and kinematics very similar to the genuine thick disk but a contrasting younger age that cannot be explained by any Milky way evolutionary models (Chiappini et al. 2015; Martig et al. 2015). The fact that these stars present large velocity dispersions suggests that they were formed in the same gas as the genuine-thick disk (Silva Aguirre et al. 2018; Miglio et al. 2021; Lagarde et al. 2021). They appear to be younger because they potentially are the outcome of binary stars mergers (Jofré et al. 2016).

- Besides the chemical thin disk, thick disk and young α-rich stars, we find in the GALAH DR3 SGB sample another four groups within the low-α regime. Some

of these stars show high *s*-process enrichment (red), some show characteristics similar to outer disk stars (cyan), and some are young and show peculiar enrichments in iron-peak elements (purple and navy blue). These population singularities can be caused by mass accretion in binary interactions and consequent passage and perturbation from dwarf galaxies. The stars marked as the outer disk (cyan) have a steep age very similar to one of the peaks in the Milky Way star formation history associated with the passage of the Sagittarius dwarf about 6.5 Gyr ago (Ruiz-Lara et al. 2020). Although the signal of this populations in the t-SNE method is weaker and can be easily perturbed by noisy data, a detailed study of these populations is still needed.

In summary, we deliver catalogues with precise astrophysical parameters for public spectroscopic surveys and for the first time, we provide age estimates on a large scale. These catalogues are fundamental for Galactic archaeology and work as optimal training sets for machine learning algorithms that extend these results to larger samples. The new approach we presented here by joining t-SNE+HDBSCAN to detect different chrono-chemical populations in the solar neighbourhood has shown to be robust across surveys of various pipelines and resolution quality, sampling a variety of chemical elements. The method is ideal to disentangle the overlapping properties of stellar populations in our Galaxy. We also make available a catalogue with the IDs of all the groups we found. In two accompanying papers, we use this technique, applied to high-resolution samples, to study the age and chemical structure of the local disk (revealing clearly distinct thin disc, thick disc, and high-alpha metal-rich components; et al. in prep., and the Galactic bulge population also in comparison to local samples, but without age information; Queiroz et al. submitted). Two recent publications make use of our datasets to succesfully investigate and characterize halo substructures (Perottoni et al. 2022; Limberg et al. 2022a). All the samples published here in conjunction with the first release of ages will play a vital role in the future. With 4MOST (de Jong et al. 2019), we can extend the volume for which this will be possible.

Acknowledgements We thank the referee for the suggestions and contructive report. The `StarHorse` code is written in python 3.6 and makes use of several community-developed python packages, among them *astropy* (Astropy Collaboration et al. 2013), *ezpadova*[22], *numpy* and *scipy* (Virtanen et al. 2019), and *matplotlib* (Hunter 2007). The code also makes use of the photometric filter database of VOSA (Bayo et al. 2008), developed under the Spanish Virtual Observatory project supported from the Spanish MICINN through grant AyA2011-24052.

Funding for the SDSS Brazilian Participation Group has been provided by the Ministério de Ciência e Tecnologia (MCT), Fundação Carlos Chagas Filho de Amparo à Pesquisa do Estado do Rio de Janeiro (FAPERJ), Conselho Nacional de Desenvolvimento Científico e Tecnológico (CNPq), and Financiadora de Estudos e Projetos (FINEP).

Funding for the Sloan Digital Sky Survey IV has been provided by the Alfred P. Sloan Foundation, the U.S. Department of Energy Office of Science, and the Participating Institutions. SDSS-IV acknowledges support and resources from the Center for High-Performance Computing at the University of Utah. The SDSS web site is www.sdss.org.

Funding for the Sloan Digital Sky Survey IV has been provided by the Alfred P. Sloan Foundation, the U.S. Department of Energy Office of Science, and the Participating Institutions. SDSS acknowledges support and resources from the Center for High-Performance Computing at the University of Utah. The SDSS web site is www.sdss.org.

SDSS-IV is managed by the Astrophysical Research Consortium for the Participating Institutions of the SDSS Collaboration including the Brazilian Participation Group, the Carnegie Institution for Science, Carnegie Mellon University, the Chilean Participation Group, the French Participation Group, Harvard-Smithsonian Center for Astrophysics, Instituto de Astrofísica de Canarias, The Johns Hopkins University, Kavli Institute for the Physics and Mathematics of the Universe (IPMU) / University of Tokyo, Lawrence Berkeley National Laboratory, Leibniz-Institut für Astrophysik Potsdam (AIP), Max-Planck-Institut für Astronomie (MPIA Heidelberg), Max-Planck-Institut für Astrophysik (MPA Garching), Max-Planck-Institut für Extraterrestrische Physik (MPE), National Astronomical Observatory of China, New Mexico State University, New York University, University of Notre Dame, Observatário Nacional / MCTI, The Ohio State University, Pennsylvania State University, Shanghai Astronomical Observatory, United Kingdom Participation Group, Universidad Na-

22 https://github.com/mfouesneau/ezpadova

cional Autónoma de México, University of Arizona, University of Colorado Boulder, University of Oxford, University of Portsmouth, University of Utah, University of Virginia, University of Washington, University of Wisconsin, Vanderbilt University, and Yale University.

Guoshoujing Telescope (the Large Sky Area Multi-Object Fiber Spectroscopic Telescope LAMOST) is a National Major Scientific Project built by the Chinese Academy of Sciences. Funding for the project has been provided by the National Development and Reform Commission. LAMOST is operated and managed by the National Astronomical Observatories, Chinese Academy of Sciences.

Funding for RAVE has been provided by: the Australian Astronomical Observatory; the Leibniz-Institut für Astrophysik Potsdam (AIP); the Australian National University; the Australian Research Council; the French National Research Agency; the German Research Foundation (SPP 1177 and SFB 881); the European Research Council (ERC-StG 240271 Galactica); the Istituto Nazionale di Astrofisica at Padova; The Johns Hopkins University; the National Science Foundation of the USA (AST-0908326); the W. M. Keck foundation; the Macquarie University; the Netherlands Research School for Astronomy; the Natural Sciences and Engineering Research Council of Canada; the Slovenian Research Agency; the Swiss National Science Foundation; the Science & Technology Facilities Council of the UK; Opticon; Strasbourg Observatory; and the Universities of Groningen, Heidelberg and Sydney. The RAVE web site is at https://www.rave-survey.org.

This work has also made use of data from *Gaia*-ESO based on data products from observations made with ESO Telescopes at the La Silla Paranal Observatory under programme ID 188.B-3002.

This work has made use of data from the European Space Agency (ESA) mission *Gaia* (www.cosmos.esa.int/gaia), processed by the *Gaia* Data Processing and Analysis Consortium (DPAC, www.cosmos.esa.int/web/gaia/dpac/consortium). Funding for the DPAC has been provided by national institutions, in particular the institutions participating in the *Gaia* Multilateral Agreement.

This work was partially supported by the Spanish Ministry of Science, Innovation and University (MICIU/FEDER, UE) through grant RTI2018-095076-B-C21, and the Institute of Cosmos Sciences University of Barcelona (ICCUB, Unidad de Excelencia 'María de Maeztu') through grant CEX2019-000918-M. FA acknowledges financial support from MICINN (Spain) through the Juan de la Cierva-Incorporcion programme under contract IJC2019-04862-I.

A.P.-V. acknowledges the DGAPA-PAPIIT grant IA103122.

TM acknowledges financial support from the Spanish Ministry of Science and Innovation (MICINN) through the Spanish State Research Agency, under the Severo Ochoa Program 2020-2023 (CEX2019-000920-S) as well as support from the ACIISI, Consejería de Economía, Conocimiento y Empleo del Gobierno de Canarias and the European Regional Development Fund (ERDF) under grant with reference PROID2021010128."

CG and EFA acknowledge support from the Agencia Estatal de Investigación del Ministerio de Ciencia e Innovación (AEI-MCINN) under grant "At the forefront of Galactic Archaeology: evolution of the luminous and dark matter components of the Milky Way and Local Group dwarf galaxies in the Gaia era" with reference PID2020-118778GB-I00/10.13039/501100011033

CG also acknowledge support from the Severo Ochoa program through CEX2019-000920-S

EFA also acknowleges support from the 'María Zambrano' fellowship from the Universidad de La Laguna.

4.A Chemical clocks dependency

In Section 4.5 we discussed the trends between ages and different abundances, and we derived chemical-clock relations based on a linear fit to GALAH and APOGEE [*s*-process/α-process] abundance ratios. Temperature and metallicity can also influence the spectroscopic pipeline and therefore will have a impact in the uncertainty and precision of the derived age. We can expect that the dispersion around the trend we detected in Figures 4.4.10 and 4.4.11 would be an increasing function as temperature increases and metallicity decreases, since those stars have lines harder to detect. We show in Figures 4.B.1 and 4.B.2 that indeed the more metal-poor stars have a larger spread around the mean trend while this effect is not as clear in Temperature since this parameter has a stronger dependence with age. We refer the reader to other chemical-clock analysis where metallicity is also considered in the fitting procedure or only a certain range of metallicity is taking into account (e.g. Casamiquela et al. 2021b; Viscasillas Vazquez et al. 2022). One can also notice that the metallicity dependence is way less strong for the [Y/Mg], which was already noticed by Nissen et al. (2020).

4.B APOGEE DR17 abundances

In this section, we investigate the abundance uncertainties and the different stellar synthesis approaches used by the ASPCAP APOGEE DR17 pipeline (García Pérez et al. 2016; Jönsson et al. 2020). Since the ASPCAP pipeline is primarily focused on and optimized for giant stars, we want to investigate how reliable the abundances used in this work are for the MSTO-SGB stars. We only show figures for the MSTO-SBG regime between temperatures of 5000K-6000K and cleaned by: SNREV > 70, ASPCAP_CHI2 < 25, ASPCAPFLAG=0, STARFLAG=0, ELEM_FE_FLAG=0. We see that the uncertainties show in Figure 4.B.3 are mostly bellow 0.3 dex for [Mg/Fe],[Si/Fe],[Al/Fe], [Ca/Fe], [Mn/Fe] and [Ni/Fe], statistics is very low for [Co/Fe] and [Ce/Fe], < 3 000. The signal-to-noise, SNREV, is higher for smaller uncertainties, as expected. Still, the quality of the match with synthetic spectral models, ASPCAP_CHI2, is worse for stars with low uncertainty, which might be an effect caused by the temperature range of these stars. Figure 4.B.3 compare the results from two different spectral synthesis codes available on the APOGEE DR17 release. The official release from APOGEE uses a new spectral synthesis code, Sysnpec (Hubeny & Lanz 2017), that can accommodate the effects of non-local thermodynamical equilibrium (non-LTE) for Na, Mg, K, and Ca (Osorio et al. 2020). Although Synspec allows for non-LTE calculations, it uses the assumption of plane parallel geometry which is not entirely valid for large giant stars. While the previous synthesis code used in the APOGEE pipelines, Turbospec (Alvarez & Plez 1998), can use spherical geometry but cannot consider non-LTE effects. The figure 4.B.4 shows non-negligible differences for several elements. We see high spreads for [Na/Fe], [Ti/Fe] and [Cr/Fe], but since those have significant uncertainties, we did not include them in the scientific analysis of this manuscript. Non-LTE effects might be able to explain the differences between the codes, especially for [Na/Fe].

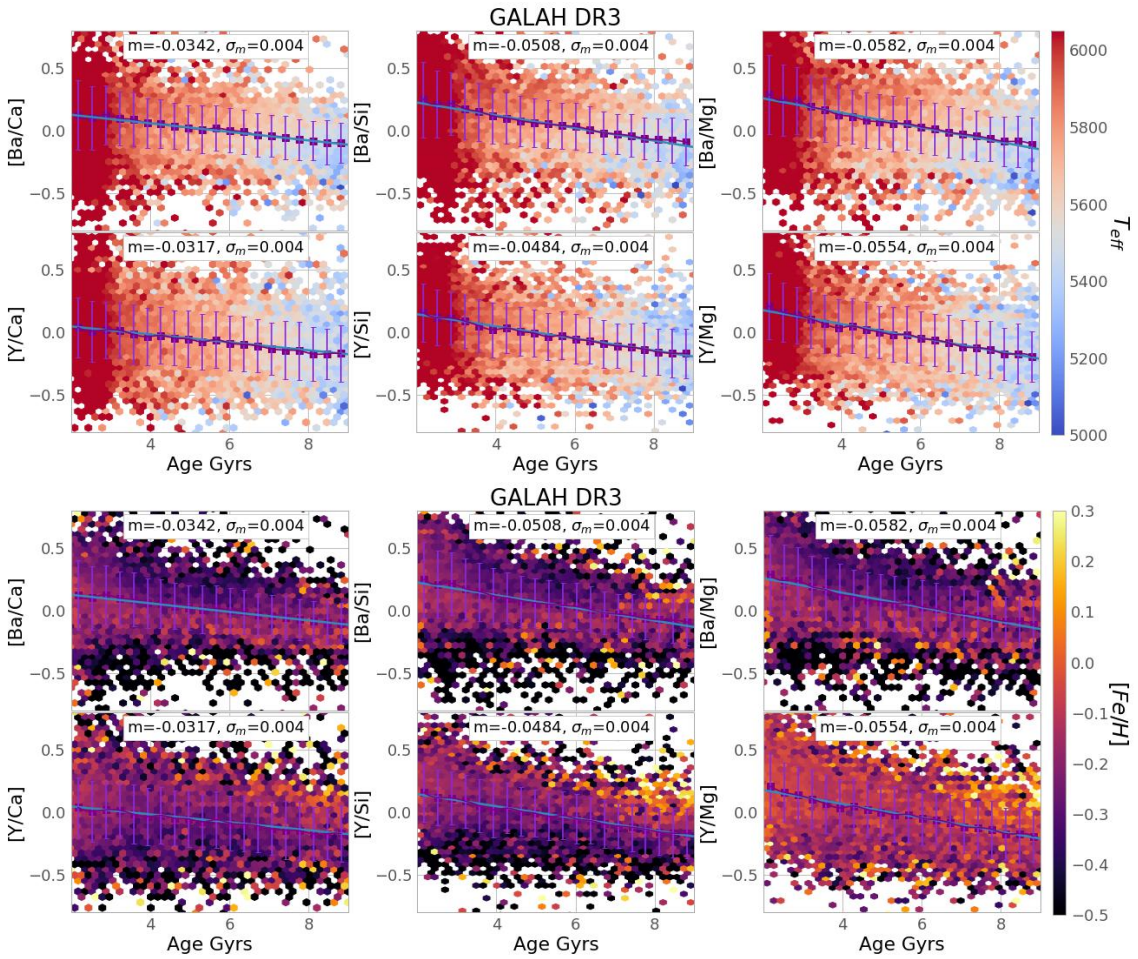

Figure 4.B.1: [s/α] abundance ratios vs. age for GALAH. The purple line shows the median abundance per age bin and the error bar represents one sigma deviation from the median as in Figure 4.4.10 but now colour coded by temperature upper panels and metallicity lower panels.

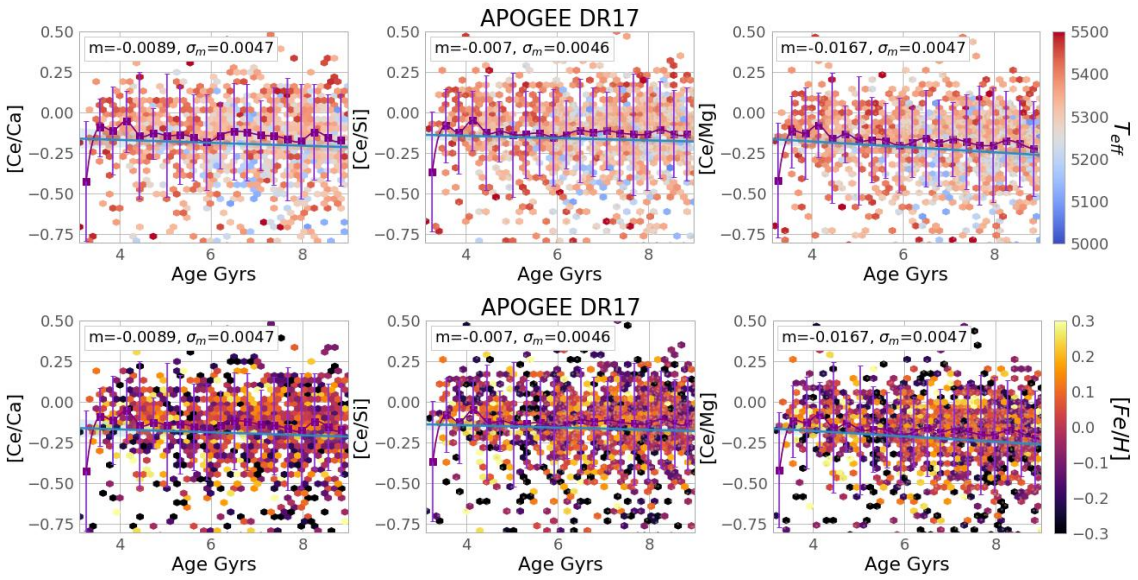

Figure 4.B.2: [s/α] abundance ratios vs. age for APOGEE. The purple line shows the median abundance per age bin and the error bar represents one sigma deviation from the median as in Figure 4.4.11 but now colour coded by temperature upper panels and metallicity lower panels.

Still, a clear shift is seen for abundances such as [Si/Fe] and [Al/Fe] for temperatures colder than 5500 K, which could be an artefact in the derivation of the abundances. We, therefore, abstain from using [Si/Fe] and [Al/Fe] for temperatures cooler than 5500. [Ce/Fe] shows no concerning differences between the two spectral synthesis codes.

4.C Additional t-SNE and HDBSCAN analysis

In this appendix, we add some additional illustrative plots to the combined t-SNE + HDBSCAN analysis performed in Sect. 4.6 for each of the three SGB samples (GALAH, APOGEE, LAMOST).

In principle, there are a number of hyperparameters both in t-SNE and in the HDBSCAN methods that need to be chosen wisely. Apart from those, the main important choice for our work is the set of input parameters and the selection cuts. We optimised the number of input chemical abundances so that as many chemical elements as possible are used without significantly diminishing the total number of stars with useful abundances. Since t-SNE cannot treat missing data, all chosen chemical abundances have to be mutually available for each star in the final dataset.

Secondly, we needed to choose a sensible configuration of hyperparameters both for t-SNE and HDBSCAN for each survey. In Figs. 4.C.1 through 4.C.6 we show a few plots to explain the choices when using the unsupervised machine learning technique, t-SNE (Hinton & Roweis 2003; van der Maaten & Hinton 2008), in section 4.6 and letting a fixed setting for HDBSCAN. We have experience with the perplexity and the random state parameter to find the optimal t-SNE projection. The perplexity controls the number of nearest neighbours while the random state only influences the local minima of the cost functions, therefore, having a minor impact on the final projection.

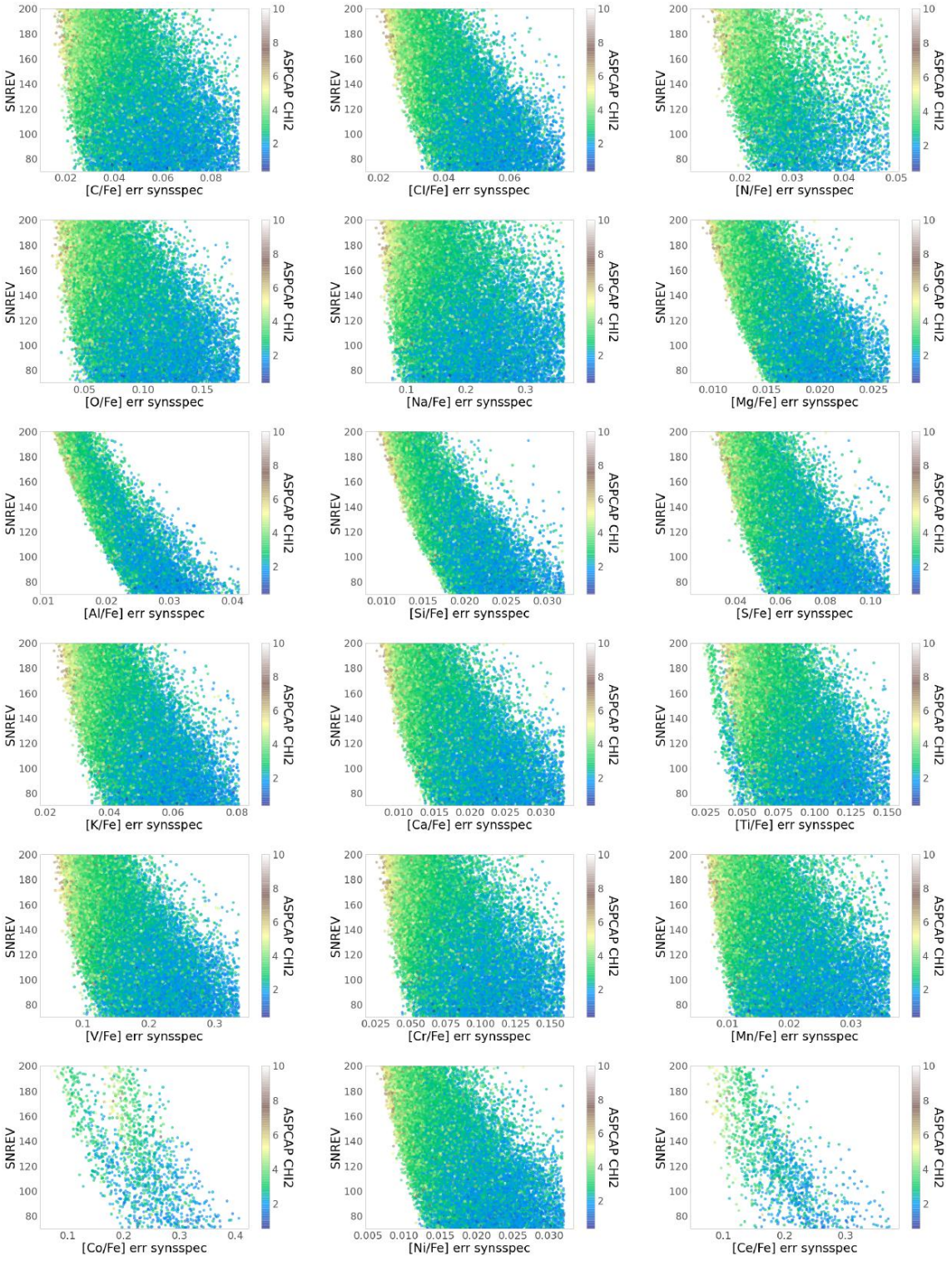

Figure 4.B.3: Abundance uncertainty vs. signal-to-noise ratio (SNREV) for each chemical species published in APOGEE DR17.

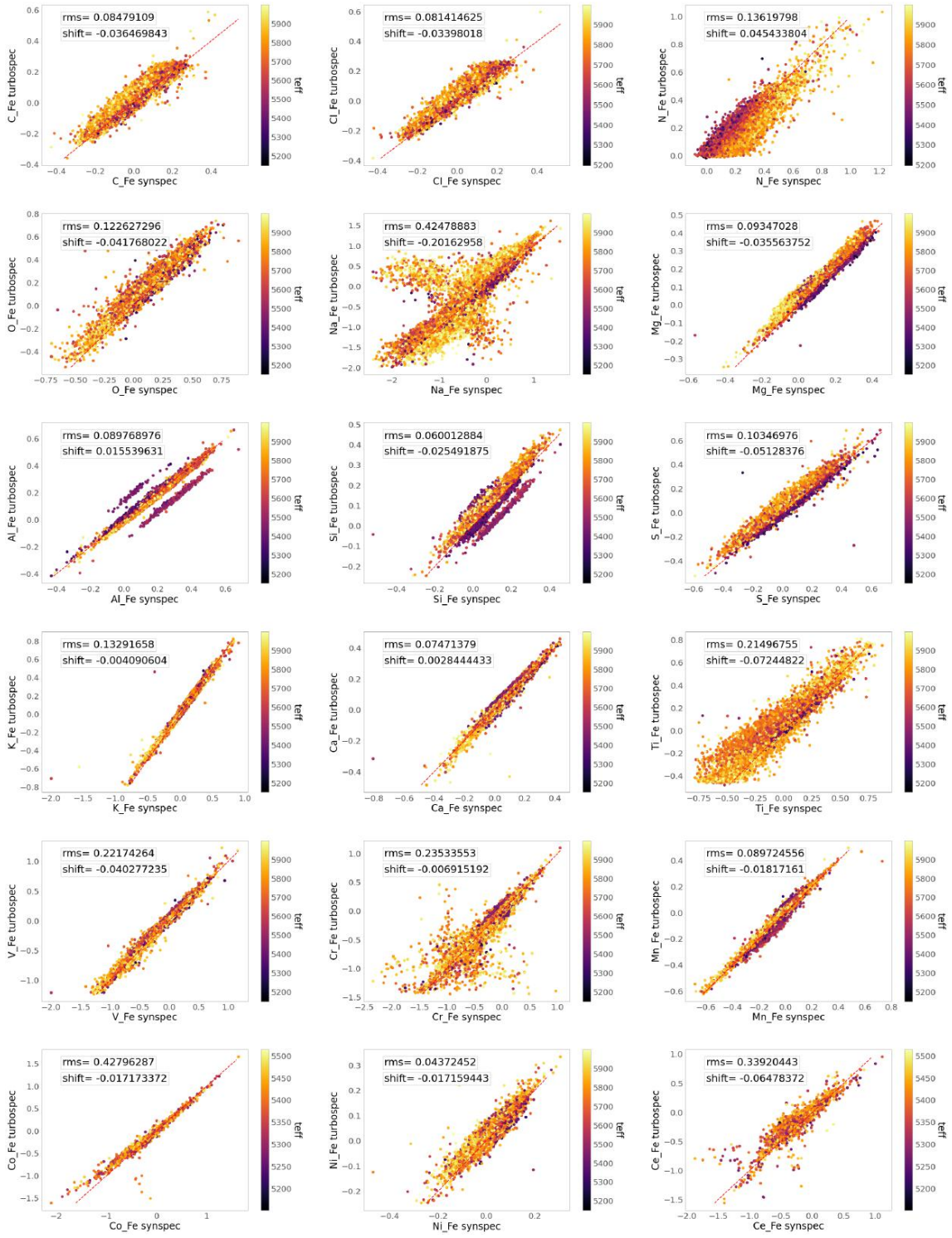

Figure 4.B.4: Comparison between turbospec and synspec APOGEE DR17

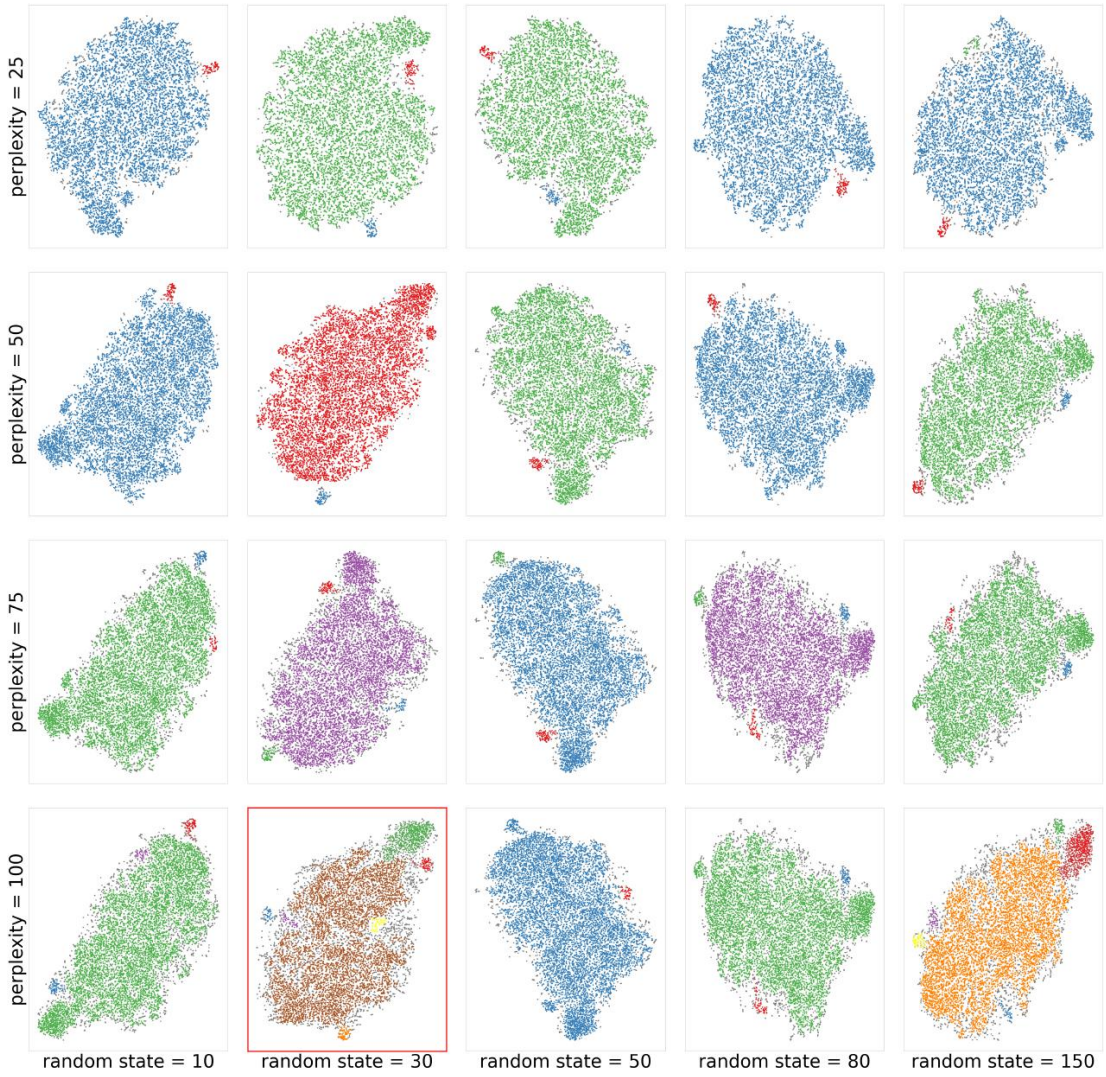

Figure 4.C.1: The t-SNE projection for the GALAH DR3 SGB sample for different perplexity and random state values. We use the HDBSCAN method for each panel on top of the t-SNE projection. The colours represent different overdensities detected by the algorithm.

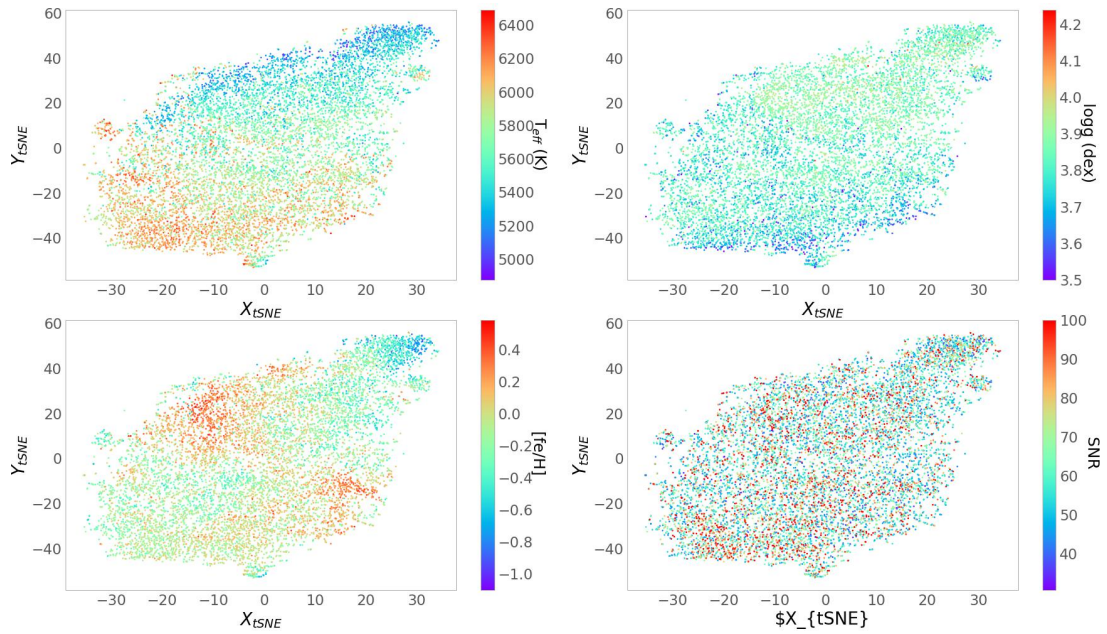

Figure 4.C.2: t-SNE projection for GALAH DR3 SGB data colour coded by $T_{\rm eff}$,$\log g$, metallicity and signal to noise.

Our goal with the method is to find a configuration to detect at least the two main structures of the disk (thick and thin). In Figures 4.C.1, 4.C.3, 4.C.5, we show different choices of t-SNE (perplexity and random_state) for a fixed HDBSCAN choice specified in Table 4.6.1 per survey. Depending on the t-SNE projection, HDBSCAN finds many small clusters. This is not desirable for our study, and we favoured the t-SNE parameters that preserve the global structures in the data.

In the case of GALAH 4.C.1, almost all perplexity values can only recover one large group and two small overdensities. Still, another substantial group can be found at large perplexities (perplexity=100) and random state values (random_state=100 or 30). For APOGEE 4.C.3, almost all solutions can find two or three main clouds. Although, in some cases of perplexity, the thin disk (the most significant cloud in all projections) breaks into many subgroups. Similarly, for LAMOST 4.C.5, only the values of perplexity=15 and 25 find two main global structures.

In summary, the perplexity and random_state are essential values, and need to be explored (Wattenberg et al. 2016), especially when we first apply t-SNE and HDBSCAN on top of it, some choices of perplexities can create patterns and lead the HDBSCAN algorithm to detect false clustering. In the t-SNE analysis of Anders et al. (2018), they also perform a Monte-Carlo experiment to account for the robustness of the grouping, we abstain from making such a test in this paper, but the robustness of the results of t-SNE+HDBSCAN configuration is supported by the fact that we repetitively find the same stellar populations (thin-disk; thick disk; young α-rich) in three completely different data sets.

We similarly chose the final HDBSCAN hyperparameters, first fixing a t-SNE configuration that visually shows two or more overdensities and then we experienced with different values for min_cluster_size, which controls the minimum size of the groupings, the min_samples, which controls how conservative the clustering is and the cluster_selection_epsilon, which controls the separation distance between the groups, for more information on the HDBSCAN parameters we

---

[23] https://hdbscan.readthedocs.io/en/latest/parameter_selection.html

Figure 4.C.3: t-SNE projection for the APOGEE DR17 SGB sample using different values of perplexity and random state. We use the HDBSCAN method for each panel on top of the t-SNE projection. The colours represent different overdensities detected by the algorithm.

recommend the reader to the following page[23]. By testing HDBSCAN hyperparameters with a fixed t-SNE configuration and vice-versa, we have settled for the values described in Table 4.6.1, which optimally separates the chemical thin and thick disks and also find other structures. The chrono-chemical groups found are also reproducible for many other hyperparameter combinations, which supports the groupings' robustness.

In Figures 4.C.2, 4.C.4, 4.C.6 we show the t-SNE projections colour-coded by different parameters. Since this method could project false groups due to artefacts in the chemical abundances derivation. In all cases, the projected t-SNE has no clear dependency on signal-to-noise, which controls the quality of the spectra. For LAMOST and GALAH there is also no clear connection between the projected density and the surface gravity, while for APOGEE Figure 4.C.4 shows that low $\log g$ is preferentially at the bottom left of the map. The temperature and metallicity seem to influence the projections for all surveys. The metallicity is information given to the t-SNE method in the form of abundance ratios; therefore, we expect to find different clumps of metallicity across the new t-SNE dimension. This might also influence the temperature distribution since stars with a certain metallicity are easier to detect at certain temperatures.

4.C.1 t-SNE robustness

Manifold learning algorithms cannot treat observational uncertainties and also do not provide uncertainties associated to the produced mapping. They merely provide a projection of a high-dimensional dataset into a lower-dimensional space. We reinforce that the primary method behind our analysis is the dimensionality reduction technique, collapsing the multiple chemical-age spaces into a 2D visualization. We then use HDBSCAN to avoid delineating the overdensities by eye. Throughout the analysis, we have already had a critical validation of the method: We recover the thin disk, thick disk and young-α-rich in three completely different surveys. Limberg et al. (2021); Ou et al. (2022) have used HDBSCAN alone to find groupings in kinematics space - and Monte-Carlo experiments were able to assign a certain probability of pertinence to the clusters. In our case, this is much more difficult since each random re-sampling of our data will result in a new projection space for t-SNE.

Here we do a small exercise to test the robustness of the groups found by t-SNE+HDBSCAN. As in Anders et al. (2018), see their Figure 5, we introduce noise to the data in a Monte-Carlo experiment test. We have sampled 20 random abundances and ages for each star using a Gaussian distribution centred in the abundance and age using its uncertainties as standard deviation. We have then run t-SNE on this increased random sample. In Figure 4.C.7, we show the result of the new t-SNE projection in this "noisy" data as grey points and with the original tagged groups in their respective colours (See Figures 4.6.3, 4.6.1 and 4.6.2) versus the original t-SNE map. For the thick, thin disk and young α-rich groups, the overdensities are preserved even with the introduced noise in all three surveys. For GALAH, some populations get dispersed by the experiment, especially the young peculiar "navy-blue" group, while the outer disk "cyan" is in the middle of the thin disk group. The high barium stars are an overdensity that remains visibly separable from the thin disk main cloud. We want to stress also that adding noise to the data may artificially blur real signals. Despite the significance of the "Cyan", "Purple" and "Navy blue" groups being less robust, these findings are still an essential first step to the investigation of these populations in the Milky Way since they present some interesting features as the peaked age of the "Cyan" group.

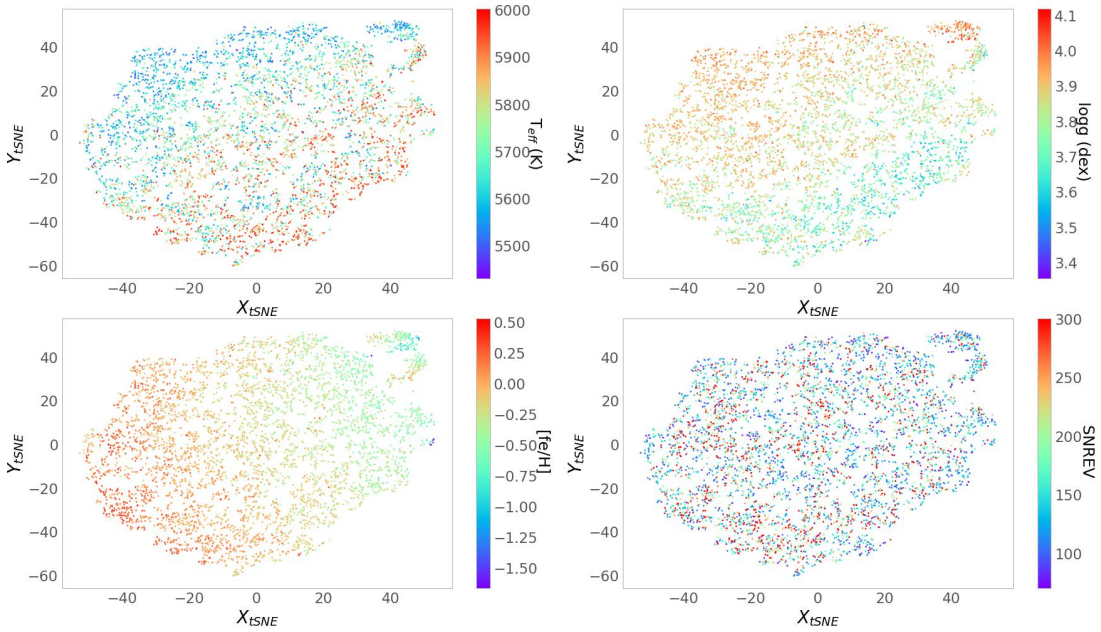

Figure 4.C.4: Same as Figure 4.C.2 but for APOGEE DR17 SGB sample

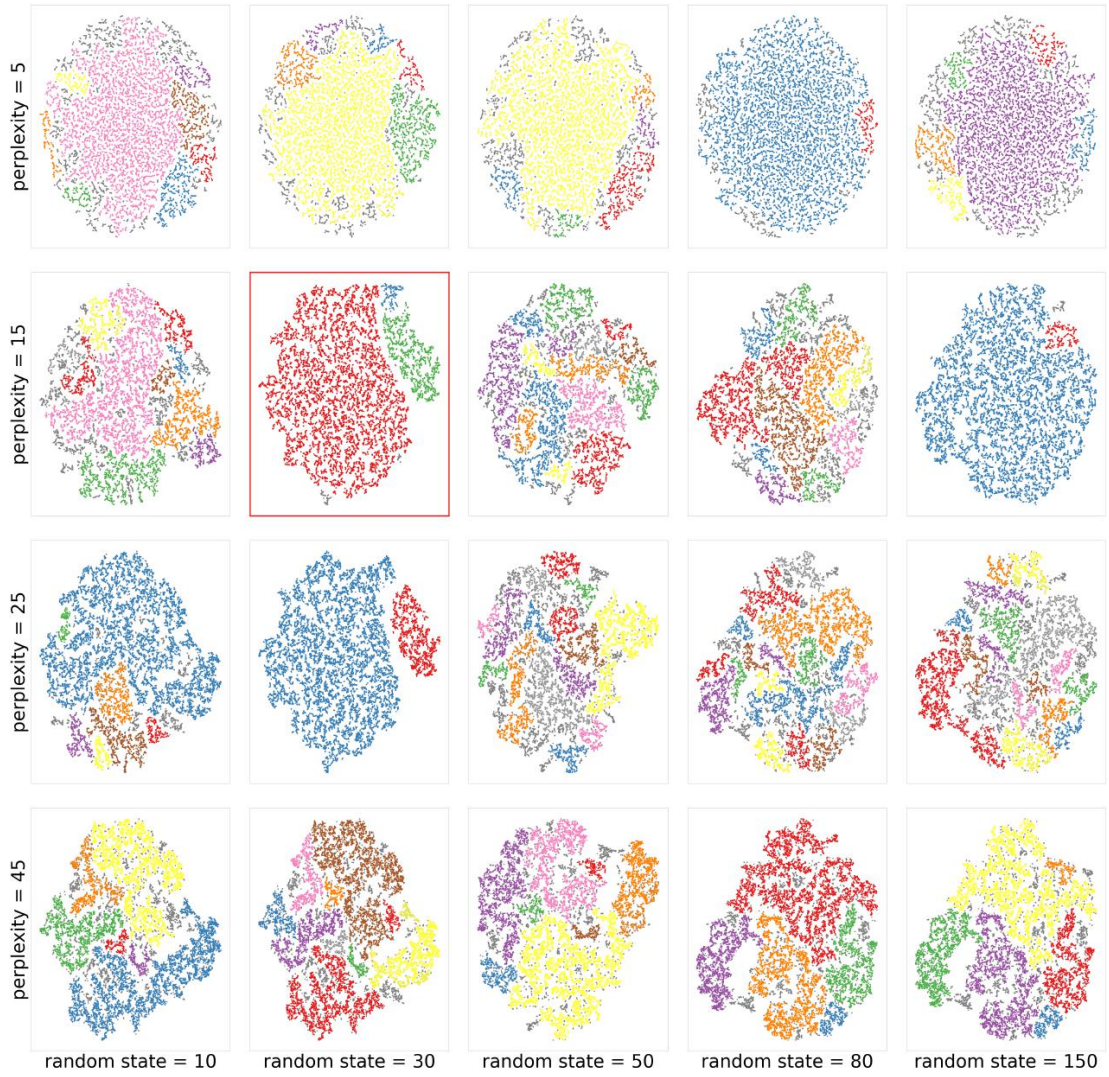

Figure 4.C.5: t-SNE projection for the LAMOST DR7 SGB sample using different values of perplexity and random state. We use the HDBSCAN method for each panel on top of the t-SNE projection. The colours represent different overdensities detected by the algorithm.

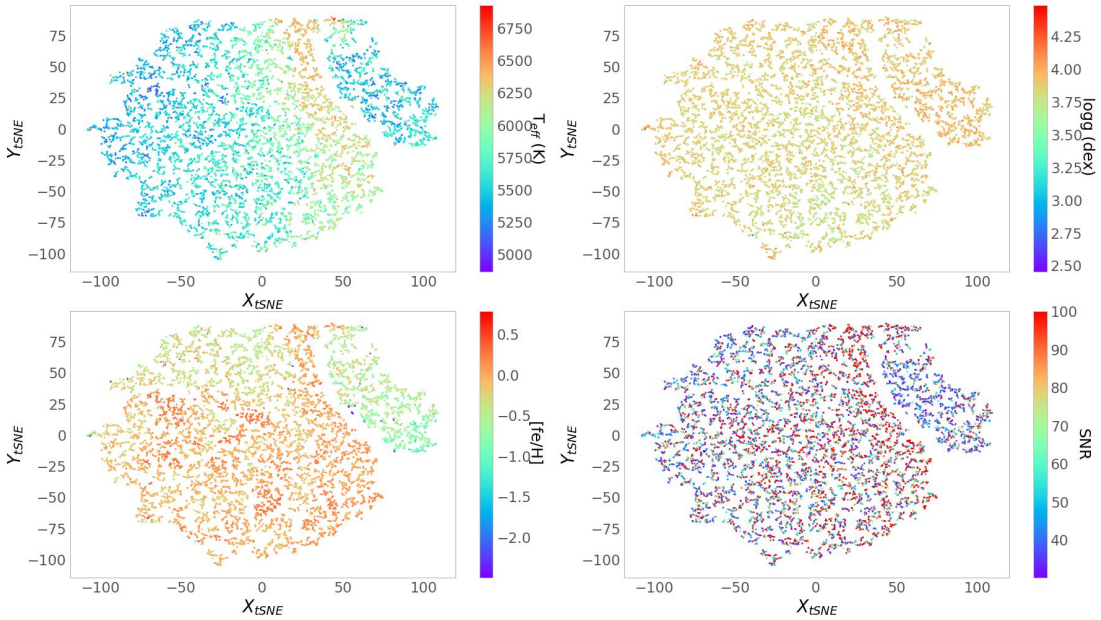

Figure 4.C.6: Same as Figure 4.C.2 but for LAMOST DR7 SGB sample

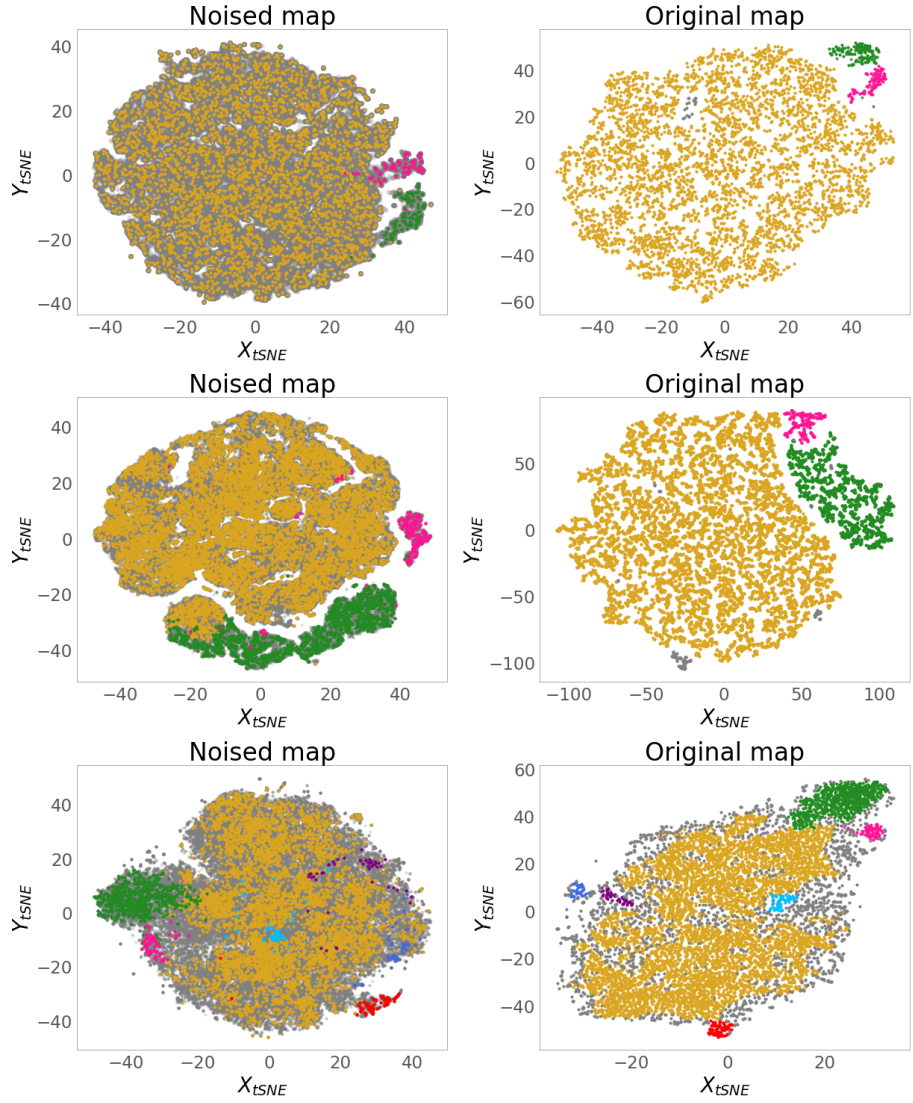

Figure 4.C.7: t-SNE projections of noised data (produced by randomly adding Gaussian uncertainties to the abundances and ages of each star) vs. original data. Top row: APOGEE. middle row: LAMOST. botton row: GALAH

5 Conclusions & Outlook

This thesis has focused on studying the disk and bulge chemo-dynamical properties and searching for the answers to the questions we have raised in the introduction, which are imperative to our understanding of the MW evolution and formation. The work we have presented here is a consequence of the colossal set of information available in the present day by spectroscopic, photometric, and astrometric surveys, which allows a detailed analysis of individual abundances and dynamical phase space for millions of stars in our Galaxy.

The insurgence of the *Gaia* ESA mission astrometry has provided a detailed tomography of the solar vicinity. With `StarHorse`, we can considerably extend the range of precise distances from the inner-most (R_{Gal}<2 kpc) to outermost (R_{Gal}<20 kpc) regions of the Galactic plane. The resulting parameters[24] of `StarHorse` discussed in Chapter 2 are crucial for scientific analyses of the Galaxy by various authors helping to characterize the merger assembly of the Galaxy (Hayes et al. 2020; Fernández-Trincado et al. 2020c,b; Limberg et al. 2021; Perottoni et al. 2022), serving as a training set for machine learning algorithms (Guiglion et al. 2020), as a comprehension of the physical carriers of diffuse stellar bands (Zhao et al. 2023), studies of the bulge samples (Razera et al. 2022; Souza et al. 2023; Schultheis et al. 2020), and as benchmark comparison with many methods (Rojas-Arriagada et al. 2020; Gudin et al. 2021; Plotnikova et al. 2022), especially as a validation of the geometric Bayesian distances from *Gaia* EDR3 (Bailer-Jones et al. 2021). Combining spectroscopy with photometry and astrometry results in significantly smaller distance uncertainties, with a mean of 5% (see Chapter 4) in relative errors compared to 15% when only using photometry and *Gaia* (Anders et al. 2022; Bailer-Jones et al. 2021). Therefore the parameters we made available are references to many methods.

Integrating data from the *Gaia* and APOGEE surveys have yielded promising results in advancing our understanding of the chemo-dynamical properties of the disk and bulge of the Galaxy. The high-resolution spectra from APOGEE allow us to gain new insights into previously obscured regions of the Galactic plane due to high levels of extinction, but with the infrared spectral range of APOGEE, we could obtain chemical abundance data in these areas for the first time. Our study has generated various maps and correlations across the disk that are crucial for quantitative comparison with chemical evolutionary stellar models as in Spitoni et al. (2021) and Matteucci (2021).

Here we provide a comprehensive examination of the questions raised in Chapter 3.1, highlighting the key findings of our study. We also detail how our work has contributed to the resolution of these questions and identify areas where further research is needed to augment our understanding of the MW.

5.1 How do the high- and low-α-sequences vary across the Galaxy?

Our study, detailed in Chapter 2, can sample thousands of stars across a wide range of Galactocentric radii using APOGEE DR16 and *Gaia* DR2 surveys. We build on the work of Anders et al. (2014); Hayden et al. (2015) to investigate the distribution of α-abundance ratios and metallicities across the Galaxy. Our results confirm previous findings, suggesting that the high-α sequence is chemically homogeneous across the Galaxy and lacks a chemical radial gradient, as reported in (Yan et al. 2019;

24 available in (https://data.aip.de/aqueiroz2020)

Bensby et al. 2011; Boeche et al. 2013). According to previous studies (Cheng et al. 2012; Anders et al. 2014), we also confirm that the chemical thick disk vanishes at $R_{\rm Gal}$ >14 kpc. This suggests the shorter scale length of the high-α sequence, whereas the low-α disk extends to 20 kpc from the MW centre. The chemical characteristics of the outer disks primarily differ from their geometric counterparts. We see that at larger radii, the thin disk starts to flare and has a larger contribution for higher $Z_{\rm Gal}$ (Minchev et al. 2019).

These characteristics align with the scenario where the thick disk formed relatively rapidly and homogeneously. The ages of Chapter 4 corroborate that the thick disk is coeval and homogeneous, as in (Miglio et al. 2021). The formation of the thick disk can be explained by an intense period of gas-rich hierarchical clustering events (Brook et al. 2004; Robin et al. 2014), and recent works are testing the contribution of the *Gaia*-Enceladus merger as a catalyst for the thick disk formation (Montalbán et al. 2021; Ciucă et al. 2022). The inner bins of the Galaxy show an extent of metal-poor stars in the high-α sequence, but further investigation is needed to understand if this extended metal-poor population is part of the enrichment of thick disk in the inner Galaxy or an independent population (Di Matteo et al. 2019).

On the other hand, the chemically thin disk presents a substantial variation across different radii. Our data suggests a positive radial [α/Fe] gradient, where the metal-rich α-poor disk becomes gradually α-enhanced in the inner bins. This trend has also been observed in previous works with APOGEE (Anders et al. 2014; Hayden et al. 2015). Low α-sequence super metal-rich stars [Fe/H] $>$ 0.45 are typically located in the inner Galaxy. As one walks to further radii, more metal-poor stars dominate the low-α regime. This is consistent with an inside-out slow formation of the thin disk and with theories suggesting that high metallicity stars found in the solar neighbourhood are the outcome of radial migration from the inner Galaxy. The enrichment in [Mg/Fe] of the inner Galaxy also supports this scenario, as Mg has a tighter relation with star formation since this element is solely produced in core-collapse supernovae

For the first time, and different than what was suggested in previous works (Hayden et al. 2015; Zasowski et al. 2019), we can show with a significant number of stars ($R_{\rm Gal}$<2 kpc, $|Z_{\rm Gal}|$<1 kpc, N>5 000) that a chemical bimodality between high- and low-α sequence is present in the most inner bins of the Galaxy. This indicates that the chemical discontinuity is a general characteristic of the chemical enrichment of the Galaxy. Our findings suggest that the Galaxy has experienced two different episodes of star formation, separated by a hiatus as described in the models of (Chiappini et al. 1997), which involves the accretion of gas-rich mergers or primordial gas from the Universe at high redshift. A duality of chemical abundances has also been observed in external Galaxies (Scott et al. 2021; Pinna et al. 2019b,a), indicating it is not a unique trait of the Milky Way, but still inconclusive if that is a standard or rare feature of galaxies in the Universe. The frequency of the chemical duality in cosmological simulations is also not entirely clear. In Buck (2020), they found the chemical dichotomy to be a recurrent feature of the simulated galaxies, while Mackereth et al. (2018) finds that as a rare scenario.

Our maps of [Al/Fe] across the Galactic plane also show a chemical bimodality unique to the inner Galaxy. This strongly indicates a different enrichment path, and [Al/Fe] may be more sensitive to this effect since it has metallicity-dependent yields.

Further research of the inner Galaxy with better coverage of chemical abundances of different nucleosynthesis origins, such as neutron-capture elements, can enlighten our comprehension of the duality in the inner Galaxy and track the different timescales of star formation. High-resolution cosmological simulations, including chemical evolutionary models, are also fundamental for further understanding the high- and low-α dichotomy in different formation scenarios.

5.2 What is the chemo-dynamical structure of the Galactic bar and inner Galaxy?

With *Gaia*, APOGEE, and `StarHorse`, we have finally started to overcome the challenges of defining a complete and accurate selection of stars in the bulge. During the course of this Ph.D, the first observations of APOGEE south were released, adding considerable coverage of the inner Galaxy and a detailed picture of the chemo-dynamical structure of the bar.

In Chapter 3, we analyze a sample of stars in the bulge region by defining a square area in Galactocentric distances, which includes approximately 25 000 stars. Our results are similar to those found by Zoccali et al. (2017), as we observe a clear distinction in the distributions of metal-rich and metal-poor stars. The metal-poor stars appear to form a spherical concentration, while the metal-rich stars are confined to low Galactic heights, with $|Z_{\rm Gal}|$<200 pc. The overall metallicity distribution of the sample shows a broad distribution with a prominent peak at high metallicities. Upon selecting a spherical region in X_{Gal} and Y_{Gal}, the distribution becomes flat from $-0.7 < [Fe/H] < 0.4$ suggesting this is the region with the most contribution of metal-poor stars. This finding was recently corroborated by Rix et al. (2022), they show that metal-poor stars selected from *Gaia* XP spectra form a spherical concentrated region around the Galactic center.

We have calculated Galactocentric cylindrical velocities using the *Gaia* proper motions and APOGEE DR16 radial velocities. We detected a clear signature of bar rotation as a quadrupole pattern in azimuthal velocity (V_ϕ) when mapped into Galactocentric coordinates X_{Gal}, Y_{Gal}. This result, previously shown in Bovy et al. (2019), was even more evident in the inner 5 kpc of the Galaxy, showing a rough estimate of the size of the bar ($\sim$ 4 kpc) and angle with the Sun-GC line ($\sim 20^\circ$). The high-resolution butterfly pattern shown in azimuthal velocities demonstrates that the `StarHorse` distances are accurate enough to reproduce the kinematic signatures of barred potentials. The data can be closely compared to dynamical models that discuss this effect (Debattista et al. 2017; Fragkoudi et al. 2020).

Furthermore, to ensure a high level of accuracy and minimize contamination from foreground stars, we have employed the reduced-proper motion technique (RPM Faherty et al. 2009; Gontcharov 2009) to filter the stars based on their colour and proper motions as measured by the *Gaia* mission. With this sub-sample of clean stars (approximately 8,000), we use the bulge potential of Portail et al. (2017) to calculate the orbits of the stars. Taking advantage of this rich data, we analyze the inner Galaxy in a different manner from previous works by studying the chemo-orbital structure jointly rather than defining samples with cuts in chemistry or kinematics, which can lead to a biases.

By constructing an orbital space defined by the maximum excursion from the plane ($|Z|_{\rm max}$) and eccentricity (Boeche et al. 2013; Steinmetz et al. 2020a), we distinguish the multiple populations that inhabit the inner Galaxy, which manifests themselves in the multi-peaked metallicity distribution (Rojas-Arriagada et al. 2020), and bimodality of [α/Fe] abundance ratio (Queiroz et al. 2020). We have classified the stars as belonging to the Galactic bar using their orbital frequencies in a probabilistic approach, utilizing several Monte Carlo realizations. The results revealed that stars with more than 80% probability of belonging to the bar are part of the α-rich and α-poor sequences, contradicting the classical picture that suggested the bar is composed only of low-α metal-rich stars (Hill et al. 2011; Babusiaux et al. 2010). Our findings reinforce that the bar is formed through secular evolution, which can trap stars from the low- and high-α regime. The fraction of metal-rich stars found in bar orbits is more prominent, indicating that the dynamics of the thin disk play a crucial role in forming the Galactic bar, but the thick disk is also not marginal in the bar formation. Our results agree with studies of metal-poor stars and RR Lyrae, which show that some of these ancient metal-poor stars significantly contribute to bar rotation as stated in Kunder et al. (2020) and Arentsen et al. (2020).

When decomposing the inner Galaxy into different cells of $|Z|_{\rm max}$–eccentricity plane, we find

that the metallicity of the stars close to the mid-plane shows a positive gradient with eccentricity, from less eccentric bins at mean [Fe/H] = 0.2 to most eccentric at [Fe/H] = 0.25. This suggests that during the secular process of the bar development, bursts in star formation can be induced thanks to gas trapping and funnelling toward the centre. The observation that the bar contains super metal-rich stars was also confirmed in the works of (Wegg et al. 2019; Lian et al. 2020) and in the lack of Cepheid observations in the innermost region of the Galaxy (Matsunaga et al. 2016).

The broad range of chemical signatures in the inner Galaxy suggests a hybrid scenario with contributions from at least two distinct stellar populations. This is clearly evident in the bimodality in [α/Fe], as well as in [Mg/Fe] and [O/Fe]. The consistency between the α abundances demonstrates the quality of the APOGEE chemical pipeline in the bulge (Jönsson et al. 2020). Enrichments that trace different timescales, such as [C/N] and [Mn/O], also support the presence of a duality, further reinforcing that populations with different star formation histories characterize the inner Galaxy.

All these findings are pivotal for the chemo-dynamical characterization of the Galactic bar. The data produced in the work of Chapter 3 will carry a legacy for many years since it is the first time we have a good sample of thousands of stars with abundances and orbits in the inner Galaxy.

5.3 Does the Milky Way have classical bulge component?

The analysis in Chapter 3 suggests the potential presence of a classical bulge in the MW, however, further evidence is needed to confirm this. Our study revealed that many metal-poor stars do not conform to the expected orbits of a bar structure and have metallicities that are lower than those of thick disk stars but not as low as those of the inner halo (-0.7 <[Fe/H]> -1.3). Additionally, many of these non-rotating metal-poor stars are located within a mean orbital radius of 3 kpc, providing evidence for the presence of a pressure-supported component. This is supported by various studies that examine the distribution and dynamics of metal-poor stars in the MW (Zoccali & Valenti 2016; Kunder et al. 2020; Arentsen et al. 2020; Rix et al. 2022). There are several possible formation scenarios for a classical bulge in the Milky Way, such as through dissipational collapse at the same time as the formation of the thick disk, hierarchical clumping before the formation of the disk, or the accretion of dwarf galaxies. For a detailed discussion of these formation scenarios, refer to session 4 of Barbuy et al. (2018). The current data and models are not sufficient to confirm the existence of a classical bulge in the Milky Way, but chemical evolutionary models require at least two populations of metal-poor and metal-rich stars to fit the observed MDFs (Bekki & Tsujimoto 2011; Grieco et al. 2012; Tsujimoto & Bekki 2012). Some models also consider an intrinsic chemical gradient of the oldest stars (Pipino et al. 2010) which could have been generated by dissipative collapse. In some models, the gradients can be explained by the contribution of the metal-poor thick disk and the metal-rich inner thin disk (Di Matteo 2016; Debattista et al. 2017; Fragkoudi et al. 2018).

Our data has further highlighted the complexity and diversity of abundance patterns in the inner region of the Milky Way galaxy. By jointly analyzing the chemical and orbital properties of stars, we found evidence for more populations than the thin and thick disks alone can account for. In order to fully understand the different populations in the inner Galaxy, it is essential to quantify the contribution of stars that belong to the disks or inner halo. Some studies propose the existence of a metal-poor extension of the thick disk, known as the "metal-weak" thick disk (Hawkins et al. 2015; Hayes et al. 2018; Di Matteo et al. 2019), which shares similar kinematic characteristics with the thick disk but extends to lower metallicities. However, identifying a population solely based on kinematics can be problematic as dynamical features can change over time, particularly in regions with strong gravitational potential and stellar interactions such as the Galactic bar. Our study, along with many others, has shown that a chemical thick disk is coeval and homogeneous throughout the

disk (Anders et al. 2014; Hayden et al. 2015; Miglio et al. 2021). Therefore, in the inner Galaxy, we might be seeing a superposition of a high-α old metal-poor population. In the different cells of the diagrams in $|Z|_{\max}$–eccentricity, we observe a clear contribution of the thick disk at intermediate values of $|Z|_{\max}$ and eccentricity, with typical local thick disk values of azimuthal velocity, further suggesting the homogeneity of the chemical thick disk.

The distributions of azimuthal velocity (V_ϕ) in the orbital space of $|Z|_{\max}$–eccentricity find amidst the metal-poor stars an extended tail of counter-rotating velocities at 3 $kpc < |Z|_{\max} > 2$ kpc. A similar feature was observed in the study of Lucey et al. (2021); after the comparison with models, they found a significant excess of counter-rotating stars. Further explanations for the presence of the metal-poor counter-rotating population include the possibility that they are associated with a proto-galactic disk that was heated by a merger event — known as the "Splash" (Belokurov et al. 2020) — or that they are the result of clumpy star formation (Amarante et al. 2020; Beraldo e Silva et al. 2021). Additionally, these stars could be the outcome of accretion from an external galaxy. However, their chemical composition does not match *Gaia*-Enceladus or that of "Heracles" debris detected in Horta et al. (2021). An accreted event or strong gas flows at the early stage of Galaxy formation could have played a major role in the establishment of a classical bulge which is in agreement with the old age of RR Lyrae stars (13.41 ± 0.54 Gyr) (Savino et al. 2020) and the observation of high redshift galaxies which show the formation of classical bulges being formed by the high amounts of dissipative gas accretion mergers (Tacchella et al. 2015; Renzini et al. 2018)

In conclusion, our study has provided further evidence for the complexity and diversity of the inner region of the Milky Way galaxy, known as the bulge. Our analysis of the stellar chemical and orbital properties has revealed the presence of multiple populations beyond the thin and thick disks. It is clear that the bulge is a complex region that has been shaped by the contribution and initial formation of all the major components of our Galaxy. Understanding and disentangling its chemodynamical history is crucial for deciphering the primordial steps of Galaxy formation and the interplay between the stellar populations. This includes the quenching in star formation manifested by the clear bimodality, the interactions between stars and dynamical instabilities that form the bar, and the disparate chemical and dynamical characteristics that some populations present, indicating accretion events.

5.4 How to date the stellar populations in our Galaxy using large spectroscopic surveys?

Determining the ages of individual stars is a difficult task. Techniques such as gyrochronology, asteroseismology, and eclipsing binaries can provide estimates with precisions down to 10%, as they rely on additional constraints such as stellar mass. However, these precise techniques are limited in their applicability due to the required long and repetitive observation time and high-resolution instruments such as Kepler (Caldwell et al. 2010). As a result, the sample size of stars that can be studied using these methods is limited (Barnes 2007; Valle et al. 2015; Anders et al. 2017b; Valentini et al. 2019).

Methods such as isochrone fitting, like `StarHorse`, can be efficient tools for deriving ages for a large sample of individual stars. However, they are heavily dependent on the underlying models. There are many degeneracies for certain evolutionary stages where multiple isochrones overlap at a wide range of metallicities and temperatures, mainly at the main sequence and red giant branch (Soderblom 2010). In Chapter 4, we present ages for a large dataset of stars in our Galaxy using `StarHorse` (Queiroz et al. submitted). However, due to the limitations of isochrone fitting, we only provide ages for the subgiant-branch (SGB) and the main sequence turn-off (MSTO), which have

been shown better precision when tested against simulations Queiroz et al. (2018). The ages for SGB are more reliable than the MSTO, as the relationship between luminosity and ages is straightforward during this stage, where stars evolve rapidly. We validate our method against similar Bayesian approaches (Xiang & Rix 2022; Mints 2020; Kordopatis et al. 2022) and benchmarks such as open clusters (Cantat-Gaudin et al. 2020). Our sample includes over four million stars with ages in the solar neighbourhood for eight different spectroscopic surveys. The resulting age samples are crucial for dating the chemical thin and thick disks. The availability of ages for such a large dataset allows us to understand the chemical-age structure of the solar vicinity with statistical significance.

We have presented in Chapter 4 the correlation between the `StarHorse` ages and the chemical abundances of stars as determined by various spectroscopic surveys. When we colour code the [α/Fe] diagram by the ages of each individual star, we confirm the long-establish result that the high-α sequence is mostly old as in Matteucci & Francois (1989); Woosley et al. (2002) and that the low-α sequence is primarily young, but at low metallicities the low-α stars are characterized by old accreted populations (Mackereth et al. 2019). Additionally, find stars between the low- and high- α populations with intermediate ages, which has been designated in the literature as a transition or bridge population and has been suggested to have a distinct origin from the chemical thick disk (Anders et al. 2018; Ciucă et al. 2021). The diagram of [α/Fe] vs age shown in Chapter 4 shows a decreasing age dispersion for the higher [α/Fe], suggesting the high-α sequence had a fast formation and is mostly coeval a result supported by precise asteroseismology measurements was (Miglio et al. 2021) which further validates our isochrone fitting age derivation.

Finally, as an ultimate validation of our ages, we found that the SGB StarHorse ages and the precise chemical abundances from the GALAH and APOGEE surveys reproduce known "chemical clocks" such as the correlation between age and abundances of neutron-capture elements and α elements. Our reported slopes for various abundance ratios, such as [Ba/Mg], [Y/Ca], and [Ba/Si], with age are consistent with previous studies in the literature (Nissen et al. 2020; Casamiquela et al. 2021b; Jofré et al. 2020). The study of chemical clocks is critical for understanding the different enrichment time scales that produced these elements. The correlations can also be used to date other stars in the Galaxy for which isochrone fitting is not possible, although it is necessary to consider the variation in the chemical space caused by Galactic dynamics out of the solar neighbourhood.

5.5 How to distinguish between chemical populations?

The availability of many chemical abundance measurements is crucial for understanding the chemical evolution of the Galaxy. It allows us to constrain the ISM enrichment from which stars were formed. The data from large-scale spectroscopic surveys, such as GALAH, APOGEE and LAMOST, provide access to over 20 abundances for hundreds of thousands of stars, enabling us to use weak chemical tagging to identify the common origin of major stellar populations (Hogg et al. 2016; Freeman & Bland-Hawthorn 2002). As shown in Anders et al. (2018) it is possible to identify different chemical populations using a dimensionality reduction algorithm.

In chapter 4, we utilize a manifold algorithm called t-SNE to effectively transform the n-dimensional chemical and age space into two dimensions, preserving the similarity between points. Unlike in Anders et al. (2018), we utilize a clustering algorithm on top of t-SNE to effectively track the populations. The addition of ages to the high-dimensional space interpreted by t-SNE is helpful, especially when the chemical abundances have large uncertainties. We have applied this method and searched for chrono-chemical groups in three different surveys: APOGEE, LAMOST medium resolution survey and GALAH. The surveys have very different chemical pipelines and resolutions; nonetheless, the method can find three chrono-chemical groups with similar chemical patterns and

ages in each of the three surveys: a genuine thick disk, young α-rich stars and the chemical thin disk.

The genuine thick disk is marked by the chemical characteristics of high [α/Fe], low metallicities, low [Ba/Fe] and high [Mg/Mn] similarly to works who investigates multiple chemical characteristics of thick disk stars (Adibekyan et al. 2012; Anders et al. 2014; Bensby et al. 2014; Delgado Mena et al. 2017). Our analysis shows that the mean age of the genuine thick disk is around 11 Gyr with a small age dispersion of 1.3 Gyr, further supporting the idea of a short formation period and that the thick disk was likely fully formed before the interaction of *Gaia*-Enceladus with our Galaxy (Miglio et al. 2021; Montalbán et al. 2021). The velocity dispersion of the genuine thick disk also shows an abrupt change compared to other groups found in our t-SNE+HDBSCAN method, indicating a distinct formation scenario for this population. The velocity dispersion of 50 km/s is in agreement with recent self-consistent dynamical models (Robin et al. 2022) and observations of thick disk formation in redshift galaxies (z~2) (Übler et al. 2019).

Our method also finds a group of young α-rich stars. They present the chemical pattern of a genuine thick disk but at significantly younger ages. Such characteristics have been detected before in Chiappini et al. (2015), where the authors argue that the current chemical evolutionary models of the MW cannot explain these atypical stars. Further observations of young-α rich stars have suggested it to be an outcome of binary interaction, where mass transfer makes these stars appear considerably younger (Jofré et al. 2016; Silva Aguirre et al. 2018; Lagarde et al. 2021). The large number of $\sim$ 400 newly discovered young α-rich stars is an excellent sample to constrain chemical evolutionary models and further study binary interactions.

The stars found by t-SNE+HDBSCAN methods that follow a chemical pattern of thin disk stars show a large dispersion in metallicity and ages and have a mean age of 5 Gyr. It is clear that the thin disk had a slow formation ranging in ages from 9 to 2 Gyr, which is consistent with the formation scenarios proposed in Chiappini et al. (1997); Minchev et al. (2013) where a second episode of gas infall form the thin disk in an inside out fashion with a slow timescale. The thin disk age distribution peaks also coincide with the influence of the Sagittarius stream as in the star formation history reconstructed by Ruiz-Lara et al. (2020).

Using data from several chemical abundances and ages in the manifold method and a clustering algorithm enabled us to classify the populations in the solar neighbourhood into a thin disk, genuine thick disk and young α-rich. The procedure is robust across spectroscopic surveys of different resolutions and chemical pipelines. The same method can be used on a larger scale and in different regions of the MW to quantify the contribution of the chrono-chemical populations across the Galaxy and will be important by the time model spectroscopic surveys as **W**HT **E**nhanced **A**rea **V**elocity **E**xplorer (WEAVE Dalton et al. 2012) and **4**-**m**etre **M**ulti-**O**bject **S**pectroscopic **T**elescope (4MOST de Jong et al. 2019) deliver their data.

5.6 Quantifying the contribution of the local thin/thick disks to the inner Galaxy

As a future work building on the research presented in this thesis, we aim to further quantify the contribution of the thin and thick disks in the inner region of the Galaxy. By utilizing the t-SNE technique in conjunction with the HDBSCAN clustering algorithm, which were presented in Chapter 4. As we suggested in this conclusion and in Chapter 3, the inner Galaxy shows signs of a superposition of multiple populations as accreted debris (Horta et al. 2021), an excess of counter-rotating stars (Queiroz et al. 2021; Lucey et al. 2021) and a high number of metal-poor stars that do not follow bar orbits (Arentsen et al. 2020; Kunder et al. 2020). On top of those stars, there is

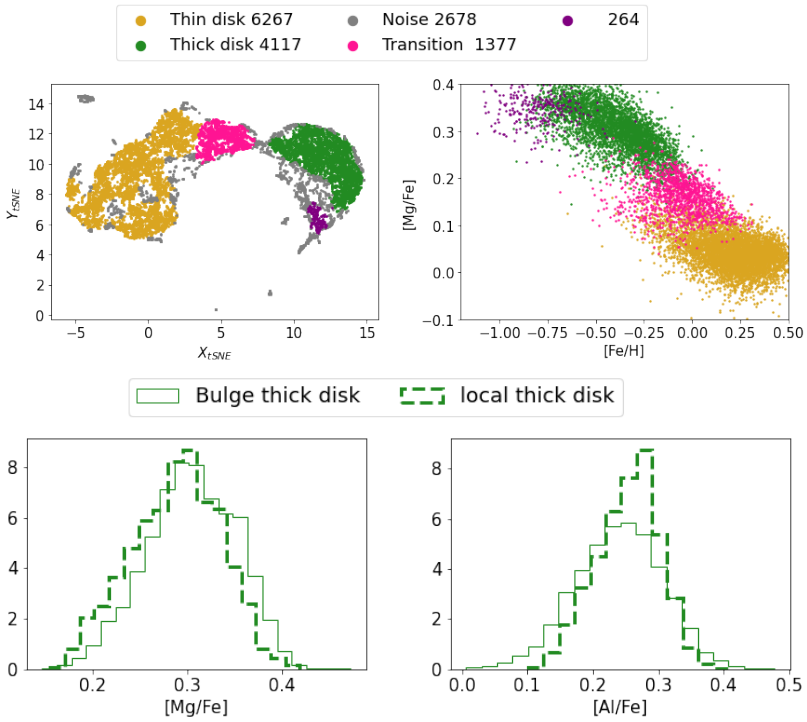

Figure 5.5.1: Upper panel: t-SNE + HDBSCAN applied to an inner Galaxy sample selected from *Gaia*+APOGEE DR17. The groups can be identified as the ones with chemical patterns of the thick disk in green, the thin disk in dark yellow, transition stars in pink and a previously unidentified group in purple. Bottom panel: histogram of the groups found by the t-SNE as the chemical thick disk locally and in the bulge. From Queiroz et al. (in prep.)

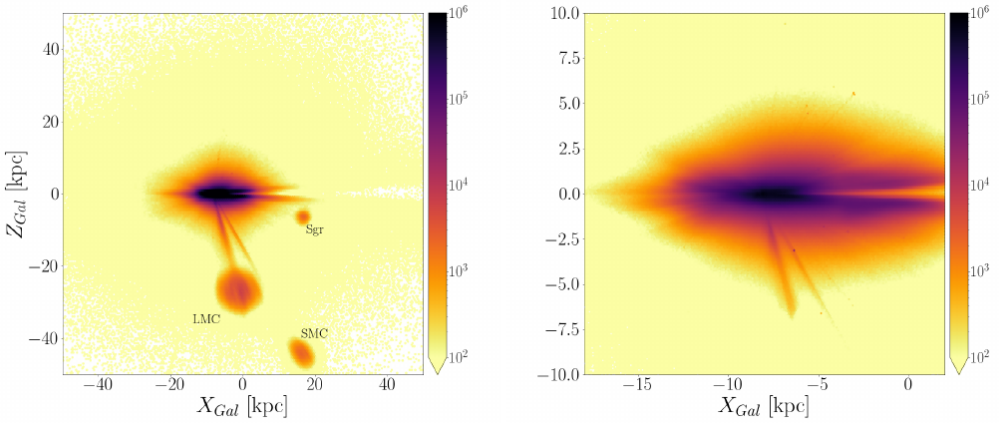

Figure 5.7.1: Galactocentic coordinates $Z_{\rm Gal}$ and $X_{\rm Gal}$ of an extended view of the Galactic halo and zoom given the Galactic disk. Data is constructed using the `StarHorse` for *Gaia* EDR3 and photometric surveys for 300 million stars up to *Gaia*-magnitude (G)<18.5. Image was taken from Anders et al. (2022)

also the contribution of the chemical thin and thick disks. As previously demonstrated, the high-α sequence is homogeneous across different Galactic radii (Anders et al. 2014; Hayden et al. 2015; Miglio et al. 2021). Therefore, we expect the inner Galaxy to exhibit similar characteristics. We use the t-SNE+HDBSCAN both in the inner Galaxy and in a local sample to compare the differences between populations in those distinct regions of the Galaxy.

In Figure 5.5.1, we demonstrate this approach using APOGEE DR17 (Abdurro'uf et al. 2022) data for a local sample (d <1 kpc; N ~ 10 000) and in the bulge (6 < d <10 kpc, N~ 15 000). We only use red giants in both samples with $\log g$ <3.0 dex. Therefore we dont have age information, but the abundances of APOGEE are very well calibrated for giants making its uncertainties smaller and more precise (Jönsson et al. 2020). The upper panel of Figure 5.5.1 shows the groups found for the inner Galaxy, where the method identifies a substantial contribution of the high-α sequence — the green group — and separates into a distinct group — the purple group — representing the more metal-poor stars. Our next step is to investigate whether this "purple" group could be a sign of the classical bulge or if it has an accreted origin as suggested by Horta et al. (2021). The multidimensional analysis of chemistry using t-SNE indicates that this "purple" population is chemically distinct from the thick disk, suggesting a different origin. The lower panels of Figure 5.5.1 also indicate that the distribution of abundances from a thick disk defined via tSNE+HDBSCAN in the local vicinity is very comparable to the thick disk in the inner Galaxy, which further supports our findings for a homogeneous thick disk. This research can better define the gradients of high- and low-α sequences, efficiently disentangling multiple populations in the inner Galaxy.

5.7 Summary and future perspectives

This thesis was assembled during a unique epoch for Galactic archaeology. The releases of *Gaia* DR2 and DR3 have had an impressive impact on our understanding of the Galaxy and made a fundamental match to spectroscopic surveys. The results of each published and submitted paper provide new and critical observational constraints to models of the formation and evolution of the MW and other galaxies. The years of this Ph.D. have also been marked by the work to process the colossal *Gaia* data with spectroscopy to deliver `StarHorse` data to the community in the form of

value-added catalogues inside the SDSS APOGEE surveys and part of astronomical databases[25]. Multiple works done in collaboration during the years of this Ph.D. have also helped shape our understanding of the structure and chemodynamical properties of our Galaxy. Most notably, the papers of Anders et al. (2019, 2022) connect the research presented in this thesis with the releases of `StarHorse` data using photometry and *Gaia* for more than 300 million stars. As we saw in Chapter 1.5, the data from (Anders et al. 2019) was paramount for a general view of the bared structure from our Galaxy. In Figure 5.7.1 we show the extent of `StarHorse` photometry across distances of 50 kpc from the Galactic plane, showing the impressive extent of the stellar halo density and the major dwarf galaxies satellites of the Milky Way. Such an extensive dataset will undoubtedly play an essential role in new science and aid in building target catalogues selection targets for recent surveys, as it has already been doing for the upcoming high-resolution survey 4MOST. Further collaborative works have led to the discovery of new members of the Sagittarius dwarf stream (Limberg et al. 2022a), including very metal-poor stars. The authors found critical chemo-kinematic differences between the stream populations, suggesting that a kinematic hot, less concentrated and metal-poor population was disrupted first from the Sagittarius dwarf. Additionally, works such as Perottoni et al. (2022); Fernández-Trincado et al. (2019b), with whom we also collaborate, have helped characterise various Galactic halo and bulge debris structures. In the bulge area, our definitions of the RPM sample in Chapter 3 have been used by further works to study globular clusters in the bulge (Souza et al. 2023) and to improve chemical abundances of APOGEE stars in the inner Galaxy (Razera et al. 2022). Future spectroscopic surveys such as 4MOST and WEAVE are promising for new and complementary works in the bulge and disks. As part of the experience gathered in this Ph.D., the author also contributes as leader of a bulge sub-survey inside 4MOST, outlining a carefully selected inner Galaxy sample to complement the data of APOGEE in the southern hemisphere (Chiappini et al. 2019).

25 https://cdsarc.cds.unistra.fr/viz-bin/cat/J/A+A/638/A76

List of publications

The Ph.D candidate has contributed to the following list of papers published and submitted to peer-review journals during her doctoral studies.

Refereed first and third author publications

1. **Queiroz, A. B. A.**, C. Chiappini, A. Perez-Villegas, A. Khalatyan, F. Anders, B. Barbuy, B. X. Santiago, M. Steinmetz, K. Cunha, M. Schultheis, S. R. Majewski, I. Minchev, et al. The Milky Way bar and bulge revealed by APOGEE and Gaia EDR3. **A&A**, 656:A156, December **2021**.
   This paper investigates the inner Galaxy with the data from *Gaia* EDR3 + APOGEE DR16 with chemical orbital maps. The publication constitutes the third Chapter of this thesis.

2. **Queiroz, A. B. A.**, F. Anders, C. Chiappini, A. Khalatyan, B. X. Santiago, M. Steinmetz, M. Valentini, A. Miglio, D. Bossini, B. Barbuy, I. Minchev, D. Minniti, and et al. From the bulge to the outer disc: StarHorse stellar parameters, distances, and extinctions for stars in APOGEE DR16 and other spectroscopic surveys. **A&A**, 638:A76, June **2020**.
   Computation of 5 million `StarHorse` distances and extinctions based on photometric, spectroscopy and astrometry. We show a chemical map across the Galaxy. The manuscript is shown in the second Chapter of the thesis.

3. F. Anders, A. Khalatyan, **Queiroz, A. B. A.**, C. Chiappini, J. Ardèvol, L. Casamiquela, F. Figueras, Ó. Jiménez-Arranz, C. Jordi, M. Monguió, M. Romero-Gómez, et al. Photo-astrometric distances, extinctions, and astrophysical parameters for Gaia EDR3 stars brighter than G = 18.5. **A&A**, 658:A91, February **2022**.
   This paper derives distances and extinction for more than 300 million stars using photometry and *Gaia* EDR3.

4. José G. Fernández-Trincado, Timothy C. Beers, **Queiroz, Anna. B. A.**, Cristina Chiappini, Dante Minniti, Beatriz Barbuy, Steven R. Majewski, Mario Ortigoza-Urdaneta, Christian Moni Bidin, Annie C. Robin, Edmundo Moreno, Leonardo Chaves-Velasquez, Sandro Villanova, Richard R. Lane, Kaike Pan, and Dmitry Bizyaev. APOGEE-2 Discovery of a Large Population of Relatively High-metallicity Globular Cluster Debris. **ApJ**, 918(2):L37, September **2021**.
   The authors detect intermediate metal-poor stars in the bulge with a very peculiar abundance of [N/Fe], indicating they are the outcome of disrupted clusters.

5. G. Guiglion, G. Matijevič, **Queiroz, A. B. A.**, M. Valentini, M. Steinmetz, C. Chiappini, E. K. Grebel, P. J. McMillan, G. Kordopatis, A. Kunder, T. Zwitter, A. Khalatyan, F. Anders, H. Enke, I. Minchev, G. Monari, R. F. G. Wyse, O. Bienaymé, J. Bland-Hawthorn, B. K. Gibson, J. F. Navarro, Q. Parker, W. Reid, G. M. Seabroke, and A. Siebert. The RAdial Velocity Experiment (RAVE): Parameterisation of RAVE spectra based on convolutional neural networks. **A&A**, 644:A168, December **2020**. This work derives stellar parameters for RAVE DR6 spectra using a machine-learning approach based on convolutional neural networks.

Submitted publications

1. **Queiroz, Anna B. A.**, F. Anders, Cristina Chiappini, and et al. StarHorse results for spectroscopic surveys + Gaia DR3: Chrono-chemical structures in the solar vicinity the genuine thick disk and young-alpha rich stars. December **2022**.
   Here, we derive ages for 4 million stars and define chemical clock relations using the GALAH precise abundances. This paper is part of the fourth Chapter of the thesis.

2. Guilherme Limberg, **Queiroz, Anna B. A.**, Hélio D. Perottoni, Silvia Rossi, João A. S. Amarante, Rafael M. Santucci, Cristina Chiappini, Angeles Pérez-Villegas, and Young Sun Lee. Phase-space Properties and Chemistry of the Sagittarius Stellar Stream Down to the Extremely Metal-poor ([Fe/H] - 3) Regime. arXive-prints, page arXiv:2212.08249, December **2022**. We find new members of the Sagittarius dwarf in a SEGUE metal-poor sample. The chemo-dynamical analysis reveals the past structure of the accreted dwarf.

3. Andres Almeida, Scott F. Anderson, Maria Argudo-Fernandez, Carles Badenes, Kat Barger, Jorge K. Barrera-Ballesteros, Chad F. Bender, Erika Benitez, ... Besser, and **Queiroz, Anna B. A.** ... et al. The Eighteenth Data Release of the Sloan Digital Sky Surveys: Targeting and First Spectra from SDSS-V. arXiv e-prints, page arXiv:2301.07688, January **2023**.
   Paper description of the SDSS 18 and the first spectra of SDSS-V

All refereed co-authored publications

1. He Zhao, Mathias Schultheis, Anke Arentsen, Georges Kordopatis, Morgan Fouesneau, Else Starkenburg, Federico Sestito, Vanessa Hill, Nicolas F. Martin, Sebastien Fabbro, and **Queiroz, A. B. A.** The Pristine Inner Galaxy Survey (PIGS) - VI. Different vertical distributions between two DIBs at 442.8 nm and 862.1 nm. **MNRAS**, 519(1):754–766, February **2023**.
   Characterization of diffuse interstellar bands found in the Pristine Survey

2. R. Razera, B. Barbuy, T. C. Moura, H. Ernandes, A. Pérez-Villegas, S. O. Souza, C. Chiappini, **Queiroz, A. B. A.**, F. Anders, J. G. Fernández-Trincado, A. C. S. Friaça, K. Cunha, V. V. Smith, B. X. Santiago, R. P. Schiavon, M. Valentini, D. Minniti, M. Schultheis, D. Geisler, J. Sobeck, V. M. Placco, and M. Zoc- cali. Abundance analysis of APOGEE spectra for 58 metal-poor stars from the bulge spheroid. **MNRAS**, 517(3):4590–4606, December **2022**.
   Derivation of abundances from a sample of APOGEE spectra in the Bulge. The authors derive Mg, O, Ce, Si, Ca and N with better precision. The distribution of abundances in the bulge supports in situ formation.

3. Hélio D. Perottoni, Guilherme Limberg, João A. S. Amarante, Silvia Rossi, **Queiroz, Anna B. A.**, Rafael M. Santucci, Angeles Pérez-Villegas, and Cristina Chiappini. The Unmixed Debris of Gaia-Sausage/Enceladus in the Form of a Pair of Halo Stellar Overdensities. **ApJ**, 936(1):L2, September **2022**.
   Chemodynamical characterization of the *Gaia*-Enceladus, Sagittarius and Hercules A'quila cloud using APOGEE, SEGUE and `StarHorse`.

4. Guilherme Limberg, Rafael M. Santucci, Silvia Rossi, **Queiroz, Anna B. A.**, Cristina Chiappini, Stefano O. Souza, Hélio D. Perottoni, Angeles Pérez-Villegas, and Fabrıicia O. Barbosa. Abundance Patterns of α and Neutron-capture Elements in the Helmi Stream. **ApJ**, 913(2):L28, June **2021**.
   The authors investigate the abundance patterns of new members from the Helmi stream, they found these stars are metal-poor and enriched in neutron capture abundance ratios.

5. José G. Fernández-Trincado, Timothy C. Beers, Dante Minniti, Leticia Carigi, Vinicius M. Placco, SangHyun Chun, Richard R. Lane, Doug Geisler, Sandro Villanova, Stefano O. Souza, Beatriz Barbuy, Angeles Pérez-Villegas, Cristina Chiappini, and **Queiroz, Anna. B. A.** et al. APOGEE discovery of a chemically atypical star disrupted from NGC 6723 and captured by the Milky Way bulge. **A&A**, 647:A64, March **2021**.
   This works finds a peculiar star that has been probability disrupted from its cluster by the potential forces of the MW bulge

6. Xinlun Cheng, Borja Anguiano, Steven R. Majewski, Christian Hayes, Phil Arras, Cristina Chiappini, Sten Hasselquist, **de Andrade Queiroz, Anna Barbara**, Christian Nitschelm, Domingo Anibal Garcia- Hernandez, Richard R. Lane, Alexandre Roman-Lopes, and Peter M. Frinchaboy. Exploring the Galactic Warp through Asymmetries in the Kinematics of the Galactic Disk. **ApJ**, 905(1):49, December **2020**.
   The study shows the vertical and horizontal motions of the stars throughout the Galactic disk, characterizing its warped signature.

7. Alvaro Rojas-Arriagada, Gail Zasowski, Mathias Schultheis, Manuela Zoccali, Sten Hasselquist, Cristina Chiappini, Roger E. Cohen, Katia Cunha, José G. Fernández-Trincado, Francesca Fragkoudi, D. A. Garcia- Hernández, Doug Geisler, Felipe Gran, Jianhui Lian, Steven Majewski, Dante Minniti, Antonela Monachesi, Christian Nitschelm, and **Queiroz, Anna B. A.** How many components? Quantifying the complexity of the metallicity distribution in the Milky Way bulge with APOGEE. **MNRAS**, 499(1):1037–1057, November **2020**.
   The paper shows a multi-peaked metallicity distribution of stars in the inner Galaxy and with Gaussian analysis describes how many components could produce such a distribution.

8. M. Schultheis, A. Rojas-Arriagada, K. Cunha, M. Zoccali, C. Chiappini, G. Zasowski, **Queiroz, A. B. A.**, D. Minniti, T. Fritz, D. A. Garcia-Hernández, C. Nitschelm, O. Zamora, S. Hasselquist, J. G. Fernández- Trincado, and R. R. Munoz. Cool stars in the Galactic center as seen by APOGEE. M giants, AGB stars, and supergiant stars and candidates. **A&A**, 642:A81, October **2020**.
   The work investigates the chemical abundances of 150 stars located in the nuclear cluster of the inner Galaxy 150pc from the Galactic Center.

9. Thomas Schmidt, Maria-Rosa L. Cioni, Florian Niederhofer, Kenji Bekki, Cameron P. M. Bell, Richard de Grijs, Jonathan Diaz, Dalal El Youssoufi, Jim Emerson, Martin A. T. Groenewegen, Valentin D. Ivanov, Gal Matijevic, Joana M. Oliveira, Monika G. Petr-Gotzens, **Queiroz, Anna B. A.**, Vincenzo Ripepi, and Jacco Th. van Loon. The VMC survey. XXXVIII. Proper motion of the Magellanic Bridge. **A&A**, 641:A134, September **2020**.
   The authors study the movements of the Magellanic clouds Bridge a tidal feature that connects the Magellanic clouds.

10. Romina Ahumada, Carlos Allende Prieto, Andrés Almeida, Friedrich Anders, Scott F. Anderson, Brett H. Andrews, Borja Anguiano, Riccardo Arcodia, Eric Armengaud, Aubert, and ... **Queiroz, Anna Bárbara de Andrade** ... et al. The 16th Data Release of the Sloan Digital Sky Surveys: First Release from the APOGEE-2 Southern Survey and Full Release of eBOSS Spectra. **ApJS**, 249(1):3, July **2020**. This work marks the releases of the SDSS DR16 and surveys such as APOGEE-2 south.

11. I. Carrillo, I. Minchev, M. Steinmetz, G. Monari, C. F. P. Laporte, F. Anders, **Queiroz, A. B. A.**, C. Chi- appini, A. Khalatyan, M. Martig, P. J. McMillan, B. X. Santiago, and K. Youakim.

Kinematics with Gaia DR2: the force of a dwarf. **MNRAS**, 490(1):797–812, November **2019**.
The authors characterize the imprints left by the Sagittarius dwarf in the phase space of *Gaia*.

12. I. Minchev, G. Matijevic, D. W. Hogg, G. Guiglion, M. Steinmetz, F. Anders, C. Chiappini, M. Martig, **Queiroz, A.,** and C. Scannapieco. Yule-Simpson's paradox in Galactic Archaeology. **MNRAS**, 487(3):3946– 3957, August **2019**.
The authors investigate the statistical effect in Galactic archaeology of determining trends from a group of subsets and from the combined subsets.

13. F. Anders, A. Khalatyan, C. Chiappini, **Queiroz, A. B.**, B. X. Santiago, C. Jordi, L. Girardi, A. G. A. Brown, G. Matijevič, G. Monari, T. Cantat-Gaudin, M. Weiler, S. Khan, A. Miglio, I. Carrillo, M. Romero- Gómez, I. Minchev, R. S. de Jong, T. Antoja, P. Ramos, M. Steinmetz, and H. Enke. Photo-astrometric distances, extinctions, and astrophysical parameters for Gaia DR2 stars brighter than G = 18. **A&A** 628:A94, August **2019**.
`StarHorse` parameters for about 300 million sources using *Gaia* DR2, the data revealed the direct density detection of the Galactic bar in the XY plane.

14. Emma Fernández-Alvar, José G. Fernández-Trincado, Edmundo Moreno, William J. Schuster, Leticia Ca- rigi, Alejandra Recio-Blanco, Timothy C. Beers, Cristina Chiappini, Friedrich Anders, Basilio X. Santiago, **Queiroz, Anna B. A.**, Angeles Pérez-Villegas, Olga Zamora, D. A. Garcia-Hernández, and Mario Ortigoza- Urdaneta. The metal-rich halo tail extended in —z—: a characterization with Gaia DR2 and APOGEE. **MNRAS**, 487(1):1462–1479, July **2019**.
A study of the kinematics of abundances for the metal-rich tail of the halo [Fe/H]> −0.75, the results suggests the presence of accreted structures.

15. C. Chiappini, I. Minchev, E. Starkenburg, F. Anders, N. Gentile Fusillo, O. Gerhard, G. Guiglion, A. Kha- latyan, G. Kordopatis, B. Lemasle, G. Matijevic, and **Queiroz, A. B. D. A.** et al. 4MOST Consortium Survey 3: Milky Way Disc and Bulge Low-Resolution Survey (4MIDABLE-LR). **The Messenger**, 175:30–34, March **2019**.
Description of the low-resolution survey of bulge and disks from the future 4MOST spectroscopic survey.

16. R. S. de Jong, O. Agertz, A. A. Berbel, J. Aird, D. A. Alexander, A. Amarsi, F. Anders, R. Andrae, B. Ansarinejad, W. Ansorge, P. Antilogus, H. Anwand-Heerwart, and ... **Queiroz, A. B. d. A.** ... et al. 4MOST: Project overview and information for the First Call for Proposals. **The Messenger**, 175:3–11, March **2019**.
Description of the 4MOST spectroscopic survey.

17. N. Grieves, J. Ge, N. Thomas, K. Willis, B. Ma, D. Lorenzo-Oliveira, **Queiroz, A. B. A.**, L. Ghezzi, C. Chiappini, F. Anders, L. Dutra-Ferreira, G. F. Porto de Mello, B. X. Santiago, L. N. da Costa, R. L. C. Ogando, E. F. del Peloso, J. C. Tan, D. P. Schneider, J. Pepper, K. G. Stassun, B. Zhao, D. Bizyaev, and K. Pan. Chemo-kinematics of the Milky Way from the SDSS-III MARVELS survey. **MNRAS**, 481(3):3244– 3265, December **2018**.
The authors find that kinematically-defined thin disk has stars of all ages and indicates that the high metallicity stars are old migrators from the inner Galaxy.

18. I. Minchev, F. Anders, A. Recio-Blanco, C. Chiappini, P. de Laverny, **Queiroz, A.,** M. Steinmetz, V. Adibekyan, I. Carrillo, G. Cescutti, G. Guiglion, M. Hayden, R. S. de Jong, G. Kordopatis, S. R. Majewski, M. Martig, and B. X. Santiago. Estimating stellar birth radii and the time evolution of Milky Way's ISM metallicity gradient. **MNRAS**, 481(2):1645–1657, December **2018**.

The work uses a relation between age, metallicity and α-abundances to estimate the radii at which stars are born.

19. F. Anders, C. Chiappini, B. X. Santiago, G. Matijevič, **Queiroz, A. B.,** M. Steinmetz, and G. Guiglion. Dissecting stellar chemical abundance space with t-SNE. **A&A**, 619:A125, November **2018**. The authors uses an unsupervised machine-learning algorithm to classify stars in different groups based on their high-dimensional chemical data.

Acknowledgments

A Ph.D is never easy and I must say that without the support and help of the people I mention here, it would have been a thousand times harder. Thank you for being part of this chaotic yet wonderful time of my life.

First and foremost, I would like to thank my supervisor Cristina Chiappini. Every time you talk about science, you do so with such a genuine excitement that is contagious. Thank you for always being open to discussion and for trusting me with the wonderful data of the last years. Thank you for not only advising me, but also standing up for me when difficult situations arised. You have taught me so much and this thesis wouldn't have been possible without you.

I would like to thank Prof. Matthias Steinmetz for supporting my position and for allowing me to show my potential as a Ph.D student at AIP. I have learnt a lot during these years and one of the richest experiences was assisting your teaching at the UP.

This thesis has benefited from the amazing `StarHorse` team: Friedrich Anders, Arman Khalatyan, Cristina Chiappini, Basilio Santiago, Samir Nepal and Marina dal Ponte. Thank you for all the efforts we shared together in the building of this code and its massive executions.

I must thank the essential co-authors and collaborators for the works mentioned in this thesis. Cristina Chiappini, Angelez Perez-Villegas, Guilherme Limberg, Beatriz Barbuy, Friedrich Anders, Matthias Steinmetz, Jose Fernandez Trincado, Ivan Minchev, Arman Khalatyan and Marica Valentini. Thank you for all the suggestions and refinement of ideas.

I would like to thank the editorial team for this thesis: Cristina, Amy, Matteo, Friedrich, and Jan. Thank you for the detailed suggestions and corrections.

I am pleased to have met and shared many memorable moments, coffee breaks, and group meetings with the Milky Way Local volume team and the Dwarf Galaxies group. I thank Roelof de Jong for leading the group and supporting the team. I especially thank Dalal, Anke, Kris, Gal, Amy, Guillaume, Erasmo, Nicolay, Alexey, Mariana, Elena and Salvatore for their friendship and for creating a cheerful atmosphere when work was stressful.

Also, I am thrilled to have found support, friendship and a fantastic time with the other colleagues I met at AIP, especially Rikke, Matteo, Edoardo, Judy, Jan, Özgün, Léna and Karl Heinz.

I thank my Mother and my Father who I could only see once during this Ph.D. It was not easy to be far, but your support could be felt constantly. I especially thank my mother for making always the best of the possibilities and enabling me to have opportunities she never could.

I am truly thankful to have shared a home with my friends Buchan and Philip. You became my second family in Potsdam, and the pandemic time would have been so terribly hard if you weren't there. You could put the positive switch on even when it seemed impossible.

I thank Franzi and Daniel for their immense support and friendship. You could always understand me, and I never felt alone in Potsdam thanks to you both.

I thank Harry, Semih and Aaron for the most fun evenings of my life. These Ph.D years were definitely a blast with your existence.

I thank my partner, Jonathan, for all the support and understanding, especially during this stressful time. Especially thank you for making such crazy and unexpected adventures with me.

I thank Samantha as my best and longest friend; it was from our many conversations on a bus coming back from school that I found the inspiration to pursue this career.

I thank my stepfather Jose D'amico who passed away in the course of this thesis. Thank you for teaching me how to see the world as a scientist.

It is with pain that I thank Cosmos. a wonderful fat silver cat that has made me smile unconditionally. I miss you.

Bibliography

Abdurro'uf, Accetta, K., Aerts, C., et al. 2022, ApJS, 259, 35

Abolfathi, B., Aguado, D. S., Aguilar, G., et al. 2018, ApJS, 235, 42

Adibekyan, V. Z., Figueira, P., Santos, N. C., et al. 2013, A&A, 554, A44

Adibekyan, V. Z., Santos, N. C., Sousa, S. G., & Israelian, G. 2011, A&A, 535, L11

Adibekyan, V. Z., Sousa, S. G., Santos, N. C., et al. 2012, A&A, 545, A32

Agertz, O., Pontzen, A., Read, J. I., et al. 2020, MNRAS, 491, 1656

Ahumada, R., Allende Prieto, C., Almeida, A., et al. 2020, ApJS, 249, 3

Alam, S., Albareti, F. D., Allende Prieto, C., Anders, F., & Anderson, S. F., e. 2015, ApJS, 219, 12

Alibert, Y. 2019, A&A, 624, A45

Allende Prieto, C., Majewski, S. R., Schiavon, R., et al. 2008, Astronomische Nachrichten, 329, 1018

Allende-Prieto, C., Sivarani, T., Beers, T. C., et al. 2008, AJ, 136, 2070

Alvarez, R. & Plez, B. 1998, A&A, 330, 1109

Alves-Brito, A., Meléndez, J., Asplund, M., Ramírez, I., & Yong, D. 2010, A&A, 513, A35

Amarante, J. A. S., Beraldo e Silva, L., Debattista, V. P., & Smith, M. C. 2020, APJ, 891, L30

Anders, F., Chiappini, C., Minchev, I., et al. 2017a, A&A, 600, A70

Anders, F., Chiappini, C., Rodrigues, T. S., et al. 2017b, A&A, 597, A30

Anders, F., Chiappini, C., Rodrigues, T. S., et al. 2016, Astronomische Nachrichten, 337, 926

Anders, F., Chiappini, C., Santiago, B. X., et al. 2018, A&A, 619, A125

Anders, F., Chiappini, C., Santiago, B. X., et al. 2014, A&A, 564, A115

Anders, F., Khalatyan, A., Chiappini, C., et al. 2019, A&A, 628, A94

Anders, F., Khalatyan, A., Queiroz, A. B. A., et al. 2022, A&A, 658, A91

Andrae, R., Fouesneau, M., Creevey, O., et al. 2018, A&A, 616, A8

Andrae, R., Fouesneau, M., Sordo, R., et al. 2022, arXiv e-prints, arXiv:2206.06138

Antoja, T., Helmi, A., Romero-Gómez, M., et al. 2018, Nature, 561, 360

Arenou, F., Luri, X., Babusiaux, C., et al. 2018, A&A, 616, A17

Arentsen, A., Starkenburg, E., Martin, N. F., et al. 2020, MNRAS, 491, L11

Astropy Collaboration, Robitaille, T. P., Tollerud, E. J., et al. 2013, A&A, 558, A33

Athanassoula, E. 2003, MNRAS, 341, 1179

Athanassoula, E. 2005, MNRAS, 358, 1477

Athanassoula, E., Machado, R. E. G., & Rodionov, S. A. 2013, MNRAS, 429, 1949

Aumer, M., Binney, J., & Schönrich, R. 2016, MNRAS, 459, 3326

Baade, W. 1946, PASP, 58, 249

Babusiaux, C. 2016, PASA, 33, e026

Babusiaux, C., Gómez, A., Hill, V., et al. 2010, A&A, 519, A77

Babusiaux, C., Katz, D., Hill, V., et al. 2014, A&A, 563, A15

Baglin, A., Auvergne, M., Barge, P., et al. 2006, in ESA Special Publication, ed. M. Fridlund, A. Baglin, J. Lochard, & L. Conroy, Vol. 1306, 33

Bailer-Jones, C. A. L. 2015, PASP, 127, 994

Bailer-Jones, C. A. L., Rybizki, J., Fouesneau, M., Demleitner, M., & Andrae, R. 2021, AJ, 161, 147

Balbinot, E. & Helmi, A. 2021, A&A, 654, A15

Balbinot, E., Santiago, B. X., da Costa, L. N., Makler, M., & Maia, M. A. G. 2011, MNRAS, 416, 393

Barbuy, B., Chiappini, C., Cantelli, E., et al. 2014, A&A, 570, A76

Barbuy, B., Chiappini, C., & Gerhard, O. 2018, ARA&A, 56, 223

Barbuy, B., Friaça, A. C. S., da Silveira, C. R., et al. 2015, A&A, 580, A40

Barbuy, B., Hill, V., Zoccali, M., et al. 2013, A&A, 559, A5

Barbuy, B., Zoccali, M., Ortolani, S., et al. 2009, A&A, 507, 405

Barden, S. C., Jones, D. J., Barnes, S. I., et al. 2010, in Society of Photo-Optical Instrumentation Engineers (SPIE) Conference Series, Vol. 7735, Proc. SPIE, 773509

Barnes, S. A. 2007, ApJ, 669, 1167

Battistini, C. & Bensby, T. 2015, A&A, 577, A9

Bayo, A., Rodrigo, C., Barrado Y Navascués, D., et al. 2008, A&A, 492, 277

Bekki, K. & Tsujimoto, T. 2011, MNRAS, 416, L60

Belokurov, V., Erkal, D., Evans, N. W., Koposov, S. E., & Deason, A. J. 2018, MNRAS, 478, 611

Belokurov, V., Sanders, J. L., Fattahi, A., et al. 2020, MNRAS, 494, 3880

Benjamin, R. A., Churchwell, E., Babler, B. L., et al. 2005, APJ, 630, L149

Bennett, M. & Bovy, J. 2019, MNRAS, 482, 1417

Bensby, T., Alves-Brito, A., Oey, M. S., Yong, D., & Meléndez, J. 2010, A&A, 516, L13

Bensby, T., Alves-Brito, A., Oey, M. S., Yong, D., & Meléndez, J. 2011, APJ, 735, L46

Bensby, T., Feltzing, S., Gould, A., et al. 2017, A&A, 605, A89

Bensby, T., Feltzing, S., & Oey, M. S. 2014, A&A, 562, A71

Beraldo e Silva, L., Debattista, V. P., Nidever, D., Amarante, J. A. S., & Garver, B. 2021, MNRAS, 502, 260

Bergemann, M., Ruchti, G. R., Serenelli, A., et al. 2014, A&A, 565, A89

Bernard, E. J., Schultheis, M., Di Matteo, P., et al. 2018, MNRAS, 477, 3507

Binney, J., Burnett, B., Kordopatis, G., et al. 2014, MNRAS, 437, 351

Binney, J., Gerhard, O., & Spergel, D. 1997, MNRAS, 288, 365

Binney, J., Gerhard, O. E., Stark, A. A., Bally, J., & Uchida, K. I. 1991, MNRAS, 252, 210

Bisterzo, S., Travaglio, C., Gallino, R., Wiescher, M., & Käppeler, F. 2014, ApJ, 787, 10

Bland-Hawthorn, J. & Gerhard, O. 2016, ARA&A, 54, 529

Bland-Hawthorn, J., Sharma, S., Tepper-Garcia, T., et al. 2019, MNRAS, 486, 1167

Blanton, M. R., Bershady, M. A., Abolfathi, B., et al. 2017, AJ, 154, 28

Boeche, C., Chiappini, C., Minchev, I., et al. 2013, A&A, 553, A19

Bossini, D., Vallenari, A., Bragaglia, A., et al. 2019, A&A, 623,, A108

Bournaud, F. 2016, Astrophysics and Space Science Library, Vol. 418, Bulge Growth Through Disc Instabilities in High-Redshift Galaxies, ed. E. Laurikainen, R. Peletier, & D. Gadotti, 355

Bovy, J., Leung, H. W., Hunt, J. A. S., et al. 2019, MNRAS, 490, 4740

Bovy, J. & Rix, H.-W. 2013, ApJ, 779, 115

Bovy, J., Rix, H.-W., & Hogg, D. W. 2012a, ApJ, 751, 131

Bovy, J., Rix, H.-W., Liu, C., et al. 2012b, ApJ, 753, 148

Bowen, I. S. & Vaughan, A. H., J. 1973, Appl. Opt., 12, 1430

Bressan, A., Marigo, P., Girardi, L., et al. 2012, MNRAS, 427, 127

Brook, C. B., Kawata, D., Gibson, B. K., & Freeman, K. C. 2004, ApJ, 612, 894

Brown, A. G. A. 2021, ARA&A, 59, 59

Brown, T. M., Ferguson, H. C., Smith, E., et al. 2003, APJ, 592, L17

Buck, T. 2020, MNRAS, 491, 5435

Buder, S., Asplund, M., Duong, L., et al. 2018, MNRAS, 478, 4513

Buder, S., Lind, K., Ness, M. K., et al. 2019, A&A, 624, A19

Buder, S., Lind, K., Ness, M. K., et al. 2022, MNRAS, 510, 2407

Buder, S., Sharma, S., Kos, J., et al. 2021, MNRAS, 506, 150

Bullock, J. S. & Johnston, K. V. 2005, ApJ, 635, 931

Burnett, B. & Binney, J. 2010, MNRAS, 407, 339

Burnett, B., Binney, J., Sharma, S., et al. 2011, A&A, 532, A113

Busso, M., Gallino, R., & Wasserburg, G. J. 1999, ARA&A, 37, 239

Caldwell, D. A., Kolodziejczak, J. J., Van Cleve, J. E., et al. 2010, APJ, 713, L92

Campello, R. J. G. B., Moulavi, D., & Sander, J. 2013, in Advances in Knowledge Discovery and Data Mining, ed. J. Pei, V. S. Tseng, L. Cao, H. Motoda, & G. Xu (Berlin, Heidelberg: Springer Berlin Heidelberg), 160–172

Cantat-Gaudin, T., Anders, F., Castro-Ginard, A., et al. 2020, A&A, 640, A1

Cantat-Gaudin, T., Jordi, C., Vallenari, A., et al. 2018, A&A, 618, A93

Canterna, R. 1975, APJ, 200, L63

Cao, L., Mao, S., Nataf, D., Rattenbury, N. J., & Gould, A. 2013, MNRAS, 434, 595

Capitanio, L., Lallement, R., Vergely, J. L., Elyajouri, M., & Monreal-Ibero, A. 2017, A&A, 606, A65

Carollo, D., Beers, T. C., Chiba, M., et al. 2010, ApJ, 712, 692

Carrillo, I., Minchev, I., Steinmetz, M., et al. 2019, MNRAS, 490, 797

Casagrande, L., Schönrich, R., Asplund, M., et al. 2011, A&A, 530, A138

Casamiquela, L., Castro-Ginard, A., Anders, F., & Soubiran, C. 2021a, A&A, 654, A151

Casamiquela, L., Soubiran, C., Jofré, P., et al. 2021b, A&A, 652, A25

Catelan, M., Borissova, J., Sweigart, A. V., & Spassova, N. 1998, ApJ, 494, 265

Cautun, M., Benítez-Llambay, A., Deason, A. J., et al. 2020, MNRAS, 494, 4291

Cescutti, G., Chiappini, C., & Hirschi, R. 2018, in IAU Symposium, Vol. 334, Rediscovering Our Galaxy, ed. C. Chiappini, I. Minchev, E. Starkenburg, & M. Valentini, 94–97

Chabrier, G. 2003, PASP, 115, 763

Chambers, K. C., Magnier, E. A., Metcalfe, N., et al. 2016, arXiv e-prints, arXiv:1612.05560

Chandrasekhar, S. 1931, ApJ, 74, 81

Cheng, J. Y., Rockosi, C. M., Morrison, H. L., et al. 2012, ApJ, 752, 51

Cheng, X. in prep., Exploring the Galactic Warp Through Asymmetries in the Kinematics of the Galactic Disk

Chiappini, C., Anders, F., & Minchev, I. 2014, in EAS Publications Series, Vol. 67-68, EAS Publications Series, 169–176

Chiappini, C., Anders, F., Rodrigues, T. S., et al. 2015, A&A, 576, L12

Chiappini, C., Frischknecht, U., Meynet, G., et al. 2011, Nature, 472, 454

Chiappini, C., Matteucci, F., & Gratton, R. 1997, ApJ, 477, 765

Chiappini, C., Matteucci, F., & Romano, D. 2001, ApJ, 554, 1044

Chiappini, C., Minchev, I., Starkenburg, E., et al. 2019, The Messenger, 175, 30

Chiappini, C., Romano, D., & Matteucci, F. 2003, MNRAS, 339, 63

Ciuca, R. & Hernández, O. F. 2020, MNRAS, 492, 1329

Ciucă, I., Kawata, D., Miglio, A., Davies, G. R., & Grand, R. J. J. 2021, MNRAS, 503, 2814

Ciucă, I., Kawata, D., Ting, Y.-S., et al. 2022, arXiv e-prints, arXiv:2211.01006

Clarke, J. P., Wegg, C., Gerhard, O., et al. 2019, MNRAS, 489, 3519

Clarkson, W. I., Sahu, K. C., Anderson, J., et al. 2011, ApJ, 735, 37

Combes, F. & Sanders, R. H. 1981, A&A, 96, 164

Contreras Ramos, R., Minniti, D., Gran, F., et al. 2018, ApJ, 863, 79

Contursi, G., de Laverny, P., Recio-Blanco, A., et al. 2022, arXiv e-prints, arXiv:2207.05368

Creevey, O. L., Sordo, R., Pailler, F., et al. 2022, arXiv e-prints, arXiv:2206.05864

Cropper, M., Katz, D., Sartoretti, P., et al. 2018, A&A, 616, A5

Cui, X.-Q., Zhao, Y.-H., Chu, Y.-Q., et al. 2012, Research in Astronomy and Astrophysics, 12, 1197

Cunha, K. & Smith, V. V. 2006, ApJ, 651, 491

Cuomo, V., Lopez Aguerri, J. A., Corsini, E. M., et al. 2019, A&A, 632, A51

Cutri, R. M., Skrutskie, M. F., van Dyk, S., et al. 2003, 2MASS All Sky Catalog of point sources.

Cutri, R. M., Wright, E. L., Conrow, T., et al. 2013, Explanatory Supplement to the AllWISE Data Release Products, Tech. rep.

da Silva, L., Girardi, L., Pasquini, L., et al. 2006, A&A, 458, 609

da Silveira, C. R., Barbuy, B., Friaça, A. C. S., et al. 2018, A&A, 614, A149

Dalcanton, J. J. & Bernstein, R. A. 2002, AJ, 124, 1328

Dalton, G., Trager, S. C., Abrams, D. C., et al. 2012, in Society of Photo-Optical Instrumentation Engineers (SPIE) Conference Series, Vol. 8446, Ground-based and Airborne Instrumentation for Astronomy IV, ed. I. S. McLean, S. K. Ramsay, & H. Takami, 84460P

Dantas, M. L. L., Smiljanic, R., Boesso, R., et al. 2022, arXiv e-prints, arXiv:2210.08510

Das, P., Hawkins, K., & Jofré, P. 2020, MNRAS, 493, 5195

Das, P. & Sanders, J. L. 2019, MNRAS, 484, 294

De Angeli, F., Weiler, M., Montegriffo, P., et al. 2022, arXiv e-prints, arXiv:2206.06143

de Jong, R. S., Agertz, O., Berbel, A. A., et al. 2019, The Messenger, 175, 3

De Silva, G. M., Freeman, K. C., Bland-Hawthorn, J., et al. 2015, MNRAS, 449, 2604

de Vaucouleurs, G. & Pence, W. D. 1978, AJ, 83, 1163

Debattista, V. P., Mayer, L., Carollo, C. M., et al. 2006, ApJ, 645, 209

Debattista, V. P., Ness, M., Gonzalez, O. A., et al. 2017, MNRAS, 469, 1587

Decin, L., Morris, P. W., Appleton, P. N., et al. 2004, ApJS, 154, 408

Dehnen, W. 2000, AJ, 119, 800

Dékány, I., Minniti, D., Catelan, M., et al. 2013, APJ, 776, L19

Delgado Mena, E., Tsantaki, M., Adibekyan, V. Z., et al. 2017, A&A, 606, A94

Devorkin, D. H. 1977, IAU Symposium, 80, 61

Di Matteo, P. 2016, PASA, 33, e027

Di Matteo, P., Haywood, M., Lehnert, M. D., et al. 2019, A&A, 632, A4

Donnan, C. T., McLeod, D. J., Dunlop, J. S., et al. 2023, MNRAS, 518, 6011

Drimmel, R. 2000, A&A, 358, L13

Du, H., Mao, S., Athanassoula, E., Shen, J., & Pietrukowicz, P. 2020, arXiv e-prints, arXiv:2007.01102

Duffau, S., Caffau, E., Sbordone, L., et al. 2017, A&A, 604, A128

Edvardsson, B., Andersen, J., Gustafsson, B., et al. 1993, A&A, 275, 101

Efremov, Y. N. 2011, Astronomy Reports, 55, 108

Eggen, O. J., Lynden-Bell, D., & Sandage, A. R. 1962, ApJ, 136, 748

Eisenstein, D. J., Weinberg, D. H., Agol, E., et al. 2011, AJ, 142, 72

El-Badry, K., Bland-Hawthorn, J., Wetzel, A., et al. 2018, MNRAS, 480, 652

Elmegreen, B. G., Bournaud, F., & Elmegreen, D. M. 2008, ApJ, 688, 67

Elyajouri, M. & Lallement, R. 2019, A&A, 628, A67

Erwin, P., Saglia, R. P., Fabricius, M., et al. 2015, MNRAS, 446, 4039

Ester, M., Kriegel, H.-P., Sander, J., & Xu, X. 1996, in Proc. of 2nd International Conference on Knowledge Discovery and, 226–231

et al., N. in prep., t-SNE on high resolution samples

Evans, D. W., Riello, M., De Angeli, F., et al. 2018, A&A, 616, A4

Fabricius, C., Luri, X., Arenou, F., et al. 2021, A&A, 649, A5

Faherty, J. K., Burgasser, A. J., Cruz, K. L., et al. 2009, AJ, 137, 1

Feltzing, S., Holmberg, J., & Hurley, J. R. 2001, A&A, 377, 911

Fernández-Alvar, E., Carigi, L., Allende Prieto, C., et al. 2017, MNRAS, 465, 1586

Fernández-Alvar, E., Fernández-Trincado, J. G., Moreno, E., et al. 2019, MNRAS, 487, 1462

Fernández-Alvar, E., Kordopatis, G., Hill, V., et al. 2021, MNRAS, 508, 1509

Fernández-Trincado, J. G., Beers, T. C., Barbuy, B., et al. 2022, A&A, 663, A126

Fernández-Trincado, J. G., Beers, T. C., & Minniti, D. 2020a, A&A, 644, A83

Fernández-Trincado, J. G., Beers, T. C., Minniti, D., et al. 2021, A&A, 647, A64

Fernández-Trincado, J. G., Beers, T. C., Minniti, D., et al. 2020b, A&A, 643, L4

Fernández-Trincado, J. G., Beers, T. C., Placco, V. M., et al. 2019a, APJ, 886, L8

Fernández-Trincado, J. G., Chaves-Velasquez, L., Pérez-Villegas, A., et al. 2020c, MNRAS, 495, 4113

Fernández-Trincado, J. G., Zamora, O., Souto, D., et al. 2019b, A&A, 627, A178

Ferrers, N. 1877, the Potentials of Ellipsoids, Ellipsoidal Shells, Elliptic Laminae, and Elliptic Rings of Variable Densities.

Fisher, D. B. & Drory, N. 2016, in Astrophysics and Space Science Library, Vol. 418, Galactic Bulges, ed. E. Laurikainen, R. Peletier, & D. Gadotti, 41

Fiteni, K., Caruana, J., Amarante, J. A. S., Debattista, V. P., & Beraldo e Silva, L. 2021, MNRAS, 503, 1418

Förster Schreiber, N. M. & Wuyts, S. 2020, Annual Review of Astronomy and Astrophysics, 58, 661

Fossati, L., Bagnulo, S., Monier, R., et al. 2007, A&A, 476, 911

Fragkoudi, F., Di Matteo, P., Haywood, M., et al. 2018, A&A, 616, A180

Fragkoudi, F., Grand, R. J. J., Pakmor, R., et al. 2020, MNRAS, 494, 5936

Frankel, N., Rix, H.-W., Ting, Y.-S., Ness, M., & Hogg, D. W. 2018, ApJ, 865, 96

Frankel, N., Sanders, J., Rix, H.-W., Ting, Y.-S., & Ness, M. 2019, ApJ, 884, 99

Frankel, N., Sanders, J., Ting, Y.-S., & Rix, H.-W. 2020, arXiv e-prints, arXiv:2002.04622

Freeman, K. & Bland-Hawthorn, J. 2002, ARA&A, 40, 487

Freeman, K., Ness, M., Wylie-de-Boer, E., et al. 2013, MNRAS, 428, 3660

Friaça, A. C. S. & Barbuy, B. 2017, A&A, 598, A121

Friedli, D., Benz, W., & Kennicutt, R. 1994, APJ, 430, L105

Fuhrmann, K. 1998, A&A, 338, 161

Fuhrmann, K. 2008, MNRAS, 384, 173

Fuhrmann, K. 2011, MNRAS, 414, 2893

Fulbright, J. P., McWilliam, A., & Rich, R. M. 2007, ApJ, 661, 1152

Gaia Collaboration, Babusiaux, C., van Leeuwen, F., et al. 2018a, A&A, 616, A10

Gaia Collaboration, Brown, A. G. A., Vallenari, A., et al. 2018b, A&A, 616, A1

Gaia Collaboration, Brown, A. G. A., Vallenari, A., et al. 2021, A&A, 649, A1

Gaia Collaboration, Katz, D., Antoja, T., et al. 2018c, A&A, 616, A11

Gaia Collaboration, Prusti, T., de Bruijne, J. H. J., et al. 2016, A&A, 595, A1

Gaia Collaboration, Vallenari, A., Brown, A. G. A., et al. 2022, arXiv e-prints, arXiv:2208.00211

Gallagher, R., Maiolino, R., Belfiore, F., et al. 2019, MNRAS, 485, 3409

Gallart, C., Bernard, E. J., Brook, C. B., et al. 2019, Nature Astronomy, 3, 932

García Pérez, A. E., Allende Prieto, C., Holtzman, J. A., et al. 2016, AJ, 151, 144

García Pérez, A. E., Ness, M., Robin, A. C., et al. 2018, ApJ, 852, 91

Gardner, J. P., Mather, J. C., Clampin, M., et al. 2006, Space Sci. Rev., 123, 485

Geisler, D., Parisi, M. C., Dias, B., et al. 2022, arXiv e-prints, arXiv:2210.02193

Georgelin, Y. M. & Georgelin, Y. P. 1976, A&A, 49, 57

Gerhard, O. 2002, in Astronomical Society of the Pacific Conference Series, Vol. 273, The Dynamics, Structure & History of Galaxies: A Workshop in Honour of Professor Ken Freeman, ed. G. S. Da Costa, E. M. Sadler, & H. Jerjen, 73

Gilmore, G. 2012, in Astronomical Society of the Pacific Conference Series, Vol. 458, Galactic Archaeology: Near-Field Cosmology and the Formation of the Milky Way, ed. W. Aoki, M. Ishigaki, T. Suda, T. Tsujimoto, & N. Arimoto, 147

Gilmore, G., Randich, S., Asplund, M., et al. 2012, The Messenger, 147, 25

Gilmore, G. & Reid, N. 1983, MNRAS, 202, 1025

Girardi, L., Dalcanton, J., Williams, B., et al. 2008, PASP, 120, 583

Gontcharov, G. A. 2009, Astronomy Letters, 35, 638

Gonzalez, O. A. & Gadotti, D. 2016, in Astrophysics and Space Science Library, Vol. 418, Galactic Bulges, ed. E. Laurikainen, R. Peletier, & D. Gadotti, 199

Gonzalez, O. A., Rejkuba, M., Zoccali, M., et al. 2013, A&A, 552, A110

Gonzalez, O. A., Rejkuba, M., Zoccali, M., et al. 2012, A&A, 543, A13

Gonzalez, O. A., Zoccali, M., Vasquez, S., et al. 2015, A&A, 584, A46

Gran, F., Minniti, D., Saito, R. K., et al. 2015, A&A, 575, A114

Grand, R. J. J., Kawata, D., Belokurov, V., et al. 2020, MNRAS, 497, 1603

GRAVITY Collaboration, Abuter, R., Amorim, A., et al. 2019, A&A, 625, L10

Green, G. M., Schlafly, E., Zucker, C., Speagle, J. S., & Finkbeiner, D. 2019, ApJ, 887, 93

Grenon, M. 1989, Ap&SS, 156, 29

Grieco, V., Matteucci, F., Pipino, A., & Cescutti, G. 2012, A&A, 548, A60

Grieves, N., Ge, J., Thomas, N., et al. 2018, MNRAS, 481, 3244

Groh, J. H., Ekström, S., Georgy, C., et al. 2019, A&A, 627, A24

Gudin, D., Shank, D., Beers, T. C., et al. 2021, ApJ, 908, 79

Guiglion, G., Matijevič, G., Queiroz, A. B. A., et al. 2020, A&A, 644, A168

Gunn, J. E., Siegmund, W. A., Mannery, E. J., et al. 2006, AJ, 131, 2332

Hasselquist, S., Hayes, C. R., Lian, J., et al. 2021, ApJ, 923, 172

Hasselquist, S., Holtzman, J. A., Shetrone, M., et al. 2019, ApJ, 871, 181

Hasselquist, S., Zasowski, G., Feuillet, D. K., et al. 2020, arXiv e-prints, arXiv:2008.03603

Hauser, M. G. 1993, in American Institute of Physics Conference Series, Vol. 278, Back to the Galaxy, ed. S. S. Holt & F. Verter, 201–205

Hawkins, K., Jofré, P., Masseron, T., & Gilmore, G. 2015, MNRAS, 453, 758

Hayden, M. R., Bovy, J., Holtzman, J. A., et al. 2015, ApJ, 808, 132

Hayden, M. R., Holtzman, J. A., Bovy, J., et al. 2014, AJ, 147, 116

Hayes, C. R., Majewski, S. R., Hasselquist, S., et al. 2020, ApJ, 889, 63

Hayes, C. R., Majewski, S. R., Shetrone, M., et al. 2018, ApJ, 852, 49

Haywood, M. 2012, in European Physical Journal Web of Conferences, Vol. 19, European Physical Journal Web of Conferences, 05001

Haywood, M., Di Matteo, P., Lehnert, M., et al. 2018a, A&A, 618, A78

Haywood, M., Di Matteo, P., Lehnert, M. D., et al. 2018b, ApJ, 863, 113

Haywood, M., Lehnert, M. D., Di Matteo, P., et al. 2016, A&A, 589, A66

Haywood, M., Snaith, O., Lehnert, M. D., Di Matteo, P., & Khoperskov, S. 2019, A&A, 625, A105

Heger, A. & Woosley, S. E. 2002, ApJ, 567, 532

Heiter, U., Lind, K., Bergemann, M., et al. 2021, A&A, 645, A106

Helmi, A. 2020, ARA&A, 58, 205

Helmi, A., Babusiaux, C., Koppelman, H. H., et al. 2018, Nature, 563, 85

Henden, A. & Munari, U. 2014, Contributions of the Astronomical Observatory Skalnate Pleso, 43, 518

Hill, V., Lecureur, A., Gómez, A., et al. 2011, A&A, 534, A80

Hilmi, T., Minchev, I., Buck, T., et al. 2020, arXiv e-prints, arXiv:2003.05457

Hinton, G. E. & Roweis, S. T. 2003, in Advances in neural information processing systems, 857–864

Høg, E., Fabricius, C., Makarov, V. V., et al. 2000, A&A, 355, L27

Hogg, D. W., Casey, A. R., Ness, M., et al. 2016, ApJ, 833, 262

Hogg, D. W. & Villar, S. 2021, PASP, 133, 093001

Holtzman, J. A., Burrows, C. J., Casertano, S., et al. 1995, PASP, 107, 1065

Holtzman, J. A., Hasselquist, S., Shetrone, M., et al. 2018, AJ, 156, 125

Horta, D., Ness, M. K., Rybizki, J., Schiavon, R. P., & Buder, S. 2022, MNRAS, 513, 5477

Horta, D., Schiavon, R. P., Mackereth, J. T., et al. 2021, MNRAS, 500, 1385

Howes, L. M., Casey, A. R., Asplund, M., et al. 2015, Nature, 527, 484

Howes, L. M., Lindegren, L., Feltzing, S., Church, R. P., & Bensby, T. 2019, A&A, 622, A27

Huang, Y., Liu, X. W., Yuan, H. B., et al. 2016, MNRAS, 463, 2623

Huang, Y., Yuan, H., Li, C., et al. 2021, ApJ, 907, 68

Hubble, E. P. 1926, ApJ, 64, 321

Hubeny, I. & Lanz, T. 2017, arXiv e-prints, arXiv:1706.01859

Huertas-Company, M., Guo, Y., Ginzburg, O., et al. 2020, arXiv e-prints, arXiv:2006.14636

Hughes, A. C. N., Spitler, L. R., Zucker, D. B., et al. 2022, ApJ, 930, 47

Hunt, E. L. & Reffert, S. 2021, A&A, 646, A104

Hunter, J. D. 2007, Computing in Science and Engineering, 9, 90

Ibata, R., Malhan, K., Martin, N., et al. 2021, ApJ, 914, 123

Ibata, R. A., Gilmore, G., & Irwin, M. J. 1994, Nature, 370, 194

Iorio, G. & Belokurov, V. 2019, MNRAS, 482, 3868

Israelian, G., Bertran de Lis, S., Delgado Mena, E., & Adibekyan, V. Z. 2014, Mem. Soc. Astron. Italiana, 85, 265

Jofré, P., Heiter, U., & Soubiran, C. 2019, ARA&A, 57, 571

Jofré, P., Jackson, H., & Tucci Maia, M. 2020, A&A, 633, L9

Jofré, P., Jorissen, A., Van Eck, S., et al. 2016, A&A, 595, A60

Johnson, C. I., Rich, R. M., Kobayashi, C., Kunder, A., & Koch, A. 2014, AJ, 148, 67

Johnson, C. I., Rich, R. M., Kobayashi, C., et al. 2013, ApJ, 765, 157

Jönsson, H., Holtzman, J. A., Allende Prieto, C., et al. 2020, arXiv e-prints, arXiv:2007.05537

Jørgensen, B. R. & Lindegren, L. 2005, A&A, 436, 127

Joyce, M., Johnson, C. I., Marchetti, T., et al. 2022, arXiv e-prints, arXiv:2205.07964

Jurić, M., Ivezić, Ž., Brooks, A., et al. 2008, ApJ, 673, 864

Katz, D., Sartoretti, P., Cropper, M., et al. 2019, A&A, 622, A205

Kawata, D., Baba, J., Hunt, J. A. S., et al. 2020, arXiv e-prints, arXiv:2012.05890

Kawata, D. & Chiappini, C. 2016, Astronomische Nachrichten, 337, 976

Kerber, L. O., Libralato, M., Souza, S. O., et al. 2019, MNRAS, 484, 5530

Kerber, L. O., Nardiello, D., Ortolani, S., et al. 2018, ApJ, 853, 15

Khan, S., Miglio, A., Mosser, B., et al. 2019, A&A, 628, A35

Khoperskov, S., Gerhard, O., Di Matteo, P., et al. 2020, A&A, 634, L8

Kobayashi, C., Karakas, A. I., & Lugaro, M. 2020, ApJ, 900, 179

Koppelman, H., Helmi, A., & Veljanoski, J. 2018, APJ, 860, L11

Koppelman, H. H., Helmi, A., Massari, D., Price-Whelan, A. M., & Starkenburg, T. K. 2019, A&A, 631, L9

Kordopatis, G., Schultheis, M., McMillan, P. J., et al. 2022, arXiv e-prints, arXiv:2206.07937

Kormendy, J. & Illingworth, G. 1982, ApJ, 256, 460

Kormendy, J. & Kennicutt, Robert C., J. 2004, ARA&A, 42, 603

Kos, J., Bland-Hawthorn, J., Freeman, K., et al. 2018, MNRAS, 473, 4612

Kruijssen, J. M. D., Pfeffer, J. L., Reina-Campos, M., Crain, R. A., & Bastian, N. 2019, MNRAS, 486, 3180

Kuijken, K. & Rich, R. M. 2002, AJ, 124, 2054

Kunder, A., Koch, A., Rich, R. M., et al. 2012, AJ, 143, 57

Kunder, A., Kordopatis, G., Steinmetz, M., et al. 2017, AJ, 153, 75

Kunder, A., Pérez-Villegas, A., Rich, R. M., et al. 2020, AJ, 159, 270

Kunder, A., Rich, R. M., Koch, A., et al. 2016, APJ, 821, L25

Kunder, A. M. 2022, Universe, 8, 206

Lagarde, N., Reylé, C., Chiappini, C., et al. 2021, A&A, 654, A13

Lagarde, N., Reylé, C., Robin, A. C., et al. 2019, A&A, 621, A24

Lallement, R., Capitanio, L., Ruiz-Dern, L., et al. 2018, A&A, 616, A132

Lallement, R., Vergely, J. L., Babusiaux, C., & Cox, N. L. J. 2022, A&A, 661, A147

Langer, N. 2012, ARA&A, 50, 107

Laporte, C. F. P., Belokurov, V., Koposov, S. E., Smith, M. C., & Hill, V. 2020, MNRAS, 492, L61

Laporte, C. F. P., Minchev, I., Johnston, K. V., & Gómez, F. A. 2019, MNRAS, 485, 3134

Leavitt, H. S. & Pickering, E. C. 1912, Harvard College Observatory Circular, 173, 1

Lebreton, Y. & Reese, D. R. 2020, A&A, 642, A88

Lee, Y. S., Beers, T. C., An, D., et al. 2011, ApJ, 738, 187

Lee, Y. S., Beers, T. C., Sivarani, T., et al. 2008, AJ, 136, 2022

Leung, H. W. & Bovy, J. 2019, MNRAS, 483, 3255

Li, Z.-Y. & Shen, J. 2012, APJ, 757, L7

Lian, J., Zasowski, G., Hasselquist, S., et al. 2020, MNRAS, 497, 3557

Limberg, G., Queiroz, A. B. A., Perottoni, H. D., et al. 2022a, arXiv e-prints, arXiv:2212.08249

Limberg, G., Santucci, R. M., Rossi, S., et al. 2021, APJ, 913, L28

Limberg, G., Souza, S. O., Pérez-Villegas, A., et al. 2022b, ApJ, 935, 109

Lindegren, L., Bastian, U., Biermann, M., et al. 2021a, A&A, 649, A4

Lindegren, L., Hernández, J., Bombrun, A., et al. 2018, A&A, 616, A2

Lindegren, L., Klioner, S. A., Hernández, J., et al. 2021b, A&A, 649, A2

Lucey, M., Hawkins, K., Ness, M., et al. 2021, MNRAS, 501, 5981

Lucey, M., Pearson, S., Hunt, J. A. S., et al. 2022, arXiv e-prints, arXiv:2206.01798

Luque, E., Queiroz, A., Santiago, B., et al. 2016, MNRAS, 458, 603

Luri, X., Brown, A. G. A., Sarro, L. M., et al. 2018, A&A, 616, A9

Mackereth, J. T., Bovy, J., Schiavon, R. P., et al. 2017, MNRAS, 471, 3057

Mackereth, J. T., Crain, R. A., Schiavon, R. P., et al. 2018, MNRAS, 477, 5072

Mackereth, J. T., Schiavon, R. P., Pfeffer, J., et al. 2019, MNRAS, 482, 3426

Madau, P., Ferguson, H. C., Dickinson, M. E., et al. 1996, MNRAS, 283, 1388

Madore, B. F. 2016, Astrophysics and Space Science Library, Vol. 418, Bulges: Seen from a Philosophically-Informed Historical Perspective, ed. E. Laurikainen, R. Peletier, & D. Gadotti, 1

Maia, M. T., Meléndez, J., Lorenzo-Oliveira, D., Spina, L., & Jofré, P. 2019, A&A, 628, A126

Maiolino, R., Russell, H. R., Fabian, A. C., et al. 2017, Nature, 544, 202

Maíz Apellániz, J. & Weiler, M. 2018, A&A, 619, A180

Majewski, S. R., Schiavon, R. P., Frinchaboy, P. M., et al. 2017, AJ, 154, 94

Majewski, S. R., Skrutskie, M. F., Weinberg, M. D., & Ostheimer, J. C. 2003, ApJ, 599, 1082

Marigo, P., Girardi, L., Bressan, A., et al. 2017, ApJ, 835, 77

Marrese, P. M., Marinoni, S., Fabrizio, M., & Altavilla, G. 2019, A&A, 621, A144

Martell, S. L., Sharma, S., Buder, S., et al. 2017, MNRAS, 465, 3203

Martig, M., Fouesneau, M., Rix, H.-W., et al. 2016a, MNRAS, 456, 3655

Martig, M., Minchev, I., Ness, M., Fouesneau, M., & Rix, H.-W. 2016b, ApJ, 831, 139

Martig, M., Rix, H.-W., Silva Aguirre, V., et al. 2015, MNRAS, 451, 2230

Massari, D., Koppelman, H. H., & Helmi, A. 2019, A&A, 630, L4

Masseron, T. & Gilmore, G. 2015, MNRAS, 453, 1855

Matijevič, G., Chiappini, C., Grebel, E. K., et al. 2017, A&A, 603, A19

Matsunaga, N., Feast, M. W., Bono, G., et al. 2016, MNRAS, 462, 414

Matsuno, T., Starkenburg, E., Balbinot, E., & Helmi, A. 2022, arXiv e-prints, arXiv:2212.11639

Matteucci, F. 1991, in Astronomical Society of the Pacific Conference Series, Vol. 20, Frontiers of Stellar Evolution, ed. D. L. Lambert, 539

Matteucci, F. 2001, The chemical evolution of the Galaxy, Vol. 253

Matteucci, F. 2012, Chemical Evolution of Galaxies

Matteucci, F. 2021, A&A Rev., 29, 5

Matteucci, F. & Francois, P. 1989, MNRAS, 239, 885

Matteucci, F., Grisoni, V., Spitoni, E., et al. 2019, MNRAS, 487, 5363

Matteucci, F., Vasini, A., Grisoni, V., & Schultheis, M. 2020, MNRAS, 494, 5534

McClure, R. D. 1983, ApJ, 268, 264

McConnachie, A. W. 2012, AJ, 144, 4

McInnes, L., Healy, J., & Astels, S. 2017, The Journal of Open Source Software, 2, 205

McWilliam, A. 1997, ARA&A, 35, 503

McWilliam, A. 2016, PASA, 33, e040

McWilliam, A. & Rich, R. M. 1994, ApJS, 91, 749

McWilliam, A., Wallerstein, G., & Mottini, M. 2013, ApJ, 778, 149

McWilliam, A. & Zoccali, M. 2010, ApJ, 724, 1491

Meléndez, J., Asplund, M., Alves-Brito, A., et al. 2008, A&A, 484, L21

Miglio, A., Chiappini, C., Mackereth, J. T., et al. 2021, A&A, 645, A85

Miglio, A., Chiappini, C., Mosser, B., et al. 2017, Astronomische Nachrichten, 338, 644

Mikolaitis, Š., Hill, V., Recio-Blanco, A., et al. 2014, A&A, 572, A33

Minchev, I., Anders, F., Recio-Blanco, A., et al. 2018, MNRAS, 481, 1645

Minchev, I., Chiappini, C., & Martig, M. 2013, A&A, 558, A9

Minchev, I., Chiappini, C., & Martig, M. 2014, A&A, 572, A92

Minchev, I. & Famaey, B. 2010, ApJ, 722, 112

Minchev, I., Famaey, B., Combes, F., et al. 2011, A&A, 527, A147

Minchev, I., Martig, M., Streich, D., et al. 2015, APJ, 804, L9

Minchev, I., Matijevic, G., Hogg, D. W., et al. 2019, MNRAS, 487, 3946

Minchev, I., Nordhaus, J., & Quillen, A. C. 2007, APJ, 664, L31

Minniti, D. 1995, AJ, 109, 1663

Minniti, D. 1996, ApJ, 459, 175

Minniti, D., Lucas, P. W., Emerson, J. P., et al. 2010, New A, 15, 433

Minniti, D., Olszewski, E. W., Liebert, J., et al. 1995, MNRAS, 277, 1293

Minniti, D., Saito, R. K., Gonzalez, O. A., et al. 2014, A&A, 571, A91

Minniti, D., White, S. D. M., Olszewski, E. W., & Hill, J. M. 1992, APJ, 393, L47

Mints, A. 2020, arXiv e-prints, arXiv:2012.09690

Mints, A. & Hekker, S. 2018, A&A, 618, A54

Miranda, M. S., Macfarlane, B. A., & Gibson, B. K. 2014, in Proceedings of XIII Nuclei in the Cosmos (NIC XIII). 7-11 July, 2014. Debrecen, Hungary. Online at http://pos.sissa.it/cgi-bin/reader/conf.cgi?confid=204, 149

Miyamoto, M. & Nagai, R. 1975, PASJ, 27, 533

Mo, H., van den Bosch, F. C., & White, S. 2010, Galaxy Formation and Evolution

Monaghan, J. J. 1992, ARA&A, 30, 543

Monari, G., Famaey, B., Carrillo, I., et al. 2018, A&A, 616, L9

Montalbán, J., Mackereth, J. T., Miglio, A., et al. 2021, Nature Astronomy, 5, 640

Morel, T., Creevey, O. L., Montalbán, J., Miglio, A., & Willett, E. 2021, A&A, 646, A78

Myeong, G. C., Belokurov, V., Aguado, D. S., et al. 2022, arXiv e-prints, arXiv:2206.07744

Myeong, G. C., Vasiliev, E., Iorio, G., Evans, N. W., & Belokurov, V. 2019, MNRAS, 488, 1235

Naidu, R. P., Conroy, C., Bonaca, A., et al. 2020, ApJ, 901, 48

Nandakumar, G., Schultheis, M., Hayden, M., et al. 2017, A&A, 606, A97

Nataf, D. M., Udalski, A., Gould, A., Fouqué, P., & Stanek, K. Z. 2010, APJ, 721, L28

Navarro, J. F., Frenk, C. S., & White, S. D. M. 1997, ApJ, 490, 493

Naylor, T. & Jeffries, R. D. 2006, MNRAS, 373, 1251

Ness, M. 2012, in Dynamics Meets Kinematic Tracers, 9

Ness, M. & Freeman, K. 2016, PASA, 33, e022

Ness, M., Freeman, K., Athanassoula, E., et al. 2013a, MNRAS, 430, 836

Ness, M., Freeman, K., Athanassoula, E., et al. 2013b, MNRAS, 432, 2092

Ness, M., Zasowski, G., Johnson, J. A., et al. 2016, ApJ, 819, 2

Ness, M. K., Johnston, K. V., Blancato, K., et al. 2019, ApJ, 883, 177

Nidever, D. L., Bovy, J., Bird, J. C., et al. 2014, ApJ, 796, 38

Nidever, D. L., Holtzman, J. A., Allende Prieto, C., et al. 2015, AJ, 150, 173

Nissen, P. E. 2015, A&A, 579, A52

Nissen, P. E., Christensen-Dalsgaard, J., Mosumgaard, J. R., et al. 2020, A&A, 640, A81

Nomoto, K., Thielemann, F. K., & Yokoi, K. 1984, ApJ, 286, 644

Nuza, S. E., Scannapieco, C., Chiappini, C., et al. 2019, MNRAS, 482, 3089

Oesch, P. A., Brammer, G., van Dokkum, P. G., et al. 2016, ApJ, 819, 129

Onken, C. A., Wolf, C., Bessell, M. S., et al. 2019, PASA, 36, e033

Oort, J. H., Kerr, F. J., & Westerhout, G. 1958, MNRAS, 118, 379

Orkney, M. D. A., Laporte, C. F. P., Grand, R. J. J., et al. 2022, MNRAS, 517, L138

Ortolani, S., Held, E. V., Nardiello, D., et al. 2019, A&A, 627, A145

Ortolani, S., Renzini, A., Gilmozzi, R., et al. 1995, Nature, 377, 701

Osorio, Y., Allende Prieto, C., Hubeny, I., Mészáros, S., & Shetrone, M. 2020, A&A, 637, A80

Ou, X., Necib, L., & Frebel, A. 2022, arXiv e-prints, arXiv:2208.01056

Pagel, B. E. J. 1997, Nucleosynthesis and Chemical Evolution of Galaxies

Pagel, B. E. J. 2009, Nucleosynthesis and Chemical Evolution of Galaxies

Palicio, P. A., Martinez-Valpuesta, I., Allende Prieto, C., et al. 2018, MNRAS, 478, 1231

Pasquini, L., Avila, G., Blecha, A., et al. 2002, The Messenger, 110, 1

Paxton, B., Bildsten, L., Dotter, A., et al. 2011, ApJS, 192, 3

Pedregosa, F., Varoquaux, G., Gramfort, A., et al. 2012, arXiv e-prints, arXiv:1201.0490

Pérez-Villegas, A., Portail, M., & Gerhard, O. 2017a, MNRAS, 464, L80

Pérez-Villegas, A., Portail, M., Wegg, C., & Gerhard, O. 2017b, APJ, 840, L2

Perottoni, H. D., Limberg, G., Amarante, J. A. S., et al. 2022, APJ, 936, L2

Pfenniger, D. 1984, A&A, 134, 373

Pietrukowicz, P., Kozłowski, S., Skowron, J., et al. 2015, ApJ, 811, 113

Piffl, T., Scannapieco, C., Binney, J., et al. 2014, A&A, 562, A91

Pinna, F., Falcón-Barroso, J., Martig, M., et al. 2019a, A&A, 625, A95

Pinna, F., Falcón-Barroso, J., Martig, M., et al. 2019b, A&A, 623, A19

Pipino, A., D'Ercole, A., Chiappini, C., & Matteucci, F. 2010, MNRAS, 407, 1347

Piskunov, N. & Valenti, J. A. 2017, A&A, 597, A16

Plotnikova, A., Carraro, G., Villanova, S., & Ortolani, S. 2022, ApJ, 940, 159

Poelarends, A. J. T., Herwig, F., Langer, N., & Heger, A. 2008, ApJ, 675, 614

Poggio, E., Drimmel, R., Andrae, R., et al. 2020, Nature Astronomy, 4, 590

Poggio, E., Drimmel, R., Cantat-Gaudin, T., et al. 2021, arXiv e-prints, arXiv:2103.01970

Poggio, E., Drimmel, R., Lattanzi, M. G., et al. 2018, MNRAS, 481, L21

Pont, F. & Eyer, L. 2004, MNRAS, 351, 487

Portail, M., Gerhard, O., Wegg, C., & Ness, M. 2017, MNRAS, 465, 1621

Portail, M., Wegg, C., & Gerhard, O. 2015, MNRAS, 450, L66

Price-Whelan, A. M., Sipőcz, B. M., Günther, H. M., et al. 2018, AJ, 156, 123

Prudil, Z., Dékány, I., Grebel, E. K., & Kunder, A. 2020, MNRAS, 492, 3408

Queiroz, A. B. A., Anders, F., Chiappini, C., & et al. submitted

Queiroz, A. B. A., Anders, F., Chiappini, C., et al. 2020, A&A, 638, A76

Queiroz, A. B. A., Anders, F., Santiago, B. X., et al. 2018, MNRAS, 476, 2556

Queiroz, A. B. A., Chiappini, C., & et al. in prep.

Queiroz, A. B. A., Chiappini, C., Perez-Villegas, A., et al. 2021, A&A, 656, A156

Raha, N., Sellwood, J. A., James, R. A., & Kahn, F. D. 1991, Nature, 352, 411

Randich, S., Gilmore, G., Magrini, L., et al. 2022, arXiv e-prints, arXiv:2206.02901

Rattenbury, N. J., Mao, S., Debattista, V. P., et al. 2007, MNRAS, 378, 1165

Razera, R., Barbuy, B., Moura, T. C., et al. 2022, MNRAS, 517, 4590

Recio-Blanco, A., de Laverny, P., Allende Prieto, C., et al. 2016, A&A, 585, A93

Recio-Blanco, A., de Laverny, P., Palicio, P. A., et al. 2022, arXiv e-prints, arXiv:2206.05541

Recio-Blanco, A., Rojas-Arriagada, A., de Laverny, P., et al. 2017, A&A, 602, L14

Reddy, B. E., Lambert, D. L., & Allende Prieto, C. 2006, MNRAS, 367, 1329

Reid, M. J., McClintock, J. E., Steiner, J. F., et al. 2014, ApJ, 796, 2

Rendle, B. M., Miglio, A., Chiappini, C., et al. 2019, MNRAS, 490, 4465

Renzini, A., D'Antona, F., Cassisi, S., et al. 2015, MNRAS, 454, 4197

Renzini, A., Gennaro, M., Zoccali, M., et al. 2018, ApJ, 863, 16

Rich, R. M. 1988, AJ, 95, 828

Rich, R. M. 1990, ApJ, 362, 604

Rich, R. M. 2013, in Planets, Stars and Stellar Systems. Volume 5: Galactic Structure and Stellar Populations, ed. T. D. Oswalt & G. Gilmore, Vol. 5, 271

Rich, R. M., Origlia, L., & Valenti, E. 2012, ApJ, 746, 59

Rich, R. M., Reitzel, D. B., Howard, C. D., & Zhao, H. 2007, APJ, 658, L29

Riess, A. G., Casertano, S., Yuan, W., et al. 2018, ApJ, 861, 126

Rim, P., Steinhardt, C., Clark, T., et al. 2022, in American Astronomical Society Meeting Abstracts, Vol. 54, American Astronomical Society Meeting Abstracts, 241.38

Rix, H.-W., Chandra, V., Andrae, R., et al. 2022, arXiv e-prints, arXiv:2209.02722

Robertson, B. E., Tacchella, S., Johnson, B. D., et al. 2022, arXiv e-prints, arXiv:2212.04480

Robin, A. C., Bienaymé, O., Salomon, J. B., et al. 2022, arXiv e-prints, arXiv:2208.13827

Robin, A. C., Reylé, C., Fliri, J., et al. 2014, A&A, 569, A13

Rodrigues, T. S., Bossini, D., Miglio, A., et al. 2017, MNRAS, 467, 1433

Rodrigues, T. S., Girardi, L., Miglio, A., et al. 2014, MNRAS, 445, 2758

Rojas-Arriagada, A., Recio-Blanco, A., de Laverny, P., et al. 2017, A&A, 601, A140

Rojas-Arriagada, A., Recio-Blanco, A., Hill, V., et al. 2014, A&A, 569, A103

Rojas-Arriagada, A., Zasowski, G., Schultheis, M., et al. 2020, MNRAS, 499, 1037

Rojas-Arriagada, A., Zoccali, M., Schultheis, M., et al. 2019, A&A, 626, A16

Romero-Gómez, M., Mateu, C., Aguilar, L., Figueras, F., & Castro-Ginard, A. 2019, A&A, 627, A150

Rossi, L. J. 2015, Astronomy and Computing, 12, 11

Rougoor, G. W. & Oort, J. H. 1960, Proceedings of the National Academy of Science, 46, 1

Ruiz-Lara, T., Gallart, C., Bernard, E. J., & Cassisi, S. 2020, Nature Astronomy, 4, 965

Ruiz-Lara, T., Matsuno, T., Sofie Lövdal, S., et al. 2022, arXiv e-prints, arXiv:2201.02405

Rybizki, J., Green, G. M., Rix, H.-W., et al. 2022, MNRAS, 510, 2597

Saito, R. K., Hempel, M., Minniti, D., et al. 2012, A&A, 537, A107

Salaris, M., Chieffi, A., & Straniero, O. 1993, ApJ, 414, 580

Sales-Silva, J. V., Daflon, S., Cunha, K., et al. 2022, ApJ, 926, 154

Salvadori, S., Ferrara, A., Schneider, R., Scannapieco, E., & Kawata, D. 2010, MNRAS, 401, L5

Sanders, J. L., Smith, L., & Evans, N. W. 2019a, MNRAS, 488, 4552

Sanders, J. L., Smith, L., Evans, N. W., & Lucas, P. 2019b, MNRAS, 487, 5188

Santiago, B. X., Brauer, D. E., Anders, F., et al. 2016, A&A, 585, A42

Savino, A., Koch, A., Prudil, Z., Kunder, A., & Smolec, R. 2020, arXiv e-prints, arXiv:2006.12507

Schlafly, E. F., Meisner, A. M., & Green, G. M. 2019, ApJS, 240, 30

Schlafly, E. F., Meisner, A. M., Stutz, A. M., et al. 2016, ApJ, 821, 78

Schönrich, R. & Binney, J. 2009, MNRAS, 399, 1145

Schönrich, R., Binney, J., & Dehnen, W. 2010, MNRAS, 403, 1829

Schramm, D. N. & Turner, M. S. 1998, Reviews of Modern Physics, 70, 303

Schultheis, M., Rich, R. M., Origlia, L., et al. 2019, A&A, 627, A152

Schultheis, M., Rojas-Arriagada, A., Cunha, K., et al. 2020, A&A, 642, A81

Schultheis, M., Rojas-Arriagada, A., García Pérez, A. E., et al. 2017, A&A, 600, A14

Scolnic, D., Casertano, S., Riess, A., et al. 2015, ApJ, 815, 117

Scott, D. W. 1992, Multivariate Density Estimation

Scott, N., van de Sande, J., Sharma, S., et al. 2021, APJ, 913, L11

Sellwood, J. A. 1981, A&A, 99, 362

Shank, D., Beers, T. C., Placco, V. M., et al. 2022, ApJ, 926, 26

Shapley, H. & Curtis, H. D. 1921, Bulletin of the National Research Council, 2, 171

Sharma, S., Hayden, M. R., & Bland-Hawthorn, J. 2020, arXiv e-prints, arXiv:2005.03646

Shaw, M., Wilkinson, A., & Carter, D. 1993, A&A, 268, 511

Shen, J., Rich, R. M., Kormendy, J., et al. 2010, APJ, 720, L72

Siebert, A., Famaey, B., Minchev, I., et al. 2011, MNRAS, 412, 2026

Silva Aguirre, V., Bojsen-Hansen, M., Slumstrup, D., et al. 2018, MNRAS, 475, 5487

Simion, I. T., Belokurov, V., Irwin, M., et al. 2017, MNRAS, 471, 4323

Skrutskie, M. F., Cutri, R. M., Stiening, R., et al. 2006, AJ, 131, 1163

Smee, S. A., Gunn, J. E., Uomoto, A., et al. 2013, AJ, 146, 32

Smiljanic, R., Korn, A. J., Bergemann, M., et al. 2014, A&A, 570, A122

Smith, M. C., Evans, N. W., Belokurov, V., et al. 2009, MNRAS, 399, 1223

Smith, R., Flynn, C., Candlish, G. N., Fellhauer, M., & Gibson, B. K. 2015, MNRAS, 448, 2934

Sneden, C., Cowan, J. J., & Gallino, R. 2008, ARA&A, 46, 241

Sneden, C., Gratton, R. G., & Crocker, D. A. 1991, A&A, 246, 354

Soderblom, D. R. 2010, ARA&A, 48, 581

Souto, D., Cunha, K., & Smith, V. V. 2021, ApJ, 917, 11

Souto, D., Cunha, K., Smith, V. V., et al. 2022, ApJ, 927, 123

Souza, S. O., Ernandes, H., Valentini, M., et al. 2023, arXiv e-prints, arXiv:2301.05227

Souza, S. O., Kerber, L. O., Barbuy, B., et al. 2020, ApJ, 890, 38

Spina, L., Meléndez, J., Karakas, A. I., et al. 2018, MNRAS, 474, 2580

Spina, L., Ting, Y. S., De Silva, G. M., et al. 2021, MNRAS, 503, 3279

Spitoni, E., Silva Aguirre, V., Matteucci, F., Calura, F., & Grisoni, V. 2019, A&A, 623, A60

Spitoni, E., Verma, K., Silva Aguirre, V., et al. 2021, A&A, 647, A73

Springel, V., White, S. D. M., Frenk, C. S., et al. 2008, Nature, 456, 73

Starkenburg, E., Martin, N., Youakim, K., et al. 2017, MNRAS, 471, 2587

Stassun, K. G. & Torres, G. 2018, ApJ, 862, 61

Stebbins, J. & Whitford, A. E. 1947, ApJ, 106, 235

Steinmetz, M., Guiglion, G., McMillan, P. J., et al. 2020a, AJ in press, arXiv:2002.04512

Steinmetz, M., Guiglion, G., McMillan, P. J., et al. 2020b, arXiv e-prints, arXiv:2002.04512

Steinmetz, M., Zwitter, T., Siebert, A., et al. 2006, AJ, 132, 1645

Sukhbold, T., Ertl, T., Woosley, S. E., Brown, J. M., & Janka, H. T. 2016, ApJ, 821, 38

Surot, F., Valenti, E., Hidalgo, S. L., et al. 2019, A&A, 623, A168

Tacchella, S., Carollo, C. M., Renzini, A., et al. 2015, Science, 348, 314

Thorsbro, B., Ryde, N., Rich, R. M., et al. 2020, ApJ, 894, 26

Tinsley, B. M. 1980, Fund. Cosmic Phys., 5, 287

Travaglio, C., Gallino, R., Arnone, E., et al. 2004, ApJ, 601, 864

Traven, G., Feltzing, S., Merle, T., et al. 2020, A&A, 638, A145

Traven, G., Matijevič, G., Zwitter, T., et al. 2017, ApJS, 228, 24

Trick, W. H., Fragkoudi, F., Hunt, J. A. S., Mackereth, J. T., & White, S. D. M. 2021, MNRAS, 500, 2645

Trumpler, R. J. 1930, Lick Observatory Bulletin, 420, 154

Tsujimoto, T. & Bekki, K. 2012, ApJ, 747, 125

Tsujimoto, T., Nomoto, K., Yoshii, Y., et al. 1995, MNRAS, 277, 945

Tucci Maia, M., Ramírez, I., Meléndez, J., et al. 2016, A&A, 590, A32

Tully, R. B., Courtois, H., Hoffman, Y., & Pomarède, D. 2014, Nature, 513, 71

Übler, H., Genzel, R., Wisnioski, E., et al. 2019, ApJ, 880, 48

Valenti, E., Zoccali, M., Gonzalez, O. A., et al. 2016, A&A, 587, L6

Valenti, E., Zoccali, M., Renzini, A., et al. 2013, A&A, 559, A98

Valentini, M., Chiappini, C., Bossini, D., et al. 2019, A&A, 627, A173

Valentini, M., Chiappini, C., Davies, G. R., et al. 2017, A&A, 600, A66

Valle, G., Dell'Omodarme, M., Prada Moroni, P. G., & Degl'Innocenti, S. 2015, A&A, 579, A59

van der Maaten, L. & Hinton, G. 2008, The Journal of Machine Learning Research, 9, 85

van Dokkum, P. G., Leja, J., Nelson, E. J., et al. 2013, APJ, 771, L35

Verma, M., Matijevič, G., Denker, C., et al. 2021, ApJ, 907, 54

Vincenzo, F. & Kobayashi, C. 2020, MNRAS, 496, 80

Virtanen, P., Gommers, R., Burovski, E., et al. 2019

Viscasillas Vazquez, C., Magrini, L., Casali, G., et al. 2022, A&A, 660, A135

Wallerstein, G. 1962, ApJS, 6, 407

Watkins, L. L., van der Marel, R. P., Sohn, S. T., & Evans, N. W. 2019, ApJ, 873, 118

Wattenberg, M., Viégas, F., & Johnson, I. 2016, Distill

Wegg, C. & Gerhard, O. 2013, The Messenger, 154, 54

Wegg, C., Gerhard, O., & Bieth, M. 2019, MNRAS, 485, 3296

Wegg, C., Gerhard, O., & Portail, M. 2017, APJ, 843, L5

Weiland, J. L., Arendt, R. G., Berriman, G. B., et al. 1994, APJ, 425, L81

Weiler, M. 2018, A&A, 617, A138

Weinberg, D. H., Holtzman, J. A., Hasselquist, S., et al. 2019, ApJ, 874, 102

Werner, M. W., Roellig, T. L., Low, F. J., et al. 2004, ApJS, 154, 1

White, S. D. M. & Frenk, C. S. 1991, ApJ, 379, 52

Williams, M. E. K., Steinmetz, M., Binney, J., et al. 2013, MNRAS, 436, 101

Wilson, J. C., Hearty, F., Skrutskie, M. F., et al. 2010, in Society of Photo-Optical Instrumentation Engineers (SPIE) Conference Series, Vol. 7735, Proc. SPIE, 77351C

Wilson, J. C., Hearty, F. R., Skrutskie, M. F., et al. 2019, PASP, 131, 055001

Wise, J. H., Turk, M. J., Norman, M. L., & Abel, T. 2012, ApJ, 745, 50

Woosley, S. E., Heger, A., & Weaver, T. A. 2002, Reviews of Modern Physics, 74, 1015

Wright, E. L., Eisenhardt, P. R. M., Mainzer, A. K., et al. 2010, AJ, 140, 1868

Wu, Y., Du, B., Luo, A., Zhao, Y., & Yuan, H. 2014, in Statistical Challenges in 21st Century Cosmology, ed. A. Heavens, J.-L. Starck, & A. Krone-Martins, Vol. 306, 340–342

Xiang, M. & Rix, H.-W. 2022, Nature, 603, 599

Xiang, M., Ting, Y.-S., Rix, H.-W., et al. 2019, ApJS, 245, 34

Xiang, M.-S., Rix, H.-W., Ting, Y.-S., et al. 2020, ApJ, 898, 28

Xu, Y., Reid, M., Dame, T., et al. 2016, Science Advances, 2, e1600878

Yan, Y., Du, C., Liu, S., et al. 2019, ApJ, 880, 36

Yanny, B., Rockosi, C., Newberg, H. J., et al. 2009, AJ, 137, 4377

York, D. G., Adelman, J., Anderson, John E., J., et al. 2000, AJ, 120, 1579

Yoshii, Y. 1982, PASJ, 34, 365

Zasowski, G., Cohen, R. E., Chojnowski, S. D., et al. 2017, AJ, 154, 198

Zasowski, G., Johnson, J. A., Frinchaboy, P. M., et al. 2013, AJ, 146, 81

Zasowski, G., Schultheis, M., Hasselquist, S., et al. 2019, ApJ, 870, 138

Zhang, X., Feng, Y., Chen, H., & Yuan, Q. 2020, ApJ, 905, 97

Zhao, G., Zhao, Y.-H., Chu, Y.-Q., Jing, Y.-P., & Deng, L.-C. 2012, Research in Astronomy and Astrophysics, 12, 723

Zhao, H., Schultheis, M., Arentsen, A., et al. 2023, MNRAS, 519, 754

Zinn, J. C., Pinsonneault, M. H., Huber, D., & Stello, D. 2019, ApJ, 878, 136

Zoccali, M., Gonzalez, O. A., Vasquez, S., et al. 2014, A&A, 562, A66

Zoccali, M., Hill, V., Lecureur, A., et al. 2008, A&A, 486, 177

Zoccali, M., Lecureur, A., Barbuy, B., et al. 2006, A&A, 457, L1

Zoccali, M., Renzini, A., Ortolani, S., et al. 2003, A&A, 399, 931

Zoccali, M. & Valenti, E. 2016, PASA, 33, e025

Zoccali, M., Valenti, E., & Gonzalez, O. A. 2018, A&A, 618, A147

Zoccali, M., Vasquez, S., Gonzalez, O. A., et al. 2017, A&A, 599, A12

Zwitter, T., Siebert, A., Munari, U., et al. 2008, AJ, 136, 421